Developments in Time-resolved Ultrafast Imaging and Spectroscopy at Terahertz Frequencies

by

Stephanie M. Teo

B. Sc. in Chemistry, McGill University (2009)

Submitted to the Department of Chemistry
in partial fulfillment of the requirements for the degree of

Doctor of Philosophy

at the

MASSACHUSETTS INSTITUTE OF TECHNOLOGY

June 2014

Signature redacted

Author ....
Department of Chemistry
May 21, 2014

Signature redacted

Certified by ....
Keith A. Nelson
Professor of Chemistry
Thesis Supervisor

Signature redacted

Accepted by ....
Robert W. Field
Chairman, Department Committee on Graduate Theses

This doctoral thesis has been examined by a Committee of the Department of Chemistry as follows:

Signature redacted

Professor Moungi G. Bawendi..... .....

Chairman, Thesis Committee

Lester Wolfe Professorship in Chemistry

Signature redacted

Professor Keith A. Nelson ....

Thesis Supervisor

Professor of Chemistry

Signature redacted

Professor Sylvia T. Ceyer..... .....

Member, Thesis Committee

J. C. Sheehan Professor of Chemistry

Developments in Time-resolved Ultrafast Imaging and Spectroscopy at Terahertz Frequencies

by

Stephanie M. Teo

Submitted to the Department of Chemistry
on May 21, 2014, in partial fulfillment of the
requirements for the degree of
Doctor of Philosophy

Abstract

Prior to the advent of high energy pulsed femtosecond lasers, the field of terahertz (THz) spectroscopy was stagnated by the lack of both high power THz sources and sensitive THz detectors. Over the past few years, it has become more 'routine' to generate and detect THz radiation between 0.1-10 THz, but there remains much room for improvement. In this work, I describe recent developments in THz detection methodology, both in a waveguide platform and in a more typical free space geometry. In the waveguide approach, THz generation, detection, and manipulation is self-contained in an on-chip system that we term the polaritonics platform, which simply consists of a single slab of an electro-optic (EO) crystal called lithium niobate. Due to the experimental geometry, we can conduct time-resolved phase-sensitive imaging of the propagating THz waves in the crystal. Alternatively, more conventional THz spectroscopy requires free space propagation between generation and detection such that a sample could be interrogated if placed between them.

Within this thesis, I present improvements in spatial resolution and signal-to-noise (S/N) to two time-resolved THz imaging instruments on the polaritonics platform: phase contrast imaging and polarization gating imaging. Across both techniques, we attained a best image resolution of less than 1.5 μm ($< \lambda/100$ at 0.5 THz), which is needed for studying very fine structures and near-fields in the THz regime, and a lowest noise floor of 0.12%, which is attractive for measuring small signals. We used THz imaging to explore wave behavior in metal-clad waveguide systems by employing indium tin oxide (ITO), which is a conductor at THz frequencies, but transparent at visible frequencies. We deemed ITO to behave similarly to an ideal metal, despite its low electrical conductivity. This presents the possibility of fabricating transparent THz-resonant metallic microstructures for near-field studies. Furthermore, we studied leaky wave behavior in the metal-clad waveguides, which presents a means for coupling THz radiation out of the waveguide.

Lastly, I describe recent developments in free space THz detection, which traditionally consists of a time-intensive optically gated measurement in a pump-probe geometry called EO sampling. Unfortunately, this method is not conducive to measurements of irreversible processes or measurements that involve resolving an additional time axis such as in two-dimensional (2D) spectroscopy experiments. In the new methodology that is discussed here, we instead acquire a THz time trace in a single laser pulse using a pair of transmission-mode glass echelon optics. We demonstrate that this single-shot method is a robust alternative to conventional scanning EO sampling that can quantitatively record THz field temporal profiles with the same S/N approximately 20 times faster than the conventional method. As a prototype 2D measurement, we applied the single-shot method to an optical pump-THz probe study of a indirect bandgap semiconductor, tin sulfide (SnS), which is currently being investigated as a material for solar cell technology. The 2D measurement made it possible to characterize carrier lifetimes and photoconductivity at THz frequencies as a function of carrier relaxation time. This initial demonstration is only the beginning of future exploration of a wide variety of systems, where we intend to extend the technique towards 2D Fourier transform THz spectroscopy to unravel behavior too complex to be resolved by linear spectra.

Thesis Supervisor: Keith A. Nelson
Title: Professor of Chemistry

Acknowledgments

Being decisive has never been my strong suit. As a kid, I imagined being *everything* when I grew up, so depending on when you asked me, I'd probably tell you something different. My earliest aspiration was to become an artist. Everyday, I'd spend countless hours sketching cartoons and then faxing them to my parents who lived on the other side of the world for most of my childhood. As the years went on, I developed a strong interest in basketball, but unfortunately my promising sports career was brought to a grinding halt by my "average" height. The decision fatigue continued on with aspirations of becoming a chef, a doctor (the other kind), and finally, settling on becoming a scientist. In some ways, where I am today feels a lot like the product of playing Russian roulette. While I never expected to be here, it has been quite the journey, and one that I do not regret embarking on.

Over the years, there have been so many people to help guide me through life, which has made making decisions astronomically easier. The following will be my attempt at thanking them, so here goes.

First off, I have to thank my advisor, Keith Nelson, who took me into his lab when I had no place to call home. Little did I know what I was getting myself into, but even from our first meeting, I knew that he was someone who I would enjoy working for. His support throughout the years was crucial to my development as a discerning researcher, and his ceaseless enthusiasm about anything science was so very contagious. I always liked talking to Keith about results, not just because of his optimism, but because he always made it feel like what you were doing was important (and that one day, just one day, you could save the world).

Upon joining the Nelson group, I never imagined that I would meet such a highly-concentrated group of life-long friends. I might as well have won the lottery on this one because graduate school would have been, in the most polite terms, just plain dull without them. The first person I met was Kit Werley. He was just full of useful knowledge, not just in concepts, but also in his ability to mentor. I was as blank of a canvas as they came in terms of ultrafast optics, but this did not deter Kit from imparting me with the foundations that I carried throughout my PhD. Working in the lab, day in and day out, was never tedious as while we busied ourselves with building complex optical setups, we also joked about everything you can and probably can't think of and listened to the latest hits as part of Kit's daily music education. I later met many other members of the lab, who made everyday a little more (and sometimes a lot) of an adventure. Dylan H. Arias, my partner in glare, forever to my right, was a source of calm and ridiculousness to say the least. Pat Wen, his deadpan humor still gets me every time. The Sharly, infinitely wise; Sharly was instrumental in giving me fresh perspectives, especially in times when projects felt like they were doomed to fail. Kara Manke, our senses of humor are forever warped, but I'm glad that we're in it together. Nate Brandt, I'll always remember our hiking adventure in snowy Nagano...and the many late nighters. Prasahnt Sivarajah, my fellow Canadian, has

been an incredible addition to Team Polaritonics, and is always up for anything, including a lot of hard work. There are many others who have made my time in the Nelson lab an unforgettable experience: Johanna Wolfson, Colby Steiner, Yongbao Sun, Jeff Eliason, Sam Teitelbaum, Alex Maznev, Jian Lu, and most recently, Brandt Pein.

I also have to thank my two partners in crime in the Nelson lab, both of who made coming into work everyday worth it. This will truly be something that I'll miss and probably never get back. Harold Hwang, the most inquisitive person I know, was always there to lend a hand, whether it was helping with data interpretation in the lab or picking me up off the ground after a hard Insanity workout. And Ben Ofori-Okai, now where do I start? Ben was the very first person I met at MIT and remains my best friend (and my every-3-hour snack buddy). He dared to teach me how to drive and I dared to teach him how to cook, are we even? Although we initially began in different research groups, I'm thankful that the universe knew better.

There were many others that contributed to my sanity and general well-being. Jennifer Scherer has been the most understanding and supportive friend, always there to lend a listening ear. Marco Jost cheered me on from day one, even when I didn't believe in myself – this fist bump is for you! Raoul(ie) Correa, my giggling partner, has been "the instigator" throughout my time here and we all 'thank' him for that. Jian Cui, although we never quite saw eye-to-eye on everything, we had our moments and I cherish them. Elizabeth Lemon, an honorary Nelson group member, I'm glad we passed the psychoanalysis test and that you let us charm you with our craziness. John Regan, it's been an eventful few years. Although I will probably never get all of your references, I'm glad I had you to make me laugh when I needed it most.

In this thesis, many of the projects would not have been possible without the hard work of our collaborators. At Boston University, I had the pleasure of working with Rick Averitt's and Xin Zhang's groups. In Chapter 3, the THz-resonant gold microstructures were made by Kebin Fan, who has a very impressive repertoire of structures he can fabricate. Also in Chapter 4, the ITO-coated lithium niobate slabs were fabricated by both Kebin Fan and Congshun Wang. Recently, we had the opportunity to work with Tonio Buonassisi's group at MIT, in particular Rafael Jaramillo and Vera Steinman, for the tin sulfide thin film samples in Chapter 6. They were very helpful and responsive, especially in a very short period of time with a lot of stress!

Over the years, I'm very happy to have friends who stuck with me through what seems to be the test of time. They were a breath of fresh air outside of my bubble here at MIT. Simone Pereira and Wayne Mah have been pillars of support ever since the good old days in college and I'm sure there are many more to come. To my oldest friends, Tessa Mathew and Chanel Bayram, it only seems like yesterday that we talked about where we would be in 10 or 15 years (and how so very old we would be) – well here we are! I must also thank my undergraduate advisor and my physical chemistry professor, Dr. Grazyna Wilczek, who has shaped me to become the scientist I am today. Coming from a big school, I found it

difficult not to feel like just a number, but Dr. Wilczek was a steady and endless source of encouragement throughout my years at McGill. She taught me to not doubt myself and forced me to excel beyond my comfort zone, and I try to live by her words every day.

Last, but definitely not least, the constant driving force behind the scenes has been the love, encouragement, and relentless support of my parents. They have been my cheerleaders throughout life, and I am grateful for all the sacrifices they have made for me and my siblings. Ahnee, as close as a mother to me, took care of us even before I was born, whether it was bringing us to Taekwondo, swimming, skating, or skiing lessons – you name it, she was there. She has been a very important source of advice and guidance...and she never fails to make me laugh (even if she doesn't know it). And to my siblings, Trey, Gill, and Ben, I honestly couldn't have asked for a better crew of the same genetic makeup to experience all of the stages that life has to offer. I am so excited to see where the future takes us and to have all of you by my side.

Stephanie Teo

May 29, 2014

For my Mom and Dad.

Contents

List of Figures

And now, for your reading pleasure $\cdots$

Chapter 1

Introduction to Terahertz Imaging and Spectroscopy

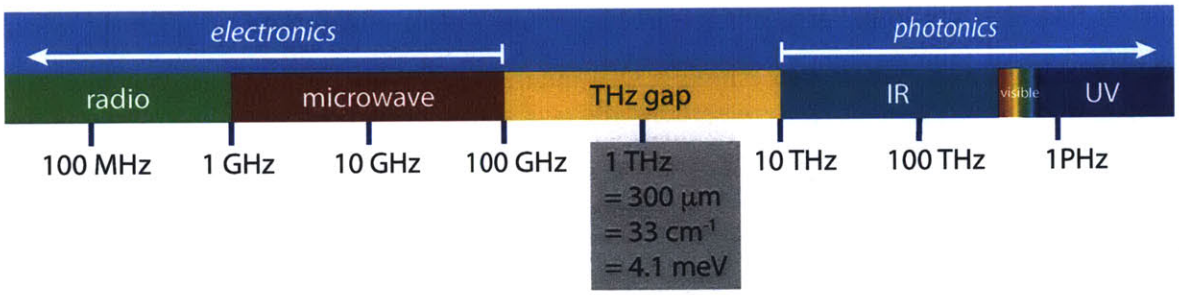

Figure 1-1: **The electromagnetic spectrum.** The THz gap (0.1-10 THz) is shown to lie between the electronics and photonics regimes.

In the electromagnetic spectrum, there is a region between electronics and photonics called "the terahertz (THz) gap". This gap, ranging from 0.1-10 THz (1 THz = 1 ps = 300 μm = 33 cm^{-1} = 4.1 meV = 47.6°K), faces many technological challenges in terms of efficient generation and sensitive detection. For THz generation, the output power of electronic oscillators decreases at higher frequencies due to higher heat dissipation from the electrons, while the emission of photons from a blackbody drops precipitously at lower frequencies according to Planck's law. Similarly, because THz radiation occurs on picosecond timescales,

the rapidly oscillating THz fields are too fast for electronics to respond, but simultaneously too slow for optical technologies. The field of THz spectroscopy has consequently lagged appreciably behind its counterparts across the electromagnetic spectrum. However, shortly after the advent of high energy pulsed femtosecond lasers, D. H. Auston and coworkers showed that it was possible to generate ultrafast broadband THz pulses by propagating femtosecond optical pulses in electro-optic (EO) materials in 1984 [1].

The development of technologies at THz frequencies has been spurred by its fundamental importance in many physical, chemical, and biological processes. For example, there exists an abundance of resonances within the THz range such as molecular rotations in gases, vibrational transitions in molecular crystals, or electronic resonances in quantum wells and quantum dots. Currently, THz spectroscopy has been used in the identification of chemical or biological materials by taking advantage of a material's unique THz resonance(s) or for studying semiconductor or protein dynamics that occur on picosecond timescales. THz radiation has also made an appearance in higher resolution airport security body scanners and biomedical sensing. However, there is still much development and understanding needed of processes occurring in the THz regime.

With the increasing bandwidth demands of a technologically-driven society, there has also been an impetus to develop THz telecommunications since only a small portion of the electromagnetic spectrum is currently allocated (radio frequencies from 9 kHz to 275 GHz). The development of THz technologies is also motivated by the impending deviation from Moore's law within this decade, which postulates the doubling of the number of transistors per integrated circuit every two years. The deviation results from the physical limitations of electronic-based transistors, with atomic-level features being the final stop for electronic computing, all the while assuming that they can be efficiently fabricated. Alternatively, all-optical computing has been vetted as a promising next-generation technology, in which electron signal carriers are superseded by photons that move at the speed of light; in this respect, moving to the THz range is a natural initial step. For example, significant ma-

nipulation of the polarization of THz light was observed as it propagated through a thin mercury telluride film under an applied external magnetic field at room temperature [2]. This resulted in a giant Faraday effect, which suggests its application in fast modulation optical transistors by simply tuning the gate voltage and/or magnetic field.

In this thesis, the central thrust that fueled the projects that I will be discussing was in the development of THz detection technologies; not only for the purpose of making the current types of measurements easier, but to extend our capabilities to measurements that were not possible just a few years ago. Firstly, it is important to understand why THz detection must be viewed as a new challenge compared to well-established detection technologies in the optical and microwave spectral ranges. In the THz regime, the relatively large wavelengths make it difficult to use regular optical components such as mirrors or lenses or to even use our intuitive sense of Gaussian beam propagation since it is impractical to treat THz beams as collimated over large propagation distances. By definition, a beam is said to be collimated if it has a Rayleigh length ($z_r = \pi w_0^2/\lambda$, where w_0 is the beam radius and λ is the wavelength) that is much longer than its propagation distance. For visible wavelengths, a collimated beam typically has a 1 mm beam waist and so the ratio of the Rayleigh length to the wavelength varies from 5 to 20 million. Scaling this ratio to the terahertz regime for 300 μm wavelength (i.e. 1 THz), even on the lower end of the ratio, means that the beam radius has to be 40 cm! Manufacturing and working with optics on this length scale is not practical, which has fundamentally stalled the development of a THz spectrometer device comparable to optical spectrometers in terms of its ease of use and compactness.

As a solution, THz waves are detected by encoding the THz signal onto optical frequency light, where electronic and optical components can be taken advantage of. However, this requires a time-intensive process through a pump-probe measurement in the time domain and subsequent Fourier transforming of the temporal waveform to obtain the THz spectrum. Of course, the development of THz detection goes hand in hand with that of THz generation, which is another strong focus of ongoing progress and development in the Nelson lab. Chap-

ter 2 describes current methodologies used for ultrafast, pulsed THz generation, which rely on the use of an amplified laser system and a nonlinear process called optical rectification in various electro-optic generation crystals. In Chapter 3, I approach THz detection from two distinct fronts: THz imaging in waveguided platforms and more conventional free space THz spectroscopy.

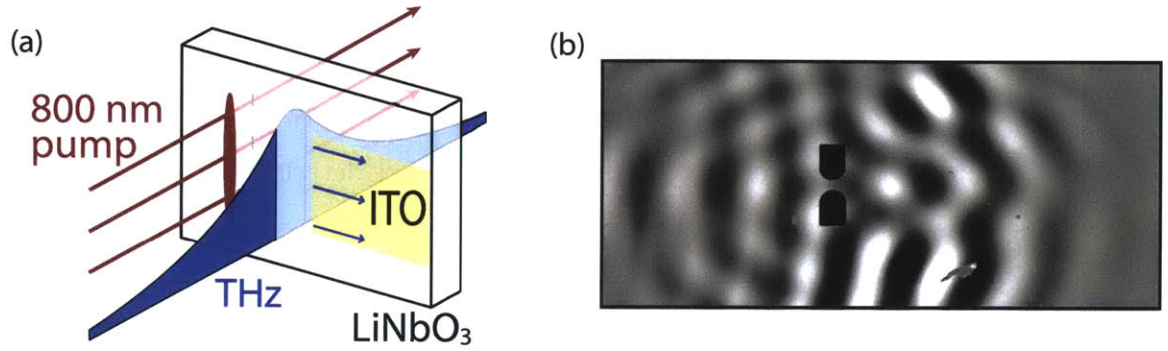

Figure 1-2: **Polaritonics platform for waveguided THz waves:** (a) A thin slab of $LiNbO_3$ allows for the generation, control, and detection of THz waves. Focusing an ultrafast near-infrared pump pulse through the slab generates THz waves that are waveguided laterally down the slab. (b) A snapshot of an image recorded using phase contrast imaging with magnification of 17× and shows a 530 GHz wave interacting with a resonant antenna pair (masked in black for clarity).

In the waveguide platform, called the polaritonics platform [3], THz waveguide modes are generated and detected directly in a single 30-50 μm thick crystal of lithium niobate ($LiNbO_3$) as seen in Fig. 1-2(a). This effectively circumvents any of the technical issues for THz optics previously described and the added difficult of guiding the THz waves into or out of the waveguide. Lithium niobate is an electro-optic crystal, which means that an applied E-field changes the index of refraction of the crystal. Subsequently, the index change induces a phase shift in an optical probe beam that also passes through the crystal, which can be detected by using a phase-sensitive detection scheme. Unique and convenient to this platform is the fact that the THz wave, generated by a focused optical pump beam, travels laterally in the slab and hence allows us to conduct time-resolved imaging of its lateral propagation with an ultrafast, expanded optical probe beam.

Recently, I have improved the spatial resolution and signal-to-noise (S/N) ratio of two THz imaging techniques called phase contrast imaging and polarization gating imaging [4]. In phase contrast imaging, I developed an imaging system that is capable of resolving features with subwavelength resolution of less than 1.5 μm ($< \lambda/100$ at 0.5 THz) and a 0.2% noise floor; this represents a 4-fold improvement in resolution compared to other methods [5]. Figure 1-2(b) shows an example of the propagation of a THz wave at one instance of time, interacting with a metal antenna structure deposited on the surface of lithium niobate. This system presents new opportunities for studying very fine structures and near-fields in the THz regime. In addition, I further improved another technique called polarization gating imaging that is typically employed for more quantitative measurements since it has a lower noise floor of 0.12%, an improvement of up to 5-fold over previous designs, and also more than sufficient spatial resolution better than 5 μm.

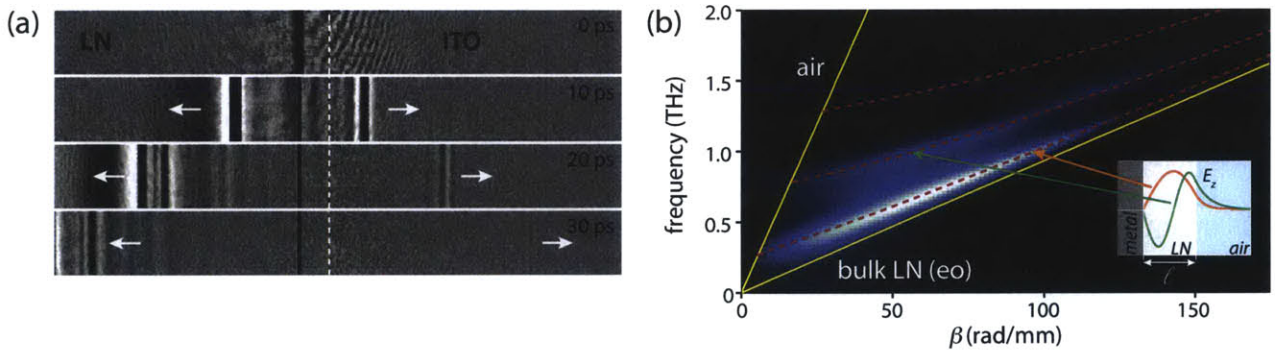

Figure 1-3: **ITO metallic slab waveguides:** (a) A time series of images of a TE mode THz electric field, collected using polarization gating imaging. The left side of the dashed line shows plain slab LN, where the THz waves are generated. The right side of the dashed line shows a region that has been coated with THz-transparent metallic ITO layer, where the waves are observed to propagate underneath. (b) Waveguide dispersion curve for TE waves in a LN waveguide (thickness $\ell = 54$ μm) with ITO deposited on one surface. Dispersion of air and bulk LN extraordinary (eo) and ordinary (o) waves are shown in yellow. Analytical solutions in dashed red are overlaid on the experimentally observed results. Inset: calculated E_z-field profiles of the two lowest order TE modes at 1 THz.

Following the development of these high-resolution and low-noise THz imaging techniques, I wanted to further exploit advantages of the compact, on-chip platform. In addition to the simultaneous generation and detection of THz waves on a single chip, the platform

is capable of manipulating and furthering our understanding of THz wave behavior and its propagation characteristics under different conditions. In Chapter 4, I studied a system composed of a metal clad planar waveguide, where the 'metal' used was a wide bandgap semiconductor, indium tin oxide (ITO). The key property that makes ITO an attractive material in our system is the fact that it is transparent to visible light (i.e. the optical imaging probe beam), but opaque (or metallic) at THz frequencies. Figure 1-3(a) shows an example of the visibility of a propagating THz wave in lithium niobate underneath the ITO layer, as given by the experimental geometry in Fig. 1-2(a). We confirmed that ITO behaves similarly to an ideal metal by comparing its waveguide dispersion to that provided by analytical theory [6], in which the measured dispersion curves in Fig. 1-3(b) showed good agreement.

Our motivation to study THz waves in this metallic clad geometry was two-fold. Firstly, in a previous study of ours, we deposited a pair of THz-resonant gold dipole antennas separated by a small gap, similar to that shown in Fig. 1-2(b), on the surface of lithium niobate and quantitatively studied the THz near-field enhancement that was primarily localized in the subwavelength gap [7]. However, the near-fields cannot be measured underneath gold, as it is opaque to the optical probe light, but measurement of the near-fields would be accessible in resonant microstructures fabricated out of ITO. Secondly, because coupling light into and out of the waveguide is very difficult, a required mechanism if the chip were designed as a signal modulation component in a device, it was natural to study leaky wave behavior. As opposed to bound waveguide modes that make up the propagating solutions to Maxwell's equations, leaky waves are unbound and as given by their name, leak or couple out of the waveguide.

In the second area of focus for the development of THz detection methodology, I returned back to the idea of a THz spectrometer where the THz waves propagate in free space (as opposed to in a waveguide). As I previously stated, because of the speed limitations of electronic instrumentation, THz detection is a time domain method, called electro-optic

sampling, that requires an iterative process to map out the temporal THz waveform by measuring it at many sequential time points. In other words, in the pump-probe geometry, an ultrafast optical probe is used to 'gate' the THz electric field and so we can resolve the field with time resolution on the order of the pulse duration of the optical probe (typically 100 fs or less). The underlying assumption here is that the process being measured is reversible and repeatable since effectively, the experiment is repeated over and over again, but measured at a different moment in time. Following a Fourier transform of the time domain data, the THz pulse's spectral content is attained, and so free space THz spectroscopy becomes analogous to frequency domain methods such as those used in optical or near-infrared detection.

The fact that the detection requires a time-intensive process becomes a problem in the measurement of processes that are irreversible since it may only be feasible to use a limited number of probe pulses (i.e. a very short observation window with little to no averaging) before the material has changed significantly through processes such as an irreversible chemical reaction, degradation, or complete destruction. Even in systems that are reversible, the time-intensive nature of the measurement negatively impacts any two-dimensional (2D) spectroscopy measurement that involves resolving a second time-axis. While there is a wealth of information that can be learnt from linear THz spectra, much of this information is often difficult to interpret. 2D measurements can help to untangle potentially convoluted responses in linear spectra by adding another axis by which we can observe the system's response as a result of an additional applied perturbation. In one aspect, 2D measurements aid in the understanding of the correlation between different degrees of freedom in a system; for example, in studying how excitonic states couple to low-lying phonon states, or how mechanical energy is transferred to high-frequency molecular bond vibrations in energetic materials. However, these kinds of experiments require substantial scaling up of experimental time (i.e. 1D scan: $\sim n$ time points, 2D scan: $\sim n^2$ time points, etc.), and are only practical with faster acquisition techniques.

As a way of circumventing the time-intensive process, I developed and evaluated two de-

tection schemes that acquired a THz time trace in a single probe pulse, which means that no iterative mapping out of the THz waveform is needed. To date, there exist several single-shot THz detection techniques, but while they have demonstrated the ability to measure a THz waveform, they have mainly been developed towards the purpose of diagnostics. In Chapter 5, I surveyed the single-shot techniques for ones that could be adapted to quantitatively measure THz electric fields with good S/N, with the end goal of surpassing conventional electro-optic sampling in terms of acquisition time. Of the two methods I tested, only one method was successful, based on a pair of transmission-mode glass stair-step optics called echelons (see Fig. 1-4(a)). When the probe beam passes through a thin and a thick echelon, each with m steps, it is split into an array of tiny 'beamlets' that are delayed incrementally in time relative to one another. The more glass a beamlet passes through, the longer the time delay. Each beamlet derived from a single probe pulse measures a different temporal slice of the THz electric field. Figure 1-4(b) shows a direct comparison of the THz time traces acquired from both the single-shot method and the conventional scanning delay-line method, which demonstrates good agreement in both amplitude and spatiotemporal waveform. The corresponding THz spectra in Fig. 1-4(c) corroborate these findings with near to identical spectral content. Most importantly, the system was optimized to acquire low-noise traces by careful selection and implementation of optical and hardware components. Overall, the single-shot system was capable of attaining the same S/N as that of the conventional scanning method in only $1/20^{\text{th}}$ the number of laser pulses, which poses a significant source of time-saving.

Although the single-shot THz detection system is not as compact in size as an optical spectrometer, there is still an obvious benefit to its significant reduction in acquisition time. The last study discussed in Chapter 6 was conducted with the aim of fully integrating the THz single-shot detection technique into a 2D measurement and evaluating its efficiency in a real scenario. This initial measurement serves as a prototype for future 2D Fourier transform THz spectroscopy, in which we intend to use a THz pump, and probe a system

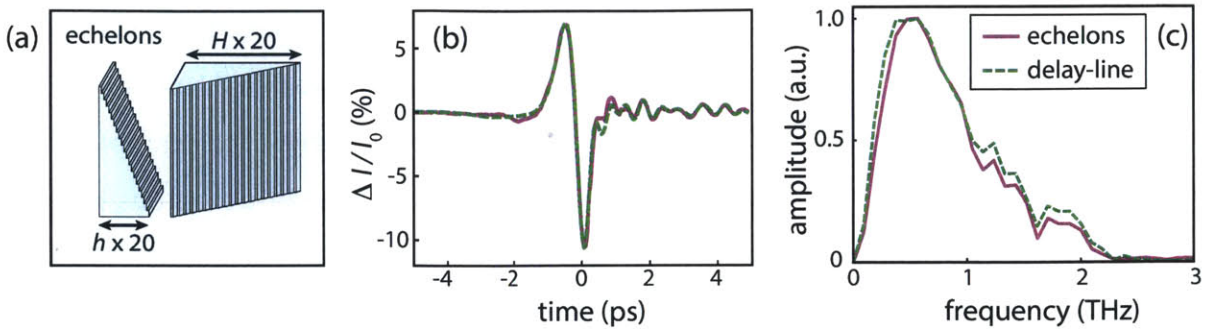

Figure 1-4: **Single-shot THz detection:** (a) A schematic of the pair of transmission-mode glass echelons. A probe beam is passed through the crossed echelons and split into a train of small beamlets that are delayed incrementally in time relative to one another. (b) A direct comparison of THz time traces between the dual echelons method and scanning delay-line method. (c) Fourier transforms of the time traces given in (b).

with responses that may have very strong frequency-dependence in the THz regime.

Time domain measurements, where both the amplitude and phase of the THz electric field are obtained, have an important added value since it allows us to measure complex optical properties (e.g., index of refraction, conductivity) of materials. The 2D measurement consisted of an optical pump-THz probe experimental setup, which was capable of measuring the minority carrier lifetime and photoconductivity of a thin-film semiconductor, tin sulfide (SnS), at THz frequencies. The carrier lifetime, the average time it takes for the carriers to relax to the bottom of the conduction band, is an important metric for characterizing the carrier dynamics in solar cell materials such as SnS [8]. In these indirect band gap semiconductors, defect sites contribute significantly to the carrier lifetime, which has important consequences on device efficiency.

Generally speaking, the development of new techniques opens the door to new varieties of measurements. Naturally, it is important to ask: what are the immediate potential systems and physics readily accessible to us as a result of the techniques developed thus far? In the near future, we intend to explore the electronic-phonon coupling in other optically-pumped systems such as organic crystals and quantum dots. As THz generation techniques continue to improve, there exists the possibility for even stronger driving of nonlinear THz

responses, which will help in the elucidation of the nature of vibrational couplings in molecular systems. Additionally in the polaritonics platform, it may be possible to measure surface plasmon phonon-polaritons by studying the modified dispersion curves, for example as a result of the coupling between surface plasmons in graphene and phonon-polaritons in LN [9]. These are just a few possibilities of systems worth investigating; further understanding of the capabilities and limits of these new techniques will help guide the way towards other interesting and unexplained phenomena.

Chapter 2

Terahertz Generation in Bulk and Waveguided Systems

2.1 Introduction

The strong drive to developing THz spectroscopy was aided by the discovery that THz radiation with suitable spectral brightness could be generated, propagated in free-space, and then separately detected [10, 11]. The significance of this simple scheme was that a sample could be placed between the generation and detection components and consequently it provided a means for spectroscopic characterization of materials in the THz regime. This was the era dominated by the photoconductive antenna, where an ultrafast laser pulse is used to generate carriers in the conduction band of a semiconductor between a pair of antennas under a voltage bias. The acceleration of carriers across the biased antenna creates a time-varying electric current that consequently reradiates electromagnetic radiation in the form of a THz pulse. The requisite generation source is a Ti:sapphire non-amplified laser (an oscillator with $\sim$ 10 nJ/pulse) that has been shown to provide a bandwidth up to 5 THz [12], but the *resonant* nature of bandgap excitation poses restrictions on the bandwidth of the

excitation pulse; additionally, the resulting bandwidth of the THz pulse is associated with the characteristic response time of the carriers instead of the excitation pulse duration.

With the shift to amplified lasers with higher pulse energies ($\sim$ 1 mJ/pulse), photoconductive antennas in the geometry described above are no longer feasible since these focused pulses would destroy the material. This led to the development of large-aperture antennas that had much larger gaps ($\sim$ 3 orders of magnitude) between the antenna electrodes and so non-focused excitation pulses could be used, but this consequently required much larger bias voltages since the THz field strength scales directly with gap size. This approach yielded almost 1 μJ/pulse [13]. However, a more practical system for attaining higher bandwidths uses a nonlinear process called optical rectification in an electro-optic (EO) crystal, which more fully utilizes the short pulse durations available from femtosecond lasers without the need of an applied voltage. These nonlinear crystals have an instantaneous optical response (compared to the dependence on the rise time of the photo-induced current in photoconductive antennas), where THz generation occurs through *nonresonant* second-order optical nonlinearities [14].

Over the past decade, there has been significant improvement in the efficiency of tabletop THz generation sources. Higher efficiency sources are important for linear THz spectroscopy and even more for the coherent control of materials and nonlinear THz spectroscopy. In contrast to more easily implemented collinear optical rectification in zincblende crystals like zinc telluride (ZnTe) and gallium phosphide (GaP), commonly used as THz probes in time-domain THz spectroscopy, optical rectification in the ferroelectric crystal lithium niobate ($LiNbO_3$, LN) has proven fruitful for high field THz generation by exploiting its large nonlinear optical parameters. Noncollinear optical rectification by using a tilted optical pump pulse front has reported pulse energies of 10-30 μJ/pulse [15,16] with relatively high pump-to-THz energy conversion efficiencies. In LN, there is strong coupling between THz electromagnetic waves and select polar lattice vibrational modes involved in the ferroelectric phase transition. The result is the generation of THz phonon-polaritons, quasiparticle analogs to alternating

current signal carriers in electronics or electromagnetic waves in photonics, which propagate at the speed of light in the material. More recently, the magnitudes of peak THz fields have even made it possible to "do chemistry" by obtaining sufficiently large field amplification in the gaps of THz resonant microstructures [7] to change the properties of materials (e.g., insulator-to-metal phase transition in vanadium dioxide [17]), a significant advancement to measurements previously limited to a material's intrinsic THz response.

An alternate to the free-space THz generation described thus far, called the polaritonics platform [3], was developed in the Nelson group for generation, control, and detection of THz waves on a single LN sample. Due to the large difference in the index of refraction at THz frequencies compared to the optical spectral range, the THz phonon-polariton waves travel primarily in the lateral direction. As a result, the different propagation directions allow for easy separation of the optical pump beam and the THz signal beam. Additionally, the sample thickness can be scaled down to the subwavelength regime to create a THz waveguide that confines the THz wave and hence creates propagating waveguide modes. Applications of this integrated platform include a means for signal processing, an architecture or testbed for photonic devices and optical components, integration of bandgap or homogenized materials, long THz-sample interaction lengths, and waveguide spectroscopy.

In this chapter, I will firstly detail broadband THz generation in bulk materials resulting from collinear and noncollinear optical rectification in ZnTe and LN, respectively, and their experimental implementation. Subsequently, I will discuss the general scheme of the polaritonics platform in the waveguide regime including analytical calculations of the generated THz waveguide modes in various geometries and polarizations, and experimental broadband and narrowband THz generation.

2.2 Terahertz Generation in Bulk Materials

2.2.1 Optical Rectification

Generally, a nonlinear optical process may be viewed from the macroscopic polarization of a medium as a function of the light-matter interactions:

$$\begin{aligned} P(\omega) &= \epsilon_0(\overline{\overline{\chi^{(1)}}}E(\omega) + \overline{\overline{\overline{\chi^{(2)}}}}E^2(\omega) + \overline{\overline{\overline{\overline{\chi^{(3)}}}}}E^3(\omega) + ...) \\ &= P^{(1)}(\omega) + P^{\mathrm{NL}}(\omega) \end{aligned} \tag{2.1}$$

where ϵ_0 is the permittivity in free space, $\chi^{(i)}$ is the i^{th}-order susceptibility tensor, $E(\omega)$ is the incident E-field , $P^{(1)}$ is the linear polarization term, and $P^{\mathrm{NL}}(\omega)$ is the collective sum of all nonlinear polarization terms. Optical mixing is a nonlinear process where waves of two frequencies ω_1 and ω_2 combine to yield new frequency components [18]; only with high-intensity pulses, such as those from amplified lasers, must the higher order terms in (2.1) that make up the nonlinear responses be considered. In a nonlinear medium, these light waves mix to generate sum-frequency generation, $\omega_1 + \omega_2$, and difference-frequency generation, $\omega_1 - \omega_2$ (among other nonlinear optical processes). For two light interactions at the same frequency, $\omega_1 = \omega_2$, the resulting wave mixing gives second-harmonic generation (SHG) and direct current (dc) pulses. In the case of an ultrafast pulse, the wave mixing may occur *within* the pulse's broad spectral bandwidth itself, where the Fourier components of the driving optical spectrum interfere to create a beating polarization at the difference frequency. This is a special case of difference-frequency generation called optical rectification.

The difference-frequency generation process that produces a pulse at THz frequency Ω can be described by the following second-order nonlinear polarization created by two optical

pump fields:

$$P^{(2)}(\Omega) = \epsilon_0 \overline{\overline{\chi^{(2)}}}(\Omega = \omega_1 - \omega_2) E_1(\omega_1) E_2^*(\omega_2) \tag{2.2}$$

$$= \epsilon_0 \overline{\overline{\chi^{(2)}}}(\Omega) E(\omega_{\text{opt}} + \Omega) E^*(\omega_{\text{opt}}) \tag{2.3}$$

where $\overline{\overline{\chi^{(2)}}}$ is the second-order nonlinear susceptibility tensor and $E_1(\omega_1) = E(\omega_{\text{opt}} + \Omega)$ and $E_2(\omega_2) = E(\omega_{\text{opt}})$ are the pump fields at optical frequencies spanning ω_{opt} to $\omega_{\text{opt}} + \Omega$. Difference-frequency mixing generates pulses with frequencies that lie in the range of dc to Ω, where for ultrafast near-infrared pump pulses, the bandwidth Ω lies in the THz range. Consequently, the polarization of the difference-frequency pulse corresponds only to the envelope of the optical pump fields and no information of the pump phases is retained. It is important to note that difference-frequency generation is only relevant for a crystal without inversion symmetry since this is an even-order process. The lowest order nonlinear response for a crystal with inversion symmetry would be a $\chi^{(3)}$-response; it is not the main mechanism for THz generation and so its treatment is omitted here.

The nonlinear interaction of the pump fields creates an oscillation of dipole moments throughout the atoms in the medium with a component at frequency Ω. The resulting nonlinear polarization, $P^{(2)}(\Omega)$, serves as the source term in Maxwell's equations, where the generation and propagation of the THz E-field may be given by the wave equation for nonlinear optical media [19]. In the frequency-domain, the wave equation is:

$$\nabla \times \nabla \times E(\mathbf{r}, \Omega) - \frac{\Omega^2}{c^2} \bar{\bar{\epsilon}}^{(1)}(\Omega) E(\mathbf{r}, \Omega) = \frac{\Omega^2}{\epsilon_0 c^2} P^{(2)}(\mathbf{r}, \Omega), \tag{2.4}$$

where $\bar{\bar{\epsilon}}^{(1)}(\Omega) = \epsilon_0 \Big(1 + \overline{\overline{\chi^{(1)}}}(\Omega)\Big)$ and c is the speed of light in vacuum. A solution to the wave equation yields the THz spectrum, $E(\Omega)$, which is determined by the material properties contained in the dielectric function $\bar{\bar{\epsilon}}^{(1)}(\Omega)$. In the time-domain, if we assume an

isotropic medium, the wave equation simplifies to:

$$\nabla \times \nabla \times E(\mathbf{r},t) + \frac{\epsilon^{(1)}}{c^2}\frac{\partial^2 E(\mathbf{r},t)}{\partial t^2} = -\frac{1}{\epsilon_0 c^2}\frac{\partial^2 P^{(2)}(\mathbf{r},t)}{\partial t^2}, \tag{2.5}$$

where $\epsilon^{(1)}$ is a scalar quantity. The wave equation in the time-domain shows that the THz E-field is the second time derivative of the optically induced nonlinear polarization, which resembles the envelope of the optical pump fields. Because the time-dependent optical pump E-fields can be represented by Gaussian envelopes, the THz waveform resembles the second derivative of a Gaussian function.

2.2.2 Collinear Phase-matched THz Generation in Zinc Telluride

2.2.2.1 The Phase Matching Condition and Coherence Length in ZnTe

For broadband optical rectification in ZnTe in a collinear geometry, higher signal generation calls for longer interaction lengths of the pump fields in the crystal, but a closer inspection of the phase matching condition is required in bulk crystals compared to generation in very thin EO crystals [20, 21] . In this case, the wave equation in (2.4) must be satisfied in particular for the difference-frequency component: $\Omega = \omega_1 - \omega_2$. Physically, the dipole moments of the atoms in the medium are oscillating with a phase that is dependent on the phase of the incident pulses; only when the dipoles oscillate in phase (in accordance with the phase matching condition to be determined) will the emitted fields interfere constructively and the overall magnitude of emission at Ω increase directly with the number of radiating atoms.

A trial solution to (2.4) when a nonlinear source term is present is a plane wave at frequency Ω propagating along the $+z$-direction (i.e. along the medium's thickness, L):

$$E_3(z,\Omega) = A_3(z,\Omega)e^{i(k_3 z - \Omega t)} + \text{c.c.}, \tag{2.6}$$

where $k_3 = \Omega n_3/c$ is the wavevector and $n_3 = \sqrt{\bar{\epsilon}(\Omega)}$ (non-magnetic) is the index of refraction

at Ω. The nonlinear source term can be represented as:

$$P_3^{(2)}(z,\Omega) = p_3(\Omega)e^{i(k_1-k_2)z}e^{-i\Omega t} + \text{c.c.}, \tag{2.7}$$

where $p_3(\Omega) = \epsilon_0\overline{\overline{\overline{\chi^{(2)}}}}(\Omega)A_1(\omega_1)A_2^*(\omega_2)$. The behavior of how the amplitude of the THz E-field changes as it propagates along $+z$ is given by the first derivative of $A_3(z,\Omega)$ with respect to z, which is found by substituting $E_3(z,\Omega)$ in the wave equation[1]

$$\frac{\mathrm{d}A_3}{\mathrm{d}z} = \frac{\Omega^2}{2\epsilon_0 n_3 c}p_3(\Omega)e^{i\Delta kz} \tag{2.8}$$

where

$$\begin{aligned}\Delta k &= k_1 - k_2 - k_3 \\ \Delta k &= k(\omega_{\text{opt}} + \Omega) - k(\omega_{\text{opt}}) - k(\Omega)\end{aligned} \tag{2.9}$$

Δk is called the wavevector mismatch and so the difference frequency generation is maximized (or "phase matched") when $\Delta k = 0$.

The importance of the phase matching condition is more easily seen by the dependence of the intensity of $E_3(z,\Omega)$ on Δk when it propagates through a nonlinear medium of length L. Firstly, the amplitude at $z = L$ is found by integrating (2.8) from $z = 0$ to $z = L$:

$$A_3(L,\Omega) = \frac{\Omega^2}{2\epsilon_0 n_3 c}p_3(\Omega)\int_0^L e^{i\Delta kz}\mathrm{d}z \tag{2.10}$$

$$= \frac{\Omega^2}{2\epsilon_0 n_3 c}p_3(\Omega)\left(\frac{e^{i\Delta kL}-1}{i\Delta k}\right), \tag{2.11}$$

[1]This requires simplification of the wave equation such that $\nabla\times\nabla\times E = \nabla(\nabla\cdot E) - \nabla^2 E \approx -\nabla^2 E$. The contribution from $\nabla\cdot E$ is negligible as a result of invoking the slowly varying amplitude approximation [18,19]: $\left|\frac{\mathrm{d}^2A_3}{\mathrm{d}z^2}\right| \ll \left|k_3\frac{\mathrm{d}A_3}{\mathrm{d}z}\right|$.

then the intensity is calculated as follows:

$$|A_3(L,\Omega)|^2 = \left|\frac{\Omega^2}{2\epsilon_0 n_3 c_0} p_3(\Omega)\right|^2 L^2 \mathrm{sinc}^2\left(\frac{\Delta k L}{2}\right)$$
$$I_3(L,\Omega) = I_3^{\max}(L,\Omega)\ \mathrm{sinc}^2\left(\frac{\Delta k L}{2}\right). \tag{2.12}$$

According to (2.12), only when $\Delta k = 0$ is the intensity of the THz field component at Ω maximized after propagating a length L.

However, this condition assumes a constant phase relationship between the generated and propagating waves. In reality, the process is not perfectly phase matched since the driving polarization at Ω goes in and out of phase repeatedly with the generated field $E_3(z,\Omega) = E_{\mathrm{THz}}(z,\Omega)$ and the conversion efficiency oscillates as $\sin(\Delta k L/2)$ instead. The non-phase-matched case is described by a characteristic length called the coherence length:

$$L_{\mathrm{coh}} = \pi/\Delta k. \tag{2.13}$$

The efficiency of broad-bandwidth generation through optical rectification in nonlinear crystals is dominated by material properties and not the spectral bandwidth available from the optical pump. In ZnTe, it is not possible to phase match across the entire THz spectrum due to strong phonon resonances at THz frequencies that cause significant dispersion. Consequently, there is a large difference between the index of refraction at optical ($n_{\mathrm{opt}}(800\ \mathrm{nm}) = 2.85$) and THz ($n_{\mathrm{THz}} > 3$ from 0-4 THz) frequencies . However, the dispersion in the optical refractive index can be taken advantage of to achieve longer coherence lengths by matching the phase velocity of the THz wave, $\nu_{\mathrm{ph,THz}}$, with the group velocity of the optical pump, $\nu_{\mathrm{gr,opt}}$ [14]. The coherence length for optical rectification can be given by:

$$L_{\mathrm{coh}}(\Omega) = \frac{\pi c_0}{\Omega\,|n_{\mathrm{gr,opt}}(\lambda_{\mathrm{opt}}) - n_{\mathrm{THz}}(\Omega)|}. \tag{2.14}$$

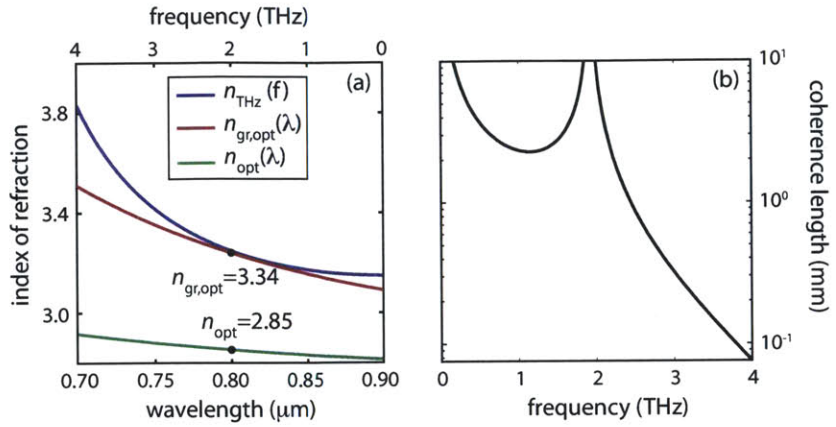

Figure 2-1: **Phase matching and coherence lengths in optical rectification in ZnTe.** (a) The index of refraction at optical and THz frequencies and also the optical group index. The optical indices at 800 nm are indicated on the plots. Due to a THz phonon resonance at 4 THz, the THz index experiences large dispersion such that phase matching with the optical index is too difficult, but collinear phase matching with the optical group index is feasible. (b) The coherence length in ZnTe as a function of THz frequency by phase matching the phase velocity of the THz wave with the group velocity of the optical pump at 800 nm. With a 1 mm thick ZnTe crystal, there is adequate phase matching up to 2.4 THz before the generation efficiency quickly diminishes.

where

$$n_{\mathrm{gr,opt}} = n_{\mathrm{opt}}(\lambda_{\mathrm{opt}}) - \lambda_{\mathrm{opt}} \left. \frac{\mathrm{d}n_{\mathrm{opt}}}{\mathrm{d}\lambda} \right|_{\lambda_{\mathrm{opt}}} \tag{2.15}$$

is the optical group index and $n_{\mathrm{THz}} = c/\nu_{\mathrm{ph,THz}}$ is the THz index of refraction. The optical [22] and THz [23] refractive indices of ZnTe have been measured as the following:

$$n_{\mathrm{opt}}^2 = 4.27 + 3.01\lambda_{\mathrm{opt}}^2/(\lambda_{\mathrm{opt}}^2 - 0.142), \tag{2.16}$$

where λ is the optical wavelength in μm.

$$n_{\mathrm{THz}}^2 = (289.27 - 6f_{\mathrm{THz}}^2)/(29.16 - f_{\mathrm{THz}}^2), \tag{2.17}$$

where $f_{\mathrm{THz}} = \Omega/2\pi$ is the frequency in THz. The optical and THz refractive indices and optical group index are plotted in Fig. 2-1(a), where it is clear that while there is a large refractive index mismatch at THz frequencies compared to the optical pump at 800 nm, the

optical group index at 800 nm demonstrates adequate group velocity dispersion to match the THz index over a broader range of frequencies. Because it is not useful to generate THz fields with an EO crystal thicker than the coherence length, it can be seen in Fig. 2-1(b) that a 1 mm thick ZnTe crystal has optimal phase matching between the THz index and the optical group index for a bandwidth of 2.4 THz; even at 2 mm thickness, the bandwidth is only reduced slightly to 2.2 THz but the generation intensity is estimated to increase by 4-fold according to (2.12). Beyond this bandwidth, the dispersion in the THz index becomes too large to be compensated by the optical group velocity dispersion.

2.2.2.2 Experimental Setup for Optical Rectification in ZnTe

Experimental implementation of optical rectification in ZnTe is straightforward since it requires a collinear phase matched geometry between the optical 800 nm pump beam and emitted THz beam. We directed a collimated, *s*-polarized ultrafast laser pulse (800 nm center wavelength, $\sim$0.76 mJ/cm^2, 50-fs transform-limited pulse duration) to overfill a 2 mm $\langle 110 \rangle$ ZnTe generation crystal ($\sim$ 1 cm beam diameter) and rejected the outgoing optical light with a piece of teflon and black polypropylene. THz generation was optimized by tuning the azimuthal angle of the crystal [24]. The THz beam was then focused with a pair of parabolas into a 1 mm ZnTe detection crystal, where the THz signal is measured by a technique called EO-sampling. This detection method will be discussed in the next chapter. Figure 2-2(a) shows an example of a THz time trace recorded with ZnTe, where a strong THz pulse is seen followed by smaller, fast oscillations; these oscillations are the free-induction decay resulting from THz absorption of ambient water vapor. The THz spectrum in Fig. 2-2(b) is simply the Fourier transform of the time trace in (a), where 10% of the maximum bandwidth is at $\sim$2.2 THz as estimated from the coherence length previously calculated in Fig. 2-1(b).

With an amplified ultrafast laser, optical rectification in zincblende crystals is typically the easiest route to obtaining moderate field strengths for a relatively broad bandwidth of 2.5

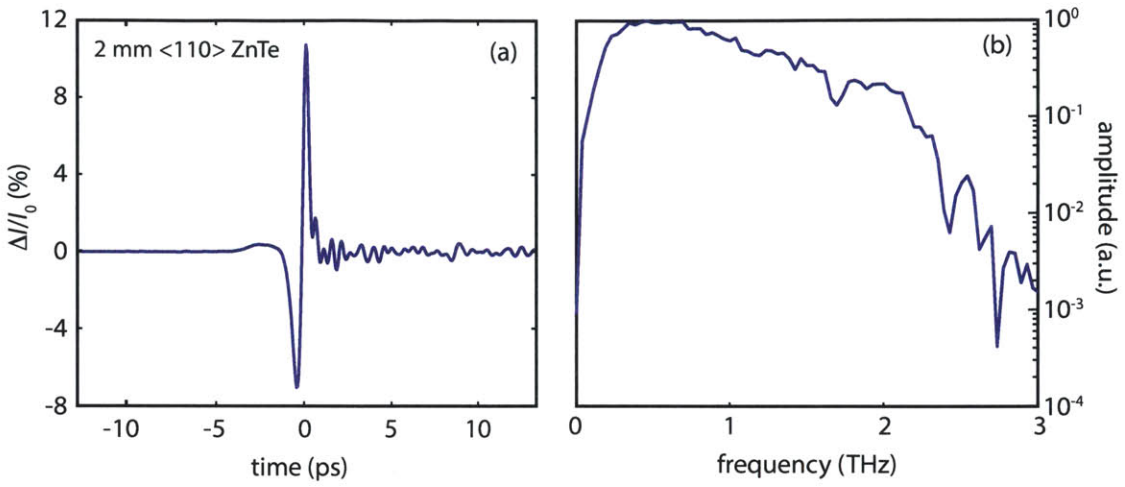

Figure 2-2: **Experimental THz generation in ZnTe.** (a) Percent signal modulation time trace of a THz signal generated by collinear phase matching in 2 mm of ⟨110⟩ ZnTe crystal. The fast oscillations following the main THz pulse is the free-induction decay (FID) due to THz absorption by the rotational modes of ambient water vapor. (b) The THz spectrum of (a) with 10% of the maximum bandwidth at ~2.2 THz as estimated from the coherence length previously. The narrow resonances (giving rise to the long ringing of the FID) of water correspond to the sharp drops in the spectral intensity across the generated bandwidth.

THz. However, the overall optical-to-THz conversion efficiency and attainable bandwidth are determined by the inherent properties of ZnTe. For example, it is difficult to maintain a large coherence length by optical group and THz phase velocity matching near the optic phonon resonance at 4 THz. The relevant effective nonlinear optical coefficient, although reasonably high in ZnTe (d_{14} = 61 pm/V in ZnTe vs. d_{33} = 154 pm/V in LN [25]), strongly affects the generation efficiency. However, the potential of these high nonlinear constants has not been fully realized since at moderately high optical pump fluences (> 0.5 mJ/cm^2 [26, 27]), there is saturation of THz generation in ZnTe due to a two-photon absorption process at 800 nm in the narrow bandgap (~ 2.25 eV) semiconductor; consequently a red shift is observed in the THz spectrum. This has a two-fold effect: the generation of free carriers leads to absorption at THz frequencies, and the two-photon absorption depletes the optical pump (although not to a large extent) [27]. Three-photon and four-photon absorption have similarly been observed to limit generation in GaP and LN, respectively. As a result, large-

aperture nonlinear crystals have been used to reduce pump fluence and suppress saturation from these multi-photon and free carrier absorptions. A larger THz spot size also can be focused more tightly at the sample for higher localized field strengths [28]. There have been studies however that show that the free carrier generation via two-photon absorption process can saturate such that at even higher pump fluence (> 6.3 mJ/cm^2), THz generation resumes quadratic dependence on pump fluence [26]. In general, optical rectification in zincblende crystals has served as a good THz probe but its relatively low field strengths (up to 10s of kV/cm) have prohibited its further use as a THz pump for nonlinear THz spectroscopy.

2.2.3 Phonon-Polariton Generation in Lithium Niobate

The term optical rectification is a broad, macroscopic description of how THz radiation is generated from nonlinear light-matter interactions. With the expansion of THz generation methods to optical rectification, came the search for the 'perfect' nonlinear crystal that has both reasonably broad THz bandwidth and high efficiency THz generation. The collinear generation scheme in zincblende crystals is experimentally convenient, but these crystals do not have the highest known nonlinear coefficients. THz generation methods have since been developed for optical rectification in ferroelectrics such as LN and lithium tantalate ($LiTaO_3$) that possess much larger nonlinear coefficients. Initially, these ferroelectrics were not exploited since they had extremely high dielectric constants (or indices) at THz frequencies and thus the phase velocity of the generated THz waves were far too slow to match the group velocity of the optical pump for sufficiently long coherence lengths.

In 2007, Yeh and coworkers [16] developed a non-collinear generation scheme in LN that used a tilted optical intensity front [29] for velocity matching of the optical pump and generated THz waves. This technique yielded an optical-to-THz energy conversion efficiency of 6.0×10^{-4} and THz pulse energies of 10 μJ, an order of magnitude in improvement over optical rectification in zincblende crystals. As a result, there has been rapid development

in THz nonlinear spectroscopies due to more accessible high power tabletop THz sources compared to the alternative of accelerator-based sources (up to 100 μJ/pulse [30]). In ferroelectrics, which possess large spontaneous polarizations, the dominant contribution to the nonlinear susceptibility is due to the ionic lattice displacements, with very little electronic contribution [31, 32]. In these ionic crystals, optical rectification near an optic phonon resonance strongly affects the frequency content and damping rate of the THz radiation. The THz wave propagates as a highly coupled entity called a phonon-polariton wave.

2.2.3.1 Macroscopic Model of Phonon-Polaritons in Ferroelectrics

A polariton is a quasiparticle that results from strong coupling between electromagnetic radiation and a collective excitation of an elementary degree of freedom (charge, spin, or lattice) in the material, with the interaction mediated through an electric or magnetic dipole. Materials have a variety of resonances such as the collective excitations of electron-hole pairs (excitons), the collective excitations of the electrons' spinsin a lattice (magnons), or the collective excitations of polar vibrational modes in a lattice (phonons). Mixed species have been observed as exciton-polaritons in semiconductors at visible frequencies, magnon-polaritons in ferromagnetic crystals at microwave frequencies, and of particular interest here, phonon-polaritons in ferroelectric crystals at far-infrared frequencies. The propagation of a polariton through a material can be described at times as having more photon character (light-like) or more material character (electronic-, magnetic-, or phononic-like), or a combination of both, depending on the regime of coupling.

In the case of phonon-polaritons in LN, there is a transverse optical (TO) phonon ($\omega_T/2\pi$ = 7.4 THz along the extraordinary axis) within the bandwidth ($\Omega \sim$ 10 THz) of our 800 nm optical pump pulse). In the ferroelectric phase in LN, the charge separation of the positively-charged lithium and niobium ions and negatively-charged oxygen ions gives rise to a spontaneous electric polarization for each unit cell in the crystal, which can couple

to the THz-frequency electromagnetic radiation. Consequently, optic phonons in these ionic crystals can be excited by a far-infrared E-field . The polar vibrations consist of positive and negative ions moving in opposite directions (i.e. out-of-phase oscillations) relative to each other and hence create a time-varying electric dipole moment. Additionally, the optic phonons can be excited by optical light through coherent Raman scattering processes, here by impulsive stimulated Raman scattering (ISRS), a second-order nonlinear process [33]. The ionic lattice displacements makes up the majority of the $\chi^{(2)}$ response with very small electronic contribution (less than 10%) [31]. The propagating THz phonon-polariton waves are both infrared and Raman active, which is allowed since LN is noncentrosymmetric.

In the limit where the wavelength of the optical lattice vibrations is much larger than the lattice constant, we can use a macroscopic description. This treatment of the polar lattice vibrations follows closely with the notation described in [34, 35] for diatomic ionic crystals. Firstly, the displacement of each unit cell is modeled as a driven, damped Lorentz oscillator with displacements given by $Q(\mathbf{r}, t)$. Because the electromagnetic and mechanical vibrations are not separable, the solutions to the coupled photon-phonon admixture must satisfy both Maxwell's equations and the lattice equations. The coupled differential equations can be represented by the following [34]:

$$\begin{bmatrix} \ddot{Q} + \Gamma\dot{Q} \\ P \end{bmatrix} = \begin{bmatrix} b_{11} & b_{12} \\ b_{21} & b_{22} \end{bmatrix} \begin{bmatrix} Q \\ E \end{bmatrix} \tag{2.18}$$

where $\dot{Q}$ and $\ddot{Q}$ are the first and second time-derivatives of Q, respectively, Γ is a phenomenological damping constant, E is the electric field, and the b-coefficients are constants to be determined that represent physical properties of the system. The expression can be expanded to give:

$$\ddot{Q}(\mathbf{r}, t) + \Gamma\dot{Q}(\mathbf{r}, t) - b_{11}Q(\mathbf{r}, t) = b_{12}E(\mathbf{r}, t) \tag{2.19}$$

$$P(\mathbf{r}, t) = b_{21}Q(\mathbf{r}, t) + b_{22}E(\mathbf{r}, t) \tag{2.20}$$

Time-harmonic trial solutions to (2.18) can be used to determine the constants of interest: $Q = Q_0 \exp(-i\omega t)$ and $E = E_0 \exp(-i\omega t)$. (2.19) is simplified and Fourier transformed to give:

$$Q(\mathbf{r}, \omega) = \frac{b_{12} E(\mathbf{r}, \omega)}{-(\omega^2 + i\Gamma\omega + b_{11})} \tag{2.21}$$

Similarly, the frequency-dependent polarization is the Fourier transform of (2.20) and substitution of Q in (2.21) yields:

$$P(\mathbf{r}, \omega) = \left[\frac{b_{21} b_{12}}{-(\omega^2 + i\Gamma\omega + b_{11})} + b_{22} \right] E(\mathbf{r}, \omega) \tag{2.22}$$

Because $P = \epsilon_0 \chi E$ and $\varepsilon/\epsilon_0 = 1 + \chi$, we can determine the frequency-dependent relative dielectric function[2]:

$$\varepsilon_r(\omega) = \frac{\varepsilon(\omega)}{\epsilon_0} = 1 + \frac{1}{\epsilon_0} \left[\frac{b_{21} b_{12}}{-(\omega^2 + i\Gamma\omega + b_{11})} + b_{22} \right] \tag{2.23}$$

where ϵ_0 is the permittivity in free space. The coupling b-coefficients can determined by taking the low and high frequency limits of (2.23), which have been experimentally measured. The dielectric function In the high frequency limit as $\omega \to \infty$ is:

$$\begin{aligned} \varepsilon_\infty &= 1 + \frac{b_{22}}{\epsilon_0} \\ \Rightarrow b_{22} &= \epsilon_0(\varepsilon_\infty - 1) \end{aligned} \tag{2.24}$$

In the absence of damping, $\omega^2 \to -b_{11}$ at the TO resonant frequency, ω_T, and so $-b_{11} = \omega_T^2$. The dielectric function In the low frequency limit as $\omega \to 0$ is:

$$\varepsilon_0 = 1 + \frac{1}{\epsilon_0} \left[\frac{b_{21} b_{12}}{\omega_T^2} + b_{22} \right] \tag{2.25}$$

[2]LN and LT are uniaxial crystals, where the principle axes directly map onto one extra-ordinary axis and two ordinary axes. Consequently, the dielectric tensor is diagonal and can be separately cast into expressions for the extraordinary and ordinary components

Since conservation of energy requires reciprocity between the coupling of the electromagnetic field to the lattice and the lattice's contribution to the polarization, then $b_{12} = b_{21}$ (see proof in Appendix V of Born and Huang [35]). Appropriate substitution and simplification of (2.25) yields:

$$\begin{aligned} b_{12} &= \omega_T \sqrt{\epsilon_0(\varepsilon_0 - \varepsilon_\infty)} \\ &= \sqrt{\epsilon_0}\sqrt{f} \end{aligned} \tag{2.26}$$

where $f = \omega_T^2(\varepsilon_0 - \varepsilon_\infty)$ represents the strength of coupling between a particular TO optic phonon mode and the electric field (and consequently also the lattice's contribution to the polarization).

2.2.3.2 Phonon-Polariton Dispersion

Mathematically, a non-zero coupling between two eigenstates acts as an external perturbation on the two-state Hamiltonian. Diagonalizing the modified Hamiltonian of the system yields new coupled eigenstates that cannot be degenerate (i.e. an avoided crossing), where the energy of one of the eigenstates is lowered compared to the initially unperturbed eigenenergy. If the energy difference between the original eigenstates is too large, then the new eigenenergies will simply approach those of the unperturbed states.

The dispersion of phonon-polaritons is described by the dispersion relation: $k = \omega n(\omega)/c_0$. The index of refraction for a nonmagnetic material is $n(\omega) = \sqrt{\varepsilon_r(\omega)}$. Firstly, the dielectric function in (2.23) can be recast in terms of the physical measurable constants:

$$\varepsilon_r(\omega) = \varepsilon_\infty + \frac{f}{\omega_T^2 - \omega^2 - i\Gamma\omega} = \varepsilon_\infty + \frac{\omega_T^2(\varepsilon_0 - \varepsilon_\infty)}{\omega_T^2 - \omega^2 - i\Gamma\omega} \tag{2.27}$$

where ε_∞ is the dielectric at all other frequencies below and above the lowest phonon frequency of interest, ω_T, and $\varepsilon_0 = \varepsilon_r(0)$ is the static dielectric constant that can be measured

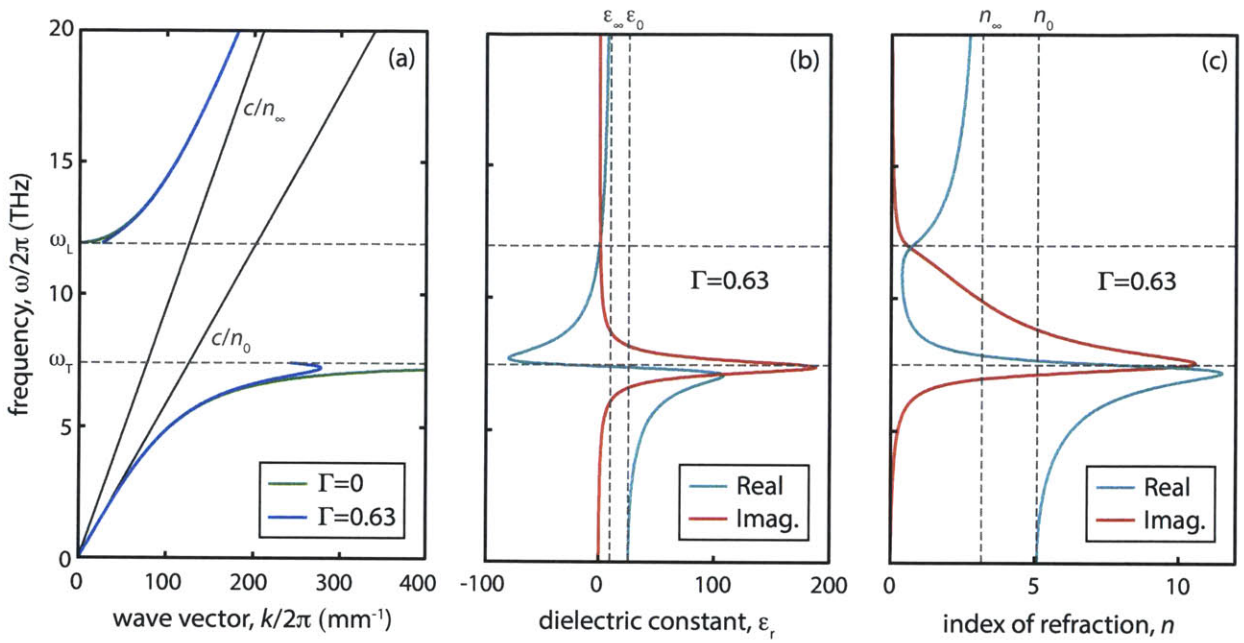

Figure 2-3: **Phonon-polariton dispersion in LN along extraordinary axis.** (a) Dispersion relation of LN with and without damping, Γ, showing the lower- and upper-polariton branches. The lower-polariton branch approaches the lowest-frequency transverse optic phonon at $\omega_T/2\pi$=7.4 THz at high wave vector. The upper-polariton branch approaches the lowest-frequency longitudinal optic phonon at $\omega_L/2\pi$=11.9 THz at zero wave vector. (b) The real and imaginary parts of the dielectric function when $\Gamma = 0.63$. (c) The real and imaginary parts of the index of refraction when $\Gamma = 0.63$.

at zero frequency. The wave vector k can then be rewritten as:

$$k = \frac{\omega}{c_0}\sqrt{\varepsilon_\infty + \frac{\omega_T^2(\varepsilon_0 - \varepsilon_\infty)}{\omega_T^2 - \omega^2 - i\Gamma\omega}} \tag{2.28}$$

If the damping term is ignored ($\Gamma = 0$), then it is possible to explicitly write expressions that correspond directly to the lower- and upper-polariton branches. In this case, we determine ω for given values of k that are real and positive.

$$\omega = \sqrt{\frac{k^2c_0^2 + \varepsilon_0\omega_T^2 \pm \sqrt{(k^2c^2 + \varepsilon_0\omega_T^2)^2 - 4(\varepsilon_\infty k^2c^2\omega_T^2)}}{2\varepsilon_\infty}} \tag{2.29}$$

The dispersion curves of the phonon-polaritons in LN are shown in Fig. 2-3(a), where

the introduction of damping leads to a non-asymptotic feature around ω_T compared to an undamped system. In using (2.28), extra care must be taken to ignore solutions where $\varepsilon_r < 0$. There is an avoided crossing between the lower- and upper-polariton branches, where no modes are allowed between frequencies ω_T to ω_L. The dielectric function is shown in Fig. 2-3(b) in the presence of damping, where the real part shows a dispersive line shape (without damping, the real part would asymptotically approach ω_T) and the imaginary part is an absorptive Lorentzian line shape (without damping, no imaginary component exists). The dispersive line shape gives rise to the behavior of the dispersion relation in Fig. 2-3(a). Because the optical waves are transverse, they can only excite the transverse phonons in LN and not the orthogonal longitudinal phonons; as a result, the dielectric function must go to zero at ω_L. This longitudinal phonon resonance can be calculated by setting (2.27) to zero in the absence of damping:

$$\omega_L = \omega_T \sqrt{\varepsilon_0/\varepsilon_\infty} \tag{2.30}$$

The index of refraction is plotted in Fig. 2-3(c), where an important observation is the near-constant index from 0-2.5 THz; this is the range for optimal phase matching for optical rectification in LN. In our experiments, we use the lower-polariton branch where material dispersion is minimized with an almost linear dispersion relation; at lower frequencies, the phonon-polariton behaves like light (lies along the light line in LN along the appropriate crystal axis, here the extraordinary axis) and at higher frequencies, the phonon-polariton behaves like a collective vibration in LN (approaches the transverse optic phonon at ω_T).

2.2.3.3 Cherenkov Radiation and Tilted Pulse Front

The nonlinear polarization given by (2.3) forms the source term for THz generation and varies in time with the group velocity of the optical pump pulse's envelope. In LN, however, the strong interaction between the displacements of the normal modes in the lattice and the generated THz E-field adds another component, derived from the low-frequency transverse

optic phonon resonance, to the polarization (see (2.20)), and consequently the group velocity of the optical pump source moves faster than the phase velocity of the generated THz radiation. This phenomenon draws strong parallels to Cherenkov radiation from a charged particle moving much faster than the velocity of the radiation it generates, except here the source is a radiating dipole moment. The emitted radiation in these cases propagates in LN at an angle $\theta_c = 63°$, the Cherenkov angle, relative to the optical pump that propagates normal to the crystal surface (see Fig. 2-4). The Cherenkov angle is found by accounting for the difference in distance propagated as a result of the large difference in group and phase velocities of the optical and THz radiation, respectively; in a time period t, the optical pump moves a distance $t \cdot \nu_{\mathrm{gr,opt}}$ through the crystal while the THz wave moves a distance $t \cdot \nu_{\mathrm{ph,THz}}$. The Cherenkov angle can be calculated geometrically:

$$\cos\theta_c = \frac{\nu_{\mathrm{ph,THz}}}{\nu_{\mathrm{gr,opt}}} = \frac{n_{\mathrm{gr,opt}}}{n_{\mathrm{THz}}} \tag{2.31}$$

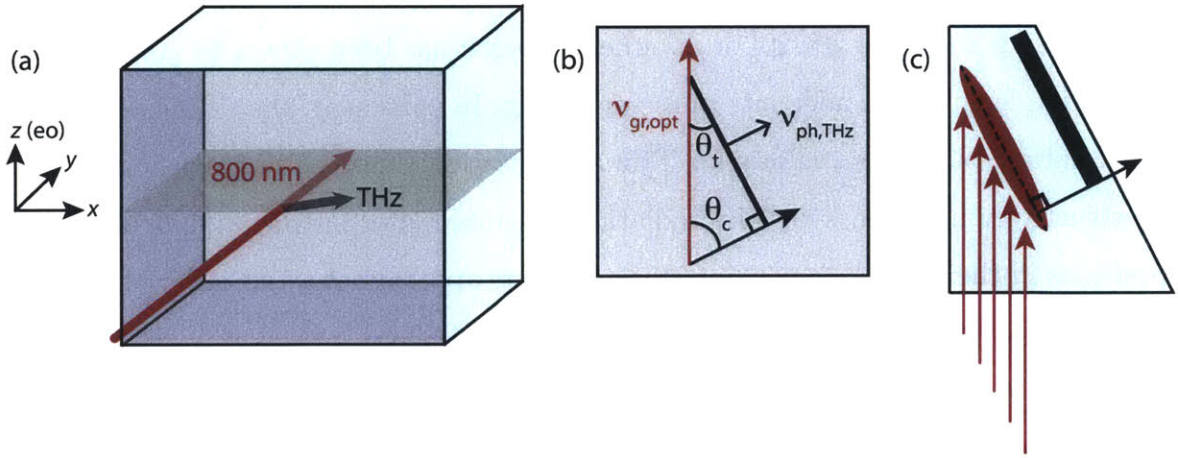

Figure 2-4: **Optical Rectification in bulk LN.** (a) An 800 nm optical pump is directed at normal incidence through a LN crystal and generates THz waves that propagate at the Cherenkov angle due to the index mismatch at optical and THz frequencies. (b) A zoomed-in view showing the Cherenkov radiation geometry of the THz phase fronts traveling at an angle $\theta_c = 63°$ to the optical pump envelope. (c) The optical pump intensity profile is tilted by θ_t but continues to propagate normal to the crystal.

Unfortunately, the large index mismatch between the optical and THz radiation leads to

relatively short coherence lengths and low generation efficiency. However, velocity matching may be attained if the optical pump intensity profile is instead tilted at angle $\theta_t = 90° - \theta_c = 27°$. The tilted optical pump continues to propagate in the forward direction with a velocity $\nu_{gr,opt}$, but its projection along the THz propagation direction is only $\nu_{gr,opt}\cos(\theta_c)$. The velocity matching condition can therefore by satisfied according to $\nu_{ph,THz} = \nu_{gr,opt}\cos(\theta_c)$ and equivalently $n_{gr,opt} = n_{THz}\cos(\theta_c)$. In LN, the optical group index is 2.25 at 800 nm [36], while the index is $\sim$ 4.96 at 1 THz [37], and thus the tilted pulse front is necessary for adequate phase matching.

Without tilting of the optical pulse front, THz plane waves can be generated by cylindrically focusing the optical pump to a narrow line such that the beam waist is much smaller than the wavelength corresponding to a period of oscillation of the generated THz field [29]. The field strengths are weak due to lack of coherent amplification, where the THz waves propagate away from the generation region at the Cherenkov angle. THz generation by tilting of the optical pulse front as shown in Fig. 2-4(c) is necessary for spatiotemporal overlap of the optical phase fronts with the generated THz phase fronts. The tilting is accomplished using a grating [16, 29] or an echelon, which has been shown to greatly improve the interaction length with adequate phase matching. In particular, the tilting of a spatially expanded optical pulse front allows for THz amplification since the propagating THz wave can constructively interfere with THz radiation generated later in time and at different lateral positions in the crystal; conversion efficiencies are approximately an order of magnitude better than for collinear generation in zincblende crystals.

In LN, due to the very high index of LN at THz frequencies, the critical angle for total internal reflection (TIR) is very small: $\theta_{cr} = \sin^{-1}(n_{air}/n_{THz}) = 11.5°$. Because the Cherenkov angle in LN is 63°, the incident angle of the THz beam at the output surface is just the complementary Cherenkov angle, $27° > \theta_{cr}$, and so the generated THz waves are bound in the crystal, unable to couple out into free-space to be applied towards spectroscopy. If the output surface is cut to match the Cherenkov angle as shown in Fig. 2-4(c), then the THz

wave is at normal incidence and so couples out into free space but experiences reflectivity losses due to the index mismatch:

$$R = \left[\frac{n_{\text{THz}} - n_{\text{air}}}{n_{\text{THz}} + n_{\text{air}}}\right]^2 = 45\%.$$

2.3 Terahertz Generation in Waveguided Systems

2.3.1 Derivation of Modes in Anisotropic Slab Waveguide

The slab waveguide confines the THz waves in its thin dimension and extends infinitely in the other two dimensions as described in the previous waveguide derivation, such that the THz waves propagate as discrete modes or eigenmodes, similar to the confinement and subsequent discretization of energy levels experienced in a 1D particle-in-a-box. For the following derivation, we consider a symmetric slab waveguide consisting of a high-index anisotropic core, specifically LN, surrounded by low-index isotropic cladding, air, on both sides; similar treatment is found in Marcuse and Kaminow [38] and Yang and coworkers [39]. We assume that the crystal is uniaxial and its optic axis is parallel to the slab surface (here as in x-cut LN). The y- and z-dimensions of the slab are assumed to extend infinitely, while the x-dimension, corresponding to the slab thickness, is confined. The waveguide modes propagate along the y-direction and extend infinitely along the z-direction. For simplicity we express the E-field as harmonic in space and time, having the general form:

$$\vec{E}(x, y, z, t) = \vec{E}(x) \exp[i(\beta y - \omega t)], \tag{2.32}$$

where $\beta = k_y$ is the propagation constant.

Here, we solve for the waveguide modes in a symmetric anisotropic waveguide, shown in Fig. 2-5, separately for two orthogonal polarizations: transverse electric (TE) and transverse magnetic (TM) polarizations (for intermediate polarization states see Ref. [39]). Here we

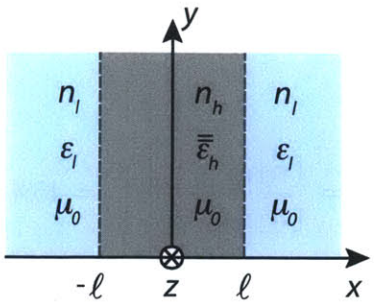

Figure 2-5: **Symmetric waveguide experimental geometry.** A schematic of a waveguide with low-index, n_{l}, cladding and high-index, n_{h}, anisotropic core. ε and μ are the permittivity and permeability in each region.

assume a nonmagnetic, lossless high-index core and a low-index cladding with purely real permittivities, $\bar{\bar{\varepsilon}}_h$ (dielectric tensor for an anisotropic material) and ε_l (dielectric constant for isotropic material) respectively, and free-space permeability, μ_0. Lossy waveguides have complex permittivities and wave vectors and have been treated by Kaminow and coworkers [6].

The general approach will be to firstly consider the bulk dispersion curves and polarizations that describe the bulk wave properties in the core and cladding. The waveguide modes are linear combinations of these bulk waves, which result from the geometric constraints of the system. The coefficients of the linear equation are determined by applying the boundary conditions across the interface described by Maxwell's equations. The result is a set a homogeneous equations that may be recast into matrix notation, where solutions exist when the determinant is equal to zero. These solutions correspond to bound, propagating waveguide modes that only exist at specific pairs of propagation constant, β, and frequency, ω, i.e. along the waveguide dispersion curves.

In this geometry, TE waves have $E_y = 0$ while TM waves have $H_y = 0$. TEM waves exist if both $E_y = 0$ and $H_y = 0$. TE modes have nonvanishing field components: E_z, H_x, and H_y. In contrast, the TM modes have nonvanishing field components: H_z, E_x, and E_y. Although the core is anisotropic, the TE-polarization modes simplify to the isotropic case since the

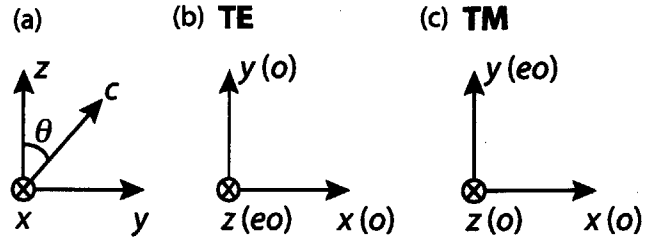

Figure 2-6: **Waveguide coordinate system.** (a) For an anisotropic system, the coordinate system for the derivations is defined as a function of θ, the angle between the z-axis and the optic c-axis of the crystal. (b) For TE waves, $\theta = 0°$, such that the c-axis lies along the z-axis. (c) For TM waves, $\theta = 90°$, such that the c-axis lies along the y-axis.

E-field , $\vec{E}(y)$, has only a single component, E_z, along the optic c-axis of the crystal (the extraordinary (eo) axis of LN) (see (Fig. 2-6(b)). This does not hold for the TM-polarization since in our experiment we rotated the c-axis of the crystal by 90° relative to the z-axis; this kept the pump polarization parallel to the eo-axis so that the largest optical nonlinear coefficient in LN, d_{33}, was used for efficient THz generation [31,40,41]. The TM case requires consideration of the anisotropy of LN since it has E-field components along the eo-axis, E_y, and the ordinary (o) axis, E_x (see Fig. 2-6(c)).

2.3.1.1 General Waveguide Information

The bulk dispersion curves are defined from the wave vector of the material: $k = \frac{2\pi}{\lambda}$. Straightforward substitution of $\lambda = c/nf = 2\pi c/n\omega$ gives the relationship between wave vector, k, and radial frequency, ω: $k^2 = k_x^2 + k_y^2 + k_z^2 = \left(\frac{\omega n}{c}\right)^2$, where c is the speed of light in vacuum and n is the index of refraction. As previously defined, the propagation constant is $k_y = \beta$ since the propagation direction is along y. The wave vector component orthogonal to the slab surface, k_x, is defined differently for the ordinary and extraordinary index of the core, $k_x = \kappa_o$ or $k_x = \kappa_e$, and the cladding, $k_x = i\alpha$. For bound/guided modes, the field must evanescently decay in the cladding, which is indicated by the imaginary wave vector component along x. In contrast, propagating or oscillatory solutions exist for the bound modes in the lossless high-index core, which have real wave vector components. Lastly, since

the field extends infinitely along z, i.e. infinite wavelength, its wave vector component is $k_z = 0$. Bulk dispersion relations of the anisotropic system describe both the ordinary and extraordinary waves of the core, LN, and of the cladding, air:

$$\text{Core, ordinary}: \quad \kappa_o^2 + \beta^2 = \left(\frac{\omega n_o}{c}\right)^2 \tag{2.33a}$$

$$\text{Core, extraordinary}: \quad \kappa_e^2 + \beta^2\left(\cos^2\theta + \frac{n_e^2}{n_o^2}\sin^2\theta\right) = \left(\frac{\omega n_e}{c}\right)^2 \tag{2.33b}$$

$$\text{Cladding}: \quad -\alpha^2 + \beta^2 = \left(\frac{\omega n_c}{c}\right)^2 \tag{2.33c}$$

where n_o and n_e are the bulk ordinary and extraordinary index of LN, respectively, and n_c is the index of the cladding, air. θ is the angle between the z-axis and the c-axis of the crystal shown in 2-6(a)). Accordingly, we see that $\theta = 0°$ for TE-polarization while $\theta = 90°$ for TM-polarization. It is important to note that in the following analyses, we are exclusively solving for the extraordinary TE and TM waves due to our experimental geometries, and any study regarding the ordinary wave counterparts is limited.

2.3.1.2 TE Modes in Anisotropic Symmetric Dielectric Slab Waveguide

The overarching goal of the following derivation is to arrive at the wave equation that relates β and ω; this requires the use of the bulk dispersion relations in (2.33) that express k_x in terms of β and ω. For any pair of β and ω, the most general form has the sum of four possible plane waves in each region: two signs for k_x and two polarizations (that map directly to TE or TM waves). In the case of only generating the extraordinary TE waves, the system simplifies to an isotropic system where $k_{x,\text{core}} = \kappa_e = \kappa$. For $\theta = 0°$, (2.33b) is simplified to a form that only contains a single refractive index, n_e. In an isotropic system, any two orthogonal polarizations may be chosen in the core and cladding. However in a uniaxial crystal, there are two convenient polarizations that allow the TE modes to be treated isotropically. A unit vector along the z-axis, $\hat{z}$, represents one choice of polarization, and the second polarization

is orthogonal to both $\hat{z}$ and k in each region. In the high-index core, the unit vector is:

$$\vec{h}^{\pm} = \frac{\vec{k}_{\mathrm{h}}^{\pm} \times \hat{z}}{\left|\left|\vec{k}_{\mathrm{h}}^{\pm} \times \hat{z}\right|\right|} = \frac{1}{\sqrt{\beta^2 + \kappa^2}} \begin{bmatrix} -\beta \\ \pm\kappa \\ 0 \end{bmatrix}, \tag{2.34}$$

similarly in the low-index cladding:

$$\vec{l}^{\pm} = \frac{\vec{k}_{\mathrm{l}}^{\pm} \times \hat{z}}{\left|\left|\vec{k}_{\mathrm{l}}^{\pm} \times \hat{z}\right|\right|} = \frac{1}{\sqrt{\beta^2 - \alpha^2}} \begin{bmatrix} -\beta \\ \pm i\alpha \\ 0 \end{bmatrix}. \tag{2.35}$$

The full form of the E-fields of the waveguide modes in each region is written as follows:

Cladding ($x \leq -\ell$):

$$\vec{E}(x) = C_1\hat{z}\exp[\alpha(x+\ell)] + C_2\hat{z}\exp[-\alpha(x+\ell)] + C_3\vec{l}^{-}\exp[\alpha(x+\ell)] + C_4\vec{l}^{+}\exp[-\alpha(x+\ell)], \tag{2.36a}$$

Core ($-\ell \leq x \leq \ell$):

$$\vec{E}(x) = A_1\hat{z}\exp(i\kappa x) + A_2\hat{z}\exp(-i\kappa x) + A_3\vec{h}^{+}\exp(i\kappa x) + A_4\vec{h}^{-}\exp(-i\kappa x) \tag{2.36b}$$

Cladding ($x \geq \ell$):

$$\vec{E}(x) = B_1\hat{z}\exp[\alpha(x-\ell)] + B_2\hat{z}\exp[-\alpha(x-\ell)] + B_3\vec{l}^{-}\exp[\alpha(x-\ell)] + B_4\vec{l}^{+}\exp[-\alpha(x-\ell)], \tag{2.36c}$$

where A_i, B_i, and C_i are scalar constants.

Upon inspection it is clear that the first polarization, $\hat{z}$, corresponds to TE modes that only have an E_z component (perpendicular to the propagation direction along y) while the second polarization, $\vec{h}^{\pm}$ and $\vec{l}^{\pm}$, corresponds to TM modes that have E_x and E_y components. Additionally, any E-field components that do not decay to zero as $x \to \infty$ cannot describe the bound modes, so exponentially increasing terms are discarded. Therefore, the TE E-fields are simplified to:

$$\text{Cladding } (x \leq -\ell): \ \vec{E}(x) = C\hat{z}\exp[\alpha(x+\ell)], \tag{2.37a}$$

$$\text{Core } (-\ell \leq x \leq \ell): \ \vec{E}(x) = A_1\hat{z}\exp(i\kappa x) + A_2\hat{z}\exp(-i\kappa x) \tag{2.37b}$$

$$\text{Cladding } (x \geq \ell): \ \vec{E}(x) = B\hat{z}\exp[-\alpha(x-\ell)] \tag{2.37c}$$

The boundary conditions are provided by Maxwell's equations, which state that tangential E- and H-fields must be continuous across the boundary. Here, these are the y- and z-components of the E- and H-fields. Since the TE modes have been described in terms of E-field, we can use Faraday's law to recast the H-field in terms of the E-field. Since we assume that the materials are nonmagnetic, $\mu = \mu_0$, and because the solutions are time-harmonic, we replace the time-derivative with $\frac{\partial}{\partial t} = i\omega$. Plugging in and rearranging Faraday's law yields:

$$\vec{\nabla} \times \vec{E} = -\mu\frac{\partial \vec{H}}{\partial t} = i\omega\mu_0\vec{H} \implies \vec{H} = -\frac{i}{\omega\mu_0}\vec{\nabla} \times \vec{E} \tag{2.38}$$

Additionally, the terms within the del operator, $\vec{\nabla}$, simplify to $\frac{\partial}{\partial y} = i\beta$, $\frac{\partial}{\partial z} = 0$, which follows from the functional form of the E-field in (2.32). Consequently, the H-field may be re-written as follows:

$$\vec{H} = \frac{-i}{\omega\mu_0}\left[-i\hat{x}\beta E_z + \hat{y}\frac{\partial E_z}{\partial x} + \hat{z}\left(i\beta E_x - \frac{\partial E_y}{\partial x}\right)\right] \tag{2.39}$$

The complete set of boundary conditions after substituting for all the magnetic fields is:

$$E_{\text{z,clad}} = E_{\text{z,core}} \tag{2.40a}$$

$$\frac{\partial E_{\text{z,clad}}}{\partial x} = \frac{\partial E_{\text{z,core}}}{\partial x} \tag{2.40b}$$

$$E_{\text{y,clad}} = E_{\text{y,core}} \tag{2.40c}$$

$$i\beta E_{\text{x,clad}} - \frac{\partial E_{\text{y,clad}}}{\partial x} = i\beta E_{\text{x,core}} - \frac{\partial E_{\text{y,core}}}{\partial x} \tag{2.40d}$$

For TE modes, only the first two boundary conditions apply, which correspond to the E_z and H_y components, respectively, while the other two boundary conditions, the E_y and H_z components, respectively, are for TM modes. The boundary conditions are evaluated at the $x = \pm\ell$. Because the system is symmetric, applying the boundary conditions at $x = +\ell$ reveals the same information as at $x = -\ell$ and so (2.37a) may be discarded due to redundancy. The geometry of the waveguide permits the propagation of symmetric and antisymmetric modes, both of which are solved for by applying the boundary conditions in (2.40a) and (2.40b) at $x = \ell$ to yield a set of homogeneous equations. For the symmetric modes, $A_1 = A_2 = A$, and the homogeneous equations in matrix form are:

$$\begin{bmatrix} \cos(\kappa\ell) & -1 \\ \kappa\sin(\kappa\ell) & -\alpha \end{bmatrix} \begin{bmatrix} A \\ B \end{bmatrix} = 0 \tag{2.41}$$

The determinant of this matrix gives a transcendental equation:

$$-\alpha\cos(\kappa\ell) + \kappa\sin(\kappa\ell) = 0 \implies \tan(\kappa\ell) = \frac{\alpha}{\kappa} \tag{2.42}$$

where the solutions correspond to the allowed waveguide modes of the system. For the

antisymmetric modes, $A_1 = -A_2 = A$, and the homogeneous equations in matrix form are:

$$\begin{bmatrix} \sin(\kappa\ell) & -1 \\ \kappa\cos(\kappa\ell) & -\alpha \end{bmatrix} \begin{bmatrix} A \\ B \end{bmatrix} = 0 \tag{2.43}$$

and similarly

$$-\alpha\sin(\kappa\ell) - \kappa\cos(\kappa\ell) = 0 \implies -\cot(\kappa\ell) = \frac{\alpha}{\kappa}. \tag{2.44}$$

Because cotangent and tangent are periodic, many solutions exist. Also, using the trigonometric identities $\tan(\theta + \pi/2) = -\cot(\theta)$ and $\tan(\theta) = \tan(\theta + m\pi)$ where m is an integer, then (2.43) and (2.44) may be combined to yield periodic solutions for both symmetric and anti-symmetric bound TE modes:

$$\tan(\kappa\ell + m\pi/2) = \frac{\alpha}{\kappa} \tag{2.45}$$

where $m = 0, 1, 2, \cdots$ represents the mode number; $m = 0$ corresponds to the lowest symmetric mode and $m = 1$ corresponds to the lowest antisymmetric mode. The bulk dispersion curves in (2.33) are used to eliminate dependence on both κ and α such that we arrive at a relation between β and ω. The resulting transcendental equation may be solved using Newton's method by bisection or other numerical solvers in Matlab. In either method, accurate bounds must be given for each solution otherwise the method will not converge to the correct waveguide modes. For numerical solvers, the transcendental function must be analytical everywhere and so it is easier to find converging solutions if we firstly define a stable parameter instead of directly solving for β: $B = (\beta/k_0)^2$, where $k_0 = \omega/c_0$ is the wave vector in free-space. The relevant bulk dispersion relations are then simplified to:

$$\kappa = k_0\sqrt{n_e^2 - B} \tag{2.46}$$

$$\alpha = k_0\sqrt{B - n_c^2} \tag{2.47}$$

The transcendental equation in (2.45) can then be rewritten as:

$$\tan^{-1}\left(\sqrt{\frac{B-n_c^2}{n_e^2-B}}\right) - k_0\ell\sqrt{n_e^2-B} + m\frac{\pi}{2} = 0 \tag{2.48}$$

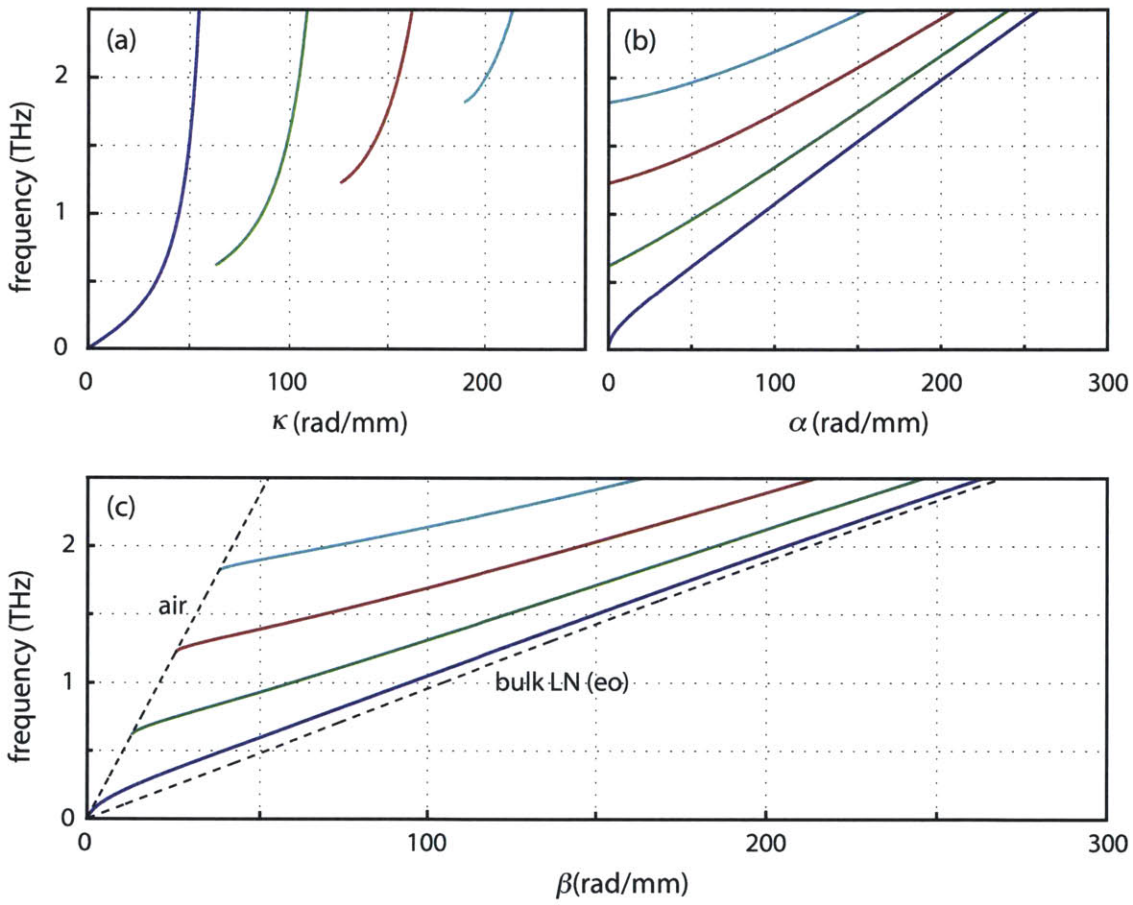

Figure 2-7: **TE dispersion curves in LN.** For the lowest four modes in a 50 μm slab of LN, the wave vectors are calculated in (a) the core, κ, (b) α, in the cladding, and (c) the propagation constant, β.

The converging solutions are only found with a numerical solver by inputting a good initial guess. In Matlab, the numerical solver `solve` was used; it is worth noting that this solver is compatible with complex values that becomes important for lossy materials. Here, we used $B = 1$, equivalent to a guess of $\beta = k_0$; once B and consequently β is determined, the internal wave vectors, κ and α can be explicitly found using (2.33). The dispersion curves

of β, κ and α are shown in Fig. 2-7. The system has no waveguide cutoff frequency, which means all frequencies are allowed to propagate in the waveguide. At low wave vectors, the waveguide mode dispersion approaches the linear dispersion of air (i.e. it is light-like), while at high wave vectors, the waveguide mode approaches the bulk dispersion curve of LN along the extraordinary axis.

Additionally, the waveguide mode profiles in (2.37) can be solved for explicitly for the symmetric and antisymmetric modes. For the symmetric modes, setting $A_1 = A_2 = 1/2$ and $B = C = \cos(\kappa\ell)$, the E-field profiles:

$$\vec{E}(x) = \hat{z}E_0 \begin{vmatrix} \cos(\kappa\ell)\exp[\alpha(x+\ell)] & x \le -\ell \\ \cos(\kappa x) & -\ell \le x \le \ell \\ \cos(\kappa\ell)\exp[-\alpha(x-\ell)] & x \ge \ell \end{vmatrix} \tag{2.49}$$

where E_0 is the amplitude of the E-field in V/m. For the asymmetric modes, setting $A_1 = -A_2 = 1/2$ and $B = -C = \sin(\kappa\ell)$

$$\vec{E}(x) = \hat{z}E_0 \begin{vmatrix} -\sin(\kappa\ell)\exp[\alpha(x+\ell)] & x \le -\ell \\ \sin(\kappa x) & -\ell \le x \le \ell \\ \sin(\kappa\ell)\exp[-\alpha(x-\ell)] & x \ge \ell \end{vmatrix} \tag{2.50}$$

The mode profiles of the lowest three TE waveguide modes are shown in Fig. 2-8.

From the dispersion curves, it is straightforward to calculate the phase index and group index of the THz waves, which are representative of the THz phase and group velocities, respectively. The effective phase index of refraction is given at every point on the dispersion curve: $n(\omega) = \beta c_0/\omega$, while the effective group index of refraction is given as the instantaneous slope at each point: $n_{gr} = \Delta\beta c_0/\Delta\omega$. The phase and group indices of the TE modes are plotted in Fig. 2-9 without accounting for material dispersion in (a) and with material dispersion in (b). For a material with negligible dispersion, at large frequencies the phase

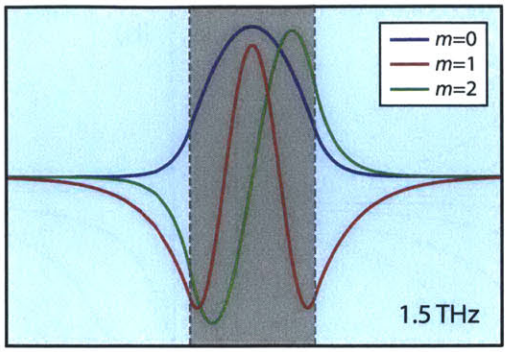

Figure 2-8: **TE waveguide mode profiles.** The lowest three modes in a 50 μm slab of LN calculated at 1.5 THz.

indices (solid lines) and group indices (dashed lines) of all waveguide modes both plateau to the bulk index of the core ($\sim$ 5 in LN) while at lower frequencies, they approach the index of the cladding (1 for air). For dispersive materials, the phase and group indices do not approach a constant bulk index since its frequency-dependence must be taken into account, which poses challenges in phase matched THz generation. Most important to take note of is the waveguide dispersion present far below the optic phonon resonance in LN at 7.6 THz, which means that wave of different frequencies within a waveguide mode travel at different speeds. We will later show how phase velocity dispersion can be used for generating narrowband THz waves. Additionally, the consistently higher group index in the higher order modes means that higher order modes (the envelopes of the fields) lag behind the lower order modes as they propagate laterally through the crystal.

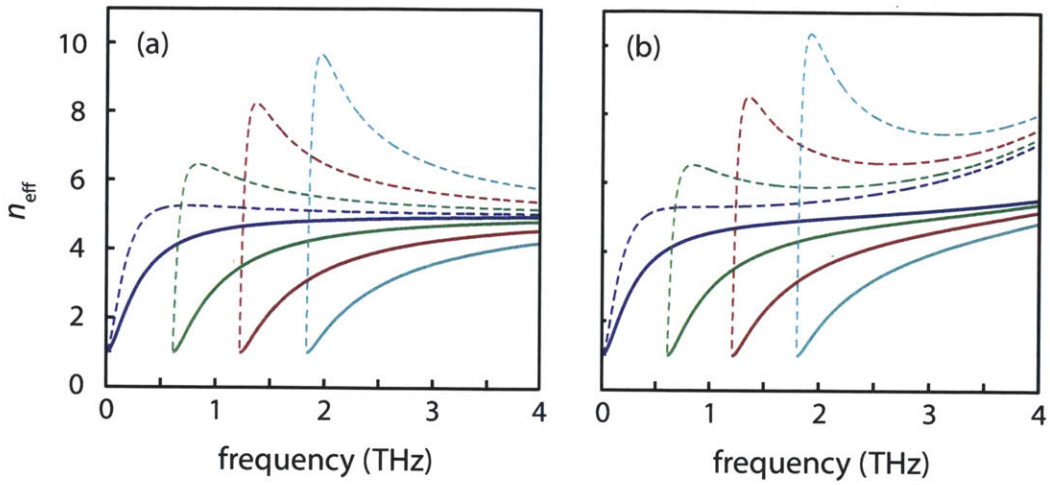

Figure 2-9: **Effective phase and group indices of TE modes in LN.** Phase (solid lines) and group (dashed-lines) indices of lowest four modes in 50 μm LN without material dispersion in (a) and with material dispersion in (b).

2.3.1.3 TM Modes in Anisotropic Symmetric Dielectric Slab Waveguide

In the TM-polarization case, the anisotropy of the core must be considered. The polarizations are uniquely defined by the extraordinary polarization, $\vec{e}$, and the ordinary polarization, $\vec{o}$. The dielectric cladding (air) is isotropic so we can choose any two orthogonal polarizations: vertical polarization, $\vec{v}$, and horizontal polarization, $\vec{h}$. Therefore, the most general form of the E-fields of the waveguide modes in each region can now be written as follows:

Cladding ($x \leq -\ell$):

$$\vec{E}(x) = C_1\hat{v}^- \exp[\alpha(x+\ell)] + C_2\hat{v}^+ \exp[-\alpha(x+\ell)] + C_3\vec{h}^- \exp[\alpha(x+\ell)] + C_4\vec{h}^+ \exp[-\alpha(x+\ell)], \tag{2.51a}$$

Core ($-\ell \leq x \leq \ell$):

$$\vec{E}(x) = A_1\vec{e}^{+}\exp(i\kappa_e x) + A_2\vec{e}^{-}\exp(-i\kappa_e x) + A_3\vec{o}^{+}\exp(i\kappa_o x) + A_4\vec{o}^{-}\exp(-i\kappa_o x) \qquad (2.51b)$$

Cladding ($x \geq \ell$):

$$\vec{E}(x) = B_1\hat{v}^{-}\exp[\alpha(x-\ell)] + B_2\hat{v}^{+}\exp[-\alpha(x-\ell)] + B_3\vec{h}^{-}\exp[\alpha(x-\ell)] + B_4\vec{h}^{+}\exp[-\alpha(x-\ell)], \qquad (2.51c)$$

where A_i, B_i, and C_i are scalar constants.

The extraordinary polarization is located in the plane containing the wave vector, $\vec{k}$, and the optic axis, $\vec{c}$, while the ordinary polarization is located orthogonal to this plane: $\vec{e} \propto \vec{k} \times (\vec{k} \times \vec{c})$ and $\vec{o} \propto \vec{k} \times \vec{c}$. The relevant vectors are defined as follows:

$$\vec{c} = \begin{bmatrix} 0 \\ \sin\theta \\ \cos\theta \end{bmatrix} \quad \text{and} \quad \vec{k} = \begin{bmatrix} \pm k_x \\ \beta \\ 0 \end{bmatrix} \qquad (2.52)$$

where θ is the angle between the z-axis and the *eo*-axis of the crystal and the appropriate k_x is applied (κ_e for $\vec{e}$ and κ_o for $\vec{o}$). In an anisotropic waveguide, the angle must be accounted for in both $\vec{e}$ and $\vec{o}$.

In terms of defining $\vec{e}$, which describes the polarization of extraordinary E-fields, the angle-dependence of the propagation constant as seen in (2.33), is taken into account by expressing it in terms of the displacement field, $\vec{D}$, since $\vec{D} \propto \vec{k} \times (\vec{k} \times \vec{c})$. The D-field is written as:

$$\vec{D} = \frac{D_0}{\sqrt{\beta^2 + \kappa_e^2}} \begin{bmatrix} \mp\beta \\ \kappa_e \\ 0 \end{bmatrix} \qquad (2.53)$$

where D_0 is the amplitude of the D-field in C/m^2.

The relationship between $\vec{D}$ and $\vec{E}$ is expressed by the constitutive relation: $\vec{E} = \overline{\overline{R}}(-\theta)\overline{\overline{\epsilon}}^{-1}\overline{\overline{R}}(\theta)\vec{D}$ where the dielectric tensor, $\overline{\overline{\epsilon}}$, has been rotated around the x-axis by θ, as in Fig. 2-6(a). For a uniaxial crystal with the principal axes chosen in Fig. 2-6(a), the dielectric tensor has the form:

$$\overline{\overline{\epsilon}} = \begin{bmatrix} \varepsilon_o & 0 & 0 \\ 0 & \varepsilon_o & 0 \\ 0 & 0 & \varepsilon_e \end{bmatrix} \tag{2.54}$$

where ε_o and ε_e are the ordinary and extraordinary permittivity, respectively, in C·V^{-1}·m^{-1}. The rotation around the x-axis is given by: $\overline{\overline{\epsilon}}' = \overline{\overline{R}}(=\theta)\overline{\overline{\epsilon}}\overline{\overline{R}}(\theta)$, where:

$$\overline{\overline{R}}(\theta) = \begin{bmatrix} 1 & 0 & 0 \\ 0 & \cos\theta & -\sin\theta \\ 0 & \sin\theta & \cos\theta \end{bmatrix} \tag{2.55}$$

We can see that when $\theta = 0°$, as in the TE cases, the rotation matrix takes on the identity form in which the dielectric tensor is unchanged and the angle of rotation can be ignored. The resulting rotated dielectric tensor for TM modes with $\theta = 90°$ is then:

$$\overline{\overline{\epsilon}}' = \begin{bmatrix} \varepsilon_o & 0 & 0 \\ 0 & \varepsilon_e & 0 \\ 0 & 0 & \varepsilon_o \end{bmatrix} \tag{2.56}$$

There are no off-diagonal terms since pure TE or TM modes do not couple to each other. For $\theta \neq 0°$ or 90°, we have TE- or TM-like modes that are superpositions of the extraordinary and ordinary waves.

The extraordinary and ordinary polarizations of the E-field when $\theta = 90°$ are then:

$$\vec{e}^{\pm} \propto \frac{1}{\sqrt{\beta^2 + \kappa_e^2}} \begin{bmatrix} \mp\beta/\varepsilon_o \\ \kappa_e/\varepsilon_e \\ 0 \end{bmatrix} \quad \text{and} \quad \vec{o}^{\pm} \propto \frac{1}{\kappa_o} \begin{bmatrix} 0 \\ 0 \\ \pm\kappa_o \end{bmatrix} = \begin{bmatrix} 0 \\ 0 \\ 1 \end{bmatrix} \tag{2.57}$$

In contrast, for the isotropic cladding, any two orthogonal polarizations may be used, where we substitute $\vec{v}$ and $\vec{h}$ in (2.51) by $\vec{z}$ and $\vec{l}^{\pm}$ (from (2.34) and (2.35)), respectively:

$$\hat{z} = \begin{bmatrix} 0 \\ 0 \\ 1 \end{bmatrix} \quad \text{and} \quad \vec{l}^{\pm} \propto \begin{bmatrix} -\beta \\ \pm i\alpha \\ 0 \end{bmatrix}. \tag{2.58}$$

We can then simplify the E-field expressions in (2.51) since TM waves are described by $\vec{e}^{\pm}$ and $\vec{l}^{\pm}$. Also, any E-field components that do not decay to zero as $x \to \infty$ are discarded. This yields:

$$\text{Cladding } (x \le -\ell): \ \vec{E}(x) = C\vec{l}^{-} \exp[\alpha(x + \ell)], \tag{2.59a}$$

$$\text{Core } (-\ell \le x \le \ell): \ \vec{E}(x) = A_1\vec{e}^{+} \exp(i\kappa_e x) + A_2\vec{e}^{-} \exp(-i\kappa_e x) \tag{2.59b}$$

$$\text{Cladding } (x \ge \ell): \ \vec{E}(x) = B\vec{l}^{+} \exp[-\alpha(x - \ell)], \tag{2.59c}$$

The TM modes are found by applying the last two boundary conditions in (2.40c) and (2.40d) at $x = \ell$, and solving separately for the symmetric and anti-symmetric modes. For the symmetric modes, $A = A_1 = A_2$:

$$\begin{bmatrix} (\kappa_e/n_e^2)\cos(\kappa_e \ell) & -\alpha \\ \sin(\kappa_e \ell) & n_c^2 \end{bmatrix} \begin{bmatrix} A \\ B \end{bmatrix} = 0 \tag{2.60}$$

The transcendental equation for symmetric TM modes is:

$$-\cot(\kappa_e \ell) = \frac{\alpha n_e^2}{\kappa_e n_c^2} \tag{2.61}$$

For the anti-symmetric modes, $A = A_1 = -A_2$:

$$\begin{bmatrix} (\kappa_e/n_e^2)\sin(\kappa_e \ell) & \alpha \\ \cos(\kappa_e \ell) & n_c^2 \end{bmatrix} \begin{bmatrix} A \\ B \end{bmatrix} = 0 \tag{2.62}$$

The transcendental equation for antisymmetric TM modes is:

$$\tan(\kappa_e \ell) = \frac{\alpha n_e^2}{\kappa_e n_c^2} \tag{2.63}$$

Again, using the trigonometric identity that $\tan(\theta + \pi/2) = -\cot(\theta)$ and $\tan(\theta) = \tan(\theta + m\pi)$, then the solution for both the symmetric and anti-symmetric TM modes can be described by:

$$\tan(\kappa_e \ell + m\frac{\pi}{2}) = \frac{\alpha n_e^2}{\kappa_e n_c^2} \tag{2.64}$$

where $m = 0, 1, 2, \cdots$ represents the mode number; $m = 0$ corresponds to the lowest anti-symmetric mode and $m = 1$ corresponds to the lowest symmetric mode.

Similar to solving for the TE modes, we also substitute $B = (\beta/k_0)^2$ to yield the following:

$$\kappa_e = \frac{n_e k_0}{n_o}\sqrt{n_o^2 - B} \tag{2.65}$$

$$\alpha = k_0\sqrt{B - n_c^2} \tag{2.66}$$

The transcendental equation can then be simplified to:

$$\tan^{-1}\left(n_e n_o \sqrt{\frac{B - n_c^2}{n_o^2 - B}}\right) - \frac{n_e k_0 \ell}{n_o}\sqrt{n_o^2 - B} + m\frac{\pi}{2} = 0 \tag{2.67}$$

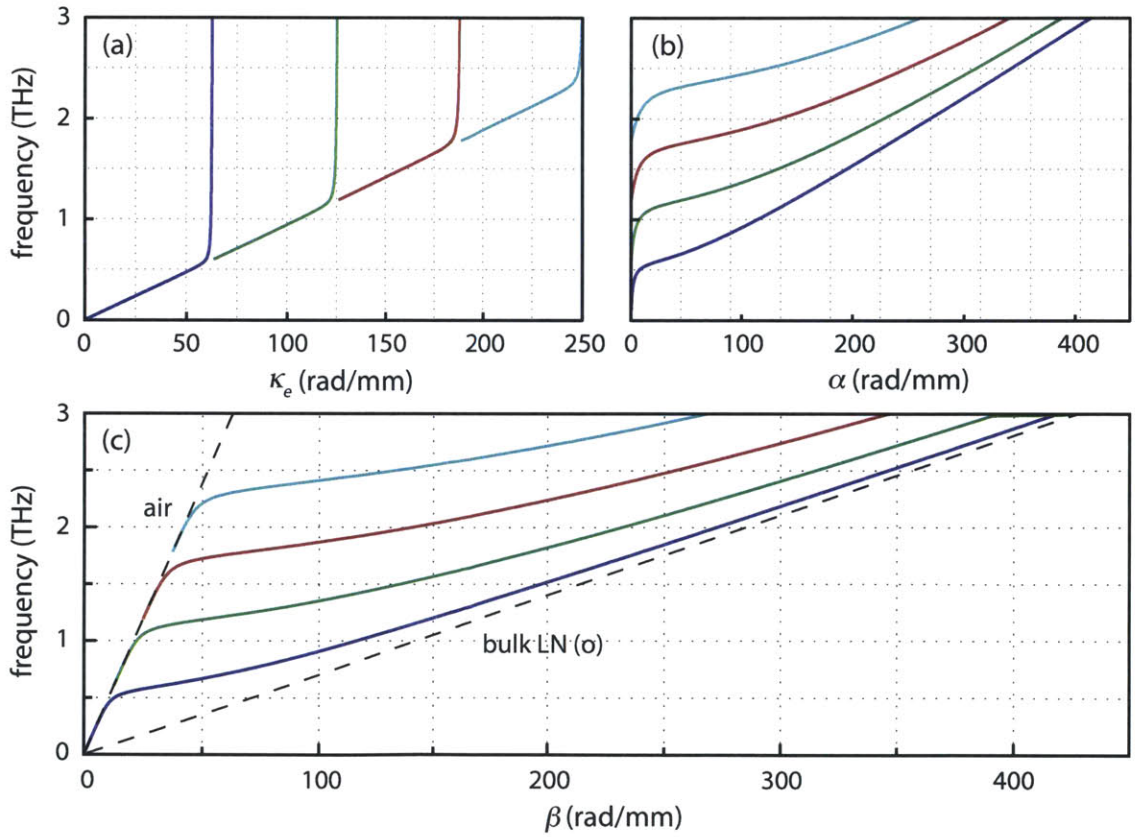

Figure 2-10: **TM dispersion curves.** For the lowest four modes in a 50 μm slab of LN, the wave vectors are calculated in (a) the core, κ_e, (b) α, in the cladding, and (c) the propagation constant, β.

The dispersion curves are shown in Fig. 2-10 and the effective phase and group indices are shown in Fig. 2-11.

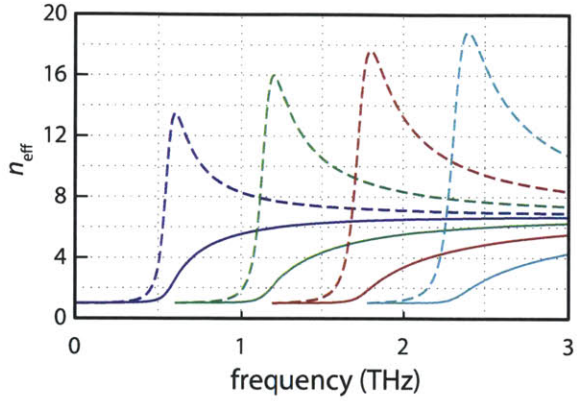

Figure 2-11: **Effective phase and group indices of TM modes in LN.** The phase (solid) and group (dashed) indices of the lowest four modes in a 50 μm slab of LN.

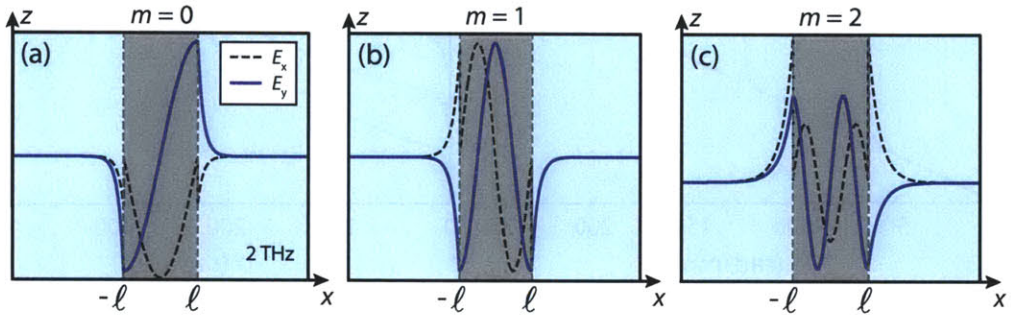

Figure 2-12: **TM mode profiles.** The E-field profiles are calculated for E_x and E_y components for (a) the lowest order m=0 mode, (b) m=1 mode, and (c) m=2 mode.

The waveguide mode profiles can be written exactly with the values of the scalar constants imposed by the boundary conditions. The symmetric TM waveguide mode profiles are found after determining the constants $A_1 = A_2 = 1/2$, $B = -C = -i\left[\kappa_e/(\alpha\varepsilon_e\sqrt{\beta^2+\kappa_e^2})\right]\cos(\kappa_e\ell)$:

$$\vec{E}(x) = \frac{D_0}{\sqrt{\beta^2+\kappa_e^2}} \left\{ i\hat{x} \begin{bmatrix} -\frac{\kappa_e\beta}{\alpha\varepsilon_e}\cos(\kappa_e\ell)\exp[\alpha(x+\ell)] \\ -(\beta/\varepsilon_o)\sin(\kappa_e x) \\ \frac{\kappa_e\beta}{\alpha\varepsilon_e}\cos(\kappa_e\ell)\exp[-\alpha(x-\ell)] \end{bmatrix} \right.$$
$$\left. + \hat{y}(\kappa_e/\varepsilon_e) \begin{bmatrix} \cos(\kappa_e\ell)\exp[\alpha(x+\ell)] \\ \cos(\kappa_e x) \\ \cos(\kappa_e\ell)\exp[-\alpha(x-\ell)] \end{bmatrix} \right\} \begin{matrix} x \le -\ell \\ -\ell \le x \le \ell \\ x \ge \ell \end{matrix} \quad (2.68)$$

The anti-symmetric TM modes profiles are similarly written with the determined constants $A_1 = -A_2 = 1/2$, $B = C = \left[\kappa_e/(\alpha\varepsilon_e\sqrt{\beta^2+\kappa_e^2})\right]\sin(\kappa_e\ell)$:

$$\vec{E}(x) = \frac{D_0}{\sqrt{\beta^2+\kappa_e^2}} \left\{ -\hat{x} \begin{bmatrix} \frac{\kappa_e\beta}{\alpha\varepsilon_e}\sin(\kappa_e\ell)\exp[\alpha(x+\ell)] \\ (\beta/\varepsilon_o)\cos(\kappa_e x) \\ \frac{\kappa_e\beta}{\alpha\varepsilon_e}\sin(\kappa_e\ell)\exp[-\alpha(x-\ell)] \end{bmatrix} \right.$$
$$\left. + i\hat{y}(\kappa_e/\varepsilon_e) \begin{bmatrix} -\sin(\kappa_e\ell)\exp[\alpha(x+\ell)] \\ \sin(\kappa_e x) \\ \sin(\kappa_e\ell)\exp[-\alpha(x-\ell)] \end{bmatrix} \right\} \begin{matrix} x \le -\ell \\ -\ell \le x \le \ell \\ x \ge \ell \end{matrix} \quad (2.69)$$

2.3.2 Experimental Broadband and Narrowband THz Generation in Lithium Niobate

2.3.2.1 THz Broadband Slab Waveguide Generation

As a modification to THz generation in bulk systems discussed in the last section, shrinking the depth dimension to a subwavelength scale relative to the THz waves forms the basis of the

THz planar waveguide. Due to the large Cherenkov angle (63°), the dominant wave vector component in the bulk crystal is in the lateral dimension such that the THz waves propagate primarily perpendicular to the propagation direction of the optical pump. The THz waves propagate as discrete waveguide modes, bound within the high-index core, as discussed in the previous section. The waveguide undergoes TIR (which is also present in bulk LN crystals), as the waves bounce back and forth from front to back surface of the thin slab of LN, with a small forward component resulting from the forward-propagating pump. Unlike for free-space THz applications, it is advantageous to have the wave confined within the slab since the generated THz waves that propagate laterally can either be manipulated by integrated structures or made to interact with a sample placed on the surface, and subsequently can be detected on the same slab sample either by imaging methods or at a single point, as discussed in the next chapter.

The generation of TE or TM modes (or a hybrid) is based on the polarization of the optical pump relative to the propagation direction of the THz waveguide modes. Experimentally, we focus an 800 nm optical pump (pulse energy of 470 μJ) to a narrow vertical line with an achromatic cylindrical lens (f = 15 cm), giving a beam waist diameter of $\sim$ 10 μm, at normal incidence to a thin slab of LN (ℓ = 30–50 μm). Figure 2-13(a) shows the experimental pumping geometry in the waveguide, where the impulsive pump generates counter-propagating THz waves traveling in the lateral directions. The propagation direction is denoted by the wave vector k in Fig. 2-13(b); TE waves are generated when the E-field of the optical pump is polarized perpendicular to k ($E_y = 0$) while TM waves are generated when the optical E-field is polarized parallel to k ($H_y = 0$). In either case, we rotated the crystal (and pump polarization) such that the extraordinary axis or optic c-axis of LN (containing the strongest nonlinear coefficient d_{33}) lies along the pump polarization direction for the highest generation efficiency, previously depicted in Fig. 2-6. However, TM generation results in a weaker pumping efficiency compared to the TE case, which can approximated by calculating the fractional modal volumes bound inside the crystal (i.e. E_y and E_z) [39].

In the waveguide regime, phase matching is not the limiting factor for attaining high field strengths since the crystal is so thin, but as in the bulk crystal, the pump intensity is limited by the damage threshold of LN. We used 0.6% MgO-doped stoichiometric LN that has been shown to have higher optical damage thresholds than undoped LN. We obtain the highest optical pump fluence by optimizing the position of the cylindrical lens to maximize the second-harmonic (400 nm) light that is also generated in the nonlinear crystal, avoiding immediate damage to the crystal. Sometimes the crystal is damaged over prolonged exposure to the tightly focused pump.

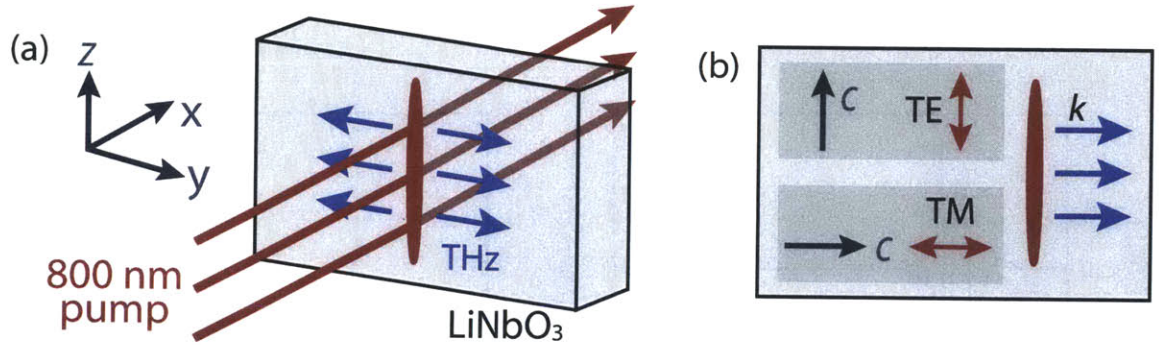

Figure 2-13: **Broadband THz generation in a LN waveguide.** (a) Schematic illustration of the experimental geometry, where a cylindrically focused 800 nm pump pulse is directed at normal incidence through a LN crystal. The generated THz waves counter-propagate in the lateral directions due to the large index difference and are waveguided down the slab by total internal reflection. (b) The requisite polarization of the optical pump relative the optic c-axis of the crystal for generating TE and TM THz waveguide modes.

An example of a broadband TE-polarized THz time trace in a 30 μm-thick slab of LN is shown in Fig. 2-14(a), measured at a distance away from the generation region. This is a clear demonstration of waveguide dispersion, where an initially single-cycle broadband pulse at the point of generation is chirped and separated into the discrete waveguide modes as they propagate at different speeds. At the initial point of generation, with no lateral propagation, the THz waveform would appear as essentially single cycle. Broadband THz generation in LN is capable of attaining bandwidths up to 2 THz, with relatively low material damping. In this trace, the first and second waveguide modes are just beginning to separate

(the first order mode runs ahead, appearing at earlier time delay, followed by the higher frequency second order mode at later time delays). Consequently, the waveguide modes are separated in time and interfere with one another, giving rise to spectral interference seen in the frequency domain (the dips in the spectrum) in Fig. 2-14(b). However, spectral interference only occurs above the cutoff frequency of the second mode (characteristically similar to the TE-mode dispersion curves in 50 μm LN shown in Fig. 2-7(c) except that the cutoff for the second mode is at 1.1 THz for a 30 μm slab of LN) since no other modes exist at frequencies below this cutoff. As the waveguide modes continue to evolve, the oscillations resulting from interference in the frequency domain become faster due to an increased time separation between the modes.

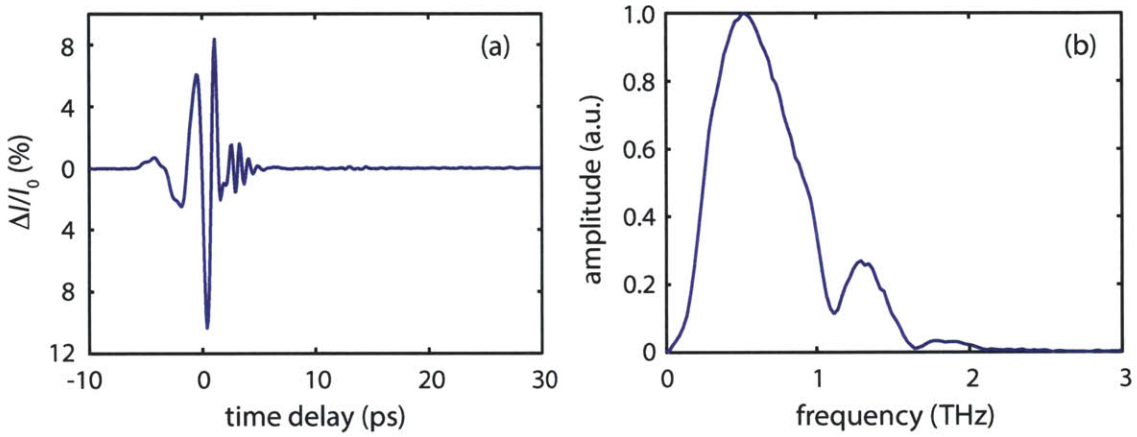

Figure 2-14: **Experimental THz broadband generation in LN Waveguide.** (a) THz time trace in 30 μm thick LN where the first and second order modes are just beginning to separate in time as they propagate at different speeds through the crystal. (b) The Fourier transform of (a) yields the THz spectrum showing bandwidth up to 2 THz. Modulation of the spectrum is a result of waveguide mode interference.

2.3.2.2 Tunable THz Narrowband Waveguide Generation

A narrowband, high-amplitude THz source is necessary to strongly and coherently drive resonant phenomena and to provide a means of isolating specific resonant responses from potentially convoluted broadband responses. In bulk LN, we observed noncollinear phase-

matched THz generation over a relatively broad range of frequencies with a tilted optical pulse front, made possible due to the linearity of the index of LN below the lowest optic phonon resonance at 7.6 THz. However, in the waveguide regime there is pronounced dispersion of the waveguide modes (in addition to material dispersion), which introduces considerable phase velocity dispersion. Waveguide dispersion can be exploited for narrowband generation by using the same concept of tilting an optical pulse front, such that the effective lateral group velocity of the optical pump matches the lateral THz phase velocity at a selected THz frequency.

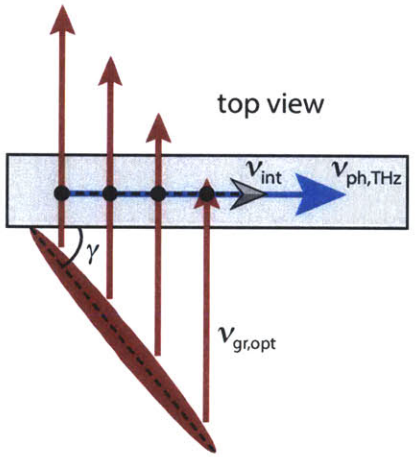

Figure 2-15: **Narrowband pumping geometry.** The optical pump is tilted at an angle, γ, and propagates at normal incidence relative to the surface of the LN crystal. The intersection velocity between the optical pump and THz waves is given by ν_{int} and is equal to the THz phase velocity, $\nu_{\text{ph,THz}}$, at a selected THz frequency.

As shown previously for the TE modes in Fig. 2-9, the THz phase velocity dispersion is clearly observed by calculating the phase index for each waveguide mode. By tuning the angle of the optical pulse front's tilt to match the THz phase index of a particular frequency, we can attain narrowband pulses for one or multiple waveguide modes. In this way, the peak of the optical pump continuously intersects the peak of the THz wave, and coherently amplifies the THz wave at the selected frequency while destructively interfering at all other frequencies. Figure 2-15 shows a top view of the experimental pumping geometry, where the following

velocity matching condition must be satisfied when $\nu_{\text{int}}(\gamma) = \nu_{\text{ph,THz}}(\omega_0)$, where the lateral intersection velocity is given by $\nu_{\text{int}}(\gamma) = \nu_{\text{gr,opt}}\cot(\gamma)$ and $\nu_{\text{ph,THz}}(\omega_0) = c/n_{\text{eff}}(\omega_0)$ is the THz phase velocity at the selected frequency ω_0. Because $\nu_{\text{gr,opt}} = c$ is the optical group velocity in air, the velocity matching condition is simplified to:

$$n_{\text{eff}}(\omega_0) = \tan(\gamma) \tag{2.70}$$

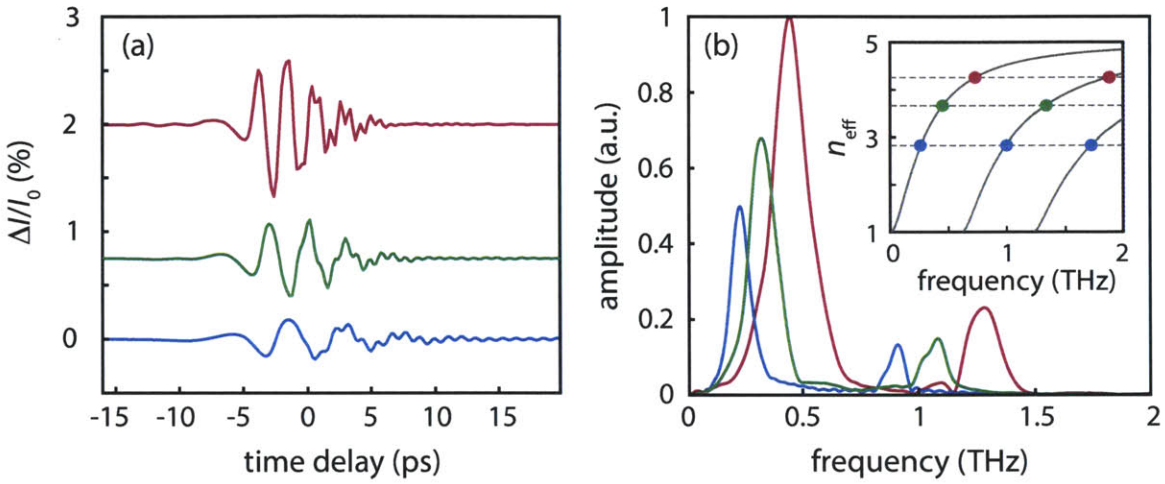

Figure 2-16: **Experimental narrowband THz generation in the waveguide.** (a) Narrowband THz time traces tuned to three different frequencies in 50 μm LN, where the first and second order waveguide modes are observed. (b) The narrowband THz spectra of (a) showing two peaks corresponding to the two modes at different frequencies. The inset shows that these modes possess the same effective index and hence both satisfy the velocity matching condition.

Narrowband generation creates multi-cycle THz waves as seen in Fig. 2-16(a) for any mode(s) that satisfies the velocity matching condition in (2.70). In the time traces, the second order mode is also present, albeit pumped less efficiently than the first order mode, since it has the same n_{eff} at a different frequency ω_0. This is made clear in the Fourier spectra of the traces in Fig. 2-16(b), where two peaks were detected for each trace (the third mode was at the edge of our bandwidth and difficult to measure). The inset in Fig. 2-16(b) demonstrates the velocity matching condition, which as observed can be satisfied by one or more modes. The relative bandwidth with respect to the center frequency is narrower at

higher frequencies since a larger number of cycles can be phase matched over the interaction length between the optical pump and THz waves, which is also evident in the time traces.

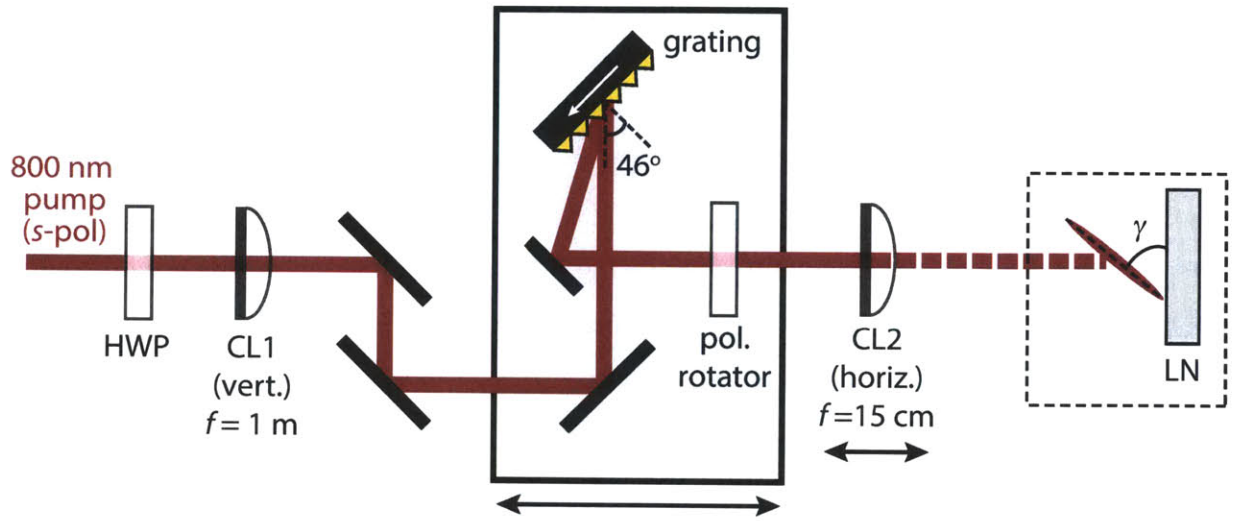

Figure 2-17: **Narrowband experimental pumping geometry.** An 800 nm pump beam is incident on a diffraction grating at 46°, and emerges tilted at an angle of 73.6°. The final tilt angle, γ, at the LN crystal, which determines the velocity matching condition, is set by the magnification ratio determined by the one-lens imaging system with an achromatic cylindrical lens. A polarization rotator is used to flip the p-polarized light off the grating back to s-polarized and parallel to the optic axis of LN for TE mode generation. The two double-sided arrows indicate adjustable stages for adjustment of the imaging ratio of the grating surface at the LN crystal.

The experimental pumping scheme, depicted in Fig. 2-18, demonstrates a way to obtain the requisite tilt angle γ of the optical pump at the LN crystal. The optical pulse front is tilted by using the m = -1 order of the diffraction grating (2000 grooves/mm) most efficient for p-polarization and imaging it using a one-lens imaging system with an achromatic cylindrical lens (CL2, f = 15 cm) onto the LN crystal. An upstream long focal length cylindrical lens (CL1, f = 1 m) is used to minimize the spot height for a higher pump fluence. The final tilt angle is then set by the initial tilt angle, γ_i, off the grating (set by the incidence angle, α) and the imaging ratio, M: $\tan(\gamma) = \tan(\gamma_i)/M$ (i.e. smaller γ for a larger M ratios). The

tilt, γ, of the m = -1 order diffraction beam is given by:

$$\tan(\gamma) = \frac{\lambda}{d\cos\beta} \tag{2.71}$$

where λ = 800 nm, d is the groove spacing in nm, and β is the angle of diffraction. The angle of diffraction is calculated using the grating equation:

$$\beta = \sin^{-1}\left(\frac{\lambda}{d} - \sin\alpha\right) \tag{2.72}$$

where α is the angle of incidence onto the grating. We used an incidence angle of 46°, which corresponds to a tilt angle of 73.6° for the -1 order diffraction beam. Lastly, a polarization rotator is used to flip the polarization of the tilted optical pump back to s-polarization, parallel to the c-axis of the LN crystal for TE waveguide mode generation.

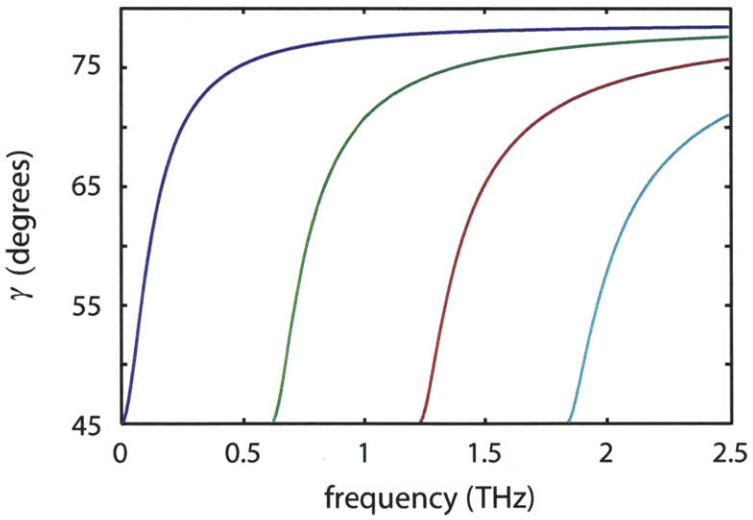

Figure 2-18: **Tilt angles for narrowband THz generation.** For a 50 μm slab of LN crystal, the tilt angle, γ is calculated as a function of frequency for the four lowest waveguide modes.

For tuning the center wavelength of the narrowband THz field, we fixed the position of the LN (image plane) and moved both the cylindrical lens and grating arrangement built on a small breadboard (object plane) together to change the magnification ratio. From

Fig. 2-18, we see that steeper tilt angles (smaller M) are needed for attaining higher center frequencies, which result in shorter interaction lengths. In the waveguide, angular dispersion off the grating and the limited depth of focus provided by a one-lens imaging system are not problems, unlike in bulk systems where they limit the interaction length and consequently the generation efficiency. In those cases, angular dispersion may be minimized by introducing the tilt with an echelon instead of a grating and two-lens imaging of the pulse front.

Chapter 3

Terahertz Detection Methodology

3.1 Introduction

As a result of the intermediate regime of THz frequencies, conventional electronic or optical detection technologies are unfeasible for either the temporal or spectral detection of THz electromagnetic waves. With the development of THz generation techniques via optical rectification in nonlinear crystals came the complementary development of coherent THz detection via the inverse process called electro-optic (EO) sampling. It is a time domain detection technique that has the unique capability of accurately measuring the amplitude and phase of the THz E-field transient. EO sampling is typically implemented with a focused optical probe beam, with a spot size much smaller than that of the THz beam at the crystal, and is referred to in this thesis as point-source THz detection. In very thin slabs of LN (i.e. THz waveguides), where the THz waves propagate primarily in the lateral direction, orthogonal to the optical pump pulse, an expanded probe beam can be used to spatially resolve the THz propagation. In the Nelson lab, we use two THz imaging techniques: polarization gating imaging that is fundamentally similar to EO sampling and phase contrast imaging that is based on refractive index contrast.

In this chapter, I will describe point-source THz detection that is used in both bulk and waveguided nonlinear crystals and recent technical improvements in the spatial resolution and signal-to-noise (S/N) of the two THz imaging techniques in the waveguide regime.

3.2 Point-source THz detection

EO sampling is based on the principle that a THz E-field can modulate the polarization of an optical probe pulse through the linear EO-effect in a nonlinear $\chi^{(2)}$ medium, referred to as the Pockels effect. [19,31]. Experimentally, the change in polarization state is temporally gated by a short optical probe pulse with femtosecond pulse duration, over which the THz E-field is averaged, and hence sets the time resolution of the measurement. A pump-probe geometry is employed where the time axis is derived from the scanning of a mechanical stage typically in the probe arm to introduce a relative time delay between the pump and probe pulses that respectively generate and measure the THz field. Point-source detection measures the THz waveform at essentially a single position and thus recovers time traces that contain no spatial content other than the location of the focused probe spot, but yields a higher S/N ratio for the THz field profile than imaging measurements. In this section, I will describe the EO effect in ZnTe and LN, the experimental implementation of EO sampling in bulk and waveguided systems, and the instrumentation required for reliable acquisition.

3.2.1 The Electro-optic Effect

The EO effect is the change in the optical refractive index of a material in response to an applied dc or time-varying E-field, such as a THz E-field. In the Pockels effect, the change in optically measured refractive index is linearly proportional to the strength of the applied

field. The linear EO effect can be described by the second order nonlinear polarization:

$$P_i(\omega) = 2\epsilon_0 \sum_{jk} \overline{\overline{\overline{\chi^{(2)}}}}_{ijk}(\omega = \omega + 0, \omega, 0) E_j(\omega) E_k(0) \tag{3.1}$$

where $E_j(\omega)$ is the E-field of the optical probe and $E_k(0)$ is the lower-frequency THz E-field. Analogous to THz generation via optical rectification, as a result of the symmetry constraints on the second order nonlinear susceptibility, the Pockels effect only exists in crystals that do not have inversion symmetry.[1] From (3.1), we observe that the nonlinear polarization is linearly dependent on the applied THz E-field, $E_k(0)$. Note that we are neglecting the nonzero value of the THz frequency because in our measurements we do not frequency-resolve the modulated optical probe field to measure its shift by that frequency.

In the following analysis, we will derive the effect of an applied THz E-field on the optically measured refractive index. For an anisotropic material, the relationship between the displacement field, $\vec{D}$, and the electric field, $\vec{E}$, of the optical probe is given by:

$$\begin{aligned} \vec{D}^{\text{opt}} &= \epsilon_0 \bar{\bar{\epsilon}} \vec{E}^{\text{opt}} \\ D_i^{\text{opt}} &= \epsilon_0 \sum_j \epsilon_{ij} E_j^{\text{opt}} \end{aligned} \tag{3.2}$$

where $\bar{\bar{\epsilon}}$ is the dielectric tensor and the terms ϵ_{ij} are its matrix elements. For a lossless medium, $\bar{\bar{\epsilon}}$ simplifies to a real, symmetric matrix, in which transformation to a new coordinate system yields a diagonal matrix [19]:

$$\bar{\bar{\epsilon}} = \begin{bmatrix} \epsilon_{xx} & \epsilon_{xy} & \epsilon_{xz} \\ \epsilon_{yx} & \epsilon_{yy} & \epsilon_{yz} \\ \epsilon_{zx} & \epsilon_{zy} & \epsilon_{zz} \end{bmatrix} = \begin{bmatrix} \epsilon_{XX} & 0 & 0 \\ 0 & \epsilon_{YY} & 0 \\ 0 & 0 & \epsilon_{ZZ} \end{bmatrix} \tag{3.3}$$

[1]For centrosymmetric crystals, the lowest order EO effect is the quadratic EO effect or the Kerr effect, in which the change in the optical refractive index depends quadratically on the applied field.

where the transformed coordinates (X, Y, Z) represents the principal-axis system. From the dielectric tensor, we can obtain the refractive index of an anisotropic medium as a function of the propagation direction, since $n = \sqrt{\epsilon/\epsilon_0}$ (assuming a non-magnetic material).

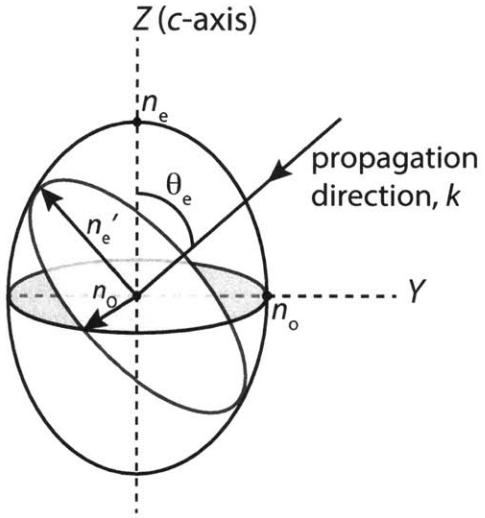

Figure 3-1: **The optical indicatrix.** A geometric representation of the refractive index of a uniaxial anisotropic system that is used to determine the permitted polarization directions and the magnitudes of the refractive index along these directions. For a uniaxial crystal, its principle axes are given by the extraordinary index, n_e, along z, and the ordinary index, n_o, along x and y. Here, an electric field propagates along k at an angle θ_e from the optical (c) or extraordinary axis along z. The two emerging polarizations lie in a plane perpendicular to k, where the intersection between this plane and the index ellipsoid forms an ellipse; the polarization directions are given by the major and minor semi-axes of the ellipse and the effective indices are given by the magnitudes of these vectors, $n_e'(\theta_e)$ and n_o.

Except for propagation along a special direction (i.e. the optical c axis in a uniaxial crystal) or polarized along one of the principle axes of the crystal (i.e. the extraordinary or ordinary axis in a uniaxial crystal), a randomly polarized beam incident at some angle on an anisotropic crystal is decomposed into two orthogonal polarization directions, with each of the beams accompanied by a unique index of refraction that gives its propagation velocity. This variation of refractive index experienced by the propagating waves is geometrically represented in the form called the optical indicatrix or index ellipsoid, depicted in Fig. 3-1. In the principle-axis system, the index ellipsoid in the absence of an applied field takes on

the simplest form:

$$\frac{X^2}{\epsilon_{XX}} + \frac{Y^2}{\epsilon_{YY}} + \frac{Z^2}{\epsilon_{ZZ}} = 1 \tag{3.4}$$

The most general form of the index ellipsoid is expressed in the arbitrary coordinate system (x, y, z):

$$\left(\frac{1}{n^2}\right)_1 x^2 + \left(\frac{1}{n^2}\right)_2 y^2 + \left(\frac{1}{n^2}\right)_3 z^2 + 2\left(\frac{1}{n^2}\right)_4 yz + 2\left(\frac{1}{n^2}\right)_5 xz + 2\left(\frac{1}{n^2}\right)_6 xy = 1 \tag{3.5}$$

where the coefficients $(1/n^2)_i$ are the optical constants along the simplified coordinate i. These subscripts are compact representations of the coordinate system:

$$1 \to x, 2 \to y, 3 \to z, 4 \to yz, 5 \to xz, 6 \to xy.$$

This particular assignment of coordinates is consistent with the notation commonly used for the EO tensor to be defined later.

The effect of the applied field on the refractive index is more clearly seen by using the impermittivity tensor, the matrix inverse of $\bar{\bar{\epsilon}}$: $\bar{\bar{\eta}} = \bar{\bar{\epsilon}}^{-1}$. (3.2) can be rearranged to yield:

$$\vec{E}^{\text{opt}} = \frac{1}{\epsilon_0}\bar{\bar{\eta}}\vec{D}^{\text{opt}} \tag{3.6}$$

$$E_i^{\text{opt}} = \frac{1}{\epsilon_0}\sum_j \eta_{ij} D_j^{\text{opt}} \tag{3.7}$$

and the index ellipsoid (3.5) is modified to include the impermittivity tensor:

$$\eta_{11}x^2 + \eta_{22}y^2 + \eta_{33}z^2 + 2\eta_{23}yz + 2\eta_{13}xz + 2\eta_{12}xy = 1 \tag{3.8}$$

The elements of the impermittivity tensor in the general and principle-axis system, respec-

tively, are:

$$\overline{\overline{\eta}} = \begin{bmatrix} (1/n^2)_1 & (1/n^2)_6 & (1/n^2)_5 \\ (1/n^2)_6 & (1/n^2)_2 & (1/n^2)_4 \\ (1/n^2)_5 & (1/n^2)_4 & (1/n^2)_3 \end{bmatrix} = \begin{bmatrix} 1/\epsilon_{XX} & 0 & 0 \\ 0 & 1/\epsilon_{YY} & 0 \\ 0 & 0 & 1/\epsilon_{ZZ} \end{bmatrix}. \tag{3.9}$$

In the presence of an applied field, the impermittivity tensor is modified to include the linear EO effect induced by the applied field:

$$\begin{aligned} \overline{\overline{\eta}} &= \overline{\overline{\eta_0}} + \overline{\overline{\Delta\eta}} \\ &= \overline{\overline{\eta_0}} + \mathbf{r}\vec{E}^{\mathrm{THz}} \end{aligned} \tag{3.10}$$

where $\overline{\overline{\eta_0}}$ is the impermittivity tensor in the absence of an applied field and $\mathbf{r} \equiv \overline{\overline{\overline{r}}}$ is the EO tensor (a rank three tensor) pertaining only to the linear EO effect; higher order terms are ignored here. Alternatively, we can write the impermittivity tensor in summation form:

$$\eta_{ij} = \eta_{ij}^{(0)} + \sum_k r_{ijk} E_k^{\mathrm{THz}} \tag{3.11}$$

Because η is real and symmetric, this implies that $\mathbf{r}$ is also real and symmetric in its first two indices, i and j. This means that we can use the compact subscript form defined previously such that $r_{ijk} \equiv r_{hk}$ where h= 1 to 6:

$$\begin{aligned} r_{11k} &\equiv r_{1k} & r_{23k} &= r_{32k} \equiv r_{4k} \\ r_{22k} &\equiv r_{2k} & r_{13k} &= r_{31k} \equiv r_{5k} \\ r_{33k} &\equiv r_{3k} & r_{12k} &= r_{21k} \equiv r_{6k} \end{aligned} \tag{3.12}$$

The change in the refractive index due to an applied THz E-field is given by the second

term in either (3.10) and (3.11). It can be written as:

$$\Delta\left(\frac{1}{n^2}\right)_i = \sum_j r_{ij} E_j^{\mathrm{THz}}, \tag{3.13}$$

where $i = 1, 2, \cdots, 6$ is the contracted coordinate notation for the indices in the impermittivity tensor and $j = 1, 2, 3$ is the direction the THz field is applied. This expression (3.13) may be rewritten in matrix representation:

$$\begin{bmatrix} \Delta(1/n^2)_1 \\ \Delta(1/n^2)_2 \\ \Delta(1/n^2)_3 \\ \Delta(1/n^2)_4 \\ \Delta(1/n^2)_5 \\ \Delta(1/n^2)_6 \end{bmatrix} = \begin{bmatrix} r_{11} & r_{12} & r_{13} \\ r_{21} & r_{22} & r_{23} \\ r_{31} & r_{32} & r_{33} \\ r_{41} & r_{42} & r_{43} \\ r_{51} & r_{52} & r_{53} \\ r_{61} & r_{62} & r_{63} \end{bmatrix} \begin{bmatrix} E_1 \\ E_2 \\ E_3 \end{bmatrix} \tag{3.14}$$

The EO coefficients r_{ij} represent the real material properties that govern how the impermittivity changes as a function of applied field strength, given in units of m/V.

Finally, the distortion of the index ellipsoid from an applied E-field can be rewritten to include the modified η_{ij} coefficients in (3.8):

$$\left[\left(\frac{1}{n^2}\right)_1 + \Delta\left(\frac{1}{n^2}\right)_1\right] X^2 + \left[\left(\frac{1}{n^2}\right)_2 + \Delta\left(\frac{1}{n^2}\right)_2\right] Y^2 + \left[\left(\frac{1}{n^2}\right)_3 + \Delta\left(\frac{1}{n^2}\right)_3\right] Z^2 + 2\Delta\left(\frac{1}{n^2}\right)_4 YZ + 2\Delta\left(\frac{1}{n^2}\right)_5 XZ + 2\Delta\left(\frac{1}{n^2}\right)_6 XY = 1 \tag{3.15}$$

where we have assumed a principle-axis coordinate system in the absence of an applied field, such that the off-diagonal impermittivity terms are zero: $(1/n^2)_4 = (1/n^2)_5 = (1/n^2)_6 = 0$. In the absence of an applied field, $E_{\mathrm{THz}} = 0$, so all the coefficients $\Delta(1/n^2)_i = 0$ and (3.15) is reduced back to (3.4).

3.2.2 The Pockels Effect in Zinc Blende Crystals

The form of the EO tensor is affected by the rotational symmetry properties of the EO crystal (i.e. the terms that must be zero as a result), which can be elucidated from knowledge of its point group. Zinc telluride (ZnTe) and gallium phosphide (GaP), cubic crystals that possess point group symmetry $\bar{4}3m$, have only one nonzero EO coefficient, r_{41} [42]. The overarching goal is to determine the direction and magnitude of the principle axes of the perturbed index ellipsoid in the presence of an applied field, as shown in Fig. 3-1; this requires coordinate transformations. Consequently, with the optical probe polarized along a predetermined direction, we can use the new coordinates to calculate the change in the probe's initial polarization, a direct result of the change in refractive index induced by an applied field.

The EO tensor for point group $\bar{4}3m$ is of the form:

$$r_{ij} = \begin{bmatrix} 0 & 0 & 0 \\ 0 & 0 & 0 \\ 0 & 0 & 0 \\ r_{41} & 0 & 0 \\ 0 & r_{41} & 0 \\ 0 & 0 & r_{41} \end{bmatrix} \tag{3.16}$$

where $r_{41} = r_{52} = r_{63}$. The modified index ellipsoid due to an applied THz E-field is given using (3.14) and (3.15):

$$\left(\frac{1}{n^2}\right) X^2 + \left(\frac{1}{n^2}\right) Y^2 + \left(\frac{1}{n^2}\right) Z^2 + 2r_{41}E_1^{\mathrm{THz}} YZ + 2r_{41}E_2^{\mathrm{THz}} XZ + 2r_{41}E_3^{\mathrm{THz}} XY = 1 \tag{3.17}$$

where the refractive indices simplify to $n_1 = n_2 = n_3 = n$ in the absence of an applied

THz field because the crystal is cubic. From (3.17), it is evident from the existence of cross terms that the coordinate system (X, Y, Z) is not the principle-axis coordinate system of the modified index ellipsoid. Two separate coordinate transformations are required to essentially 'undo' the distortions imposed on the index ellipsoid by the THz E-field , which allows us to directly infer the direction the field is applied along (i.e. its polarization) and its corresponding strength. The two transformations are detailed carefully by Planken *et al.* in [43] for EO detection in ZnTe.

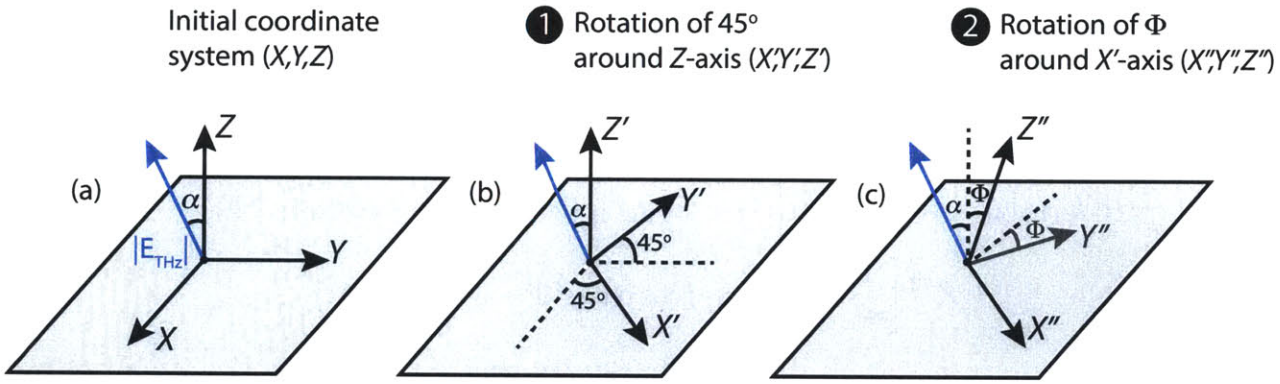

Figure 3-2: **Two coordinate transformations in zinc blende EO crystals.** A THz E-field, polarized at an angle α relative to the Z (001) crystallographic axis and with magnitude $|E_{\mathrm{THz}}|$, is applied to the crystal and distorts the index ellipsoid. In order to determine the extent of the distortion, which is directly related to the EO tensor and THz field strength, we need to determine the new set of principle axes through a sequence of coordinate transformations of the initial unperturbed axes. (a) shows the initial coordinate system (X, Y, Z) in the absence of a THz field. (b) shows the first coordinate transformation that requires a rotation of 45° around the Z-axis to obtain (X', Y', Z'). (c) shows the second coordinate transformation by an angle Φ that is dependent on the initial THz polarization angle α. Appropriate substitution of the transformed coordinates into the index ellipsoid expression puts it into the principle axes frame (X'', Y'', Z'').

Figure 3-2 illustrates the two coordinate transformations that are needed to assign a principle-axis system to the modified ellipsoid. The first transformation is a 45° rotation around the Z axis, which transforms the X and Y axes, but leaves the Z axis unchanged; this results in the new axes (X', Y', Z') as seen in Fig. 3-2(b). For a THz pulse propagating along the (110) axis, the following simplification is used $E_2^{\mathrm{THz}} = -E_1^{\mathrm{THz}}$. The index ellipsoid

in (3.17) is recast in the (X', Y', Z') coordinate system:

$$X'^2\left(\frac{1}{n^2}+E_3^{\mathrm{THz}}r_{41}\right)+Y'^2\left(\frac{1}{n^2}-E_3^{\mathrm{THz}}r_{41}\right)+Z'^2\frac{1}{n^2}+2\sqrt{2}E_1^{\mathrm{THz}}r_{41}Y'Z'=1 \qquad (3.18)$$

Elimination of the last cross term requires a transformation around the X' axis by an angle Φ. If we express the THz E-field in terms of the angle α between the THz polarization and the Z axis, then the components of the field can be rewritten as: $E_3^{\mathrm{THz}} = E_{\mathrm{THz}}\cos\alpha$ and $E_1^{\mathrm{THz}} = \frac{1}{\sqrt{2}}E_{\mathrm{THz}}\sin\alpha$ where $E_{\mathrm{THz}} = \left|\vec{E}_{\mathrm{THz}}\right|$; the magnitude and direction of the THz E-field are shown in Fig. 3-2(a). The index ellipsoid following this transformation to the final coordinate system $(X'', Y''Z'')$ shown in Fig. 3-2(c) is simplified using trigonometric identities to yield:

$$\begin{aligned} X''^2\left(\frac{1}{n^2}+E_{\mathrm{THz}}r_{41}\cos\alpha\right)+Y''^2\left[\frac{1}{n^2}-E_{\mathrm{THz}}r_{41}\left(\cos\alpha\sin^2\Phi+\cos(\alpha+2\Phi)\right)\right] \\ +Z''^2\left[\frac{1}{n^2}-E_{\mathrm{THz}}r_{41}\left(\cos\alpha\cos^2\Phi-\cos(\alpha+2\Phi)\right)\right] \\ +\underbrace{Y''Z''E_{\mathrm{THz}}r_{41}\left(\sin 2\Phi\cos\alpha+2\cos 2\Phi\sin\alpha\right)}_{=0}=1 \end{aligned} \qquad (3.19)$$

The remaining cross term $Y''Z''$ is assumed to be zero if its coefficients are zero; this condition is satisfied for the angles:

$$\begin{aligned} \tan(2\Phi+m\pi) &= -2\tan\alpha \\ 2\Phi &= -\tan^{-1}(2\tan\alpha)-m\pi \end{aligned} \qquad (3.20)$$

where the angle Φ is dependent on the initial angle α between the THz polarization and Z-axis in the original coordinate system, and α is bound according to:
$(m-1/2)\,\pi \le \alpha < (m+1/2)\,\pi$, for $m = 0, 1, 2, \cdots$.

Assuming that $\Delta\left(1/n^2\right) \ll 1/n^2$, then the following differential relation is valid:

$$\frac{\mathrm{d}(1/n^2)}{\mathrm{d}n} = -2n^{-3} \tag{3.21}$$

Then we can replace the differential form by the finite linear difference Δ to reveal the relationship between Δn and $\Delta(1/n^2)$. Substitution and rearrangement of (3.21) yields:

$$\Delta n = -\frac{1}{2}n^3\Delta(1/n^2). \tag{3.22}$$

Lastly, the new index along each axis is simply:

$$n' = n + \Delta n. \tag{3.23}$$

For propagation of an optical probe along the X'' axis, we intersect a plane at $X'' = 0$ with the modified index ellipsoid in the principle-axis system. The plane should pass through the origin of the ellipsoid and is perpendicular to the X'' axis. The resulting intersection forms an ellipse, which is found by setting $X'' = 0$ in (3.19), and consequently the impermittivities of interest lie along Y'' and Z'':

$$\frac{1}{n^2_{Y''}}(\alpha) = \frac{1}{n^2}\underbrace{-E_{\mathrm{THz}}r_{41}\left[\cos\alpha\sin^2\Phi + \cos(\alpha+2\Phi)\right]}_{=\Delta(1/n^2)_{Y''}}, \tag{3.24a}$$

$$\frac{1}{n^2_{Z''}}(\alpha) = \frac{1}{n^2}\underbrace{-E_{\mathrm{THz}}r_{41}\left[\cos\alpha\cos^2\Phi - \cos(\alpha+2\Phi)\right]}_{=\Delta(1/n^2)_{Z''}}. \tag{3.24b}$$

In the principle-axis coordinate system derived here, it is straightforward to determine the terms in (3.19) that are responsible for the change in impermittivity, $\Delta\left(1/n^2\right)$, being the second term in each expression in (3.24). Using (3.22) with substitution of the change in

impermittivity in (3.24), the new refractive indices are:

$$n_{Y''}(\alpha) \approx n + \frac{n^3}{2} E_{\mathrm{THz}} r_{41} \left[\cos\alpha \sin^2\Phi + \cos(\alpha + 2\Phi)\right], \tag{3.25a}$$

$$n_{Z''}(\alpha) \approx n + \frac{n^3}{2} E_{\mathrm{THz}} r_{41} \left[\cos\alpha \cos^2\Phi - \cos(\alpha + 2\Phi)\right]. \tag{3.25b}$$

Note that $n_{Y''} \neq n_{Z''}$, which means that the initially spherical indicatrix under an applied THz E-field becomes elliptical and that the crystal goes from being isotropic to biaxial ($n_{X''} \neq n_{Y''} \neq n_{Z''}$). As a consequence, an optical probe initially linearly polarized at an angle θ relative to the crystallographic Z axis and propagating along X'' experiences different indices along the new axes Y'' and Z'' and hence each of its polarization components accumulates different amounts of optical phase. The optical probe emerges from the crystal elliptically polarized due to the THz-induced birefringence (see probing geometry in Fig. 3-3).

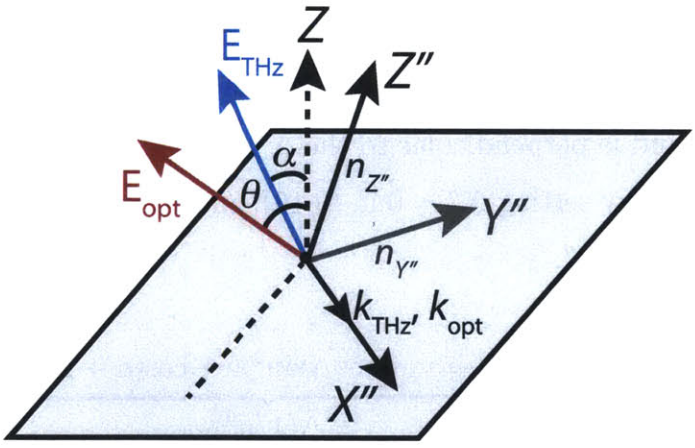

Figure 3-3: **Experimental EO probing geometry in zinc blende crystals.** This schematic illustration of the beam geometry in the crystal shows the polarizations and propagation directions of the optical probe and the applied THz field in the transformed principle axis coordinate system. The THz E-field is polarized at an angle α and the optical probe is polarized at an angle θ relative to the Z (001) axis of the crystal and both beams propagate together along the new principle-axis X''. As a result of the THz induced birefringence, there are two allowed polarization directions along Y'' and Z'' with corresponding modified refractive indices, $n_{Y''}$ and $n_{Z''}$. Because $n_{Y''} \neq n_{Z''}$, the optical probe becomes elliptically polarized as it propagates through the crystal.

3.2.3 The Pockels Effect in Lithium Niobate

EO detection in zinc blende crystals is the most widespread since it allows for detection of THz E-fields in the collinear geometry, a direct result of the requisite phase matching described in the previous chapter for THz generation. However, in the polaritonics platform (also described in Ch. 2), the large index difference at THz and optical frequencies in EO crystals, such as lithium niobate (LN) and lithium tantalate (LT), is utilized since it allows for generation and detection in the same sample. LN is a trigonal crystal with point group symmetry $3m$ and therefore its EO tensor takes on the form:

$$r_{ij} = \begin{bmatrix} 0 & -r_{22} & r_{13} \\ 0 & r_{22} & r_{13} \\ 0 & 0 & r_{33} \\ 0 & r_{51} & 0 \\ r_{51} & 0 & 0 \\ -r_{22} & 0 & 0 \end{bmatrix} \tag{3.26}$$

where $r_{22} = -r_{12} = -r_{61}$, $r_{51} = r_{42}$, and $r_{13} = r_{23}$. The modified index ellipsoid due to an applied THz E-field is given using (3.14) and (3.15):

$$\left[\left(\frac{1}{n^2}\right)_1 - r_{22}E_2 + r_{13}E_3\right] X^2 + \left[\left(\frac{1}{n^2}\right)_2 + r_{22}E_2 + r_{13}E_3\right] Y^2 + \left[\left(\frac{1}{n^2}\right)_3 + r_{33}E_3\right] Z^2 + 2r_{51}E_2YZ + 2r_{51}E_1XZ - 2r_{22}E_1XY = 1. \tag{3.27}$$

In our experiments, we use x-cut LN, such that $n_1 = n_2 = n_o$, and $n_3 = n_e$, where n_o and n_e are the ordinary and extraordinary refractive indices, respectively. In the probing geometry, we use an optical probe propagating at normal incidence to the crystal (i.e. along X) and

so we can simplify the indicatrix above to be in the most relevant form by setting $X = 0$:

$$\left[\frac{1}{n_o^2} + r_{22}E_2 + r_{13}E_3\right] Y^2 + \left[\frac{1}{n_e^2} + r_{33}E_3\right] Z^2 + 2r_{51}E_2 YZ = 1. \tag{3.28}$$

For the THz field strengths in the polaritonics platform, the induced changes in impermittivity from off-diagonal components are much smaller than those from the on-diagonal terms and can be discarded [44]. Therefore, the indicatrix is cast in the principle axis coordinate system with no off-diagonal terms:

$$\left[\frac{1}{n_o^2} + r_{22}E_2 + r_{13}E_3\right] Y^2 + \left[\frac{1}{n_e^2} + r_{33}E_3\right] Z^2 = 1. \tag{3.29}$$

Note that since there are no mixed terms, no coordinate transformations are required and the modified index ellipsoid lies along the original principle axes of the crystal (unlike in zinc blende crystals). From this expression, we see that the modified refractive indices along the ordinary and extraordinary axes are:

$$n_o' = n_o - \frac{1}{2}n_o^3 (r_{22}E_2 + r_{13}E_3) \tag{3.30a}$$

$$n_e' = n_e - \frac{1}{2}n_e^3 (r_{33}E_3)\,. \tag{3.30b}$$

Therefore, an optical probe propagating along X accumulates different amounts of phase along the ordinary and extraordinary axes, resulting in a phase shift between the emerging orthogonal polarization components of the probe.

3.2.4 Electro-optic Phase Retardation

The optical phase difference introduced by the THz E-field is the quantity that we wish to determine since it is a quantitative measurement of the THz field strength given the EO coefficients. Here, we consider an optical probe propagating along the principle axis x' of

the modified ellipsoid; at $x' = 0$ the optical field is split into two orthogonal states polarized along the other two principle axes, y' and z', with the corresponding indices of refraction, $n_{y'}$ and $n_{z'}$. These two polarizations lie in the $y'z'$ plane, perpendicular to the incident probe, and propagate along x'. The time-dependent E-fields of these components are:

$$E_{y'} = A \exp\left[i\left(k_{y'}x' - \omega t\right)\right] \tag{3.31a}$$

$$E_{z'} = A \exp\left[i\left(k_{z'}x - \omega t'\right)\right] \tag{3.31b}$$

where $k = 2\pi n/\lambda_{\text{opt}}$ is the wave vector component along the appropriate axis for the optical wavelength, λ_{opt}, and refractive index, n. Therefore, the phase accumulated by the optical probe in either polarization direction is given by:

$$\phi_{y'}(x') = 2\pi \frac{n_{y'}}{\lambda_{\text{opt}}} x' \tag{3.32a}$$

$$\phi_{z'}(x') = 2\pi \frac{n_{z'}}{\lambda_{\text{opt}}} x' \tag{3.32b}$$

For a crystal of thickness, ℓ, the phase difference between the two orthogonal components is called the EO phase retardation, $\Delta\phi$, which is related directly to the THz E-field. It is simply calculated as the difference of the phases given in (3.32):

$$\begin{aligned} \Delta\phi &= \phi_{y'}(\ell) - \phi_{z'}(\ell) \\ &= 2\pi \frac{\ell}{\lambda_{\text{opt}}} \left(n_{y'} - n_{z'}\right) \end{aligned} \tag{3.33}$$

Because the THz E-field causes an *induced* phase shift in the optical probe, the static index terms may be ignored and only the change in the index, Δn, is considered. Assuming the index is of the form $n' = n + \Delta n$, then we can separate the phase shift into the static and induced phase shift terms since $\Delta\phi = \Delta\phi_{\text{st}} + \Delta\phi_{\text{ind}}$. Explicitly, the phase shifts can be

written as:

$$\Delta\phi_{\text{st}} = 2\pi\frac{\ell}{\lambda_{\text{opt}}}(n_y - n_z) \tag{3.34a}$$

$$\Delta\phi_{\text{ind}} = 2\pi\frac{\ell}{\lambda_{\text{opt}}}(\Delta n_y - \Delta n_z)\,. \tag{3.34b}$$

For ZnTe considered in Section 3.2.2, the relative phase shift only arises from the induced change in the indices (i.e. the material has no static birefringence, $\Delta\phi_{st} = 0$); substitution of the modified indices in (3.24) gives:

$$\Delta\phi = \Delta\phi_{\text{ind}} = 2\pi\frac{\ell}{\lambda_{\text{opt}}}\frac{r_{41}n^3}{2}E_{\text{THz}}\left[2\cos(\alpha + 2\Phi) - \cos\alpha\cos(2\Phi)\right]. \tag{3.35}$$

This expression shows that the phase shift depends on the polarization direction and strength of the THz field. According to experimental results presented by Planken *et al.*, the largest detected signal occurs when the polarization directions of the THz and optical probe are parallel ($\theta = \alpha$) or perpendicular ($\theta = \alpha + 90°$) to each other. This is different from the commonly chosen relative angle of 45° used for optical Kerr detection or more relevantly for the Pockels effect in LN to be shown later. The THz polarization that gave the largest detected E-field amplitude occurred at $\alpha = 90°$ for either the parallel or perpendicular probing scheme, which subsequently sets Φ in (3.20), and the relative phase shift in (3.35).

For LN in Section 3.2.3, the induced relative phase shift is:

$$\Delta\phi_{\text{ind}} = 2\pi\frac{\ell}{\lambda_{\text{opt}}}(\Delta n_{\text{o}} - \Delta n_{\text{e}}) \tag{3.36a}$$

$$= -2\pi\frac{\ell}{\lambda_{\text{opt}}}\frac{n_{\text{o}}^3(r_{22}E_2 + r_{13}E_3) - n_{\text{e}}^3 r_{33}E_3}{2}. \tag{3.36b}$$

In LN, a probe polarized at 45° experiences a horizontal and vertical phase shift according to this expression.

The phase shift is an interesting quantity because for certain values, the crystal under an

applied field can act either as a quarter-wave plate ($\Delta\phi = \pi/2$) to yield circularly polarized light, or as a half-wave plate ($\Delta\phi = \pi$) to yield an orthogonally polarized beam, relative to the linearly polarized direction of the input optical probe. In the next section, we will calculate the detected intensity modulation, also directly proportional to the THz E-field, through a phase-to-amplitude conversion process.

3.2.5 Electro-optic Sampling

3.2.5.1 The Detected Electro-optic Signal

Because photodiodes are square law or intensity detectors that are unable to detect phase, we need to convert the phase into an amplitude change. This concept of phase-to-amplitude conversion forms the basis of EO sampling and also detection in both imaging techniques to be described later. Experimentally, a quarter-wave plate and a Wollaston polarizer are placed after the detector crystal, and the intensity of two emerging orthogonal polarizations are measured on a photodiodes. The EO-detection scheme is presented in Fig. 3-4, where the orientation of the incoming optical probe and principle axes of the EO crystal are specified for LN.

If we first consider the case *without* an EO crystal in place, an input optical probe is firstly linearly polarized at 45° and then passed through a quarter-wave plate at 0°. The quarter-wave plate introduces a relative $\pi/4$ phase shift between the horizontal and vertical polarization components of the probe and consequently the beam emerges circularly polarized. Lastly, the phase-to-amplitude conversion process is carried out by using a polarizer, in this case a Wollaston prism oriented at 45°, such that the circularly polarized beam is split *equally* into +45° and −45° polarization components. Two photodiode detecters record the intensities of the probe for both components, which are equal to each other ($I_1 = I_2$).

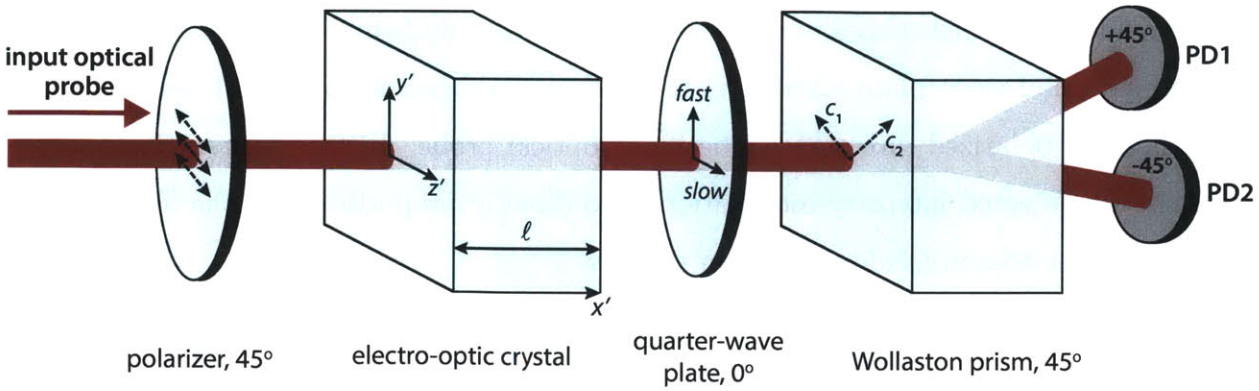

Figure 3-4: **Ideal EO sampling geometry in LN.** An input optical probe is linearly polarized at 45° and propagates along the x'-direction in the EO crystal. In this case, an applied THz E-field induces changes in the refractive index along the principle axes y' and z'. An optical probe experiences a relative phase shift, $\Delta\phi$ due to the EO crystal and an additional $\pi/4$ phase shift from the quarter-wave plate. A Wollaston prism splits the optical probe into two orthogonal polarization states at $\pm 45°$, which are detected by two photodiodes.

In the case where an EO crystal is placed after the initial polarizer, the optical probe may experience a static phase shift for inherently birefringement materials or an induced phase shift from an applied E-field, as described in Section 3.2.4. This means that when it passes through the quarter-wave plate, the emerging beam becomes elliptically polarized and hence it is split unevenly into $\pm 45°$ polarizations by the Wollaston prism, leading to unequal intensities on the photodiodes ($I_1 \neq I_2$). The differential intensity is calculated as $\Delta I_i = I_i - I_0$, where I_i is the intensity in the presence of an applied field for photodiodes $i = 1, 2$ and I_0 is the intensity of the probe in the absence of an applied field. A THz E-field can modulate the detected intensity, which we exploit to extract a THz time trace: $E_{\mathrm{THz}} \propto \Delta\phi \propto \Delta I / I_0$.

The intensities of the orthogonal components can be analytically cast using the Jones calculus formalism [45] developed for polarizing elements and light. The following matrix

operations are used to yield the resulting E-field of the optical probe emerging at $+45°$:

$$\begin{aligned}\begin{bmatrix} E_{+45} \\ E_{-45} \end{bmatrix} &= \underbrace{\frac{1}{2}\begin{bmatrix} 1 & 1 \\ 1 & 1 \end{bmatrix}}_{\text{Polarizer at } +45°} \underbrace{e^{i\pi/4}\begin{bmatrix} 1 & 0 \\ 0 & i \end{bmatrix}}_{\text{quarter-wave plate}} \underbrace{\begin{bmatrix} 1 & 0 \\ 0 & e^{i\Delta\phi} \end{bmatrix}}_{\text{EO crystal}} \underbrace{E_0\begin{bmatrix} 1 \\ 1 \end{bmatrix}}_{45° \text{ polarized light}} \\ &= \frac{1}{2}E_0\begin{bmatrix} 1+ie^{i\Delta\phi} \\ 1+ie^{i\Delta\phi} \end{bmatrix}\end{aligned} \tag{3.37}$$

where E_0 is the amplitude of the probe E-field in the absence of an applied field. The intensity, $I = EE^*$, is calculated to be:

$$I_{+45°} = I_0\left(1 - \sin\Delta\phi\right). \tag{3.38}$$

Similarly, a calculation performed for $-45°$ yields:

$$I_{-45°} = I_0\left(1 + \sin\Delta\phi\right). \tag{3.39}$$

The signal modulation is then simply:

$$\Delta I_{\mp}/I_0 = \pm\sin\Delta\phi, \tag{3.40}$$

where $\Delta I_{\mp} = I_{\mp} - I_0$. The implementation of balancing is implemented by subtracting the signal modulations of the orthogonal polarizations:

$$\begin{aligned}\frac{\Delta I}{I_0} \equiv \frac{\Delta I_-}{I_0} - \frac{\Delta I_+}{I_0} &= 2\sin(\Delta\phi) \\ &\approx 2\Delta\phi\end{aligned} \tag{3.41}$$

where for small $\Delta\phi$, the detected signal is doubled while noise that is non-polarization sensitive is suppressed (since noise fluctuations change $\Delta\phi$ with the same sign for both

polarizations). It is preferable to have small phase shifts (i.e. small THz field strengths and crystal lengths) such that we can make this approximation and detect in the linear regime for quantitative measurements.

In LN, for a z-polarized THz TE E-field ($E_2 = 0$), the induced signal modulation detected using EO detection is:

$$\frac{\Delta I_{\mp}}{I_0} \approx \pm 2\pi \frac{\ell}{\lambda_{\text{opt}}} \frac{n_e^3 r_{33} - n_o^3 r_{13}}{2} E_{\text{THz}}. \tag{3.42}$$

For ZnTe, although the input polarization state and principle axes are oriented differently, the signal modulation detected is the same. Planken and coworkers calculated the signal modulation as a function of the polarization direction of the optical probe and applied THz field [43]:

$$\frac{\Delta I_{\mp}}{I_0}(\alpha, \theta) \approx \pm \sin\left[2(\theta - \Psi)\right] \Delta\phi(\alpha). \tag{3.43}$$

3.2.5.2 Other Considerations

The quarter-wave plate is used to introduce a static $\pi/4$ phase-shift, which effectively yields 50% intensity transmission in the absence of an applied field. This falls in the linear regime of the sinusoidal response, where positive and negative amplitudes of the THz E-field can be monitored. Without a quarter-wave plate, the result is a homodyne detected signal that is proportional to $\Delta\phi^2$, and so the sign of the signal is lost. This crossed polarizer EO sampling geometry has been used for detecting very weak signals since this is essentially a background-free measurement and amplifies the signal modulation in the nonlinear detection regime. In order to recover the sign of the field, the static birefringence in the EO crystal is used as a small bias to have near zero transmission [46].

It is of interest to note that the same outcome results from switching the angle of the quarter-wave plate to 45° and the Wollaston prism to 0° to yield vertical and horizontal polarizations at the photodiodes. This is useful in imaging methods where we need the + and - polarizations to be vertically aligned, such that both polarization states can fit on the

same detector (e.g., CCD chip). In this case, a rotated quarter-wave plate is substituted into (3.37) with the use of rotation matrices, and vertical or horizontal linear polarizers as the last element in the series. A quarter-wave plate with its fast axis at 45° has the form:

$$\mathrm{QWP}_{45^\circ} = e^{i\pi/4}\begin{bmatrix} 1-i & 1+i \\ 1+i & 1-i \end{bmatrix} = \begin{bmatrix} 1 & i \\ i & 1 \end{bmatrix}$$

Also, the static birefringence that gives rise to the static phase shift, $\Delta\phi_{st}$ is removed by tilting of the quarter-wave plate around its fast axis until both photodiodes have equal intensity (in the absence of a THz field). Therefore, this compensates by introducing more or less phase along the slow axis to match the phase shift along the fast axis. Therefore, the quarter-wave plate simply introduces an additional phase shift, γ in the component:

$$\mathrm{QWP}_{0^\circ,\mathrm{tilt}} = e^{i\pi/4}\begin{bmatrix} 1 & 0 \\ 0 & ie^{i\gamma} \end{bmatrix}$$

where $\gamma = -\Delta\phi_{st}$. A common mistake is to compensate the static shift by rotating the angle of the wave plate while keeping the polarizer unchanged, but this mixes the two orthogonal polarization states together and the detected signal is not of the form derived above.

3.2.6 Pump-probe Geometry for time domain THz Detection

Due to the lack of a THz spectrometer that spectrally resolves a THz pulse, EO sampling relies on a pump-probe geometry that records a THz time trace. This detection scheme captures both the amplitude and phase of the THz pulse in the time domain, which may be Fourier-transformed to yield the corresponding frequency domain spectrum. Figure 3-5(a) shows a general schematic of the pump-probe geometry used for EO detection, specifically in the polaritonics platform, but encompasses the same detection method used in free-space THz experiments.

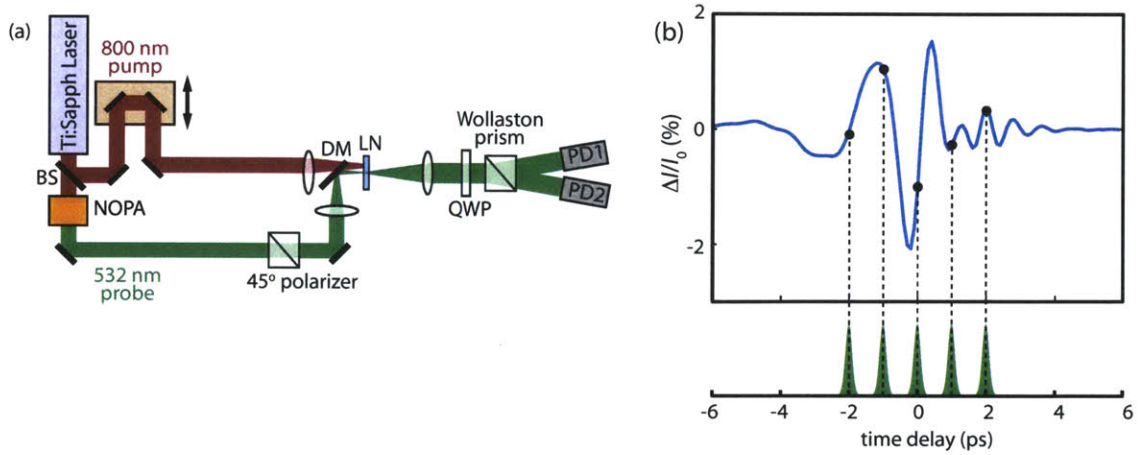

Figure 3-5: **EO sampling pump probe geometry.** (a) A general schematic of EO sampling in the polaritonics platform. The 800 nm laser is initially split into the pump and probe arms. The pump is time delayed relative to the probe by scanning a mechanical delay stage. (b) The optical probe acts as a gate pulse that samples the THz waveform at different pump-probe time delays; the THz field is averaged over the probe pulse duration, setting the time resolution of the measurement.

Initially, an 800 nm ultrafast pulse (1.5 mJ/pulse, $\sim$ 80 fs, 1 kHz) is split into the "pump" and "probe" arms by a beamsplitter; typically 90% or higher is allocated to the pump arm since minimal fluence is needed for the optical probe. The pump is directed into a mechanical delay stage, where its movement lengthens or shortens the pump arm's total path length from the beam splitter to the LN sample. In the polaritonics platform, the probe arm is directed into a non-collinear optical parametric amplifier (NOPA) to generate light with 532 nm center wavelength and polarized at 45°. In free-space THz setups, the probe is an 800 nm beam since THz generation and THz detection occur in spatially distinct parts of the setup, and so spectral filtering of the 800 nm pump is not required since it can be blocked or filtered out upstream. The pump and probe arms are recombined by a dichroic mirror and focused onto the same spot in the LN sample. In free-space setups, the pump and probe are recombined by either a pellicle beam splitter (transparent to THz wavelengths, but partially reflective to optical wavelengths) or directing the optical probe through a drilled hole in the last THz focusing parabolic mirror.

As described in the last section, the THz waves modulate the polarization of an optical

pulse via the Pockels effect and the THz-induced phase shift is converted to an amplitude change by using a quarter-wave plate and a Wollaston polarizer. The two emerging orthogonal polarization states are then detected on a pair of photodiodes for balanced detection. In our experiments, we measure a time-dependent signal modulation, $\frac{\Delta I}{I_0}(t)$, since its quantity is directly proportional to the amplitude of the THz waveform according to (3.42), only scaled by a set of constants.

The femtosecond optical probe acts as an optical gate pulse since it is temporally much shorter than the period of a THz pulse. The optical gate essentially averages the THz pulse over its pulse duration. Strictly speaking, the detected signal modulation is the convolution of the THz E-field with an optical gate pulse: $\Delta I/I_0 \propto E_{\mathrm{THz}} \bigotimes E_{\mathrm{opt}}$, but in the limit of a very short gate pulse (i.e. 100 fs or shorter), the measured signal is simply proportional to the THz field, which in our case is essentially constant over that duration.

Figure 3-5(b) illustrates the pump-probe technique where the x-axis represents the time delay between the pump and probe arms introduced by the mechanical delay stage. At one fixed time delay, the THz E-field, $E_{\mathrm{THz}}(t)$, and the probe pulses are time-coincident at some point in the THz field profile at the detection crystal, and a signal modulation proportional to the E-field amplitude at one instance of time is measured. By stepping the time delay between the pump and probe, a full time trace of the propagating THz field is recovered. The probe pulse duration is inversely proportional to the detectable bandwidth ($\sim$ 10 THz for 100 fs pulse), but typically the detectable bandwidth is limited by optical rectification in the EO crystal.

3.2.7 Signal Detection with Data Acquisition System

As an alternative to using a lock-in amplifier, we use a data acquisition (DAQ) system that measures the energy of every pulse at a rate limited by the maximum sampling rate of the card [47]. In this section, I will describe the general guide to setting up a DAQ system

and discuss its benefits compared to the lock-in and its flexibility in adapting arbitrary measurement schemes.

3.2.7.1 THz Detection Instrumentation

In the pump-probe geometry described, every laser pulse detected by the photodiodes is measured using the DAQ system, with its sample clock synchronized to the repetition rate of our 1 kHz laser. In this method, the measurable quantity that is directly related to the pulse energy of the optical probe is the peak voltage of each electrical pulse (the integrated voltage would have also worked). The general layout of the instrumentation for the DAQ system is shown in Fig. 3-6(a).

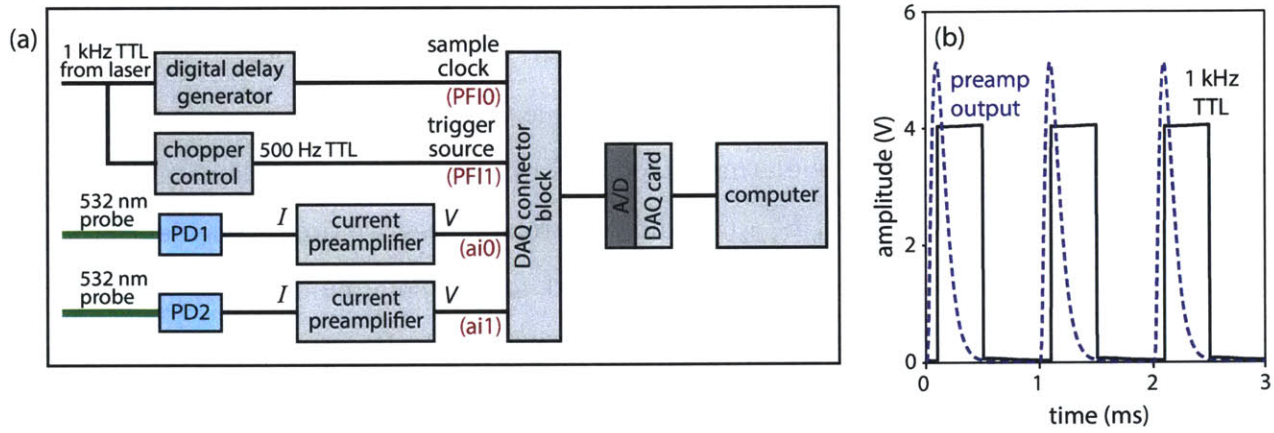

Figure 3-6: **DAQ system layout.** (a) The basic DAQ system consists of detectors, a computer, and a DAQ card that interfaces the detector with the computer. In our system, the current outputs of the photodiodes are both sent to current preamplifiers. The filtered and amplified voltage outputs are analog signals that are sent to a DAQ connector block (channels ai0 and ai1). A precisely delayed 1 kHz sample clock from a digital delay generator and a 500 Hz trigger source from a chopper control are digital signals that are also connected to the DAQ block (PFI0 and PFI1). The analog and digital signals are sent to a DAQ card, which has an analog-to-digital (A/D) converter at its front end. The digitized signals are then manipulated using a computer. (b) The evolution of the pulses on an oscilloscope shows how the rising edge of the 1 kHz TTL sample clock is positioned to lie at the peak voltage of the preamplifier voltage output. The DAQ card records the voltage whenever it detects this rising edge.

Firstly, the current output from the photodiodes is directed into a low-noise current preamplifier (Stanford Research Systems, SR570) that serves two purposes: it filters/amplifies

the signal and converts the current signal into a voltage; this is an analog signal. Also, a 1 kHz transistor-transistor logic (TTL) signal directly from the laser is fed into both a digital delay generator and a chopper control unit (connected to a chopper in the THz pump arm). The digital delay generator (Stanford Research Systems, DG535) is used to precisely delay the input TTL such that its rising edge is aligned with the peak voltage of the preamplifier output (see Fig. 3-6(b)). We filter out the high frequency components by using the 3 kHz low pass filter setting on the preamplifier; this causes the voltage to evolve more slowly so that we can accurately measure the peak with minimal error from jitter of the sampling clock, but it also allows the signal to decay to zero within 1 ms.

The chopper control that sets the chopping frequency and phase of the THz pump is also synchronized to the 1 kHz output and then down-counted to 500 Hz, the maximum pump modulation frequency. This ensures that every other pump pulse is blocked, which means the probe pulse alternates between measuring I (THz pump present) and I_0 (THz pump absent). The output TTL from the chopper control unit is used to trigger the acquisition so that we know the order in which the pulses, I and I_0, are collected in. This allows us to correctly calculate the signal modulation:

$$\frac{\Delta I}{I_0} = \frac{I - I_0}{I_0}.$$

The two analog voltage signals from the photodiodes are sent into the analog inputs, and the sample clock and trigger sources are sent into the digital inputs, of a DAQ connector block. The DAQ connector block simplifies the connections while shielding the signals from interfering with other electrical sources that can produce crosstalk. Subsequently, a DAQ card (National Instruments, PCI-6281, 18 bit analog input resolution, 625 kS/s sampling rate) performs analog-to-digital conversion on the analog input signals so that the digital signals may be manipulated by a computer. Whenever the DAQ card detects the rising edge of the external sampling clock, it records the voltage of the digitized signal.

The settings on the preamplifiers that we have found that give the best signal-to-noise are the following:

- Filter type: 12 dB low-pass filter
- Filter frequency: 3 kHz (below 1 kHz the signals decay too slowly)
- Sensitivity: 20-50 nA/V
- Gain mode: low noise

The amount of gain needed depends on the energy of the pulses impinging on the photodiodes, which cannot be set too high otherwise electronic noise becomes noticeable. Typically, we need to use neutral density (ND) filters in the probe arm since the intensity saturates the photodiodes. The intensity of the probe is chosen to be in the linear response regime of the photodiodes, which is easily assessed on an oscilloscope by adding a 0.3 ND filter in the probe; this should halve the intensity of photodiode output in the linear response regime. Also, when the sensitivity is set on the preamplifier to 50 nA/V for example, the next lowest setting at 20 nA/V should saturate the preamplifier in order to reduce the amount of gain required.

3.2.7.2 Advantages of DAQ System

The immediate advantage of the DAQ system is that in addition to having a comparable sensitivity to the lock-in, it allows us to fully quantify our laser noise performance as a result of *in silico* data processing (e.g., chopping, balancing, and averaging). It also has the ability to directly measure the physically relevant quantity $\Delta I/I_0$ for balanced detection, given in (3.41), while the lock-in can only detect the difference between the two input signals from the photodiodes, $I_1 - I_2$. Because we measure every pulse (both THz present, I, and THz absent, I_0), the balanced signal does not drift in the presence of large laser fluctuations since these are corrected for by the division of I_0. The lock-in requires a separate measurement

of I_0 either before or after the experiment and thus cannot account for dynamical laser fluctuations.

Additional capabilities unique to the DAQ system are its capability to conduct "fast scanning", which is most useful in situations where real-time feedback is needed for optimization of alignment or pump-probe overlap. A lock-in amplifier is not capable of attaining scan rates of sufficient speed since it uses an exponential averaging algorithm that heavily weighs the signal at earlier time delays. Therefore, before acquiring data at each new time delay, the lock-in must wait several time constants to remove the parasitic contributions from earlier time delays. Alternatively, the DAQ system weighs the values of all pulses equally. In principle, a THz time trace can be measured with a minimum of two laser pulses per time point at the maximum pump modulation frequency of 500 Hz. This means that instead of immobilizing the stage at a fixed position and averaging many shots, we can continuously scan the stage and collect laser pulses at a constant set velocity to the target end position (the longest time delay). The velocity of the stage, given the laser repetition rate, sets the number of pulses averaged at each time delay; to average more pulses, a slower stage velocity is used.

3.2.7.3 Differential Chopping

The DAQ system is also useful in two-pump experiments, where the implementation of differential chopping makes it possible to deconvolute the contribution from each pump separately and also the coupling between the two pumps, while maintaining detection at a high frequency for noise suppression. The ability to simultaneously extract signals derived from only one pump is also useful for correcting for pump scatter that affects the noise floor. In differential detection, each pump is chopped at an even integer fraction of the laser repetition rate. For differential detection with the lock-in amplifier, a laser repetition rate of R gives maximum pump modulation of $R/4$ and the other at $R/6$, leading to a detection

frequency at $R/12$; this is highest modulation frequency since the lock-in detects at $R/2$. Alternatively, the DAQ system detects at R, and the maximum pump modulations are $R/2$ and $R/4$, giving a detection frequency at $R/4$.

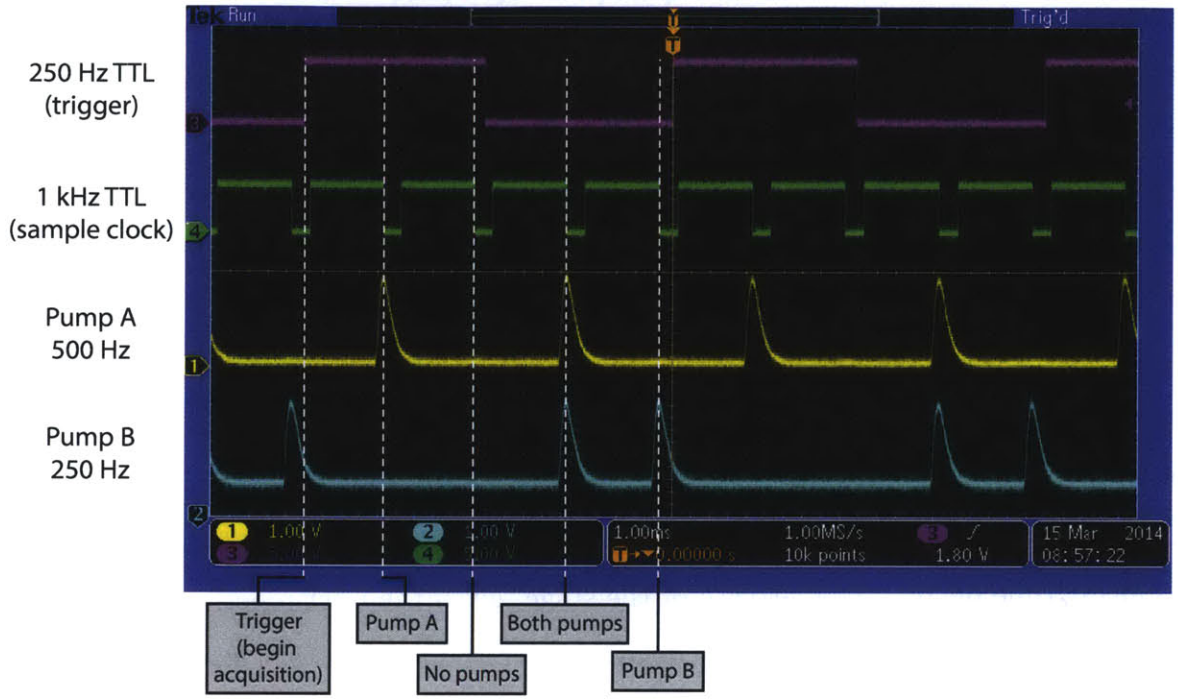

Figure 3-7: **The implementation of differential chopping in the DAQ system.** For a 1 kHz laser repetition rate, the maximum detection frequency for differential chopping is 250 Hz. Here, two pumps are chopped at 250 Hz and 500 Hz. A 250 Hz TTL pulse triggers the acquisition and the 1 kHz TTL sets the external sampling clock. In this scope trace, the falling edge is shown to coincide with the measured peak voltage. The pulse sequence is known to be: Pump A, No pumps, Both pumps, and Pump B, which allows us to extract traces due to just one of the pumps or both pumps.

We have tested this by modulating a THz pump (A) at 500 Hz and an optical pump (B) at 250 Hz, see Fig. 3-7. The sequence order of the measured traces is determined by looking at the outputs on an oscilloscope as seen in Fig. 3-7. A 250 Hz TTL from the pump B chopper control triggers the acquisition and the 1 kHz TTL from the laser serves as the sample clock. After receiving the trigger, the measurements are acquired at the falling edge of the 1 kHz TTL in the following order: (1) pump A (S_{+-}) (2) no pumps (S_{--}) (3) both pumps (S_{++}) (4) pump B (S_{-+}), where "+" is the pump present and "-" is the pump

absent. The signal resulting from the coupling between the pumps is given by the following operations: $(S_{++} - S_{+-} - S_{-+} + S_{--})/S_{--}$.

3.3 Phase-sensitive THz Imaging Techniques

This section is a modified version of the publication:
Christopher A. Werley*, **Stephanie M. Teo***, Benjamin K. Ofori-Okai*, Prasahnt Sivarajah, and Keith A. Nelson, "High-resolution, Low-noise Imaging in THz Polaritonics," *IEEE THz Science & Technology*, vol. 3, no. 3, pp. 239-247, 2013. (*equal contribution)

As an alternative to using a focused optical probe beam, an expanded optical probe beam can be used to retrieve additional two-dimensional spatial information about the propagating THz pulse. The waveguided polaritonics platform forms the basis of two THz imaging techniques that use different techniques for phase-to-amplitude conversion. Time-resolved imaging of propagating electromagnetic waves at THz frequencies provides deep insights into the waves and their interactions with a variety of photonic elements. As new components for THz control are developed, such as metamaterial microstructures that display deep sub-wavelength E-field localization, finer spatial resolution and more sensitive imaging techniques are required to study them. Here we introduce key advances in the optical design and lock-in image acquisition at 500 Hz for the complementary imaging techniques of phase contrast and polarization gating.

3.3.1 Introduction to THz Imaging in the Polaritonics Platform

Ultrafast optical pulses can efficiently generate THz frequency electromagnetic radiation in the ferroelectric crystal LN via impulsive stimulated Raman scattering [33]. The THz field can either be transmitted out of the crystal as a source for intense, free-space THz radiation [16, 29] or used directly in the LN crystal for on-chip applications. This on-chip system is compact, avoids free-space coupling losses, and offers possibilities for smooth interfacing

between THz and other optoelectronic components commonly built in LN such as optical modulators for telecommunication. On-chip control of THz in a slab of ferroelectric crystal, termed THz polaritonics [3], has witnessed significant developments in the last 15 years. These include versatile control and enhancement of generated THz waveforms due to spatial and temporal control of the driving optical fields [48–50] and the development of integrated photonic elements such as waveguides [51–53], diffractive elements [53, 54], interferometers [51], filters [55], photonic crystals [52, 56], resonators [41, 57], and antennas [7].

Of central importance to studying both THz generation and photonic elements has been the ability to image the spatial and temporal evolution of the E-field of the THz wave using time-resolved, phase sensitive imaging [5, 58–60]. The presence of sub-wavelength E-field structure in the near-field of metallic components has motivated the development of imaging techniques with improved resolution, and the desire to study weak E-fields in a variety of situations has continually driven methodological refinements that improve the signal-to-noise ratio (S/N). Here we carefully explain the new optical design and acquisition methodology that yields higher spatial resolution and S/N than previously described THz imaging methods [5]. Using improved optics to increase the numerical aperture (NA) while minimizing aberration results in a 4-fold finer resolution of 1.5 μm ($\lambda/100$ at 0.5 THz). In addition, the new acquisition methodology uses a high-speed complementary metal-oxide-semiconductor (CMOS) camera for lock-in imaging at 500 Hz, which yields a minimum signal detection threshold of $\Delta I/I_0 > 0.2\%$. This high detection frequency is much faster than the 0.25 Hz rate used previously with a charge-coupled device (CCD) camera. Depending on details of laser noise and illumination geometry, the high-frequency detection can reduce noise by up to 5-fold. The ability to quantitatively record E-fields of electromagnetic waves with sub-cycle temporal and $\lambda/100$ spatial resolution lets us study the interactions between light and photonic components in unparalleled detail. Since Maxwell's equations are scale-invariant, insights gained at THz frequencies can be equally well applied to infrared and optical components where such high-resolution imaging is considerably more challenging.

Thus our methodology can be used to develop insight about plasmonic structures such as antennas and metamaterials and purely dielectric structures such as photonic crystals at wavelengths spanning the electromagnetic spectrum.

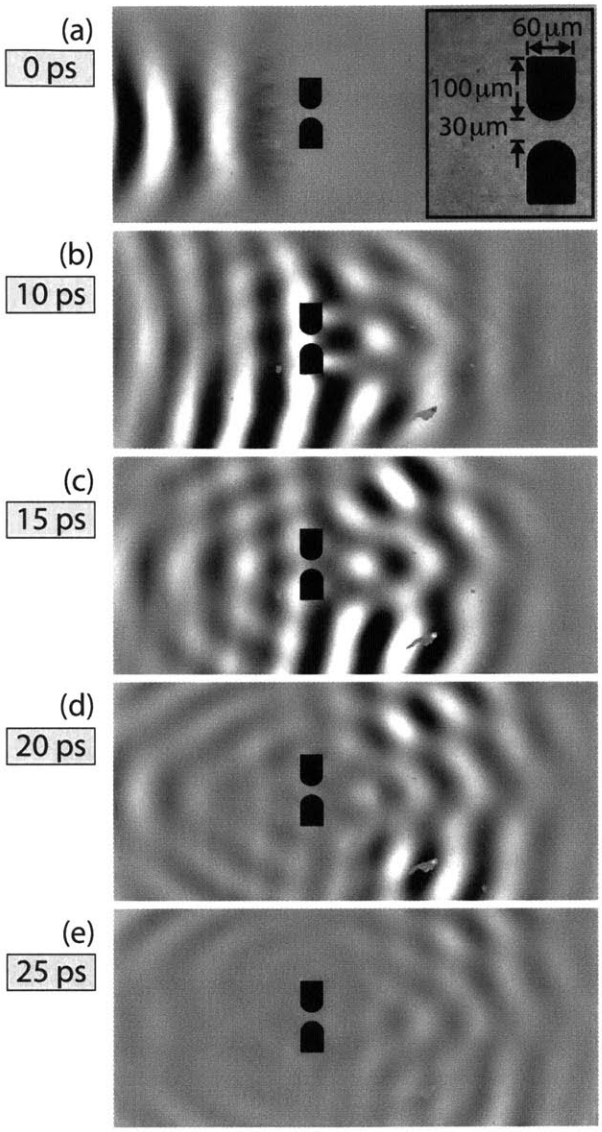

Figure 3-8: **Movie frames of propagating THz waves.** The data were recorded using phase contrast imaging with magnification of 17× and show a 530 GHz wave interacting with a resonant antenna pair (masked in black for clarity). (a) The rightward propagating THz wave just before interaction with the antenna. The inset shows the antenna dimensions. (b)-(e) The time-progression of the THz field showing the interference between the incident wave and the complicated far-field radiation pattern of the antenna. (e) The field has mostly propagated away from the antenna by 25 ps.

When an optical pulse generates THz radiation in a slab of LN, the large mismatch in velocities causes the THz wave to be emitted as Cherenkov radiation [31] and propagate mainly in the lateral direction, orthogonal to the pump pulse. If the LN crystal is thin, the THz field is waveguided within the slab. As the THz field propagates, it changes the refractive index of the LN via the electro-optic effect. In the majority of experiments the THz field is polarized along the optic axis, so:

$$\Delta n = -\frac{1}{2} n_e^3 r_{33} E_{\mathrm{THz}} \tag{3.44}$$

with n_e the extraordinary index of refraction and r_{33} the appropriate electro-optic tensor component. Equation (3.44) assumes vertically polarized probe light as is used in phase contrast imaging; for horizontally polarized light n_e is replaced with n_o and r_{33} is replaced with r_{13}. An expanded optical probe pulse will experience a spatially dependent phase shift directly proportional to the spatially dependent THz-induced change in index:

$$\Delta\phi(x,y) = 2\pi \frac{\ell}{\lambda_{\mathrm{opt}}} \Delta n(x,y), \tag{3.45}$$

with ℓ the slab thickness and λ_{opt} the optical wavelength in free space. If the sample were imaged directly onto a camera without modification, the THz signal would not be visible because it is a phase image. A phase sensitive imaging technique converts the phase information into amplitude information that can be detected by the camera. Dividing the signal image (when the THz is present) by a reference image (when the THz is absent) enables imaging of the spatial profile of the THz wave and quantitative measurement of E-field amplitudes. Finally, the full temporal evolution of the wave is recorded by stepping the time delay between pump and probe pulses.

An example of the data that can be collected with this technique is illustrated by the series of images in Fig. 3-8, in which an initially rightward propagating THz wave interacts

with a 200 nm thick gold antenna pair deposited onto the surface of LN (see Multimedia 1 in [4]). The driving field, visible in Fig. 3-8(a), is an intense, multi-cycle THz wave [50] whose frequency is tuned to a higher order resonance of the antennas at 530 GHz. The evanescent field of the THz, which extends into the air on either side of the slab, interacts directly with the antenna and induces electrons in the metal to oscillate in a complex mode pattern with a vertical node bisecting the antennas and multiple horizontal nodes. This mode radiates a complex pattern into the far-field, most clearly visible in Fig. 3-8(d). The far-field pattern can be seen as six diverging waves propagating roughly along 2, 3, 4, 8, 9, and 10 o'clock. In addition there is field enhancement, which is difficult to see at this magnification, at the corners and edges of the antenna.

A previous study of phase-sensitive imaging techniques for polaritonics compared Talbot imaging, Sagnac interferometry, phase contrast, and polarization gating and found that Talbot imaging and Sagnac interferometry could not quantitatively measure THz fields [5]. Further analysis showed that phase contrast imaging had the highest imaging resolution, while polarization gating imaging provided the most reliable quantification of THz field strengths and had the best S/N. We present new optical designs of both methods, which result in finer resolution, and discuss a novel detection procedure using a high-speed camera that reduces noise.

3.3.2 Experimental and Results

The pump and probe pulses and THz generation geometry are the same in both methods. The THz radiation is generated by an intense optical pump pulse from a regenerative Ti:Sapphire amplifier (800 nm center wavelength, 100 fs duration, 1 mJ pulse energy, 1 kHz repetition rate). The probe pulse (100 fs duration, 1 μJ pulse energy) is the output of a home-built noncollinear optical parametric amplifier (NOPA) tuned to 532 nm. A NOPA is used because it is desirable for the probe pulse to be spectrally separated from both the 800

nm pump and the 400 nm light created by efficient second harmonic generation (SHG) of the pump light in the LN sample. A spectral filter can then be used to reject all pump light, and there is no need to insert a spatial filter, such as a razor blade, which can easily block some of the diffracted probe light important for high-resolution imaging. 532 nm light in particular is chosen for the probe because of the abundance of high-quality optics at this wavelength. The pump is delayed relative to the fixed probe by a scanning delay line. The two beams are recombined just before the sample with a dichroic mirror. The x-cut LN slab, here 30 μm thick, has its optic axis oriented vertically, parallel to the polarization of the pump pulse, to take advantage of the largest nonlinear tensor component for THz generation. The slab is thinner than the THz wavelength, so the THz is waveguided; different waveguide modes and waveguide dispersion are clearly visible [39]. The metal microstructures are 200 nm thick gold on a thin chromium adhesion layer deposited by optical lithography directly on the surface of the LN slab.

3.3.2.1 Phase Contrast Imaging

Phase contrast imaging is a method that generates contrast in transparent samples with variations in thickness or refractive index [61], and is often used in biology to image cells. In polaritonics, we use an adaptation of phase contrast imaging that enables quantitative measurement of small THz-induced phase shifts [5,60]. The vertically polarized probe beam is spatially filtered by a pinhole and expanded so its intensity profile is smooth and slowly varying across the region of interest on the sample (see Fig. 3-9). In this case, the phase-to-amplitude conversion required to visualize the THz wave is achieved with a phase mask placed in the Fourier plane, also called the back focal plane or conjugate plane, of the imaging system. The 0^{th} order beam is focused to a small spot in the center of this plane, while the light diffracted off the THz wave and other structures is spatially separated from this point and spread throughout the plane. Our phase mask, made by e-beam lithography,

is a low-distortion, flat fused silica plate with a 25 × 25 μm recessed square etched into its center. The depth of the recess is set so that the 0^{th} order beam, which passes though the square, experiences a $\lambda/4$ phase shift relative to the diffracted light. When the diffracted light and 0^{th} order beam recombine in the image plane, they interfere and cause amplitude modulation. For small THz-induced phase shifts, the signal at the camera is [62]:

$$I(x,y) \approx I_0(x,y)\left[1 - 2\Delta\phi(x,y)\right]. \tag{3.46}$$

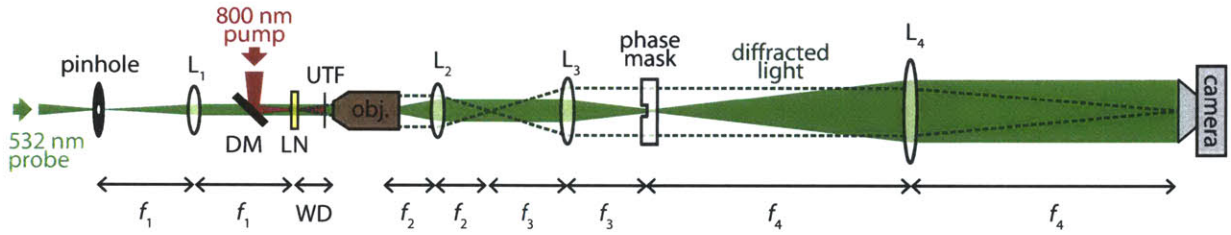

Figure 3-9: **Phase contrast imaging experimental diagram.** L Lens; DM Dichroic Mirror; LN LN sample; UTF Ultra-thin Filter; WD Working Distance. The phase mask introduces a $\lambda/4$ shift between the 0^{th} order beam and diffracted light, enabling interference and phase-to-amplitude conversion at the camera. The pinhole is relay imaged onto the phase mask so the entire 0^{th} order beam fits through the depression, and the sample is relay imaged onto the camera for high-resolution imaging.

As is typical for imaging systems, the resolution is improved by increasing the NA. Design of the polaritonics system, however, is constrained by the fact that the 1 mJ, 100 fs pump pulse will destroy an objective lens if it passes through (experimentally confirmed). To maximize the distance of the objective from the sample, we used a long working distance (WD), large aperture, M Plan Apo objective (Mitutoyo 378-803-2, NA = 0.28, WD = 33.5 mm). A high-damage-threshold filter must be placed between the sample and objective, as close to the objective as possible to allow the pump beam to diverge and lower its intensity over a longer distance. Most objectives are designed to image through a piece of glass (either a microscope slide or cover slip), and so to achieve aberration-free diffraction-limited performance, the filter thickness must match the designed glass thickness. In our system, we used a hard dielectric filter deposited on a 300 μm thick slab of fused silica (CVI Melles

Griot part: SWP-0-R800-T400-ET-25.4-0.30-UV), which caused no noticeable degradation in image quality when oriented orthogonal to the probe beam propagation direction.

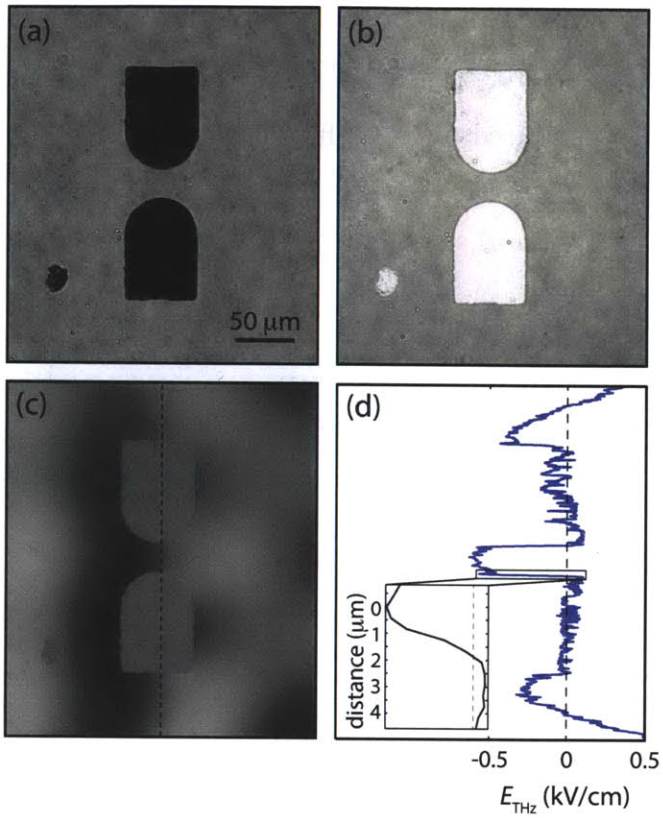

Figure 3-10: **Phase-contrast imaging of a pair of antennas at 30× magnification.** (a) An optical image of antenna without the phase mask. (b) An optical image of antenna with phase mask, which displays minimal degradation compared to (a). (c) THz image calculated by dividing signal image (THz present) by reference image (THz absent) shows in-focus structures with smooth THz field gradients. (d) A lineout of the image of the THz field along the dashed line in (c) shows the resolution of the imaging system. The field changes from 90% signal strength to 10% signal strength in 1.5 μm .

Once the specifications of the objective were determined, the remainder of the design followed naturally. The phase mask must be placed in a Fourier plane, but the back focal plane of the objective is located within its housing, so the Fourier plane must be re-imaged onto the phase mask. To ensure that the entire 0^{th} order beam passes through the depression in the phase mask, a pinhole is imaged onto the phase mask. For lenses L_2 and L_3 in Fig. 3-9, which are relatively short-focal-length lenses that must have minimal aberration,

we used 3-element, air-spaced aplanat lenses capable of diffraction-limited performance (CVI Melles Griot parts: LAP with companion APM). Lenses L_1 and L_4, whose performance is less demanding, were cemented achromatic doublets. There are several considerations in choosing the other focal lengths in the system. The probe spot size at the sample must be larger than the longest THz wavelength under study, but should be as small as possible to minimize intensity and chance of damage at the focus in the objective and phase mask and to maximize intensity in the highly expanded beam at the camera. The pinhole size and focal length of L_1 were chosen so only a small ~ 2.6 mm diameter region of the sample was illuminated. Lenses f_2 and f_3 must apply the appropriate magnification to the image of the pinhole so it easily fits through the 25 μm depression in the phase mask, and must have sufficient NA to capture all the 0^{th} order beam and diffracted light. Finally, f_4 sets the overall magnification of the imaging system, which generally must be sufficiently large such that the resolution is limited by diffraction and not detector pixelation. The parameters chosen were: pinhole aperture = 100 μm , $f_1 = 200$ mm, $f_{\text{obj}} = 20$ mm, $f_2 = 66$ mm, $f_3 = 83$ mm, and $f_4 = 750$ mm. Because of the large magnification ($M = 30\times$), the probe intensity at the detector was greatly reduced (approximately by $1/M^2$) and so we used a low-noise CCD camera for detection (see Section IIC for a full discussion of detectors).

The resolution of the imaging system is shown in Fig. 3-10. Figure 3-10(a) shows an optical image without the phase mask in place, demonstrating the native resolution of the imaging system. When the beam was imaged through the phase mask in Fig. 3-10(b), interference with the 0^{th} order beam causes an expected inversion in the image. There is minimal degradation in image quality except for a narrow diffraction ring around sharp features, which does not appear to reduce the resolution. Figure 3-10(c) shows a zoomed-in view from the time-series in Fig. 3-8, where field localization and sharp edges in the field can be recorded with approximately the native image resolution. A line-out of the THz E-field in Fig. 3-10(d) shows that the field changes from 90% to 10% maximum signal strength over a distance of 1.5 μm.

The measured resolution is slightly worse than the predicted diffraction-limited resolution of 950 nm. There is a small amount of aberration in the imaging system from the ultra-thin filter, phase mask, and imperfect lenses, but this does not explain the entire difference. The primary source of blurring is from pointing instability of the coherent probe beam. As the pointing changes, the diffraction rings at the edges of sharp structures move, and when multiple laser shots are averaged together (either directly on the CCD chip or digitally) the edges are effectively softened. Thus the highest resolution can only be achieved when exposures are short (less than roughly 10 ms), and signal and reference images are collected close together in time. This has important ramifications for choosing the optimal detector (see Sec. 3.3.2.3).

3.3.2.2 Polarization Gating Imaging

The major alternative to phase contrast imaging is polarization gating imaging. At 5 μm, its spatial resolution is not as fine as for phase contrast, but polarization gating enables the suppression of laser noise with balanced imaging and its self-compensating geometry facilitates quantitative measurement of THz E-fields. The experimental setup is shown in Fig. 3-11. Like in phase contrast imaging, the incoming probe light is spatially filtered by a pinhole and expanded to be larger than the region of interest on the sample. Here, however, the input polarization is set to 45°. Instead of detecting absolute phase shifts, the polarization gating technique is sensitive to the relative phase shift between vertically and horizontally polarized light (identical to point source EO sampling in LN described in Sec. 3.2.5). Using (3.44) and (3.45), we get:

$$\begin{aligned}\Delta\phi(x,y) &= -2\pi\frac{\ell}{\lambda_{\text{opt}}}\left[\Delta n_{\text{v}}(x,y) - \Delta n_{\text{h}}(x,y)\right] \\ &= -2\pi\frac{\ell}{\lambda_{\text{opt}}}\left(n_{\text{e}}^3 r_{33} - n_{\text{o}}^3 r_{13}\right) E_{\text{THz}},\end{aligned} \tag{3.47}$$

with Δn_{v} and Δn_{h} the induced index changes for vertical and horizontally polarized light, n_{e} and n_{o} the extraordinary and ordinary index for optical-frequency light, and r_{33} and r_{13} the appropriate electro-optic coefficients.

In a typical polarization gating measurement, the sample is placed between a pair of crossed polarizers, and the induced polarization change is detected as an amplitude change after the second polarizer. LN, however, is strongly birefringent so the THz-induced polarization change rides on top of a large static polarization change. An additional complication is that inhomogeneous sample thickness leads to spatial variation in the static polarization state. To solve this problem, we used a self-compensating geometry where the sample corrects for itself. The LN crystal is imaged with a $4f$ imaging system onto a retro-reflecting mirror, and then re-imaged back onto itself. The double pass through the quarter-wave plate, whose fast axis is parallel to the input polarization (see Fig. 3-11), flips the vertical and horizontal polarizations.

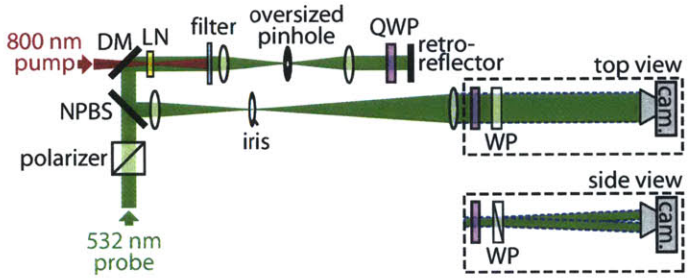

Figure 3-11: **Experimental setup for polarization gating imaging.** DM Dichroic Mirror; LN $LiNbO_3$ sample; QWP Quarter Wave Plate; NPBS Non-Polarizing Beamsplitter; WP Wollaston Prism. The $LiNbO_3$ sample is re-imaged back onto itself via a retro-reflecting mirror, with the beam polarization flipped to compensate static crystal birefringence. The sample and THz wave launched by the pump pulse are then imaged onto the camera. The side view shows how the Wollaston prism splits the two polarizations for balanced imaging on the same detector chip.

After the second pass through the sample, the static phase shift is removed and the polarization state is returned to 45°. Just before the probe pulse's second pass through the crystal, the pump pulse launches the THz wave and the spatially dependent phase shift from (3.47) is induced in the probe. The sample is then imaged onto the camera, and the final

quarter wave plate and polarizer convert the change in polarization state into amplitude. The final polarizer is a Wollaston prism, which splits the two orthogonal polarization states so that both are imaged onto the same detector chip. Jones matrix analysis [63] shows that the signal on the detector is [5]:

$$I^{\pm}(x,y) = I_0^{\pm}(x,y)\left[1 \pm \sin\left(\Delta\phi(x,y)\right)\right], \tag{3.48}$$

where "+" is the top image and "-" is the bottom image, corresponding to vertical and horizontal polarizations (see Fig. 3-12(a)). Because the signal modulation is equal in magnitude but opposite in sign for the two polarizations, subtraction doubles the signal strength, while common mode laser noise, which has the same sign in both sub-images, is cancelled. Image registration is achieved with an affine transformation in Matlab.

To achieve optimal resolution, there are several important but somewhat subtle elements in the optical design. The first stems from the fact that transmission through a slab (such as a beamsplitter) introduces significant aberration in the image. Thus it is important that the image is reflected off both the dichroic mirror and the non-polarizing beamsplitter. The second consideration relates to the pinhole in the $4f$ imaging system. Without the pinhole, the image from the retro-reflector must be exactly mapped back onto the sample itself, which is difficult to implement perfectly and results in some degradation of the final resolution. The pinhole blocks light diffracting at high angles off fine structures in the sample, so in the final image sharp edges are only captured by the second pass through the slab. If the pinhole is too small, however, the polarization self-compensation scheme that corrects for variations in sample thickness will be defeated. Since slab thickness generally varies smoothly on a long length scale, light is diffracted off this inhomogeneity at very small angles. In the Fourier plane of the imaging system, this diffracted light is tightly clustered near the focus of the 0^{th} order beam in the center of the plane, so an oversized pinhole passes this information. We used a 100 μm pinhole, which is large enough for the polarization compensation to work well

but small enough to improve the final image resolution. Another important consideration is the choice of final polarizer. When using a cube polarizing beamsplitter, it is difficult to fully maintain the polarization state and route both images (in focus) onto the same detector chip. In contrast, a Wollaston prism has excellent polarization performance and the routing is trivial. When we used a Wollaston prism at 10°, however, we found that the image was significantly blurred due to refraction. Ultimately, we found that a Wollaston prism with a small divergence angle (1.5°, United Crystals) maintained the advantages in polarization and routing, and did not noticeably degrade the image.

The last consideration was specifications of lenses and imaging NA. For imaging the near-fields of metallic structures deposited on the surface of the LN slab, phase contrast is the preferred method. Polarization gating is more typically used for imaging structures where air-gaps have been cut through the entire slab waveguide using laser machining [64]. The LN slabs are typically 30-50 μm thick, and the E-field of the lowest slab waveguide mode is relatively uniform through the depth of the slab [39]. The propagating THz fields are best recorded when the depth of field (DoF) is roughly equal to the slab thickness and the entire sample is in focus. Both the resolution, the Airy disk radius r_{Airy} in the Rayleigh definition, and depth of field are related to the optical wavelength, λ_{opt}, and the NA [65]:

$$r_{\text{Airy}} \approx 0.61\lambda_{\text{opt}}/\text{NA} \tag{3.49}$$

$$\text{DoF} \approx \lambda_{\text{opt}}/\text{NA}^2 \tag{3.50}$$

where we have assumed that no immersion fluid has been used when imaging. Setting the DoF to 50 μm, we find that the optimal NA is 0.1 and the diffraction-limited image resolution is 3 μm. In our experiments, we used cemented achromatic doublets for all the lenses. The lens responsible for the NA of the imaging system, which is near the non-polarizing beamsplitter in Fig. 3-11, had a diameter of 5 cm and a focal length of 15 cm. The NA was set using an iris in the conjugate plane (see Fig. 3-11).

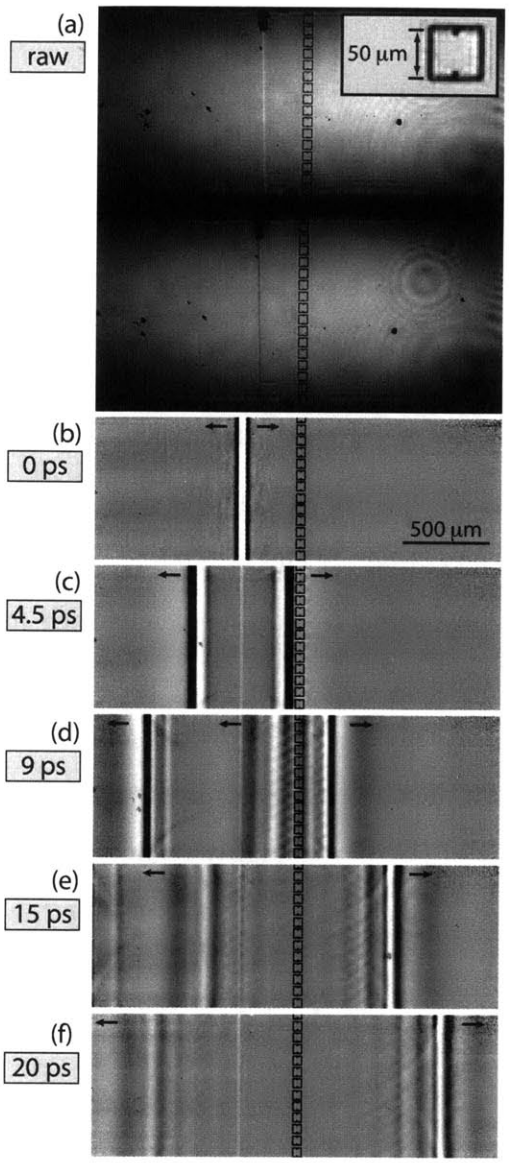

Figure 3-12: **THz wave propagation recorded with polarization gating imaging.** (a) Raw images on detector, which show the two polarization states (vertical, top and horizontal, bottom). The inset shows an expanded view of one of the gold microstructures, which demonstrates the resolution finer than 5 μm. (b)-(f) A time sequence showing the spatiotemporal evolution of the THz wave as it propagates and interacts with the microstructures (false colored black for clarity in (b)-(f)). The arrows at the top of each wave packet indicate the direction of propagation. Initially, the pump launches counter-propagating, broadband THz waves. The leftward propagating waves pass out of the field of view within 15 ps while the rightward propagating waves interact with the microstructure array. Both reflected/diffracted and transmitted/diffracted waves are clearly visible.

Figure 3-12 and Multimedia 2 in [4] show the high-resolution, low-noise imaging possible with polarization gating. Fig. 3-12(a) is a raw image collected using the polarization gating system. The sample is a 30 μm thick slab of LN with a column of 200 nm thick gold microstructures deposited on its surface using optical lithography. This microstructure shape, which has electric but not magnetic resonances, is a common building block in metamaterials [66–68]. The microstructures, 50 $\times$ 50 μm squares with short, inward-pointing arms separated from each other by 15 μm (see inset of Fig. 3-12(a)), are resolved to better than 5 μm in the raw image. Fig. 3-12(b)-(f) are frames from Multimedia 2 showing a THz wave interacting with the microstructure array. The frame at $t = 0$ ps shows the generation of counter-propagating, broadband THz waves. Due to the resonances of the microstructures, the array acts like a filter in that some frequencies are strongly reflected or diffracted while others pass through almost unperturbed. The flat backgrounds in these frames and the accompanying movie (Multimedia 2 in [4]) demonstrate the advantages of balancing for noise reduction. Balancing, coupled with the use of a high-speed camera described in Section IIC, has made these the lowest noise polaritonics imaging measurements to date. The low noise, quantitative field extraction due to self-compensation, and $\sim \lambda/25$ image resolution make polarization gating imaging the preferred method for many polaritonics measurements.

3.3.2.3 Detection Procedure and Electronics

In addition to the optical designs for phase contrast and polarization gating described above, both an appropriate acquisition methodology and imaging detector are critical for making low-noise measurements. For these techniques, the two major noise contributions are instability in the probe and electrical noise of the detector. Typically, laser fluctuations are dominated by $1/f$ noise, where the noise amplitude is inversely proportional to the frequency [69]. This noise can be suppressed both by balancing and by detecting at a high frequency, as is commonly done in point-probe measurements with a lock-in amplifier. Here,

this means acquiring the signal and reference images as close together in time as possible. In contrast, electrical noise from the camera is uncorrelated white noise that can only be reduced by averaging or using a low-noise detector. The ideal camera would have extremely low electrical noise and be fast enough to synchronize to the repetition rate of our 1 kHz laser, which would enable signal detection at the maximum pump modulation frequency of 500 Hz. In practice, no such detector exists so we compare the two limiting cases: a low-noise but slow CCD camera and a fast but high-noise CMOS camera. Although CCD cameras have typically been used in the past [5, 39, 56, 60], we show that the fast CMOS system has better performance in most situations.

Our low-noise detector was a scientific grade Princeton Instruments PIXIS CCD camera (2048 × 2048 pixels, 16 bit, maximum full-chip frame rate of 0.5 Hz, 0.03% dark RMS noise). The high-speed detector was a Photron FASTCAM 1024PCI CMOS camera (1024 × 1024 pixels, 10 bit, 1 kHz maximum full-chip frame rate, 0.2% dark RMS noise). The CCD was triggered using a 1 kHz TTL signal from the laser and acquired data at a rate of approximately one image every two seconds (including file transfer time). To avoid exposing the chip while the built-in CCD camera shutter was opening (~25 ms), we placed a 700-μs shutter in the probe upstream of the camera. This secondary shutter was triggered to open after the camera shutter had opened fully and to close before the camera shutter started closing. Therefore with a 75 ms exposure time, the CCD chip would be exposed to the probe for only 50 ms, equivalent to 50 consecutive laser pulses. In sharp contrast to the 0.5 Hz CCD, the CMOS camera was synced to the 1 kHz laser and each probe pulse was collected as a separate image. For acquisition with both the CCD and CMOS cameras, the pump was modulated as quickly as possible given the camera frame rate. Because of the modulation, the pump was blocked and the THz pulse was absent in every other frame of the recording, and these served as the reference. The THz-induced phase shift (and consequently the THz E-field) was determined by dividing the signal image by the reference image as given by (3.48). Pump modulation was carried out with a mechanical shutter when detecting with

the CCD camera, while an optical chopper set to 500 Hz was used with the CMOS camera.

The noise performances of the two detectors were directly compared by recording a series of images in an unstructured LN slab in the same way a THz movie is recorded, but with the pump blocked to remove the THz signal. The image sequence was recorded using the polarization gating imaging system so the effects of balancing could be quantified. While the CMOS camera is capable of collecting many images in the same time that the CCD can collect a single frame, the large data volume (2 Gbyte/sec data rate for full frame recording) requires a much longer download time. We took this into account when recording the image sequences, and held the pixel number and total acquisition time constant. For both cameras, the average signal image and average reference image were calculated and then divided to give ratio images. Balanced images were calculated by subtracting the top and bottom ratio images. The unbalanced and balanced images are shown in Fig. 3-13.

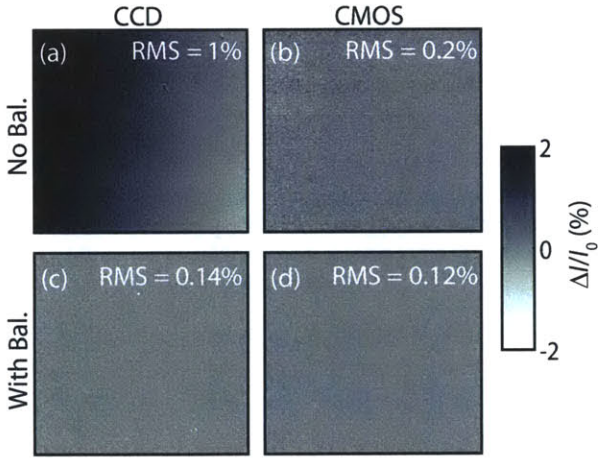

Figure 3-13: **Noise images using CCD and CMOS based cameras.** (a) and (b) show the ideally flat pictures calculated by dividing signal images by reference images and averaging. Pointing and spatial beam profile fluctuations between signal and reference images and detector noise lead to spatial variations in the image. (c) and (d) demonstrate further noise suppression by balancing, calculated by subtracting the top image on the chip from the bottom one.

The value in the upper right hand corner of each image shows the RMS deviation across the image. Fig. 3-13(a) and (b) show the results without balancing. Both detectors show long length scale noise due to pointing changes and fluctuations in the spatial beam mode

profile between collection of signal and reference images, but it is significantly suppressed by high-frequency detection in the CMOS camera. For the CCD, the mean of the image is not zero; this further demonstrates the disadvantage of detecting at a low frequency. The balanced images are shown in Fig. 3-13(c) and (d). Balancing suppresses laser noise at all frequencies, and is particularly effective at suppressing long length scale noise (compare Fig. 3-13(a) to (c) or Fig. 3-13(b) to (d)). For the CCD, where electrical noise is insignificant, balancing reduces RMS noise by a factor of 10, while it is decreased by only a factor of 2 for the noisier CMOS detector.

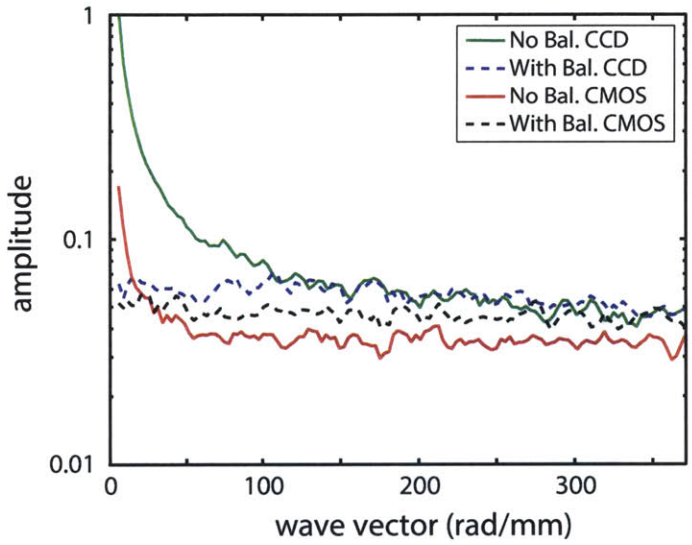

Figure 3-14: **Wave vector-dependent noise distribution.** For both the CCD and the CMOS camera, the largest noise contributions are at low wave vector and result from laser pointing and spatial beam profile fluctuations. Balancing greatly reduces these effects, but adds a factor of for electrical noise, leading to larger noise amplitudes at high wave vectors for the CMOS camera.

To analyze structure within the noise and further study the relative effects of laser fluctuations and electrical noise, we calculate the frequency- and wave vector-dependent noise distributions. To do this, we took a 2-dimensional slice $S(x, y = \text{const}, t)$ out of the 3-dimensional movie data. A 2D Fourier transform gives the wave vector-frequency noise distribution. The data (not shown) were roughly uniform along the frequency axis, and so the results were averaged over frequency to give the noise amplitude as a function of wave

vector as shown in Fig. 3-14.

For both the CCD and the CMOS cameras, noise is many times larger at low wave vectors, consistent with the slow variation across the images in Fig. 3-13(a) and (b). Balancing suppresses this low wave vector noise for both cameras, but the high-wave vector behavior is very different. For the CMOS camera, balancing causes a 1.3-fold increase in the high-wave vector noise, roughly the factor of $\sqrt{2}$ expected when subtracting two numbers with uncorrelated uncertainty. This suggests that random electrical noise is significant for the CMOS detector, but not for the CCD, which does not display this effect. We conclude that for the CCD detector, measurement noise is dominated by laser fluctuations, while both laser and electrical noise matter for the CMOS camera.

The analysis shows that although the CMOS chip has higher electrical noise than the CCD, the ability to detect at a high frequency and average more images in the same amount of time provides adequate compensation in our system. This high-frequency detection is especially useful if balancing is not an option (as in phase contrast imaging). There are two important situations, however, where the noisier CMOS detector is less effective. The first is when the intensity of light at the detector is limited, as may be the case in very high-magnification imaging systems, where dark counts are a significant fraction of the total signal. The second is when a low-noise light source is used for the probe. In our measurements, the NOPA used to generate the probe light suffers from pointing instability and roughly 2% RMS amplitude fluctuations, so balancing and high frequency chopping are essential for efficient noise suppression. If imaging were implemented with a very stable laser, then the relative importance of detector noise would be increased and it is likely that the CCD camera would have better overall performance. Further noise suppression would be possible if either the noise of the detector could be reduced or if more averaging were possible. The latter is possible as data transfer rates become faster, since for the CMOS camera almost all the data collection time is spent transferring the images to the computer memory and about 1% of the time is spent recording images. A future alternative is the scientific CMOS (sCMOS)

camera, which offers a potentially advantageous compromise between noise and speed. It has a noise performance comparable to CCDs but detects at rates 100× faster, and can have high data transfer speeds.

3.3.3 Conclusions

Our results show that for both phase contrast and polarization gating imaging designs, it is possible to acquire optical images of samples with near diffraction-limited resolution. When dividing by the reference to convert optical images to THz images, there is only a slight degradation in resolution. Given the huge wavelength mismatch between visible and THz light, $\lambda(1\text{ THz}) > 500 \times \lambda(532\text{ nm})$, THz waves can easily be imaged in the deep sub-wavelength regime providing detailed insight into the near-field behavior of photonic structures.

Phase contrast imaging, optimized for high-resolution study of THz fields interacting with metal structures, had an NA of 0.28 and spatial resolution of 1.5 μm. Further increase of the NA is possible, but damage from the intense optical pump makes this very challenging. Polarization gating was optimized to study fields spanning the depth of a 30-50 μm thick LN slab. Optimizing for this large depth of field limits the NA to about 0.1 and the resolution to about < 5 μm, still deeply subwavelength for the THz light. Self-compensation of static phase variation from the sample facilitates quantitative E-field extraction, and balancing reduces noise. Both phase contrast and polarization gating can be detected at high frequency with a high-speed camera to reduce noise, resulting in noise floors of 0.2% and 0.12%, respectively. Further significant noise reduction should be possible using high-speed, low-noise cameras based on the development of sCMOS technology. We anticipate that these imaging techniques will enable a new generation of studies on structures such as THz metamaterials and photonic crystals. The high resolution also opens interesting possibilities for studying waves with much shorter wavelengths, such as acoustic waves.

Chapter 4

THz Metallic Slab Waveguides

4.1 Introduction

Photonic elements such as metamaterials, bandgap crystals, and optical modulators are key components in next-generation optical signal processing and telecommunications systems. A powerful tool for studying and building intuition about such systems is the polaritonics platform [3], in which terahertz-frequency (THz) light is generated and detected optically in a thin slab of an electro-optic crystal, typically lithium niobate (LN). Metallic and dielectric photonic components can be fabricated directly onto the crystal slab [7, 53, 64], and THz waves can be visualized [4] as they propagate at the speed of light and interact with these components. These on-chip capabilities create an integrated environment for THz spectroscopy, signal processing, and the development of photonic devices. In this chapter, we deposit indium tin oxide (ITO) on one surface of the LN slab to enable direct visualization of metal-clad waveguide modes, and we assess the potential for using ITO in THz devices.

The broad set of tools and capabilities in the polaritonics system results from its unique experimental geometry. THz waves are generated via impulsive stimulated Raman scattering [33] by focusing an intense, ultrafast near infrared (NIR) pump pulse through a thin LN

crystal. Due to the large mismatch between refractive indices at THz and NIR frequencies, THz waves propagate laterally, perpendicular to the pump pulse if it is at normal incidence, and are waveguided within the slab [3, 39] (see Fig. 4-10). As the THz waves propagate through the crystal, they modify the refractive index of LN via the electro-optic effect. An image of the spatially-dependent index change, $\Delta n(y, z)$, can be recorded with an expanded probe beam and a phase-sensitive imaging technique [4, 5]. By recording the image with variable probe pulse delays relative to the pump pulse, one can assemble a movie of the propagating THz wave. The method is capable of measuring THz electric fields (E-fields) quantitatively and non-invasively with deep-subwavelength resolution ($\sim \lambda/100$ at 0.5 THz). These capabilities have enabled the study of a diverse set of photonic components including reflectors, diffractive elements, resonators, waveguides, and antennas [7, 39, 53, 56, 70].

4.2 Bound Modes in Planar Metal Slab Waveguides

For a better understanding of the experimental results on metallic slab waveguides, it is instructive to firstly be familiar with the perfect metal slab waveguide. The following derivation builds on the derivation of the transverse electric (TE) and transverse magnetic (TM) waveguide modes in the plain symmetric slab waveguide (refer to Ch. 2, Sec. 2.3.1 for more detailed explanations); only the most relevant equations will be re-stated here.

We consider a slab waveguide consisting of an anisotropic core surrounded by an ideal metal cladding on one or both sides to give either the asymmetric or the symmetric waveguide system, respectively. The anisotropic core, being x-cut LN, is uniaxial and its optic axis is parallel to the slab surface. The y- and z-dimensions of the slab are assumed to extend infinitely, while the x-dimension, corresponding to the slab thickness, is confined. The waveguide modes propagate along the y-direction, $k_y = \beta$, and extend infinitely along the z-direction, $k_z = 0$. In the core, the propagating bound modes are described by real transverse wave vector components, $k_x = \kappa_e = \kappa$, while in the cladding, the field evanescently decays to

zero along the transverse direction, $k_x = i\alpha$. The metal claddings are assumed to be perfect conductors with lossless reflection, such that $\vec{E} = 0$ and $\vec{H} = 0$ inside the metal itself.

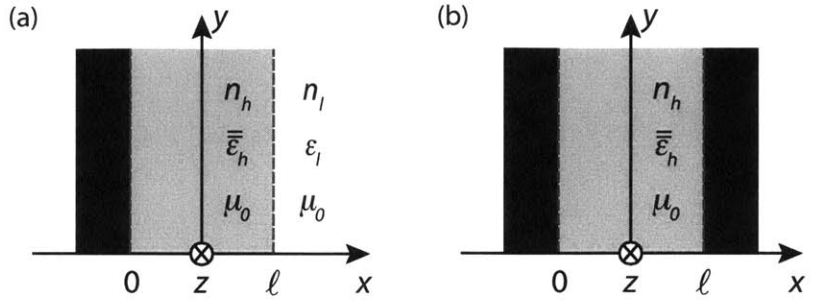

Figure 4-1: **Asymmetric and symmetric metal slab waveguide geometries.** (a) Asymmetric waveguide experimental geometry with perfect conductor cladding (left), low-index, n_l, cladding (right), and high-index, n_h, anisotropic core. (b) Symmetric waveguide experimental geometry with high-index core surrounded by perfect conductor cladding on both sides. ε and μ are the permittivity and permeability, respectively, in each region.

In this derivation, we treat the TE and TM polarizations separately and solve for the waveguide modes in an anisotropic waveguide in each of the experimental geometries shown in Fig. 4-1. We assume a nonmagnetic, lossless high-index core and a low-index cladding with purely real permittivities, $\bar{\bar{\varepsilon}}_\mathrm{h}$ and ε_l, respectively, and free-space permeability, μ_0. The same coordinate system depicted in Fig. 2-6 is used for our experimental geometry in ITO waveguides, where $\theta = 0°$ for TE waves and $\theta = 90°$ for TM waves. Because we experimentally only generate the extraordinary waves in the core, the relevant bulk dispersion relations are:

$$\text{Core, extraordinary, TE}: \quad \kappa_\mathrm{e}^2 + \beta^2 = \left(\frac{\omega n_\mathrm{e}}{c}\right)^2 \tag{4.1a}$$

$$\text{Core, extraordinary, TM}: \quad \kappa_\mathrm{e}^2 + \beta^2\left(\frac{n_\mathrm{e}^2}{n_\mathrm{o}^2}\right) = \left(\frac{\omega n_\mathrm{e}}{c}\right)^2 \tag{4.1b}$$

$$\text{Cladding}: \quad -\alpha^2 + \beta^2 = \left(\frac{\omega n_\mathrm{c}}{c}\right)^2 \tag{4.1c}$$

where n_o and n_e are the bulk ordinary and extraordinary index of LN, respectively, and n_c

is the index of the cladding, air.

4.2.1 TE Modes in Asymmetric and Symmetric Metal Waveguides

For extraordinary TE modes, according to (4.1a), the anisotropic system reduces to the isotropic case. In an isotropic system, the modes may be described by an arbitrary choice of two orthogonal polarizations. In the lab frame, the convenient choices are a unit vector along the z-axis, $\hat{z}$:

$$\hat{z} = \begin{bmatrix} 0 \\ 0 \\ 1 \end{bmatrix} \tag{4.2}$$

and $\vec{h}^{\pm}$ in the high-index core or $\vec{l}^{\pm}$ in the low index cladding are given by:

$$\vec{h}^{\pm} = \frac{1}{\sqrt{\beta^2 + \kappa^2}} \begin{bmatrix} -\beta \\ \pm\kappa \\ 0 \end{bmatrix}, \tag{4.3}$$

similarly in the low-index cladding:

$$\vec{l}^{\pm} = \frac{1}{\sqrt{\beta^2 - \alpha^2}} \begin{bmatrix} -\beta \\ \pm i\alpha \\ 0 \end{bmatrix}. \tag{4.4}$$

The first polarization maps directly to the TE modes of concern here, while the second polarization maps directly to the TM modes, in isotropic systems. The TE E-fields can be

described in each region:

$$\text{Cladding } (x \leq 0): \ \vec{E}(x) = C\hat{z}\exp[\alpha(x+\ell)], \tag{4.5a}$$

$$\text{Core } (0 \leq x \leq \ell): \ \vec{E}(x) = A_1\hat{z}\exp(i\kappa x) + A_2\hat{z}\exp(-i\kappa x) \tag{4.5b}$$

$$\text{Cladding } (x \geq \ell): \ \vec{E}(x) = B\hat{z}\exp[-\alpha(x-\ell)] \tag{4.5c}$$

These expressions ensure that the TE E-fields decay to zero as $x \to \infty$. Because tangential E- and H-fields (the y- and z-components) must be continuous across the boundary, the relevant boundary conditions given by Maxwell's equations for the TE modes are:

$$E_{z,\text{clad}} = E_{z,\text{core}} \tag{4.6a}$$

$$\frac{\partial E_{z,\text{clad}}}{\partial x} = \frac{\partial E_{z,\text{core}}}{\partial x} \tag{4.6b}$$

4.2.1.1 TE Modes of Asymmetric Metal Waveguides

For the asymmetric metal waveguide in Fig. 4-1(a), the boundary conditions in (4.6) are applied at the LN-metal interface ($x = 0$) and LN-air interface ($x = \ell$). At $x = 0$, the boundary conditions show that $A_1 = -A_2 = A$, which gives a sinusoidal E-field. The equations yield a set of homogeneous equations that can be recast in the following matrix:

$$\begin{bmatrix} \sin(\kappa\ell) & -1 \\ \kappa\cos(\kappa\ell) & \alpha \end{bmatrix} \begin{bmatrix} A \\ B \end{bmatrix} = 0 \tag{4.7}$$

For a homogeneous system, a solution exists when the determinant is zero; the determinant can easily be calculated analytically from the matrix to yield:

$$\tan(\kappa\ell + m\pi) = -\kappa/\alpha \tag{4.8}$$

where $m = 0, 1, 2, \cdots$ represents the mode number for the periodic solutions. The bulk dispersion curves in (4.1) are used to eliminate dependence on both κ and α such that we arrive at a relation between β and ω. The resulting transcendental equation may be solved using Newton's method by bisection or other numerical solvers in Matlab. In both cases, accurate bounds must be given for each solution; otherwise the method will not converge to the correct waveguide modes. The solved dispersion curves are shown in Fig. 4-2, where the system has a waveguide cutoff frequency, as will also be observed in the other polarizations and geometries discussed later.

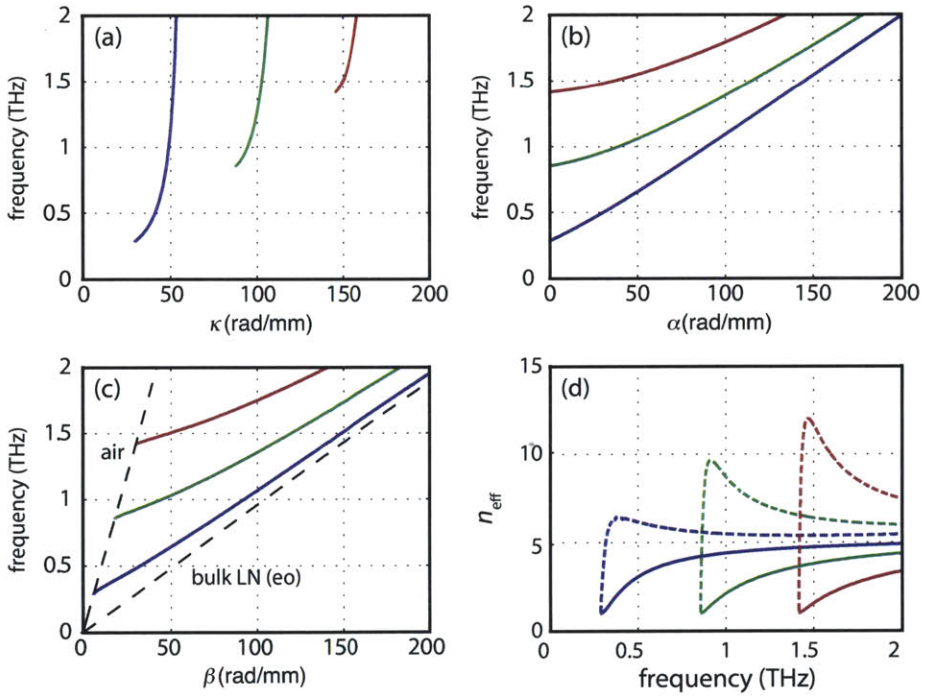

Figure 4-2: **TE dispersion curves and effective indices in asymmetric metal-clad waveguide.** For the lowest three TE modes ($\ell = 54$ μm): (a) The frequency-dependent propagating wave vector in the LN core, κ. (b) The frequency-dependent evanescent wave vector, α, in the air cladding. (c) Waveguide dispersion curves (solid lines) of the first three modes and bulk dispersion curves (dashed lines) of LN core along the extraordinary axis and air cladding. (d) The effective phase (solid) and group index (dashed) as a function of frequency.

Interestingly, the TE waves for the asymmetric slab reproduce the results for the asymmetric TE modes of a plain slab of LN of twice the thickness (this will also be shown to be

true for TM) given previously in (2.44). This is the case because the antisymmetric modes in a plain slab have a node (i.e. fields go to zero) located in the transverse center of waveguide. This resembles an asymmetric metal waveguide with a core twice as thick, with the metal cladding located in the center, and thus the field is zero at the LN-metal interface to satisfy the boundary condition. Physically, the boundary condition is satisfied because the incident and reflected waves off the metal interface are 180 degrees out of phase and destructively interfere at the surface.

In addition, the waveguide mode profiles in (4.5) are solved for explicitly as follows for $A = 1/2,\ B = \sin(\kappa\ell)$:

$$\vec{E}(x) = \hat{z}E_0 \begin{vmatrix} 0 & x \leq 0 \\ \sin(\kappa x) & 0 \leq x \leq \ell \\ \sin(\kappa\ell)\exp[-\alpha(x-\ell)] & x \geq \ell \end{vmatrix} \tag{4.9}$$

where E_0 is the amplitude of the E-field in V/m. The mode profiles of the lowest three TE waveguide modes are shown in Fig. 4-3.

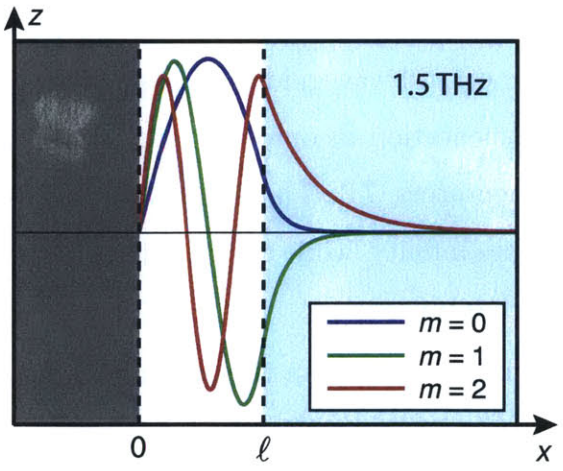

Figure 4-3: **TE modes in an asymmetric metal-clad waveguide.** The E_z-field profiles of the lowest three TE modes at 1.5 THz.

4.2.1.2 TE Modes in Symmetric Metal Waveguides

The symmetric metal waveguide in Fig. 4-1(b) is also evaluated at either $x = 0$ or $x = \ell$. Similarly here, at $x = 0$, the boundary condition shows that $A_1 = -A_2 = A$. With only a single unknown variable, A, we apply the first boundary condition in (4.6) at $x = \ell$ to yield the following homogeneous equation:

$$A\sin(\kappa\ell) = 0 \tag{4.10}$$

The expression is satisfied for the periodic solutions $\kappa\ell = m\pi$, where $m = 1, 2, 3, \cdots$ are the allowed mode numbers.

In this case, the propagation constant is *frequency-independent* for each mode as seen in Fig. 4-4(a). The dispersion curves for the allowed waveguide modes are easily determined by substituting the wave vector κ into (4.1a). The dispersion curves are shown in Fig. 4-4(b), where the modes approach the bulk dispersion of LN along the extraordinary axis. It is interesting to note that at very low wave vectors, the dispersion curve is nearly flat. Because the slope of the dispersion curve, $\mathrm{d}\omega/\mathrm{d}k$, signifies the group velocity, at low wave vectors the wave has almost zero group velocity and is referred to as 'slow light'. This phenomenon has been observed in photonic crystal waveguides [71], which have been exploited for optical modulation devices for implementation in optoelectronic systems [72], optical buffers [73], and dynamic dispersion compensators [74]. This is corroborated by the effective group index in Fig. 4-4(c), which approaches infinity, while the effective phase index approaches zero and so the phase velocity approaches infinity.

The waveguide mode profiles are solved in the core, given in (4.5b), for $A = 1/2$:

$$\vec{E}(x) = \hat{z}E_0 \left| \begin{array}{c|c} 0 & x \le 0 \\ \sin(\kappa x) & 0 \le x \le \ell \\ 0 & x \ge \ell \end{array} \right. \tag{4.11}$$

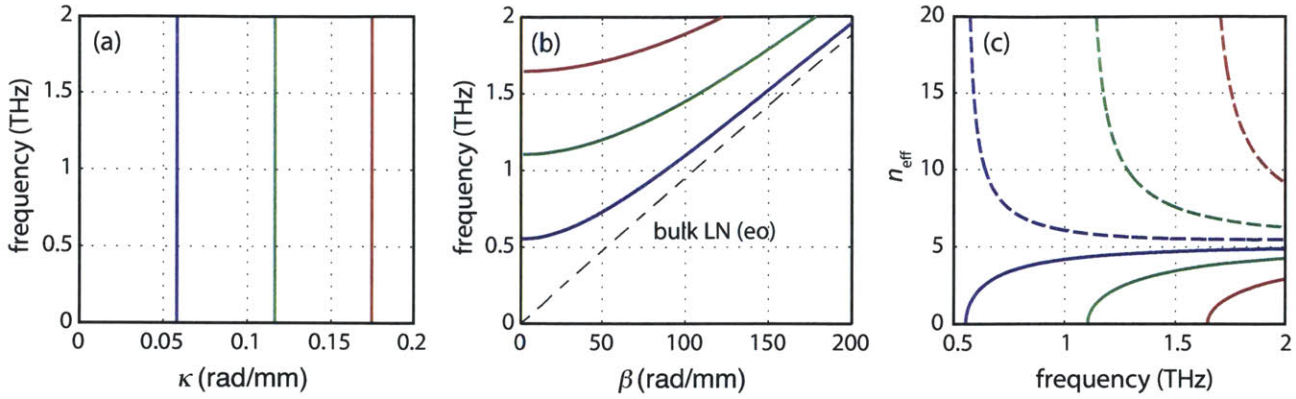

Figure 4-4: **TE dispersion curves and effective indices in a symmetric metal-clad waveguide.** For the lowest three TE modes ($\ell = 54$ μm): (a) The fequency-independent wave vector in the core, κ. (b) The waveguide dispersion curves (solid lines) and bulk dispersion curve of LN core along the extraordinary axis (dashed line). (c) The effective phase (solid) and group index (dashed) as a function of frequency.

where E_0 is the amplitude of the E-field . The mode profiles of the lowest three TE waveguide modes are shown in Fig. 4-5, which are analogous to the allowed states in a 1D particle in a box system.

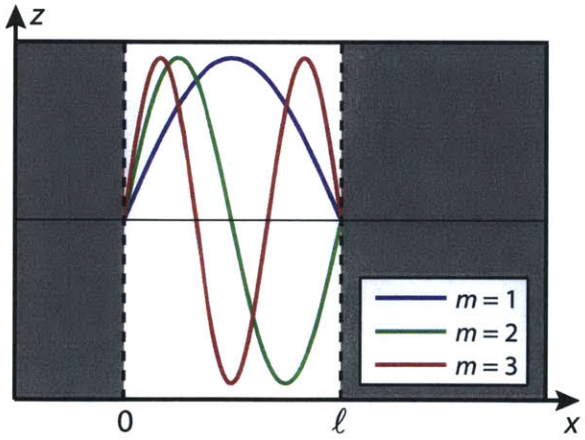

Figure 4-5: **The lowest three TE modes in a symmetric metal-clad waveguide.** (a) Frequency-independent E_z-field profiles and (b) waveguide dispersion curves (solid lines) and bulk dispersion curve of LN core along the extraordinary axis (dashed line).

4.2.2 TM Modes in Asymmetric and Symmetric Metal Waveguides

For the TM-polarization, the anisotropy of the core must be treated since there are E-field components along both extraordinary and ordinary axes. For anisotropic systems, the allowed polarizations are uniquely defined by the extraordinary polarization, $\vec{e}$, and the ordinary polarization, $\vec{o}$. The extraordinary and ordinary polarizations of the E-field when $\theta = 90°$, derived previously in Sec. 2.3.1.3, are:

$$\vec{e}^{\pm} \propto \frac{1}{\sqrt{\beta^2 + \kappa_e^2}} \begin{bmatrix} \mp\beta/\varepsilon_o \\ \kappa_e/\varepsilon_e \\ 0 \end{bmatrix} \quad \text{and} \quad \vec{o}^{\pm} \propto \frac{1}{\kappa_o} \begin{bmatrix} 0 \\ 0 \\ \pm\kappa_o \end{bmatrix} = \begin{bmatrix} 0 \\ 0 \\ 1 \end{bmatrix} \tag{4.12}$$

where $\varepsilon_o = n_o^2$ is the dielectric constant for the ordinary axis and $\varepsilon_e = n_e^2$ is the dielectric constant for the extraordinary axis. In contrast, the isotropic cladding may still be described by the orthogonal polarizations defined for the isotropic TE case previously in (4.2) and (4.4).

Because a TM mode is purely characterized by its H_z-component (or its complementary E_x and E_y components), we find that the extraordinary polarization corresponds to a TM wave and that the ordinary polarization corresponds to a TE wave. The E-fields of the TM waves can be expressed in each region as follows:

$$\text{Cladding } (x \leq 0): \ \vec{E}(x) = 0 \tag{4.13a}$$

$$\text{Core } (0 \leq x \leq \ell): \ \vec{E}(x) = A_1\vec{e}^{+}\exp(i\kappa x) + A_2\vec{e}^{-}\exp(-i\kappa x) \tag{4.13b}$$

$$\text{Cladding } (x \geq \ell): \ \vec{E}(x) = B\vec{l}^{+}\exp[-\alpha(x-\ell)] \tag{4.13c}$$

These expressions ensure that the TM E-fields decay to zero as $x \to \infty$. The relevant boundary conditions for the TM modes correspond to the tangential E_y and H_z fields. The

H-field in terms of the E-field components are:

$$\vec{H} = \frac{-i}{\omega\mu_0}\left[-i\hat{x}\beta E_z + \hat{y}\frac{\partial E_z}{\partial x} + \hat{z}\left(i\beta E_x - \frac{\partial E_y}{\partial x}\right)\right]. \tag{4.14}$$

Therefore, the TM boundary conditions are:

$$E_{y,\text{clad}} = E_{y,\text{core}} \tag{4.15a}$$

$$i\beta E_{x,\text{clad}} - \frac{\partial E_{y,\text{clad}}}{\partial x} = i\beta E_{x,\text{core}} - \frac{\partial E_{y,\text{core}}}{\partial x} \tag{4.15b}$$

4.2.2.1 TM Modes in Asymmetric Metal Waveguides

The TM modes of the asymmetric waveguide in Fig. 4-1(a) are determined by applying the boundary conditions in (4.15) at $x = 0$ or $x = \ell$. At $x = 0$, the boundary conditions show that $A_1 = -A_2 = A$. The relations yield a set of homogeneous equations that can be recast in the following matrix:

$$\begin{bmatrix} \frac{\kappa}{\varepsilon_e}\sin(\kappa\ell) & \alpha \\ \cos(\kappa\ell) & 1 \end{bmatrix} \begin{bmatrix} A \\ B \end{bmatrix} = 0 \tag{4.16}$$

The resulting transcendental equation that describes the TM modes is:

$$\tan(\kappa\ell + m\pi) = \frac{\alpha\varepsilon_e}{\kappa}, \tag{4.17}$$

where $m = 0, 1, 2, \cdots$ represents the mode number for the periodic solutions. It can be seen that the TM waveguide modes derived here are simply the asymmetric TM modes of a symmetric waveguide with dielectric claddings (i.e., a slab of LN surrounded by air cladding) for a slab of twice the thickness as derived in Sec. 2.3.1.3 (compare with (2.63)), for the same reasons described for TE waves in an asymmetric metal slab waveguide.

The dispersion curves of the lowest three TM modes are shown in Fig. 4-6(a)-(c). The TM modes have components that travel at the speed of light in air at low wave vectors and have no cutoff frequency, analogous to those observed for TM modes in the plain slab. The effective indices are shown in Fig. 4-6(d), where both the phase and group index approach the bulk ordinary index of LN at high frequencies and approach the index of air at low frequencies. While the phase index monotonically increases with frequency, the group index initially increases rapidly and then decreases to approach the bulk index (attributed to the curvature in the dispersion curve in Fig. 4-6(c). It is interesting to note that the odd order modes are symmetric in E_y and antisymmetric in E_x with respect to the transverse direction.

The waveguide mode profiles in (4.13) are solved for explicitly as follows with $A = 1/2$, $B = \frac{\kappa}{\varepsilon_e \alpha}\sin(\kappa\ell)$:

$$\vec{E}(x) = \frac{D_0}{\sqrt{\beta^2+\kappa^2}} \begin{cases} i\hat{y}\begin{bmatrix} 0 \\ (\kappa/\varepsilon_e)\sin(\kappa x) \\ (\kappa/\varepsilon_e)\sin(\kappa\ell)\exp[-\alpha(x-\ell)] \end{bmatrix} \\ \qquad - \hat{x}\begin{bmatrix} 0 \\ (\beta/\varepsilon_o)\cos(\kappa_e x) \\ \frac{\kappa}{\varepsilon_e\alpha}\sin(\kappa\ell)\beta\exp[-\alpha(x-\ell)] \end{bmatrix} \end{cases} \begin{matrix} x \le 0 \\ 0 \le x \le \ell \\ x \ge \ell \end{matrix} \quad (4.18)$$

The mode profiles and dispersion curves of the lowest three TM waveguide modes are shown in Fig. 4-7.

4.2.2.2 TM Modes in Symmetric Metal Waveguides

The TM modes of the symmetric waveguide in Fig. 4-1(b) are similarly determined at the boundary conditions in (4.15a) at $x = 0$ and $x = \ell$. At $x = 0$, the boundary conditions show

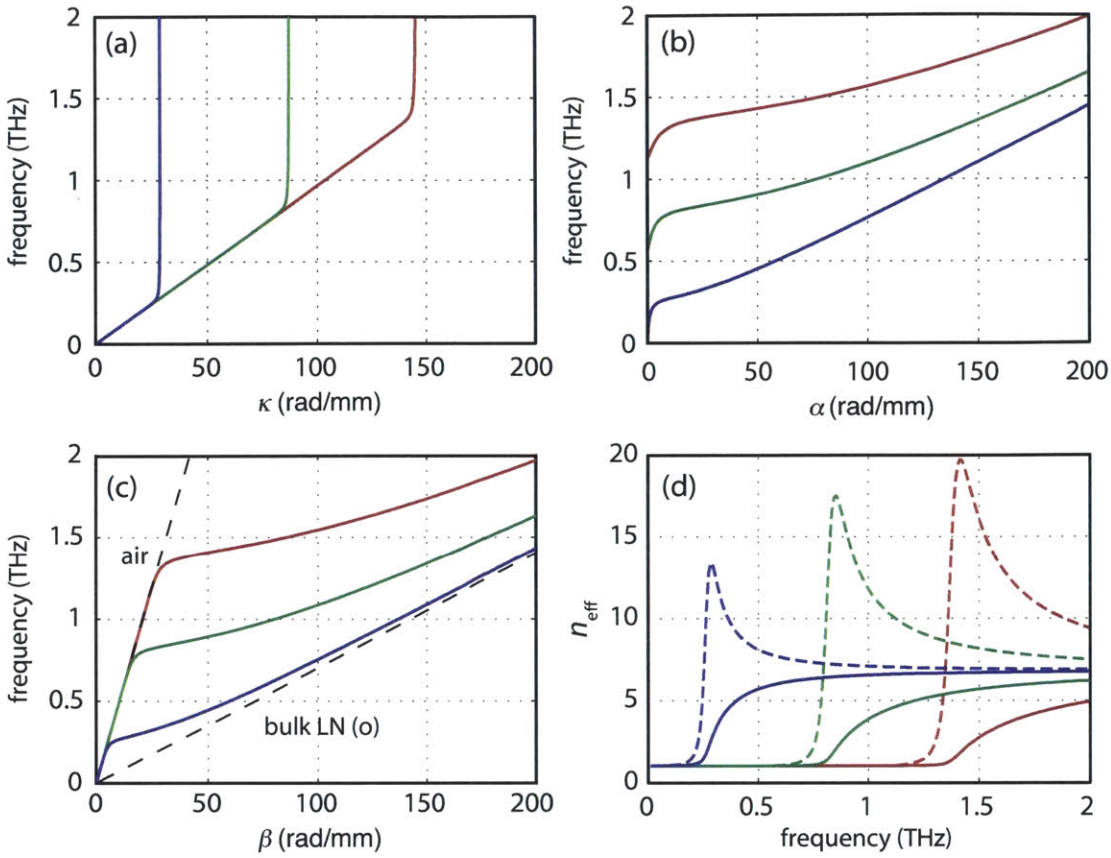

Figure 4-6: **TM dispersion curves and effective indices in an asymmetric metal-clad waveguide.** For the lowest three TM modes ($\ell = 54$ μm): (a) The frequency-dependent propagating wave vector in the LN core, κ. (b) The frequency-dependent evanescent wave vector, α, in the air cladding. (c) Waveguide dispersion curves (solid lines) of the first three modes and bulk dispersion curves (dashed lines) of LN core along the ordinary axis and air cladding. (d) The effective phase (solid) and group index (dashed) as functions of frequency.

that $A_1 = -A_2 = A$. The resulting homogeneous equation is:

$$A\sin(\kappa\ell) = 0 \tag{4.19}$$

Periodic solutions exist at $\kappa\ell = m\pi$, where $m = 0, 1, 2, 3, \cdots$ represents the mode number. The solution here bears the same functional form as that for the extraordinary TE wave solution analog in the previous section. Consequently, the frequency-independent wave vector

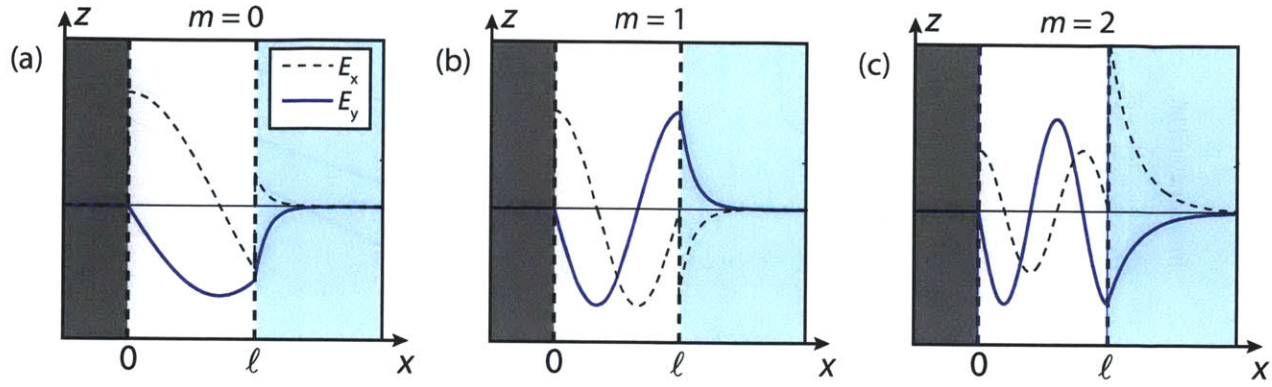

Figure 4-7: **The lowest three TM modes in an asymmetric metal-clad waveguide.** The TM E-field profiles (E_x and E_y) of (a) $m = 0$ mode, (b) $m = 1$ mode, (c) $m = 2$ mode.

in the core between the TE and TM modes in symmetric metal slab waveguides are identical as observed in Fig. 4-8(a). The TM dispersion curves closely resemble the analogous TE dispersion curves, but approach the ordinary index of LN at high wave vectors, or at high frequencies for the effective indices, in Fig. 4-8(b) and (c).

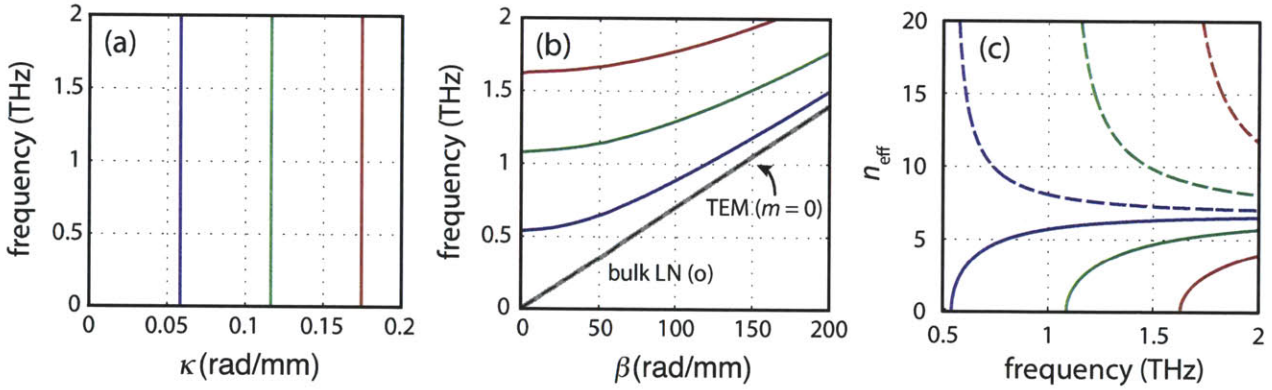

Figure 4-8: **TM dispersion curves and effective indices in a symmetric metal-clad waveguide.** For the lowest three TM modes ($\ell = 54$ μm): (a) The fequency-independent wave vector in the core, κ. (b) The waveguide dispersion curves (solid lines) and bulk dispersion curve of LN core along the extraordinary axis (dashed line). (c) The effective phase (solid) and group index (dashed) as a function of frequency.

However, the TM modes possess a special case, in that the lowest order TM mode, $m = 0$, is a TEM wave since it satisfies the previously described conditions: $E_y = 0$ and $H_y = 0$, while E_x and H_z are non-zero. This differs from the TE wave analog in the Sec. 4.2.1.2

where $m \neq 0$ and TEM mode solutions are not allowed since they cannot satisfy the required conditions without setting all fields to zero ($\vec{E}(x) = 0$ and $\vec{H}(x) = 0$). The TEM mode has no cutoff frequency. Additionally, TEM modes have perfectly linear dispersion, coinciding with the bulk dispersion curve in LN along the ordinary axis; since $\kappa = 0$, then in accordance with (4.1b): $\beta = \omega n_o/c$. It follows that both the group and phase velocities are equal to c/n_o. This means that the TEM wave travels through the waveguide at the speed of light in the medium, LN, *without* bouncing back and forth between the two metal boundaries. This differs from the higher order TM modes that have nonzero k_x components. Another implication is that the TEM modes have no dependence on the transverse x-coordinate, such that the E-field (from (4.22)) and H-field (from (4.14)) profiles are constant across x in the core. The E-field is given as:

$$\vec{E}(x) = \hat{x} D_0/\varepsilon_o = \hat{x} E_0 \tag{4.20}$$

and consequently the H-field is:

$$\vec{H}(x) = \hat{z} \frac{\beta}{\omega \mu_0} E_0 \tag{4.21}$$

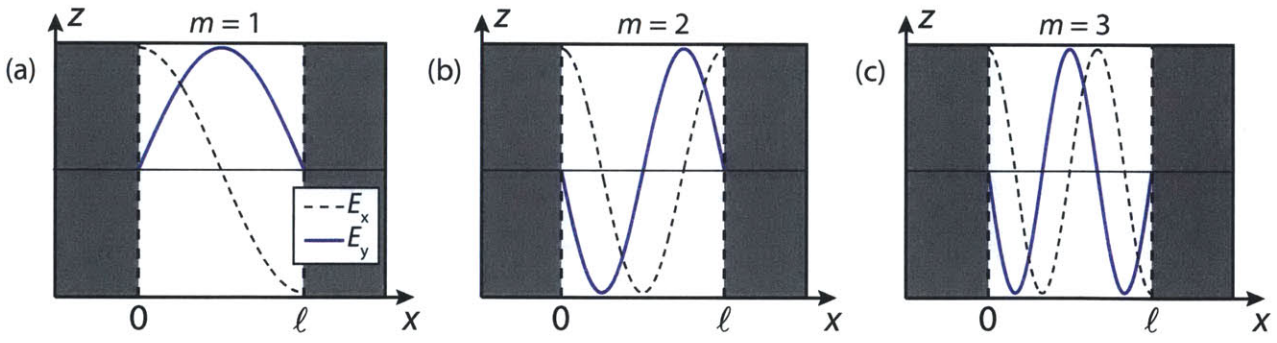

Figure 4-9: **TM modes in a symmetric metal-clad waveguide.** The lowest three TM E-field profiles (E_x and E_y) of (a) $m = 1$ mode, (b) $m = 2$ mode, (c) $m = 3$ mode.

The TM waveguide mode profiles (for $m > 0$) are solved for explicitly in the core as

follows where $A = 1/2$:

$$\vec{E}(x) = \frac{D_0}{\sqrt{\beta^2 + \kappa^2}} \left\{ i\hat{y} \left(\frac{\kappa}{\varepsilon_e} \sin(\kappa x) \right) - \hat{x} \left(\frac{\beta}{\varepsilon_o} \cos(\kappa x) \right) \right\} \quad 0 \leq x \leq \ell \tag{4.22}$$

The mode profiles of the lowest three TM waveguide modes (excluding the $m = 0$ mode) are shown in Fig. 4-9.

4.3 ITO-coated Planar Waveguides

In the polaritonics platform, metals are an important class of materials because of their strong interactions with light and unique optical properties. Metal microstructures can be used, for example, to enhance E-fields and localize light well below the diffraction limit [7, 17, 75, 76], or to modify the effective dielectric properties of a substrate such as in metamaterials [77]. Solid sheets of metal modify boundary conditions and dispersion of waveguides [78]. A drawback to using conventional metals on the polaritonics platform, however, is that they are opaque to optical light and thus the THz fields underneath the metal microstructures cannot be visualized. Here we investigate the potential for the optically transparent electrical conductor ITO to substitute for ordinary metals in the polaritonics platform.

Transparent ITO films have convenient applications as transparent electrodes in flat panel displays and solar cells or as the anode contact in organic light-emitting diodes, which exploit the relatively high carrier concentration in the n-type semiconductor. The bandgap in ITO is $\sim$ 3.5-4.3 eV [79], too large to permit the absorption of visible photons, giving rise to its optical transparency, but ITO is opaque to ultraviolet light due to valence band to conduction band absorption. More relevantly, ITO displays metal-like behavior at THz frequencies [80] as a result of free carrier absorption that occurs within the conduction band itself.

4.3.1 Experimental Setup

The ITO-coated waveguides were fabricated by temporary attachment of a delicate, 54-μm thick x-cut LN slab (10 × 11 mm) to a silicon wafer with a thin layer of photoresist. Following this, a 2.7-μm-thick film of ITO (10wt% of SnO_2) was sputtered in a square pattern (5 × 5 mm) onto part of the slab as shown schematically in Fig. 4-10. Annealing the sample at 400°C for one hour in a nitrogen atmosphere increased the DC conductivity of the ITO, as measured with a four-point probe, from $\sigma_{dc} = 1.7 \times 10^{-2}$ S/cm to 2×10^2 S/cm. Although the attained conductivity was low compared to ITO films often claimed in literature ($\sigma_{dc} \sim 10^4$ S/cm [81]), it is sufficiently high to waveguide THz fields with behavior expected for metal-clad waveguides as will be described below. The ITO layer was optically transparent, evident by the optical image shown in Fig. 4-11(a).

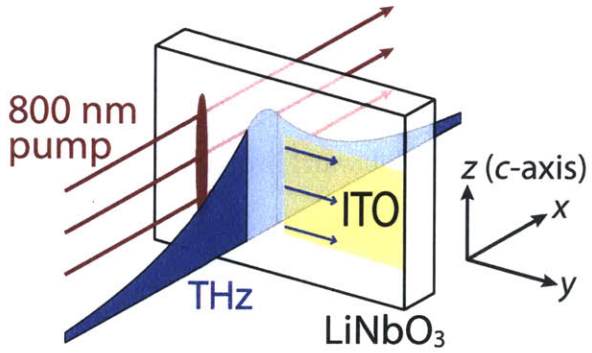

Figure 4-10: **A schematic illustration of the ITO-coated waveguide on the polaritonics platform.** A 2.7-μm-thick film of ITO is deposited on one side of a thin slab of $LiNbO_3$. The laterally propagating THz wave interacts with the modified LN waveguide (i.e. the asymmetric metal waveguide), which has different propagation properties compared to a plain slab.

The NIR pump pulse (1.5 mJ, 80 fs, 800 nm center wavelength, 1 kHz repetition rate from a Ti:sapphire regenerative amplifier) was focused to a vertical line with a cylindrical lens to generate a pair of broadband counterpropagating, initially single-cycle THz waves in the slab that travel perpendicular to the line focus (see Fig. 4-11(b)). TE modes (E-field polarized along the direction of the line focus) were generated when the pump light polarization and optic c-axis (z-axis in Fig. 4-10) of the LN crystal were aligned along the

direction of the line focus and perpendicular to the THz wave propagation direction (y-axis). TM modes (E-field polarized out of the plane of the slab and along the THz wave propagation direction) were generated when the light polarization and c-axis were parallel to the propagation direction [39]. In both cases, the optical probe pulse (200 nJ, 100 fs, 532 nm center wavelength generated with a non-collinear optical parametric amplifier) was polarized at a 45° angle relative to the c-axis of LN. The sample was imaged onto a camera in the polarization gating configuration [4], where phase information in the sample was converted into amplitude information at the camera with the appropriate polarization optics. The image resolution was 5 μm and the magnification of the system was 3.3×.

4.3.2 Data Analysis and Discussion

4.3.2.1 Dispersion of Bound Modes in ITO Waveguides

Figure 4-11(b) shows a selection from the complete set of recorded THz E-field images at a series of pump-probe time delays. The leftward propagating wave travels unimpeded through the uncoated slab. Part of the rightward propagating wave reflects off the edge of the ITO-coated region of the slab (dashed white line in Fig. 4-11(a)), and the rest propagates under the optically transparent ITO layer. THz E-fields underneath the ITO are directly and clearly observed. For each image in the series (i.e. each time delay) we averaged over the uniform, vertical dimension, conserving the information in the lateral propagation direction, and placed the resulting vectors in different rows of a matrix. The compiled space-time plot, shown in Fig. 4-11(c), compactly shows the full evolution of the THz E-field, where dispersion, interference, and reflection of the waveguide modes are apparent.

An experimentally measured dispersion curve can be calculated by taking the 2D Fourier transform of a space-time plot like the one in Fig. 4-11(c). Figure 4-12 shows the dispersion curves determined for TE and TM modes. Analytical waveguide dispersion curves for ideal metal-coated LN derived in the previous section are overlaid on the experimental results.

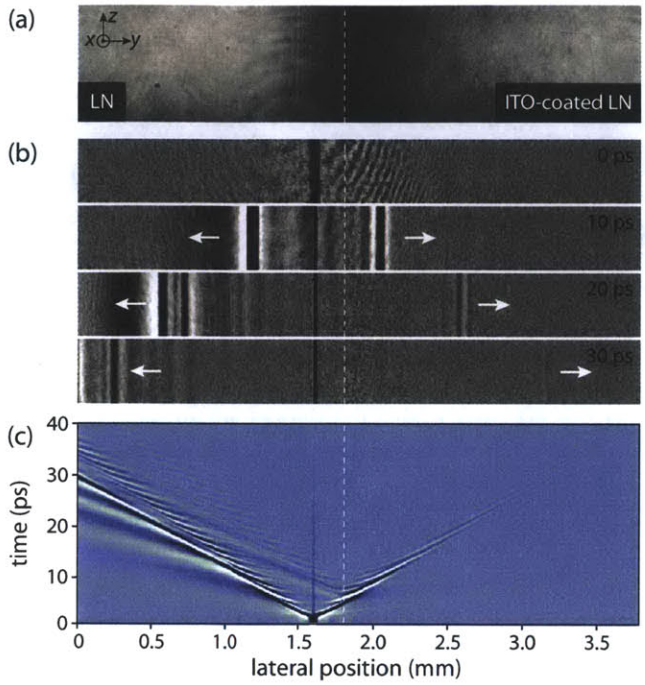

Figure 4-11: **Experimental image processing.** (a) A raw image of an ITO-coated slab of LN (right side) that demonstrates the optical transparency of the ITO. The vertical dashed line represents the separation between uncoated LN (left) and ITO-coated (right) areas. (b) A time series of images of a TE mode THz E-field, collected using polarization gating imaging. A signal image $I(y, z, t)$ recorded at variable time t following THz field generation by the pump pulse was divided by a reference image $I_0(y, z, t)$ recorded with the THz field absent and $[(I - I_0)/I_0](y, z, t)$ was determined to produce the images shown. The THz E-field is directly proportional to $\Delta I/I_0$, (c) THz E-field evolution as a function of space and time derived from averaging over the vertical dimension of a series of images including those in (b).

For a LN waveguide with ITO coated on one side, the experimental TE dispersion curves in Fig. 4-12(a) demonstrate good agreement with theoretical solutions for the perfect metal analog. The cutoff frequency, evident at 270 GHz, is a feature that is non-existent in uncoated dielectric waveguides. The TM modes in Fig. 4-12(b) however, do not have a cutoff frequency. The calculated transverse field profiles for the two lowest order TE and TM modes at 1 THz are shown in the inset of Fig. 4-12(a) and (b), respectively. We expect a potential for further dispersion control in on-chip THz components including the extension to a symmetric metal-waveguide geometry for both TE and TM mode excitations (see Sec. 4.2. For the following analyses, we focused exclusively on the TE modes since the generation efficiency in the

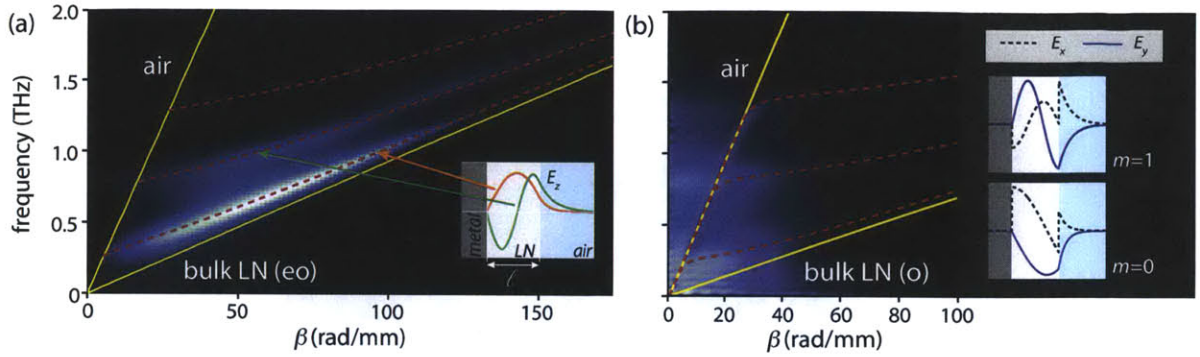

Figure 4-12: **TE and TM dispersion curves in asymmetric ITO waveguides.** Waveguide modes in a LN waveguide (thickness $\ell = 54$ μm) with ITO deposited on one surface. Dispersion of air and bulk LN extraordinary (eo) and ordinary (o) waves are shown in yellow. Analytical solutions in dashed red are overlaid on the experimentally observed results. The insets show cross-sectional views of the slab. (a) TE modes. Inset: calculated E_z-field profiles of the two lowest order TE modes at 1 THz. (b) TM modes. Inset: calculated E_x and E_y-field components of the two lowest order TM modes at 1 THz.

crystal was higher than that of TM modes [39].

4.3.2.2 Leaky Waves in Asymmetric ITO Waveguides

The advancement in optical waveguide technology spurred the development of many sophisticated computation algorithms for modeling of waveguide behavior. These numerical solvers such as finite-difference [82] or finite-element [83] have the ability to calculate the modes and complex propagation constants in the waveguides. However, there is little understanding of the physical meaning of complex propagation constants that correspond to the leaky modes in a waveguide that exist even in the absence of material damping [84]. The numerical solvers discover the leaky modes if the constraint that the modes are true eigensolutions of the waveguide are relaxed and so the initially generated leaky modes represent 'almost' guided solutions. Experimentally, leaky waves were first observed in 1961 at microwave frequencies with an electric line source over a grounded dielectric slab waveguide [85].

Physical interpretation of guided modes in Fig. 4-13(a) is straightforward since the waves evanescently decay in the cladding (purely imaginary wave vector) and oscillate in the core (purely real wave vector for a lossless material). Leaky modes in Fig. 4-13(b), however, are

difficult to interpret because the wave vectors are complex and lead to unphysical behavior at the limits $x \to \pm\infty$; they have been deemed 'improper modal solutions' to the waveguide. The solution was demonstrated to be physical in restricted regions of propagation where the exponentially growing field has a finite amplitude by using a simple ray picture [86]. Leaky waves have complex propagation constants in the longitudinal and transverse directions, which mean that they attenuate as they propagate longitudinally and they exponentially grow transversely. In contrast, surface waves are proper modal solutions that have pure attenuation in the transverse direction. In general, the theory of leaky waves is more complicated than that of surface waves, but leaky waves present new, interesting capabilities for integrated optics applications. For example, leaky waves have a longitudinal phase velocity greater than the speed of light, whereas surface waves are slow. Leaky waves are also not bound to the surface and so they can radiate out of the waveguide, unlike surface waves [85].

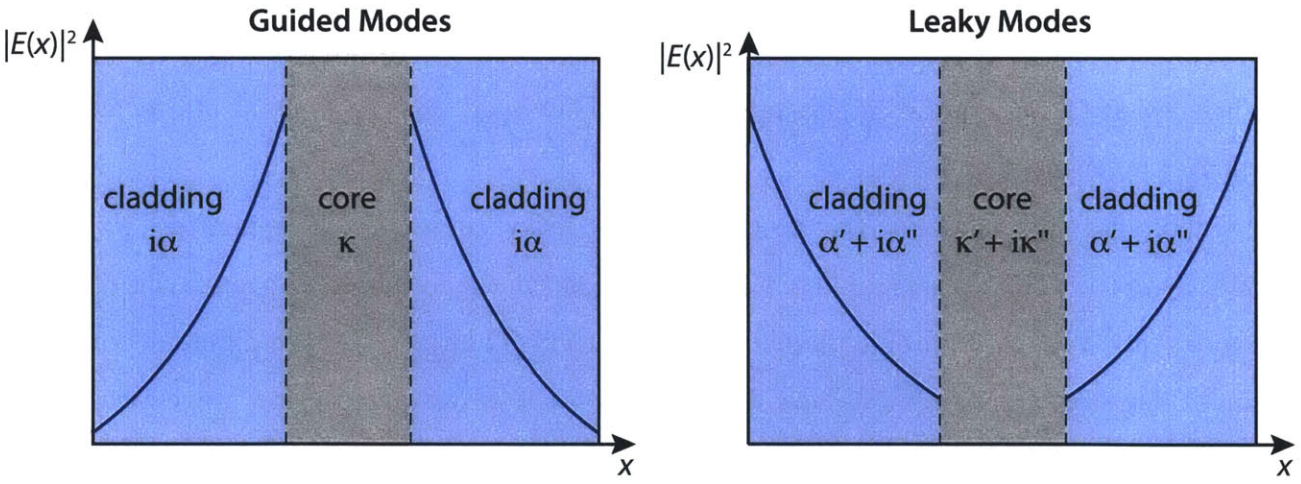

Figure 4-13: **Guided and leaky waveguide modes.** The mode power, $|E(x)|^2$, along the transverse direction of a 1D waveguide for (a) the guided modes, which have a purely real propagation constant, $k_x = \kappa$, in the core and purely imaginary propagation constant, $k_x = i\alpha$, in the cladding such that the wave decays to zero at $x \pm \infty$. (b) the leaky modes that have complex propagation constants in the cladding and core, where the wave in the cladding grows exponentially at $x \pm \infty$. This is an unphysical solution in general, but it is valid under some restricted regions of propagation.

In Figure 4-12(b), there are some signals detected due to "leaky" modes, i.e. unbound modes that lie outside the light lines in the dispersion curves [84]; these are not eigenmodes

of the system, and therefore are not guided within the structure. In particular, leaky modes outside the light line of air exist, in addition to the bound TM modes, and thus have phase velocities faster than the speed of light. Firstly let us consider the bound TM modes that are waveguided in the slab by total internal reflection (TIR) at the air-LN interface and the metal cladding. The bound modes have the ability to propagate indefinitely (neglecting material damping) since they are perfectly reflected at every interface. The dispersion curves of the bound modes are given as the dashed-red lines in Fig. 4-14(a). In the corresponding space-time plot in Fig. 4-14(b), we observe a portion of modes that have linear dispersion, traveling at the speed of light in air, and also a portion of modes that approach the light line of the ordinary axis of LN. However, any waveguide, regardless of the specifics of the cladding or core materials, possesses leaky modes that exist from partial reflections off the core-cladding interface [87]. Leaky modes are not bound and propagate at an angle less than the critical angle for TIR at the air-LN interface. Every successive reflection off the LN-air interface results in progressive leakage of amplitude, while we assume reflection with perfect efficiency at the LN-metal interface; in reality, ITO is an imperfect metal and constitutes another interface with leakage.

We found that the only way to generate the leaky modes was to generate THz waves directly in the ITO-coated region of the slab (and not in the uncoated slab since this required appropriate THz mode-profile matching to cross the ITO interface where different boundary conditions were imposed). We excited the leaky TM waves at very low wave vectors, as seen in Fig. 4-14(a), by using a loosely focused optical pump (width on the order of $\sim$ 100 μm). In order to increase the visibility of these modes, we isolated the leaky modes that appear at different regions of the dispersion curve. We did this by Fourier filtering the appropriate portion of the dispersion curve, the air light cone, in Fig. 4-14(c) and then inverse Fourier transforming back to the time-domain to study the propagation in the space-time plot in Fig. 4-14(d). Careful consideration of the results is needed since the Fourier filtering introduces an artifact that corresponds to the sharp contrast introduced in the

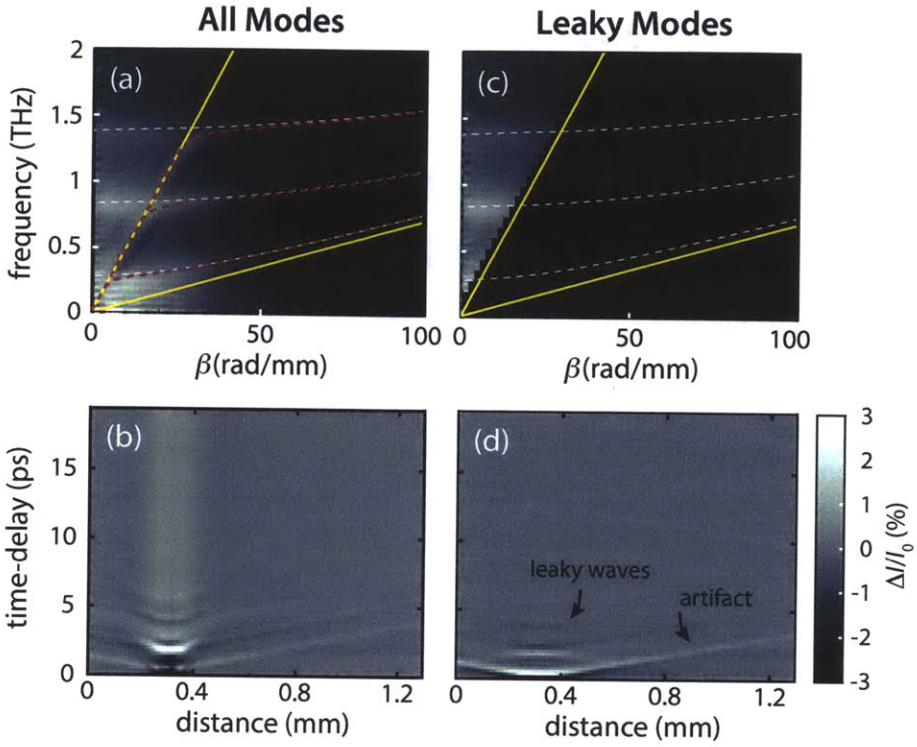

Figure 4-14: **Leaky TM waves in asymmetric ITO waveguides.** (a) The experimental dispersion curves for the TM modes in an asymmetric metal waveguide of thickness $\ell = 54$ μm, with the calculated solutions (dashed red) overlaid. The solutions of the symmetric modes of a symmetric metal waveguide for a waveguide of thickness 2ℓ. The corresponding space-time plot is shown in (b). (c) The Fourier filtered dispersion curve of the leaky modes that lie above the light line of air with near zero group velocity. The corresponding Fourier filtered space-time plot in (d) shows the leaky waves that oscillate in time but propagate short distances.

Fourier filtered dispersion curve along the light line; the artifact appears in the space-time plots, which denoted in Fig. 4-14(d). From the space-time plot, the leaky modes did not propagate appreciably from the generation region, but still oscillate in time, before decaying due to Fresnel losses across the interface. Similarly, the leaky waves show close to zero group velocity, observed from the small slope in the dispersion curves.

In terms of modeling our observation of the leaky waves, if we assume that the wave does not immediately leak out but instead partially reflects off the LN-air interface, the waveguide system resembles a symmetric metal waveguide, derived in Sec. 4.2.2.2. We found that the leaky modes have the same dispersion characteristics as the odd order modes (symmetric

in E_y) in a symmetric metal waveguide of twice the thickness, which are overlaid as the white-dashed lines in Fig. 4-14(a) and (c); this is similar to the conclusion derived for the bound TM modes in the asymmetric waveguide in Sec. 4.2.2.1 that had identical dispersion to that of the asymmetric bound modes in plain slab LN of twice the thickness. The overlaid plots only allude to the real part of the propagation constant because leaky waves have complex propagation constants. The imaginary part of the propagation constant is the decay constant or the inverse of the $1/e$ propagation distance, which has been calculated for a slab waveguide by Hall and Yeh [88]. Haus and Miller describe the leaky modes as being analogous to resonant states in a Fabry-Perot cavity, which exist when the cavity length is an integral number of half wavelengths [87]. The symmetric modes in a Fabry-Perot cavity have the relationship:

$$m(\lambda/2) = L, \tag{4.23}$$

where $m = 1, 3, 5, \cdots$. This solution is analogous to the modes that have symmetric transverse field profiles in E_y in a symmetric metal waveguide (see Fig. 4-9). The incident and reflected waves at either metal interface are 180° out-of-phase and consequently destructively interfere and hence satisfy the boundary conditions. However, in an asymmetric metal waveguide, a wave incident at the LN-air interface experiences no phase shift since it is moving from higher to lower refractive index. The boundary condition at the LN-metal interface is therefore only satisfied by a round trip of a wave (i.e. LN-metal $\rightarrow$ LN-air $\rightarrow$ LN-metal). Consequently, the condition that must now be satisfied is:

$$m(\lambda/2) = 2L, \tag{4.24}$$

where $m = 1, 3, 5, \cdots$. This solution corresponds to the symmetric modes of a symmetric metal waveguide of twice the thickness. Only the symmetric modes survive since the reflected waves off the LN-air interface are in-phase with the incident wave and constructively interfere

(see Fig. 4-15(a)). In contrast, the waves of the antisymmetric modes, with an integer number of full wavelengths, reflect off the LN-air interface 180° out-of-phase with the incident wave across its entire transverse dimension and so the incident and reflected waves completely cancel everywhere due to destructive interference (see Fig. 4-15(b)).

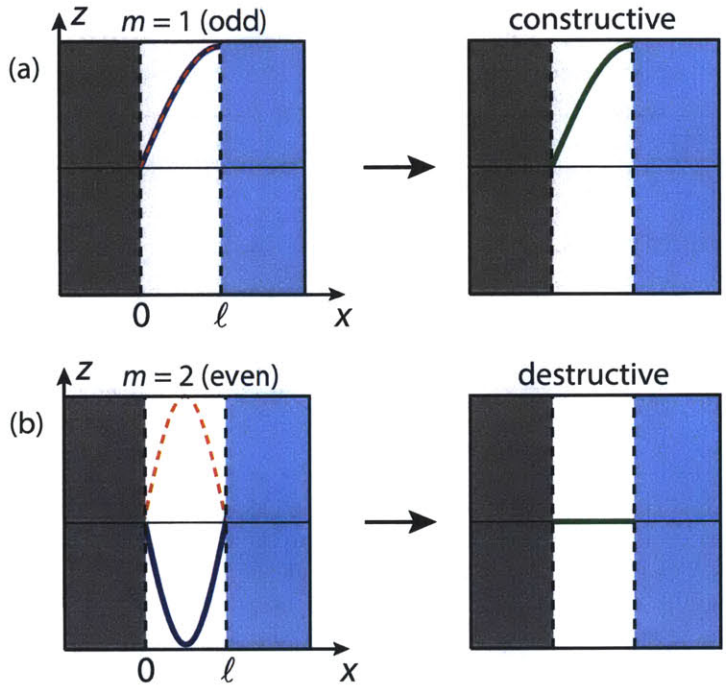

Figure 4-15: **Leaky waves resemble Fabry-Perot cavity modes.** (a) For a single-sided metal waveguide, the leaky waves resemble the odd order modes ($m = 1, 3, 5, \cdots$) in a Fabry-Perot cavity (of twice the thickness) that have symmetric transverse field profiles. This schematic illustration demonstrates constructive interference between incident and reflected waves off the LN-air interface for the $m = 1$ mode. (b) In a single-sided metal waveguide, none of the leaky modes resemble the even order modes ($m = 2, 4, 6, \cdots$) of a Fabry-Perot cavity that have asymmetric transverse field profiles. This schematic illustration shows purely destructive interference between the incident and reflected waves off the LN-air interface for the $m = 2$ mode.

The number of reflections before the TM wave decays may be approximated by calculating the reflection coefficient in moving from medium 1, LN, to medium 2, air [89]:

$$\Gamma^{(1)} = \frac{\sqrt{1-\sin^2\theta_1} - \sqrt{1-\sin^2\theta_1\left(\frac{n_1^2}{n_2^2}\right)}\frac{n_1}{n_2}}{\sqrt{1-\sin^2\theta_1} + \sqrt{1-\sin^2\theta_1\left(\frac{n_1^2}{n_2^2}\right)}\frac{n_1}{n_2}} \tag{4.25}$$

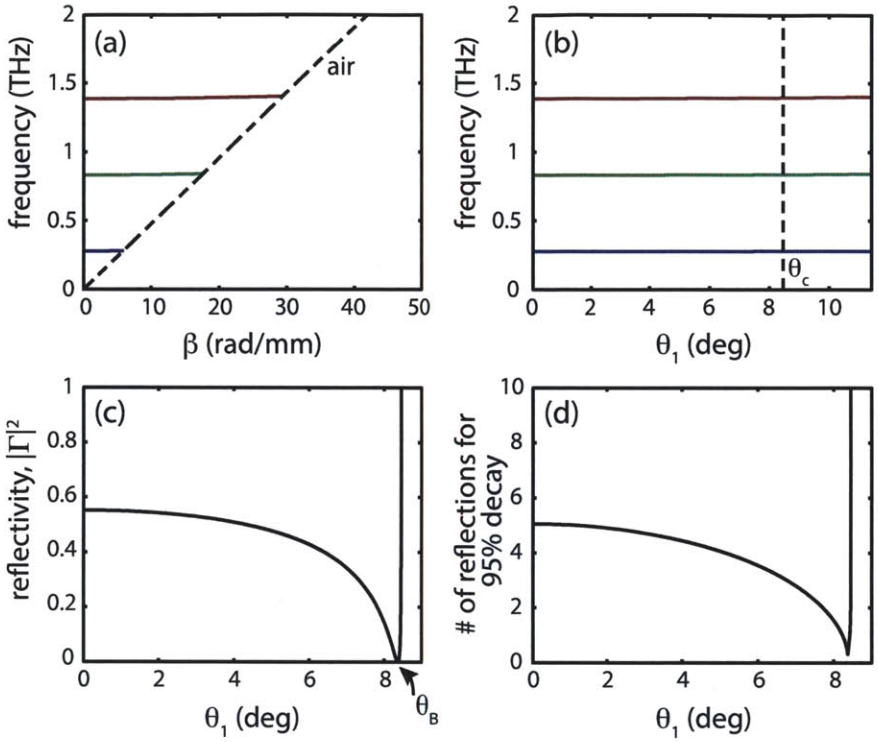

Figure 4-16: **Propagation of leaky TM waves.** (a) The calculated real part of the dispersion curve for the lowest three symmetric modes in a symmetric metal waveguide, corresponding to the leaky TM modes, and the air light line. (b) Calculated incidence angle, θ_1, at the LN-air interface for the lowest three leaky modes. The critical angle $\theta_c = 8.46°$. (c) The reflectivity as a function of incidence angle. The Brewster angle, $\theta_B = 8.37°$, indicates where there is no reflection. Above the critical angle, no leaky waves exist. (d) The number of reflections off the LN-air boundary before the wave decays to 5% of its initial value as a function of incidence angle.

where θ_1 is the angle of incidence in medium 1 relative to the normal of the interface, $n_1 = n_o$, and $n_2 = 1$. The angle of incidence of the leaky waves can be calculated directly from the calculated values of β and κ for a symmetric metal waveguide of thickness 2ℓ using (4.19):

$$\theta_1(\omega) = \tan^{-1}\left(\frac{\beta(\omega)}{\kappa}\right). \tag{4.26}$$

The propagation constants, β, for the three odd order modes (i.e. $m = 1, 3, 5$), which correspond to $\mathrm{Re}(\beta)$ of the leaky modes, are shown in Fig. 4-16(a), and the corresponding angle of incidence at the waveguide interface for these modes are shown in Fig. 4-16(b). The

critical angle, θ_c, at the LN-air interface for TM modes with H_z along the ordinary axis is 8.46°. Above θ_c, the leaky waves by definition cannot exist since they are not bound. In our results, we observe a feature that loosely resembles an 'avoided crossing' in the dispersion curves in Fig. 4-14(a), where there is a reduced intensity of modes between the leaky and guided modes that agrees well with the onset of an incidence angle larger than the critical angle. The reflectivity, $R = |\Gamma|^2$, is straightforward to calculate using (4.25). Because the angle of incidences for all the modes shows the same flat structure, only one TM reflectivity plot is shown in Fig. 4-16(c), where at angles less than the Brewster angle, $\theta_B = 8.37°$, the reflectivity is less than 55%. The number of reflections off the LN-air interface (assuming perfect reflection off the metal interface) until the wave is attenuated by 95% (or 5% of its maximum value) is shown as a function of θ_1 in Fig. 4-16(d); at angles less than the Brewster angle, the leaky waves reflect a maximum of 5 times off the LN-air interface at normal incidence (i.e. no forward propagating component) and even less at other incidence angles.

4.3.2.3 Reflection Efficiency and Resistive Damping in ITO Waveguides

In order to demonstrate the reflection efficiency over a range of frequencies, we used a thinner LN slab ($\ell = 30$ μm) with ITO coated on one side so that the cutoff frequency fell well within our THz pulse bandwidth and strong signals could be observed at lower frequencies. We generated a low frequency, TE-polarized, narrowband THz wave using a tilted optical pulse front [50]. This generation method, in which the optical pump profile moves laterally along with the THz wave for several millimeters at the speed of a selected frequency component, allows for high spectral brightness at this frequency, which was tuned to 0.25 THz, far below the cutoff frequency of 0.50 THz. The resulting multicycle THz wave images are compactly represented in the 2D space-time plot in Fig 4-17(a). A majority of the incident field is reflected, but it is clear that a significant portion is also lost, possibly through scattering off

the interface into free space. There is a small transmitted component that can be observed, which corresponds to both evanescent waves below the cutoff frequency and also a weakly excited bound mode at 1.2 THz due to the nature of the phase-matched generation process.

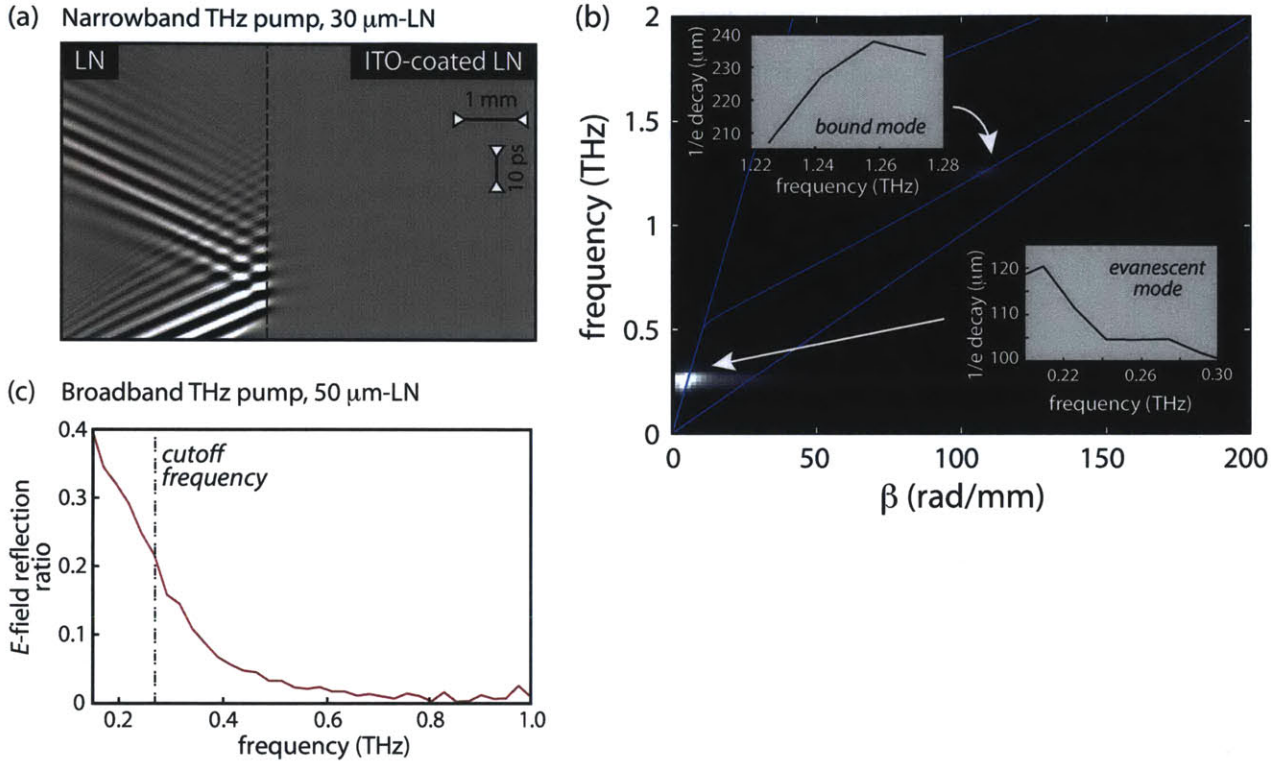

Figure 4-17: **Reflection efficiency of TE waves in asymmetric ITO waveguides.** 2D space-time plot of an asymmetric ITO-clad slab of thickness 30 μm, with the incident THz frequency tuned to 0.25 THz, well below the cutoff frequency at 0.50 THz. (b) The dispersion curve for the narrowband space-time plot in (a). The decay lengths are shown for the evanescent mode below the cutoff frequency and the bound mode at 1.2 THz. (c) The frequency-dependent amplitude reflection coefficient for a THz E-field incident from an uncoated region of a 54-μm thick LN slab onto an ITO-coated region.

The frequency-dependent $1/e$ decay lengths of the modes can be found by firstly Fourier transforming along the time axis of the space-time plot to yield frequency vs. time and then extracting the decay constant, α, following an exponential fit of the E-field to $E \propto E_0 e^{-\alpha y}$. In Fig. 4-17(b), we calculated the decay lengths for the evanescent waves to be less than 120 μm. They show a roughly $1/\sqrt{f}$ scaling that is similar to that of a skin depth of a material, in this case governed by the boundary conditions of a waveguide. Alternatively, the bound

mode is an allowed mode that is able to propagate and carry energy, and has a decay length roughly twice as large. The decay length appears to increase monotonically with frequency, which is more indicative of other loss mechanisms such as resistive material or scattering losses in ITO or LN.

Returning to the broadband signals in the 54-μm thick LN slab, we show a more comprehensive frequency-dependent reflection ratio in Fig. 4-17(c). We calculated the frequency-dependent E-field reflection ratio for the lowest waveguide mode using the incident and reflected waves near the ITO interface as seen left of the dashed line in Fig. 4-11(c). Even below the cutoff frequency (vertical dot-dashed line in Fig. 4-17(c)), the reflection ratio is only in the 20-40% range. Approximately 60-80% of the field (or $\sim 85-95\%$ of the energy) is scattered into free space or transmitted into the metallic waveguide. Above the cutoff frequency, there is incomplete transmission of the field across the interface, but the reflection ratio for the bound modes continuously drops, reaching nearly zero by 600 GHz.

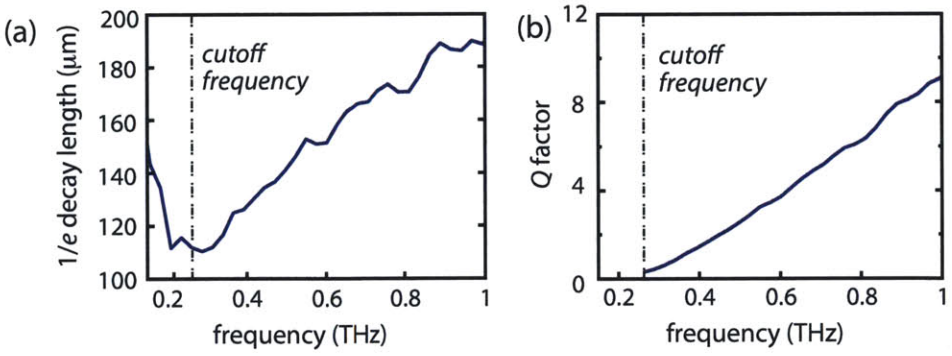

Figure 4-18: **Decay length and Q-factor of TE waves in an asymmetric ITO waveguide.** (a) The $1/e$ decay length as a function of frequency. (b) The frequency-dependent quality factor (Q) for propagation in the ITO-coated region of the bound TE modes.

It is evident from Fig. 4-11 that the field that is transmitted into the ITO-coated region suffers far stronger loss at all frequencies than the field in uncoated LN. Figure 4-18(a)

displays the attenuation length and also the quality factor Q given by:

$$\begin{aligned} Q(\omega) &= \omega\tau(\omega)/2 \\ &= \beta(\omega)d(\omega)/2 \end{aligned} \tag{4.27}$$

where the envelope of the E-field at radial frequency ω decays exponentially as $E(t) \propto E_0 \exp(-t/\tau)$. Equivalently, the Q-factor can be calculated from the decay length, d, from the transmission of the field in the ITO-coated slab and the propagation constant, $\beta(\omega)$, that were previously calculated for the bound modes. The low Q-factor is indicative of extremely strong damping of the bound modes at all frequencies where resistive losses dominate.

In general, the results show that our ITO layer is a relatively poor metal in the THz frequency range, as it is according to DC measurements. For comparison, the DC conductivity of gold is 4.10×10^5 S/cm [90]. We note that some resonant structures of practical interest have extremely strong radiative damping, and in those cases it may be possible to use ITO for metallic coatings in THz devices. For example, measurements have shown that $Q \sim 1$ for a gold dipole antenna at 255 GHz [7] and $Q \sim 4$ for a gold split-ring resonator at 1 THz [91]. For such functionalities, even quite high resistive loss could be tolerated.

4.3.3 Conclusions

In conclusion, direct visualization of THz wave propagation and dispersion in ITO-clad LN waveguides has been carried out, revealing bound waveguide modes, leaky modes, and near-field evanescent waves. Direct observation of leaky modes and near fields in the THz polaritonics platform may be exploited for characterization of a wide range of photonic devices. This may enable detailed testing of device designs even if other metals besides ITO are preferred for practical implementation. Study of THz fields in metamaterial structures such as dipole antennas and split-ring resonators, with direct visualization in the metal-coated regions as well as the near fields between them, may also be possible.

The results showed that the 2.7-μm-thick ITO film used in our structure behaves as a poor metal at THz frequencies. It is possible that improved deposition methods may yield ITO films with higher THz conductivity and lower loss, widening the range of waveguide applications that exploit the optical transparency and THz metallic properties of ITO. Extensive control over the waveguide behavior including dispersion and radiative coupling of leaky modes can be achieved by varying the slab thickness, THz polarization, and coating of the metal onto one or both slab surfaces. Despite its high losses, ITO-coated LN exhibited sufficiently high Q for applications in which optically transparent, highly radiative resonant structures are desired in the THz frequency range.

Chapter 5

Single-shot THz Detection

Multidimensional spectroscopy at visible and infrared frequencies has opened a window into the transfer of energy and quantum coherences at ultrafast timescales. For these measurements to be performed in a manageable amount of time, one spectral axis is typically recorded in a single laser shot. An analogous rapid-scanning capability for THz measurements will unlock the multidimensional toolkit in this frequency range. Here we first review the merits of existing single-shot THz schemes and discuss their potential in multidimensional THz spectroscopy. We then introduce improved experimental designs and noise suppression techniques for the two most promising methods: frequency-to-time encoding with amplitude encoding spectral interferometry and angle-to-time encoding with dual echelons. The acceleration in acquisition time will compress day-long scans to hours, and hence presents a practical means for exploring many new multidimensional THz measurements.

5.1 Introduction

The advancement of terahertz (THz) spectroscopy has relied on the increasing sensitivity and resolution of optical detection methods for ultrafast THz waveforms. In this regime, THz

time domain spectroscopy (THz-TDS) is used to measure the full time-dependent waveform of the THz electric field (E-field) [92]. A common technique employs electro-optic (EO) sampling with a mechanical scanning delay-line [31]. This classic approach has its temporal resolution given by the probe pulse duration, which is typically much shorter than a THz period, and its time window set by etaloning effects in the EO detection crystal or the sample. Early THz-TDS focused on measuring the linear THz response of a system at equilibrium, but has since advanced to more complex pump-probe geometries capable of measuring dynamics of reversible processes following photoexcitation.

THz-TDS is limited, however, by its inherently multi-shot, scanning approach. The time-intensive nature of this method is unfeasible for the observation of rapid time dynamics of phenomena that are irreversible (e.g., material damage, irreversible chemical reactions, or structural phase transitions) or experiments that use THz sources with large shot-to-shot fluctuations. In addition, a scanning technique is impractical for low duty cycle experiments that use lasers or other THz sources with low repetition rates. These motivations have driven the development of THz single-shot diagnostic techniques up to now, but when used in conjunction with averaging, single-shot methods also have the potential to drastically reduce the time required to record high signal-to-noise ratio (S/N) scans.

One important class of experiments that will benefit from such a reduced scan time is multidimensional THz spectroscopy where a THz probe field is fully time-resolved as a function of pump-probe time delay. Here, the pump-induced response is measured as the time-evolution of the change in the THz probe spectrum. In general, multidimensional studies aim to uncover the relationships between different degrees of freedom in a system (nuclear, vibrational, rotational, or electronic) that are otherwise difficult to unambiguously isolate from the vast number of observed responses. There has already been an effort in this respect, for example in studying spin-spin couplings in complex molecular systems using 2D nuclear magnetic resonance spectroscopy [93], coherence transfer using 2D infrared vibrational spectroscopy in organic solutions [94], or 2D visible electronic spectroscopy for

studying electronic couplings in photosynthetic systems [95] and GaAs quantum wells [96] and exciton-phonon coupling in molecular aggregates [97].

In the THz regime, many studies only measure the average THz probe response (the peak or integrated power) at various pump-probe time delays. This approach has proven useful for measuring carrier dynamics using an optical pump in silicon on sapphire [98], microcrystalline silicon [99], graphene [100] and InAs/GaAs quantum dots [101] or carrier dynamics using a THz pump in semiconductors [102, 103]. Other examples include the study of optically pumped liquid solvation dynamics [104, 105] and an optically induced phase transition in vanadium dioxide [106]. An important distinction is made between these measurements and ones in which the THz probe is spectrally resolved for a limited number of fixed pump-probe time delays such as in the photoconductivity study of liquid n-hexane using a UV pump [107] and the determination of relaxation dynamics of carriers and excitons in GaAs-AlGaAs multiple quantum wells [108].

While these THz probe experiments are sufficient for observing dynamics, they lack the ability to deduce the extent of coupling between THz-resonant degrees of freedom; this would require a comprehensive study of a spectrally resolved THz probe as a function of a near-continuous sweep of pump time delays. More recently, there has been endeavor to perform true 2D THz spectroscopy to elucidate the coupling between electronic degrees of freedom in quantum wells and graphene [109–112]. However, the technological barriers in THz generation and detection have limited the measurement of THz nonlinear signals to this small subset of systems, which have relatively large transition dipole moments arising from strong electronic resonances. Additionally, an exciting area unique to the THz realm is the study of intermolecular and low-frequency intramolecular motion using multidimensional vibrational THz spectroscopy, but progress in this area is still in its early stages.

A class of materials that poses key challenges in the understanding of coherent coupling and energy transfer across many different degrees of freedom is energetic materials. In these systems, mechanical energy from a shock front is up-converted to high-frequency molecu-

lar vibrations that lead to initiation of a chemical reaction [113]. Comprehensive studies of the intricate vibrational couplings throughout such a system embody the motivation for development of 2D techniques across the electromagnetic spectrum. One study that has started to observe these couplings used 2D Raman-THz spectroscopy to observe the collective intermolecular modes of water molecules [114], but proved difficult to characterize the spectral response due to a limited observation temporal window. For low-frequency vibrational couplings, these nonlinear signals are even smaller than those observed in [109–112] and typically have narrower spectral features that are only resolved with sufficiently large time windows. Furthermore, all of these multidimensional THz time domain measurements require substantial scaling up of total experimental time with the number of time points (i.e. 1D scan: $\sim n$ time points, 2D scan: $\sim n^2$ time points, etc.), which makes faster acquisition techniques crucial for their practical implementation.

In view of the shortfalls of conventional scanning THz-TDS, a proposed detection scheme is one that accurately recovers the entire THz waveform in a single laser shot and has a sufficiently long time window to provide the desired resolution in the THz spectrum. Furthermore, under equal averaging times the S/N of the recorded single-shot THz trace should surpass that recorded using the traditional scanning method. Here, we will review a number of single-shot methods and compare them to traditional EO sampling, the gold standard for accurately recording THz traces. We compared the different single-shot methods based on their temporal resolution, time window, accurate reproduction of the THz E-field, and the anticipated S/N, and selected two of the most promising techniques to try experimentally: amplitude encoding spectral interferometry and dual echelons.

For these two single-shot methods, we constructed experimental setups that implemented balancing and high-frequency modulation of the pump for optimal noise suppression in addition to averaging. The designs allowed for rapid switching between single-shot detection and scanning delay-line detection without perturbing the THz generation so that we could directly verify the single-shot method's ability to accurately measure THz waveforms and

compare their S/N to that of the standard methodology.

5.2 Review of Existing THz Single-Shot Methods

To date there has been little emphasis on single-shot methods as reliable, quantitative and quick data acquisition techniques for spectrally resolving a THz probe field between 0.1-10 THz. Many of these single-shot methods have a tradeoff between fast experimental acquisition and some fundamental capabilities that will be discussed below. In this case, we deviate from the objectives of irreversible single-shot experiments or diagnostic techniques. While there still exist stringent noise floor requirements, there is also a new regime for acquisition. More extensive averaging to yield markedly improved sensitivity would enable the measurement of weak, but reversible phenomena, or small changes in strong signals where a large dynamic range is needed in addition to high sensitivity.

A worthwhile technique will not make major concessions compared to traditional delay-line EO sampling, in that the temporal resolution should be close to the transform-limited pulse duration, a sufficient observation temporal window must be available and straightforward incorporation of noise suppression techniques should yield high S/N. Optimally, the experimental geometry would allow the THz beam to be focused at the EO crystal for higher sensitivity and accuracy and not require routine and/or intensive calibration prior to the measurement. Figure 5-1 schematically compares conventional EO sampling in (a) to a selection of existing THz single-shot techniques in (b)-(f). For each method we will discuss temporal resolution, feasibility of a time window of 10 ps, ability to accurately record the THz waveform, practicality to implement balancing for noise suppression, and overall ease of implementation; the key characteristics are summarized later in Table 5.1 in Sec. 5.2.6.

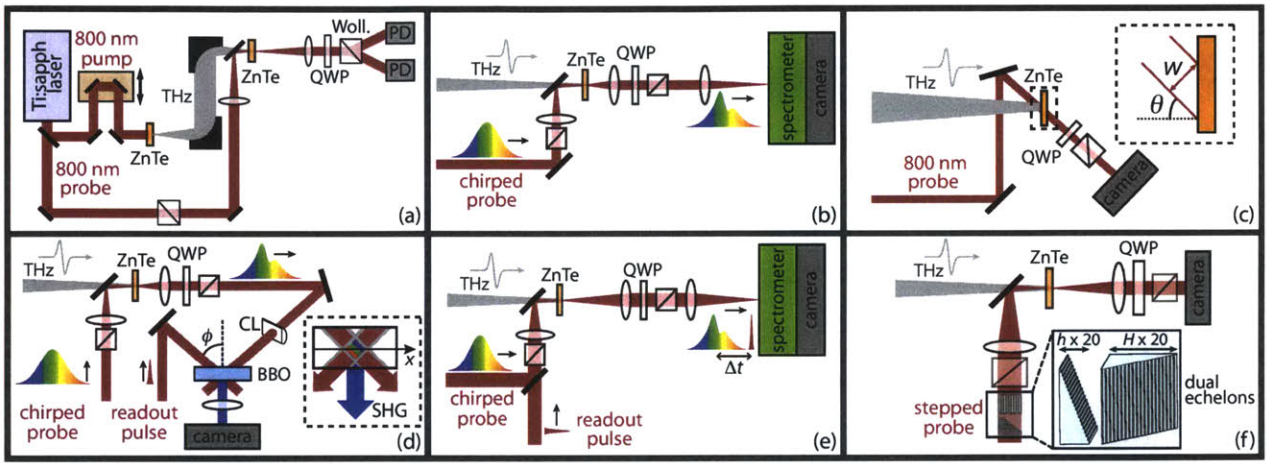

Figure 5-1: **Comparison of single-shot THz methods and conventional EO sampling.**(a) Conventional scanning EO sampling with balanced detection using a quarter-wave plate (QWP), Wollaston prism (Woll), and two photodiodes (PD). (b) Frequency-to-time mapping by spectrally encoding a THz pulse onto a linearly chirped probe in a collinear geometry. The chirped probe is then read out on a spectrometer. (c) Non-collinear crossing of an 800 nm probe pulse with an expanded THz beam at ZnTe detection crystal. The inset shows that crossing the probe beam an angle θ maps time delay to transverse position on the crystal, which is then imaged onto a camera. (d) Space-to-time mapping in time domain non-collinear SHG cross-correlation, in which a THz pulse is encoded onto a chirped probe as in (b). The THz-imprinted probe is then vertically focused to a line with a cylindrical lens (CL) and crossed with a short readout pulse in a SHG crystal at an angle of 2ϕ. The inset shows a zoomed in view of the intersection of the two beams in the SHG crystal, where different frequencies of the chirped probe map to different transverse positions. The spatial profile of the SH signal, $S(x)$, recovers the temporal intensity profile of the chirped probe, which is detected by a camera. (e) amplitude encoding spectral interferometry time delays a temporally short readout pulse by Δt relative to the chirped probe and subsequently detects a spectral interference at the spectrometer. A suitably short readout pulse sets the time resolution and recovers the envelope of the THz-imprinted chirped optical probe. (f) Angle-to-time encoding using two crossed glass echelon optics, each with 20 steps, to create a pulse train of 400 beamlets that are incrementally time delayed relative to one another. The beamlets and THz beam are collinearly focused to the same spot at the ZnTe cyrstal, but the beamlets are imaged to different locations on the camera. The detected grid pattern is made up of individual square regions that sequentially read out the THz waveform.

5.2.1 Frequency-to-time Encoding with a Chirped Probe

Fig. 5-1(b) illustrates the spectral encoding method, in which a linearly chirped probe pulse is used to yield frequency-to-time mapping of a THz waveform in a single laser shot [115]. As in EO sampling, the THz field modulates the chirped probe polarization, which upon passing through a polarization-sensitive analyzer is converted to an intensity modulation corresponding to the THz field. The chirped probe is directed into a spectrometer, where an intensity-modulated spectrum is detected on a camera.

A caveat exists however since allocating a single frequency component to a single time delay violates the uncertainty principle. While increasing the chirp elongates the time window, imprinting the THz field onto a narrower range of frequency components degrades time resolution [116,117]. The time resolution is given by $\sqrt{\tau_0 \tau_{ch}}$ where τ_0 is the transform-limited pulse duration and τ_{ch} is the chirped pulse duration; for example, a 100-fs transform-limited input pulse that is chirped to 10 ps results in a time resolution of 1 ps. Using a laser with larger bandwidth coupled with a higher chirp rate was proposed as a way to lead to better time resolution [115], although high-bandwidth lasers are less efficient for THz generation [103]. Alternatively, a distinct white-continuum probe pulse, independent of the pump arm, could be used. Moreover, in instances where the time resolution was insufficient for monitoring fast processes, the signal was shown to possess distortions depending on whether the THz fields were strong or weak compared to the background [118,119]. Only under strict conditions were these distortions eradicated, particularly by using a chirped probe pulse duration optimized for a fixed THz pulse duration [120], which only emphasizes the intricate balance between time resolution and the chirp rate.

Albeit the implementation of spectral encoding is technically the most simple, its most serious detriment is the degradation of time resolution along with the inherent limit on the temporal window for distortion-free measurements. In addition, the mapping assumes a linear relationship between temporal chirp rate and frequency, which if not satisfied re-

quires more careful characterization to avoid inaccuracies in recovering the THz waveform. The method is however capable of implementing balancing by introducing the bias with a quarter-wave plate and a polarizing beamsplitter. Consequently, the response is linear and quantitative compared to the initial demonstration in [115], which only used the inherent static birefringence in the EO crystal [46].

It was later proposed that the direct time-frequency mapping could be deconvolved with in-line spectral interferometry [121, 122], where the leak-through probe, resulting from static birefringence in the EO crystal or slight detuning of the crossed polarizers, interferes in the frequency domain with the amplitude-modulated signal. With no direct association of frequency to time, the analysis should recover a time-resolution inversely proportional to the full spectral bandwidth of the probe. However, this is a numerical reconstructive approach that relies on accurate characterization of the chirped probe pulse up to second-order dispersion (group delay dispersion). The method was experimentally demonstrated as a better diagnostic tool in terms of time resolution compared to spectral encoding, but ultimately the deconvolution algorithm is imperfect and introduces numerical artifacts that are not conducive to reliable spectroscopic applications. In addition, balancing cannot be implemented since the small bias necessary for large fringe contrast (i.e. for high sensitivity) can only be introduced and subsequently detected in one polarization state.

5.2.2 Space-to-time Encoding with Non-collinear Geometry or Collinear Tilted Probe Intensity Front

For a time-space encoding method of non-collinear crossing [123] or tilting of the optical probe intensity front with a prism or grating [124, 125], the transverse profile of the optical probe pulse samples the THz field at different times when they spatially overlap in the detection crystal as depicted in Fig. 5-1(c). The mapping between space-coordinate, x, to time-coordinate, t, is calculated geometrically, depending only on the angle θ between the

THz beam and the optical probe ($t = x\tan\theta/c_0$), where c_0 is the speed of light in vacuum. The time window, ΔT, is determined by the width of the probe beam, w, which along with θ, are adjustable parameters ($\Delta T = w\tan\theta/c_0$). For both of the described space-to-time encoding methods, a time window of 10 ps and 45° relative angle between the THz and optical beams requires a probe width of 3 mm.

In either the non-collinear or tilted pulse front geometry, there is minimal degradation of time resolution due to phase mismatch between the group index of the optical probe and the phase index of the THz field in the EO crystal [14, 126] since for most crystals the coherence length is large for a wide range of frequencies when $\theta \leq 45°$. Instead, the time resolution is dominated by dispersive propagation and absorption of the THz pulse in the crystal [126, 127]. In the case of using a collinear tilted pulse front, the angular dispersion introduced in the optical probe by dispersive elements typically increases the measured pulse duration, but this is relatively negligible for detection crystals thinner than $\sim$ 1 mm with a 50 fs transform-limited pulse [128]; the effect is exacerbated for thicker crystals and shorter initial pulse durations.

There are however several considerations for this geometry in terms of applying it toward sensitive THz spectroscopy. Firstly, attaining larger time windows requires that the focused THz spot size at the detector crystal increase accordingly to a width of $W = w/\cos\theta$ ($\sim$ 4 mm for the parameters given above) and diminishes the THz field by $1/W$. This metric of W though only serves as a lower bound since in reality an ultra-broad-bandwidth Gaussian THz pulse has both a spatially dependent E-field amplitude and spectral content due to diffraction [129]. In typical EO sampling, the spectrum of the THz field is essentially spatially invariant because the focused optical probe is much smaller than the THz spot size; for example, a THz field with a full width half maximum (FWHM) of 1 mm varies by less than 1% of its peak value for an optical probe focused to 40 μm. In the single-shot scheme, the corresponding THz beam size, W, to achieve a near uniform spectral distribution across the probe at the detection crystal is approximately 100 times larger with an expanded

optical probe of $W = 4$ mm. These concerns pose obstacles with regards to the complete mapping of nonlinear responses in multidimensional studies, where the preferred broadband THz probes [24,130] are generally weaker compared to tilted pulse front generation in lithium niobate that yields smaller bandwidth [16].

Consequently, in both the non-collinear geometry [123] and collinear tilted probe [124] methods, a crossed-polarizer configuration that exploits the small static birefringence in the nonlinear crystal was used in order to maximize the detected modulation depth [46]. The distortions introduced by detecting in the quadratic regime are small for weak signals, but typically an involved initial calibration is required that measures the nonlinearity of every pixel in the detector array [124]. While the calibration also reports on the THz beam's spatial profile, it only normalizes for amplitude variation across the THz focal spot and is unable to capture the spectral variation. Nonlinear detection schemes often have non-trivial balancing implementation or completely lack the ability as a trade-off for larger signals, and so the shot-to-shot changes in the spatial beam profiles cannot be suppressed. Overall, the single-shot method has demonstrated merits for linear spectroscopy in systems where the absorptions are strong, but the barriers discussed hinder its practical implementation in nonlinear spectroscopy.

5.2.3 Space-to-time Encoding with Time Domain Non-collinear Second-harmonic Cross-correlation

In this technique the THz signal is first imprinted on a chirped optical probe pulse like in Sec. 5.2.1. However, in this case the time profile of the probe is read out by crossing it at angle 2ϕ with a short recross-correlationadout pulse in a β-barium borate (BBO) crystal to produce a type I second-harmonic (SH) signal as shown in Fig. 5-1(d) [131]. The crossing of the two beams at an angle maps time delay onto transverse position, where different frequencies of the chirped pulse are projected onto different locations at the BBO crystal

(see inset of Fig. 5-1(d)), similar to that in a single-shot optical autocorrelator [132]. The spatial profile of the SH beam, $S(x)$ is recorded on a CCD array, which is represented as an intensity cross-correlation between the two pulses: $S(x) = \int_{-\infty}^{\infty} I_{\rm ch}(\tau) I_{\rm r}(t+\tau) d\tau$, where $I_{\rm ch}$ and $I_{\rm r}$ are the intensities of the chirped probe pulse and short readout pulse, respectively. For a suitably short readout pulse, $S(x)$ gives the temporal intensity profile of the chirped probe since $\lim_{I_{\rm r}(t)\to\delta(t)} S(x) = I_{\rm ch}(t)$. The time window is given by $\Delta T = 2w \sin\phi/c$ and directly depends on the spatiotemporal overlap of the two beams across a width, w, in the BBO crystal, where ϕ is the angle in free space. For a 10 ps window at an angle of 15°, the overlap width needs to be $\sim$ 6 mm.

Although similar to the space-to-time mapping described in Sec. 5.2.2, this method does not require any prior calibration of the THz spatial profile across the detector crystal, consideration of spectral variation, or an expanded THz spot size. This is because both the chirped probe and THz beam are collinearly focused at the EO crystal as in conventional EO sampling. Also, there is no assumption made about the frequency dependence of the chirp compared to spectral encoding [115], although spatial chirp could introduce inaccuracies in the recovery of the temporal waveform. The time resolution is affected by factors such as material dispersion that stretches the pulses, particularly in the chirped probe containing the THz dynamics, group velocity mismatch between the non-identical pulses, and phase mismatch between the fundamental and SH beams in the BBO crystal. However, if a very thin SHG crystal is used, the dominant source of the degradation of time resolution arises from THz dispersion and absorption in the EO detector crystal, prior to the SH readout process.

Unfortunately, just as is the case for many intensity autocorrelators [132,133], this experimental setup calls for the accurate alignment of three sensitive degrees of freedom (horizontal and vertical angle-tuning for phase-matching and coincidence in time) for the independently crossed beams. There is also the complexity of relying on another nonlinear process, SHG, in addition to the EO effect, which makes the signal inherently noisier and weaker. Using larger

beam widths and BBO crystal dimensions lengthens the time window, but this consequently reduces SHG efficiency and affects the sensitivity of the measurement. Furthermore, noise suppression with balancing cannot be implemented in an optimal or convenient way due to the strict conditions on proper phase matching and input polarizations for SHG.

5.2.4 Temporal cross-correlation using Linear Spectral Interferometry

Matlis and coworkers demonstrated another variant of the THz cross-correlation technique, shown in Fig. 5-1(e), between a chirped probe and a short readout pulse using linear spectral interferometry [134]. The retrieval of the full E-field of an optical probe in this way has been demonstrated earlier in frequency domain holography [135, 136] and single-shot supercontinuum spectral interferometry [137]. Firstly, a THz signal is encoded onto a chirped probe pulse by collinearly focusing them at the EO detection crystal. Time-delaying a readout pulse by Δt from the THz-imprinted chirped pulse introduces a phase difference, $\Delta\phi(\omega)$, in the readout field of $\omega\Delta t$ for the frequency component ω and gives rise to a spectral interference pattern. The measured interferogram at the spectrometer may be written as:

$$T(\omega) = \left|\tilde{E}_{\mathrm{ch}}(\omega) + \tilde{E}_{\mathrm{r}}(\omega)e^{i\omega\Delta t}\right|^2 = \left|\tilde{E}_{\mathrm{ch}}(\omega)\right|^2 + \left|\tilde{E}_{\mathrm{r}}(\omega)\right|^2 + \tilde{E}^*_{\mathrm{ch}}(\omega)\tilde{E}_{\mathrm{r}}(\omega)e^{i\omega\Delta t} + c.c. \qquad (5.1)$$

where $\tilde{E}_{\mathrm{ch}}(\omega) = \left|\tilde{E}_{\mathrm{ch}}(\omega)\right| e^{i\phi_{\mathrm{ch}}(\omega)}$ and $\tilde{E}_{\mathrm{r}}(\omega) = \left|\tilde{E}_{\mathrm{r}}(\omega)\right| e^{i\phi_{\mathrm{r}}(\omega)}$ are the amplitude and phase of the E-fields of the chirped probe and readout pulses, respectively, and *c.c.* is the complex conjugate of the preceding cross-term. This expression may be rewritten to include the relative phase difference between the pulses in the spectral domain, $\Delta\phi(\omega) = \phi_r(\omega) - \phi_{\mathrm{ch}}(\omega)$:

$$T(\omega) = I_{\mathrm{ch}}(\omega) + I_{\mathrm{r}}(\omega) + \sqrt{I_{\mathrm{ch}}(\omega)I_{\mathrm{r}}(\omega)}\cos(\Delta\phi(\omega) + \omega\Delta t) \qquad (5.2)$$

where $I_{ch}(\omega)$ and $I_r(\omega)$ are the spectral intensities of the chirped probe and readout pulses, respectively.

In the time domain, the response is simply the inverse Fourier transform of Eq. 5.2:

$$\mathcal{F}^{-1}[T(\omega)](t) = I_{ch}(t) + I_r(t) + f(t - \Delta t) + f(-t - \Delta t)^* \tag{5.3}$$

where $f(t - \Delta t) = \int_{-\infty}^{\infty} E_{ch}^*(\tau) E_r(t - \Delta t + \tau) d\tau$ is the cross-correlation between the chirped probe pulse and the short readout pulse. The first two terms are the non-interfering autocorrelation components that are centered at $t = 0$, and make up the DC response. In contrast, the cross-correlation terms are separated from the DC response and are centered at $\pm\Delta t$ and are derived from the spectral interference. For a readout pulse of suitably short pulse duration and negligible spectral phase variation, the cross-term yields the chirped E-field in amplitude and phase: $\lim_{E_r(t)\to\delta(t)} f(t - \Delta t) = E_{ch}(t)$. Therefore, a THz signal can be encoded in either the amplitude or phase of the chirped probe and subsequent extraction of a THz trace is possible given a reference interferogram in the absence of a THz pulse. Here, the time resolution is set by the pulse width of the readout pulse E-field, τ_0, and the time window corresponds to the pulse width of the chirped probe E-field, τ_{ch}.

As for any highly sensitive interferometric measurements, there are stringent experimental conditions required for accurate implementation. The fidelity of the fringes is only maintained for collinear beams with high relative optical phase stability and good spatial beam mode matching. For the long observation time windows required, more effort is needed for precise alignment since it calls for the use of non-common-path optics. Also, spatial chirp resulting from an imperfect compressor or stretcher would affect the spectral interference. In principle, the time window is freely adjustable by changing the chirp rate, but in practice is limited by the resolution of the spectrometer, which must be capable of resolving the finest fringe widths. Since the E-fields do not overlap temporally, increasing τ_{ch} for larger time windows leads to an increase in the corresponding time delay, Δt; this yields finer fringes in

the interferogram with fringe widths inversely proportional to Δt.

In terms of sensitivity, the technique employs a linear detection scheme that is capable of measuring small-amplitude signals and also allows for easy implementation of balancing for amplitude encoding of the THz field on the chirped probe pulse. Alternate phase-encoding spectral interferometry with a single chirped pulse [134] or with two chirped pulses in single-shot supercontinuum spectral interferometry [137] is otherwise similar except the lack of a polarization-sensitive scheme prevents the use of balanced detection; also an additional measurement of the reference phase through cross-phase modulation is needed [137]. The phase-encoding scheme is more pertinent to the measurement of intense THz E-fields since very large phase differences can be detected [138] without causing over-rotation (i.e., for induced phase differences more than 90°) in the EO crystal.

5.2.5 Angle-to-time Encoding with Transmissive dual echelons

This single-shot technique is built around a complementary pair of custom-made transmission-mode echelons, optics that look like glass stairways (see inset of Fig. 5-1(f)) [139,140]. When the probe beam passes through a pair of a thin and a thick echelon, each with m steps, it is split into an array of tiny "beamlets" that are delayed incrementally in time relative to one another. The more glass a beamlet passes through, the longer the delay. By design, an integer number of small steps of height, h, in the thin echelon introduces the same time delay as a single large step of height, H, in the thick echelon or simply $H = mh$ where m is an integer. The beamlets are all focused to the same spot on the detector crystal (as a pulse train), but they separate after the crystal and are imaged onto distinct regions of a camera. Modulation of the pulse train in time is mapped onto modulation of intensity in the image, making it possible to record the entire THz trace with a single laser shot. The time resolution of transmissive echelons is roughly the time delay introduced by the smallest step increment, $h\Delta n/c_0$, where the index difference is $\Delta n = n_{\text{glass}} - n_{\text{air}} \approx 0.5$, convoluted

with the pulse duration. The time window is given by the total time delay resulting from all m steps of the largest step increments, $mH\Delta n/c_0$. For a 10 ps window with 20-step glass echelons, the smallest steps are 15 μm (or 25 fs) and the largest steps are 300 μm (or 500 fs).

Transmission through the glass echelons leads to broadening of the optical probe, but is dependent on the material properties, spectral bandwidth of the pulse, and length of propagation in the medium. Since the probe passes through different thicknesses of glass, each beamlet experiences a different amount of pulse broadening. An estimation of the upper limit of broadening that degrades temporal resolution for a bandwidth of $\sim$ 20 nm (a 50 fs transform-limited pulse) centered around 800 nm and a thickness of 10 mm is at most 4 fs [78] (see Sec. 5.4.2), which is negligible for monitoring THz dynamics. The degradation of time resolution only becomes noticeable for ultra-broad bandwidth lasers ($<$ 20 fs transform-limited pulses). Implementation of this method requires fairly minimal modification to the probe arm in a conventional free space THz detection setup and avoids the need for a high-resolution spectrometer, noncollinear geometries, stretchers or compressors, or more involved nonlinear optical measurements, although it does require custom-fabricated echelon optics. Unfortunately, due to the imaging-based detection, any physical defects in the echelons or aberrations in other optical components that degrade image resolution could affect the recovery of the THz waveform. Finally, the method retains the ability for balanced detection, but requires in-focus imaging of both polarization states on the camera.

5.2.6 Summary of Single-shot Methods

Table 1 summarizes the methods presented above, highlighting the desired criteria for a fast-acquisition method with high S/N. With respect to these criteria, we have chosen to explore the viability of two techniques: amplitude encoding spectral interferometry described in Sec. 5.2.4 and EO-imaging with transmissive dual echelons in Sec. 5.2.5. These techniques possess high time resolution and reasonable time window limits, allow the THz beam and

Method	Time resolution	Time window	Beams focused?	Technical considerations compared to EO sampling	Additional Notes
Spectral encoding, Fig. 5-1(b) [115]	$\sqrt{\tau_0 \tau_{ch}} > \tau_0$	τ_{ch}	Yes	• Requires a grating compressor or stretcher and spectrometer	• Time resolution degraded for long time windows • Distortions introduced for monitoring processes faster than time resolution
Non-collinear crossing, Fig. 5-1(c) [123, 124]	τ_0	$\frac{w \tan\theta}{c_0}$	No	• Requires expansion of THz spot size at EO crystal • Nonlinear detection schemes make balanced detection difficult or impossible • Intensive calibration needed to remove distortions due to spatial beam inhomogeneity and nonlinear response	• Expansion of THz beam for a longer time window reduces S/N significantly; difficult to detect in linear regime
SHG cross corelation, Fig. 5-1(d) [131]	τ_0	$\frac{2w \sin\phi}{c_0}$	Yes	• Requires sensitive alignment for proper phase matching in SHG crystal. • Balanced detection is non-trivial.	• Detection of nonlinear process is inherently noisier and weaker. • Expanded probe beams for large time windows lowers SHG efficiency. • Spatial chirp distorts recovered temporal waveform.
Amplitude-encoded spectral interferometry, Fig. 5-1(e) [134]	τ_0	τ_{ch}	Yes	• Interferometrically stable conditions and precise alignment needed • Requires a grating compressor/stretcher and high-resolution spectrometer.	• Linear detection scheme gives high sensitivity. • amplitude encoding scheme allows for balanced detection. • Time window is limited by spectral resolution of spectrometer.
Dual transmissive echelons, Fig. 5-1(f), [140]	$\frac{h\Delta n}{c_0}$	$\frac{mH\Delta n}{c_0}$	Yes	• Requires custom-fabricated glass echelons. • Imaging based detection requires high optical quality components and imposes restrictions on experimental design.	• Pulse broadening in glass echelons for 10 ps time window is minimal for transform-limited pulse durations $\geq$ 50 fs. • Reflection mode echelons also an option for very large time windows or broad bandwidth lasers.

Table 5.1: **Summary of THz single-shot detection methods.**

optical probe to be focused at the EO crystal, and allow for straightforward noise suppression with balanced detection. The following sections provide analyses on the quantitative ability, noise floor, and technical ease of implementation of each method.

5.3 Amplitude Encoding Spectral Interferometry

As stated previously, spectral interferometry is capable of attaining the transform-limited temporal resolution with a variable chirped probe to control the time window. Here, we directly compare this method to the scanning delay-line method to demonstrate the extent of its capabilities.

5.3.1 Experimental Design

The measurements were conducted with a 1-kHz amplified titanium-sapphire laser with a center wavelength at 800 nm, a pulse energy of 1.5 mJ, and a pulse duration of 80 fs (50 fs transform-limited). The experimental setup in Fig. 5-2 was designed for convenient and accurate comparison between the single-shot method and the conventional delay-line pump-probe method. The pump beam was directed into a 2 mm thick ZnTe crystal to generate THz pulses via optical rectification [24] and the THz output was imaged onto a 1 mm thick ZnTe detection crystal with a pair of parabolic mirrors. The identical THz generation setup was also used in the dual echelons technique described later in Sec. 5.4. The first beamsplitter (90%R) separates the pump and probe beams while the second beamsplitter (70%R) creates the chirped probe and readout arms. Prior to entering the second beamsplitter, the beam was spatially filtered with a pinhole to decrease spatial interference upon recombination of both beams. The chirped probe and readout pulse must be combined at the third beamsplitter (50%R) with equal intensities to ensure the strongest modulation depths of the interferogram; the second beamsplitter accounts for the loss upon emerging from the dual-

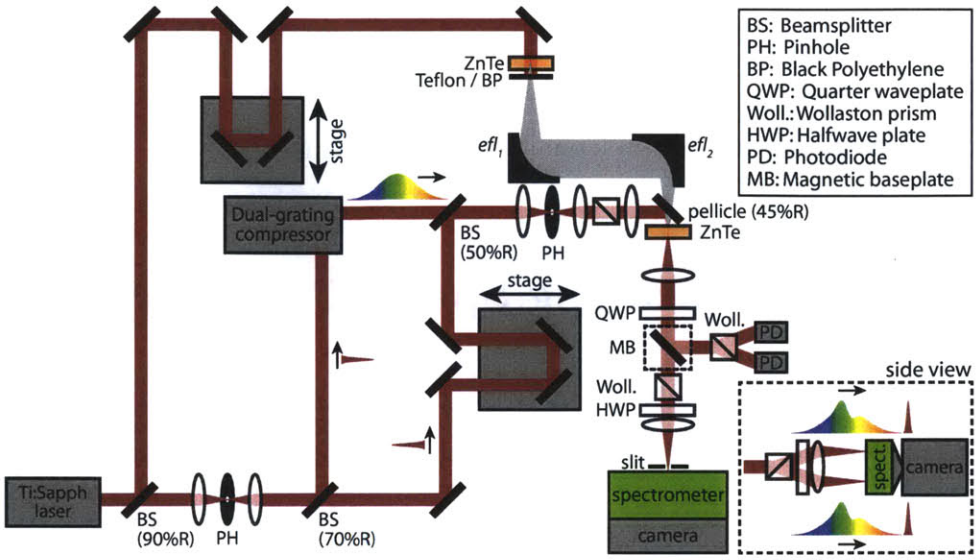

Figure 5-2: **THz spectral interferometry experimental setup using amplitude encoding scheme.** The input laser is initially split into the optical pump for THz generation and the optical probe. The optical probe is further split to give a chirped probe pulse (via a dual-grating compressor) and a short readout pulse, which are time delayed relative to one another by a stage. The THz pulse is imprinted onto the amplitude of the chirped probe at the ZnTe detector crystal, where both beams are focused. Both the chirped probe and readout pulses are directed into a spectrometer and the spectral interference is imaged onto a camera. In single-shot, both stages are fixed during the measurement. For the conventional delay-line method, the chirped probe is blocked, and the short readout pulse is used as the EO sampling probe.

grating compressor. The dual-grating compressor consisted of two 830.8 grooves/mm pulse compression gratings to introduce linear spectral chirp with minimization of spatial chirp; in the experiments, the optical probe was chirped to $\tau_{ch} \approx 7$ ps limited by the resolution of the spectrometer.

As for any interferometer, the importance of the collinearity of the interfering beams is extremely strict; in particular for spectral interference, excellent collinearity is needed to eliminate spatial interference artifacts from inhomogeneous beam profiles or crossing at an angle. Interferometers with common path optics would circumvent the collinearity difficulties, but since phase masks or two-dimensional pulse shapers cannot achieve the long temporal chirp widths desired, we had to employ the dual-grating compressor in one arm as described above. Following the recombination beamsplitter, we aligned each arm through

a 25-μm pinhole and the spectrometer entrance slit closed down to 10 μm. In addition, a motorized stage was incorporated into the readout arm to set the time delay, Δt, between the two pulses. Once set, this stage is immobilized for the entirety of the measurements. Similarly, the stage in the pump arm for THz generation is set to temporally overlap the chirped probe and then also fixed for the single-shot measurement.

For both single-shot measurements and scanning EO sampling, balanced detection was implemented with a quarter wave plate and a Wollaston prism. For the single-shot method, a small splitting-angle Wollaston prism was used to ensure that both spectrograms were imaged onto the camera. The emerging beams of orthogonal polarization were focused onto the slit of the spectrometer. A half wave plate (HWP) was used to compensate for the polarization-dependent efficiency of the grating in the spectrometer by rotating the polarization of the beams to 45°, yielding equal intensities at the detector.

The single-shot detector was a homebuilt spectrometer coupled to a high-speed 10-bit CMOS camera (Photron, Fastcam 1024 PCI, 1024×1024 pixel chip). The spectrometer had a 1200 grooves/mm grating to yield a wavelength range of $\Delta\lambda = 30$ nm and calibration of 0.03 nm/pixel. The camera is capable of recording images at 1000 frames per second while synched to the 1 kHz laser (its performance is detailed in [4]). For the conventional scanning delay-line method, the signal was recorded using a data acquisition card and a pair of low-noise photodiodes (Hamamatsu, S2281) [47]. For both methods, the pump beam was chopped at the maximum modulation frequency of 500 Hz such that alternate probe pulses record the signal and reference. Detection at a higher frequency allows for quick acquisition of an interferogram for every pulse and effectively reduces $1/f$ noise associated with pointing instability and laser drift, which is most important in this case for optical phase stability to prevent the fringe pattern from washing out.

5.3.2 Methodology and Data Processing

Before elaborating on the details of THz spectral interferometry, I will first give a generalized description of optical heterodyne detection to clarify the description given in Sec. 5.2.4.

5.3.2.1 Optical Heterodyne Detection and Fourier Transform Spectral Interferometry

Square-law detectors (e.g., cameras, photodiodes, spectrometers) are electronic devices that integrate a signal over time, and hence measure the intensity of the signal, I_{det}. The oscillations of E-fields, where $A(t)$ and $\phi(t)$ are the time-dependent amplitude and phase, cannot be measured directly in the optical frequency range (on the order of $\sim 10^{14}$ Hz) since time-integrating electronics are unable to respond quickly enough to the changing signal. The detector is only sensitive to the time-averaged energy, which is directly proportional to I_{det}. For a spectrometer, this means that while signal amplitude information, $A(\omega)$ is conserved, any information about its phase, $\phi(\omega)$, is inherently lost. The intensity of an E-field, $\tilde{E}(\omega) = \tilde{A}(\omega)e^{i\phi(\omega)}$, detected by a spectrometer is:

$$I_{\text{det}}(\omega) = \langle \left|\tilde{E}(\omega)\right|^2 \rangle_t = \langle \tilde{E}(\omega)\tilde{E}^*(\omega) \rangle_t = \langle \tilde{A}(\omega)^2 \rangle_t \tag{5.4}$$

Spectral interferometry is a technique that uses optical heterodyne detection to retrieve the spectral phase of ultrafast pulses. This requires interference of a reference beam (typically a local oscillator at a nearby frequency) with the signal beam of interest, both of which are superposed at the detector. While intensity detectors cannot measure absolute phase, they are sensitive to the relative phase between the reference and signal, $\Delta\phi(\omega) = \phi_{\text{ref}}(\omega) - \phi_{\text{sig}}(\omega)$. The relative phase difference creates interference fringes at a beat frequency, which effectively shifts the high-frequency signal to a lower carrier frequency that is electronically detectable. The interference of the two spatially overlapped beams is measured simultaneously by a

spectrometer:

$$I_{\text{det}}(\omega) = \left|\tilde{E}_{\text{sig}}(\omega) + \tilde{E}_{\text{ref}}(\omega)\right|^2 = \left|\tilde{E}_{\text{sig}}(\omega)\right|^2 + \left|\tilde{E}_{\text{ref}}(\omega)\right|^2 + \left|\tilde{E}^*_{\text{sig}}(\omega)\tilde{E}_{\text{ref}}(\omega)\right| e^{i\Delta\phi(\omega)} + c.c. \quad (5.5)$$

where *c.c.* is the complex conjugate of the preceding cross-term. This expression is simplified to:

$$I_{\text{det}}(\omega) = I_{\text{sig}}(\omega) + I_{\text{ref}}(\omega) + 2\cos\Delta\phi(\omega)\sqrt{I_{\text{sig}}(\omega)I_{\text{ref}}(\omega)} \quad (5.6)$$

The first two terms are the non-oscillating homodyne components, which correspond to a frequency-dependent dc offset in the detected intensity. In contrast, the cross-term with cosine dependence causes modulation across the slowly varying spectrum and contains the relative spectral phase difference information. The sum-frequency spectral phase also exists but again is too fast for electronic detection in the optical regime and is omitted from the analysis.

Spectral interferometry is a linear technique with high sensitivity and so small signals may be measured independent of their magnitudes relative to that of the reference pulse; in many cases, this fact is exploited for signal gain since the amplitude of the downshifted difference frequency component depends on the amplitude of the reference that is typically larger than that of the signal. However, because $\Delta\phi(\omega)$ is measured through its cosine, this means that the phase difference can only be measured for discrete frequencies when $\Delta\phi(\omega) = 2\pi$ (i.e. at the cosine maxima) [141]. As a means of circumventing this problem, a time delay, Δt, is introduced in the reference beam, which results in a linear phase factor of $\omega\Delta t$. Now, cosine reaches its maximum when $\Delta\phi(\omega) = 2\pi - \omega\Delta t$ and so phase differences smaller than 2π can be measured. A modification of Eq. 5.5 gives:

$$I_{\text{det}}(\omega) = \left|\tilde{E}_{\text{sig}}(\omega) + \tilde{E}_{\text{ref}}(\omega)e^{i\omega\Delta t}\right|^2 = \left|\tilde{E}_{\text{sig}}(\omega)\right|^2 + \left|\tilde{E}_{\text{ref}}(\omega)\right|^2 + f(\omega)e^{i\omega\Delta t} + c.c. \quad (5.7)$$

where $f(\omega) = \left|\tilde{E}^*_{\text{sig}}(\omega)\tilde{E}_{\text{ref}}(\omega)\right| e^{i\Delta\phi(\omega)} = \mathcal{F}[f(t)]$.

This expression is similarly simplified to:

$$I_{\text{det}}(\omega) = I_{\text{sig}}(\omega) + I_{\text{ref}}(\omega) + 2\sqrt{(I_{\text{sig}}(\omega)I_{\text{ref}}(\omega)}\cos\left(\Delta\phi(\omega) + \omega\Delta t\right) \tag{5.8}$$

Therefore, the oscillation of the spectral interference is set by both the time delay and the difference in absolute spectral phase between the two pulses.

An inverse Fourier transform is applied to the spectral intensity in Eq. 5.8, using the cross-correlation theorem and the Fourier shift theorem, to yield the spectrometer signal in the time domain:

$$\mathcal{F}^{-1}[I_{\text{det}}(\omega)](t) = I_{\text{sig}}(t) + I_{\text{ref}}(t) + f(t-\Delta t) + f(-t-\Delta t)^* \tag{5.9}$$

where $f(t-\Delta t) = \int_{-\infty}^{\infty} E^*_{\text{sig}}(\tau)E_{\text{ref}}(t-\Delta t+\tau)d\tau$ is the cross-correlation term. The first two terms in Eq. 5.9 are the non-interfering autocorrelation terms that are centered at $t = 0$. In contrast, the cross-correlation terms are separated in time since they are centered at $t = \pm\Delta t$. The time delay is set such that the spectrometer is capable of resolving the finest fringes (fringe width $\propto 1/\Delta t$) and that the cross-correlation terms are not overlapped with the autocorrelation terms for accurate phase retrieval. The spectral interference term of interest is obtained by applying a filter that isolates the cross-term, $f(t-\Delta t)$, at $t = +\Delta t$ (the other cross-correlation term at negative times reveals the same information when the ordering of events is symmetric in time). Alternatively, the autocorrelation terms could have been directly subtracted off earlier in the frequency domain if the signal and reference spectra were also measured independently, which would allow for smaller values of Δt. The isolated cross-term is then Fourier transformed back to the frequency domain and the phase $\omega\Delta t$ is removed by setting $t' = t - \Delta t$ to yield $f(\omega) = \mathcal{F}[f(t')]$:

$$I_{filt}(\omega) = \sqrt{I_{\text{sig}}(\omega)I_{\text{ref}}(\omega)}e^{i\Delta\phi(\omega)}. \tag{5.10}$$

Finally, since the absolute reference phase is a known value:

$$\phi_{\text{ref}}(\omega) = (\omega - \omega_0)\Delta t, \tag{5.11}$$

subtracting ϕ_{ref} from $\Delta\phi(\omega)$ and dividing by the amplitude of the reference, $I_{\text{ref}}(\omega)$ in Eq. 5.9 recovers the amplitude and phase of the signal:

$$I_{\text{filt}}(\omega) = \sqrt{I_{\text{sig}}(\omega)}e^{-i\phi_{\text{sig}}(\omega)}. \tag{5.12}$$

5.3.2.2 THz Spectral Interferometry

In the linear EO effect for ZnTe, the THz E-field-induced birefringence is $\delta(t) = -\gamma E_{\text{THz}}(t)/2$, where $\gamma = 2\pi\ell n_0^3 r_{41}/\lambda_{\text{opt}}$, ℓ is the crystal thickness, n_0 is the index in the absence of a THz field at λ_{opt}, the optical probe wavelength, and r_{41} is the appropriate coefficient of the EO tensor [43]. When the probe polarization is oriented 45° relative to the principal axes of the THz-induced index ellipsoid, the measured signal intensity, I, in the limit of weak THz modulation strengths or small δ is:

$$I^{\pm}(t) = I_0(t)(1 \pm \sin\delta(t)) \approx I_0(t)(1 \pm \delta(t)), \tag{5.13}$$

where I_0 is the intensity in the absence of the THz E-field and "+" and "-" signify horizontal and vertical polarizations of the optical probe, respectively. This signifies a conversion of the induced change in the probe's polarization to an amplitude modulation with a quarter wave plate and Wollaston prism. Implementation of balancing doubles the detected signal modulation while canceling common mode noise:

$$\frac{\Delta I^{+}(t)}{I_0(t)} - \frac{\Delta I^{-}(t)}{I_0(t)} = 2\sin\delta(t) \approx 2\delta(t) \tag{5.14}$$

where $\Delta I^{\pm}(t) = I^{\pm}(t) - I_0(t)$.

In spectral interferometry, the THz E-field may be encoded in the amplitude or the phase of the probe, only depending on the polarization of the probe relative to the principal axes of the THz-induced birefringence [127, 134]. Because only the amplitude encoding scheme allows for balanced detection, the following analysis omits THz E-field measurement through the probe's phase and instead focuses on retrieval through extracting the chirped probe's envelope. In the time domain, the chirped probe's E-field in the absence of a THz pulse can be written as: $E_{\mathrm{p},0}(t) = \epsilon_{\mathrm{p},0}(t)e^{i\Phi_{p,0}(t)}$ where $\epsilon_{\mathrm{p},0}(t)$ and $\Phi_{\mathrm{p},0}(t)$ are its time-dependent amplitude and phase, respectively. Just as in conventional EO sampling, amplitude encoding requires the probe's polarization to lie between the principal axes of the crystal at 45°, which results in the THz E-field imprinted only on the amplitude of the transmitted probe: $E_{\mathrm{p,THz}}(t) = \epsilon_{p,THz}(t)e^{i\Phi_{\mathrm{p},0}}(t) = E_{\mathrm{p},0}(t)\sqrt{1 \pm \delta(t)}$. Consequently, the signal modulation and THz E-field are conveniently extracted from the envelopes of both $E_{\mathrm{p},0}$ and $E_{\mathrm{p,THz}}$:

$$\frac{\Delta I^{\pm}(t)}{I_0(t)} = \mp\gamma E_{\mathrm{THz}}(t)/2 = \frac{\epsilon^2_{\mathrm{p,THz}}}{\epsilon^2_{\mathrm{p},0}} - 1. \tag{5.15}$$

As described previously in Sec. 5.2.4, recovery of the THz waveform using amplitude encoding depends on extraction of $\epsilon_{\mathrm{p}}(t)$ using a temporally short readout pulse separated by a relative time delay of Δt. An example of a pair of raw interferograms with balancing implemented and THz signal present is shown in Fig. 5-3(a). We integrated over the (+) and (-) polarization interferograms to recover a spectrum from each; the spectrum for the (+) polarization is shown in Fig. 5-3(b). The asymmetry in the frequency of fringe oscillations depends on whether the readout pulse leads the blue or red spectral components of the chirped probe in time. Similarly, a reference interferogram and spectra for both polarizations are acquired in a successive laser shot in the absence of a THz pulse. In accordance with Eq. 5.3, the spectra in Fig. 5-3(b) were inverse Fourier transformed to the time domain; the modulus is shown for the (+) polarization in Fig. 5-3(c). Since the cross-correlation peaks at $\pm\Delta t \approx 5$ ps represent the envelope of the chirped probe, the THz signal modulation

was calculated using Eq. 5.15 by simply squaring and dividing the signal and reference time domain traces (taken with two laser pulses) in Fig. 5-3(c) and subtracting unity. A zoomed-in view around $+\Delta t$ is shown for both polarizations in Fig. 3(d); however, in these traces the THz signal is barely distinguishable from the noise. Fortunately, the noise is largely correlated and hence effectively suppressed by balancing as seen in Fig. 5-3(e), where noise is reduced and the THz signal is doubled as predicted by Eq. 5.14. These results can be compared to those predicted by a numerical calculation following the procedure outlined Sec. 5.3.2 and illustrated in Fig. 5-4.

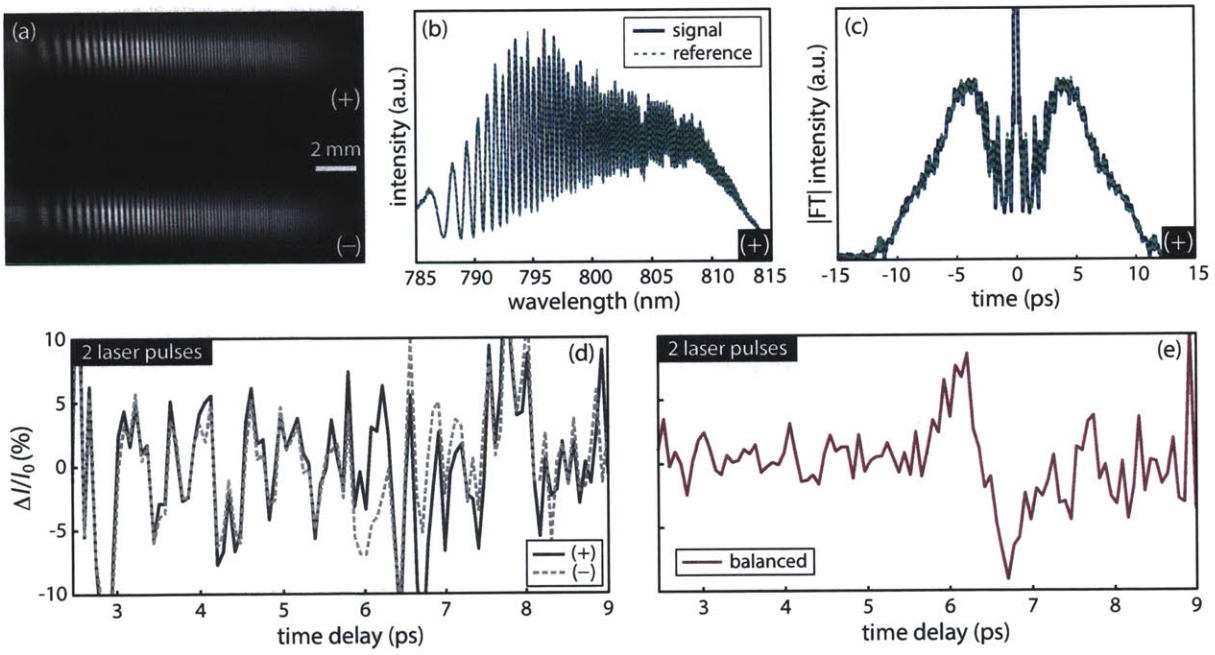

Figure 5-3: **THz spectral interferometry data processing.** (a) Raw interferogram showing (+) and (-) detected polarizations. (b) is given by integrating over the vertical dimension in the (+) interferogram in (a). (c) Modulus of the Fourier transform of the spectral interference in (b), which corresponds to the amplitude of the cross-correlation between the chirped probe and readout pulse E-fields (i.e. approximately the envelope of the chirped probe) in the time domain. (d) Unbalanced time traces collected in two laser pulses for both polarization states by dividing the signal and reference traces in (c) and subtracting unity. With no averaging, the THz signal is indistinguishable from the noise. (e) Balanced time trace collected in two laser pulses following subtraction of (+) and (-) traces in (d), which reveals the THz signal.

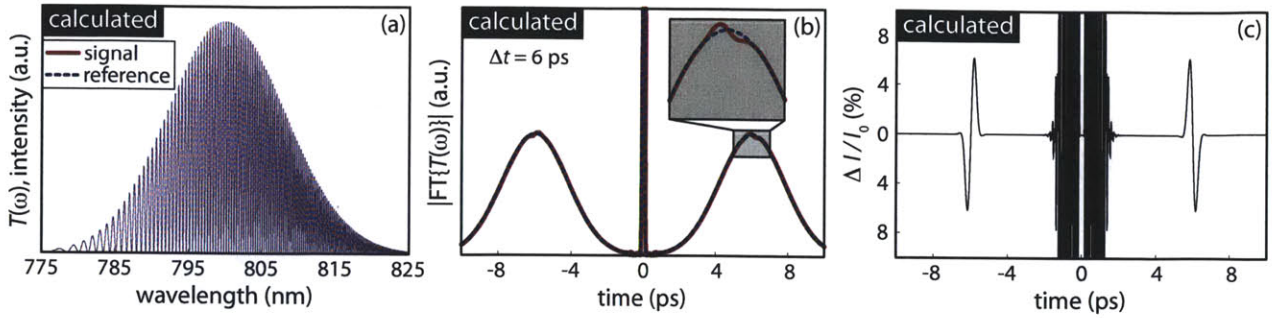

Figure 5-4: **Calculated results for the (+) polarization demonstrating the methodology.** (a) Spectral interference of chirped probe and readout Gaussian pulses. (b) Modulus of Fourier transform of (a). (c) THz time trace given by dividing the signal and reference in (b).

5.3.3 Experimental Results and Discussion

5.3.3.1 Characteristics of the raw spectra and time domain data

The spectral interference, as given by Eq. 5.1, shows fast modulations introduced by the linear phase factor of $\omega\Delta t$ on top of a large, slowly varying background corresponding to the sum of the spectral intensities of the chirped probe and readout pulses. Consequently, the signal interferogram does not change significantly compared to the reference interferogram due to a relatively small signal modulation caused by the THz pulse. These spectra also lack full modulation depths of the fringes, which indicate unequal amplitudes of the readout and chirped probe beams. The asymmetry in modulation depths spectrally varies, which is evidence of spatial chirp in the system.

In the Fourier transforms of the spectra in Fig. 5-3(c), the cross-correlation features differ noticeably from the predicted smooth Gaussian spectra simulated in Fig. 5-4(a). Narrow filtering of pulse bandwidth appears as oscillations in the time domain, but since most of the laser's bandwidth ($\Delta\lambda_{\mathrm{FWHM}} = 20$ nm) was captured by the spectrometer ($\Delta\lambda_{\mathrm{FWHM}} = 30$ nm), these oscillatory artifacts should be minimal. The roughness in the time domain traces may be due to the non-Gaussian envelope of the spectral interferogram in Fig. 5-3(b). There are a multitude of causes for this including the inherent laser mode, self-phase modulation, or material absorption in either the readout or chirped probe beams. Further testing or

simulation is needed to determine the origin of this source of noise.

5.3.3.2 Assessment of quantitative ability and noise floor

The most important aspect of the study was to determine whether the amplitude encoding spectral interferometry method reproduced the THz signal quantitatively with a lower noise floor for a fixed acquisition time compared to conventional EO sampling. By conserving the total number of laser pulses, the THz time trace in Fig. 5-5(a) is evidence that the method maintains the high temporal resolution of the scanning method by incorporating a short readout pulse, a result of solely using a chirped probe [115]. This is further substantiated by the fact that no distortions were introduced, which emerge when the phenomena under study occur on timescales too fast compared to the measurement's time resolution [118,119]. Although the temporal dynamics were closely matched, the absolute THz signal measured differed from the delay-line method, depending strongly on the alignment of the interferometer. THz fields were consistently measured to be larger by up to a factor of two. The reliability of having pure spectral interference is a leading source of the discrepancy, which is obscured by factors such as non-collinearity between the beams and inherent characteristics of the individual pulses. The THz spectrum in Fig. 5-5(b), given by the Fourier transform of Fig. 5-5(a), has approximately the same bandwidth as that measured using the delay-line. However, due to the short useable temporal range in spectral interferometry, the measurement yielded quite poor spectral resolution.

It is evident in Fig. 5-5(a) that spectral interferometry yields a noisier time trace than the delay-line method for the same acquisition time. Since the single-shot methodology records all n time points simultaneously, for the same acquisition time it should be able to average a factor of n more traces than the delay-line method (disregarding computational processing time). Ideally, the noise of one single-shot trace would have the same noise level as a single trace acquired by the delay-line method, but expectedly there is a tradeoff between

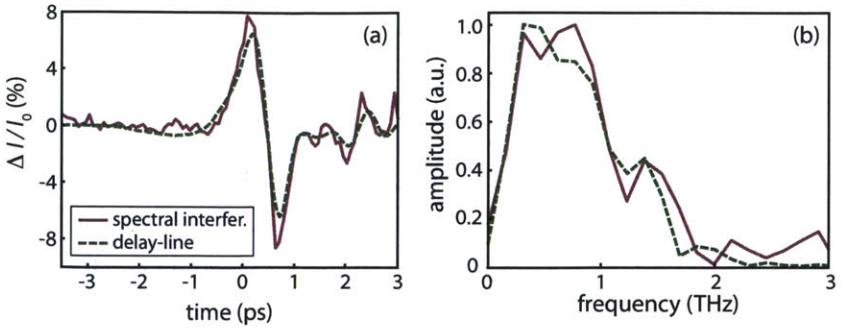

Figure 5-5: **Direct comparison between THz spectral interferometry and conventional EO sampling.** (a) Averaged and balanced THz time traces for THz spectral interferometry and scanning delay-line method. (b) Normalized Fourier transforms of the time traces given in (a).

acquisition speed and baseline noise. Although averaging reduces random noise by a factor of $\sqrt{n}$, the initial baseline noise of a single-shot trace is too large to be sufficiently suppressed by averaging. We measured the respective noise of each method as the uncertainty in $\Delta I/I_0$ across the time trace in the absence of THz pulses (not shown) to be 0.13% using spectral interferometry and 0.06% using the delay-line method with the same number of laser pulses (6400 total laser pulses).

In this system, laser noise presents itself in similar ways to conventional EO sampling with a photodiode (e.g., intensity fluctuations, electronic detector noise), but also in new respects. More stringent conditions are required for low-noise interferograms since laser pointing fluctuations compounded with spatial chirp dynamically change the spectral interference compared to just measuring intensity changes with a large-area photodiode. Additionally, spectral changes in pulses with a non-Gaussian spectrum may change on a shot-to-shot basis. The last, but most important concern is with regards to optical phase stability in the system that also drifts from shot to shot, between successive signal and reference acquisitions. Relative phase shifts between the signal and reference interference patterns manifest themselves strongly when the two time domain traces in Fig. 5-3(c) are divided to yield Fig. 5-3(d). Ultra-high phase stability is extremely difficult to attain since the experimental design calls for the use of non-common-path optics to introduce high chirp rates; an improvement in

phase stability is gained by from detecting at a higher frequency.

Overall, amplitude encoding spectral interferometry has proven to be able to detect THz E-fields with high temporal resolution and close to quantitative field strengths. But its poor noise performance and oversensitivity to alignment, spectral fluctuations, and high optical phase stability cannot be ignored since the measurement of small nonlinear signals is of interest. Previously, spectral interferometry was only demonstrated as a means of detecting intense THz pulses emitted from electron bunches using a high-power laser-plasma accelerator [142], but these field strengths are 3-4 orders of magnitude larger than the absolute signals or relative induced changes we intend to detect. While spectral interferometry is also routinely used in 2D electronic spectroscopy, the observable is subtly different since the signal is the mere existence of the cross-correlation peak itself (a higher contrast measurement) and not small changes in the spectral interference as is the case here.

5.4 Dual Echelons Method

Previous studies using dual echelons have focused on optical pump-probe measurements of irreversible processes [143, 144] and also more relevantly on diagnostics for real-time characterization of THz pulses [140]. Here, we intend to transform the method into a robust technique for multidimensional THz spectroscopy by implementing detection at a higher frequency with balanced detection and multi-shot averaging.

5.4.1 Experimental Design

The sequentially time delayed beamlets can be introduced by using either transmission-mode echelons or reflection-mode echelons. Typically, for relatively small time windows ($\sim$ 10 ps) and small bandwidth laser pulses, transmission-mode echelons are practical. They introduce little temporal chirp (see following Sec. 5.4.2) and allow for adequate imaging quality of

the beamlets. However, for longer time windows, the thickness of the transmission-mode echelons scales linearly, introducing more chirp, but most detrimentally prevents in-focus imaging of the all the beamlets due to the accompanying need for a greater depth of focus. In these cases, reflection-mode echelons are more desirable, but require an additional two-lens $4f$ imaging system that has a larger experimental footprint. These two setups will be discussed in the following sections.

5.4.1.1 Current experimental setup using transmission-mode echelons

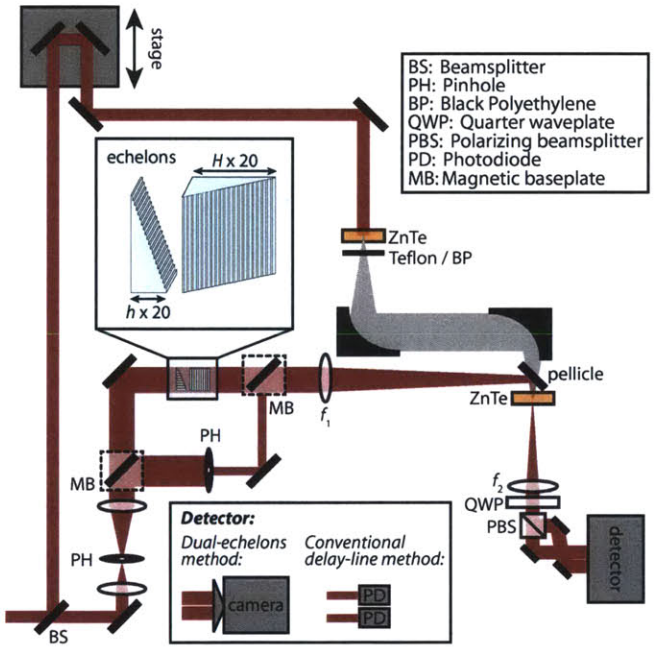

Figure 5-6: **The experimental setup showing convenient switching between dual echelons and delay-line methods and balanced EO detection.** The input laser is split into the optical pump for THz generation and the optical probe. An expanded probe beam is directed through a pair of echelons. The inset shows a schematic illustration of dual 20-step echelons used to generate 400 pulses incrementally delayed in time (not drawn to scale). The large echelon (right) has a step height of $H = 300$ μm and the small echelon (left) has a step height of $h = 15$ μm. The beamlets and THz beam are both focused at the ZnTe detector crystal. Then, the beamlets are imaged onto a camera. Alternatively, in conventional EO sampling, the probe is re-directed to bypass the echelons and detected with a pair of photodiodes.

We used two transmissive echelons, each of which is a right-angled prism with a staircase structure along its hypotenuse surface: one with large steps (step height $H = 300$ μm, time

step = $H\Delta n/c$ = 500 fs) and one with small steps (step height h = 15 μm, time step = $h\Delta n/c$ = 25 fs) each having transverse dimensions of 15 mm × 15 mm (see inset of Fig. 5-6). Each echelon has 20 steps to yield a total of 400 pulses incrementally delayed in $\sim$ 25 fs time steps with an overall time window of 10 ps. The echelons were fabricated by depositing index-matched epoxy onto the hypotenuse of a right-angled fused silica prism and molding the epoxy with steps of the appropriate size [145]. A competing fabrication technology for higher optical quality transmissive echelons is to stack and chemically bond thin layers of fused silica, which can be obtained from Okamoto Optics, Japan [145]. Alternatively, reflection-mode echelons, which are more favorable when much larger temporal windows are desired (for higher spectral resolution) or for setups with very broad bandwidth lasers, can be obtained from Sodick F.T., Japan; these echelons have recently been demonstrated to measure THz E-fields [146].

The optical probe either passed through the echelons and was imaged onto a camera for single-shot detection or was focused as a single beam through the sample and detected with photodiodes for conventional point-probe detection with a scanning delay-line. For the dual echelons method, it is important for the optical probe to be expanded and spatially filtered with a pinhole to give a homogeneous beam profile. The THz beam and optical probe, either the multiple beamlets from the echelons or a single beam for standard detection, were combined with a pellicle beamsplitter such that they propagated collinearly through the detection crystal. The high optical quality ZnTe crystal produced images with relatively sharp features and minimal diffraction. Unlike optical pump experiments, the relatively large THz pump spot at the sample focus ($\sim$ 1 mm diameter) compared to the tightly focused optical probe ($\sim$ 50 μm diameter), relaxes the constraint that each beamlet hit precisely the same spot to experience the same pump strength; this also has favorable consequences in response to pointing fluctuations that pose serious challenges for optically pumped single-shot experiments. It was possible to switch rapidly between single-shot and point-probe detection without modifying the pump arm by inserting or removing both magnetic baseplates under

mirrors as shown in Fig. 5-6 and also swapping the detector. The THz-induced modulation of the probe beam was detected using the standard EO sampling configuration with a quarter-wave plate and polarizing beamsplitter.

For balanced detection in the single-shot echelon setup, both polarization states emerging from the polarizing beamsplitter are imaged onto the camera. A raw picture showing the pair of orthogonal polarization states acquired in a single laser shot is shown in Fig. 5-10(a). For both images to be in focus, the path length from the detection crystal to the camera must be the same for the transmitted and reflected beams emerging from the polarizing beamsplitter. The beam transmitted through the polarizing beamsplitter was reflected directly to the detector while the reflected beam was routed to the detector slightly off right-angle using a pair of mirrors (Fig. 5-6). A polarizing beamsplitter was used due to the high optical quality required for near aberration-free imaging; alternatively, a small-splitting-angle, high optical quality Wollaston prism could be used [4].

5.4.1.2 Proposed experimental setup for longer time windows using a reflection-mode echelon

For the reflection-mode echelon scheme, only the large echelon that provides the long time delay needs to be switched since, for example, making it twice as thick for a time window twice as long would exacerbate the imaging concerns with the current large transmission echelons and would increase temporal broadening of the beamlets (although not a large concern for THz dynamics). On the other hand, doubling the steps of the small echelon is inconsequential to the measurement. In the design of the reflective echelon, we require optically smooth surfaces that have relatively high reflectivity for 800 nm. We have found that a gold-coated echelon structure, similar to an echelle grating with relatively low groove density, could satisfy these conditions. These optics possess the same saw-tooth groove pattern and are optimized for large incidence angles (or high diffraction orders); due to low angular dis-

persion, these optics behave similarly to a mirror. We have had these optics custom-made by Sodick F.T. based in Japan (American distributor: Sodick, Inc.). The manufacturer has the capability of fabricating echelons with high optical quality and high tolerance limits over the structure's characteristic parameters, in particular the cross-sectional profile of the grooves.

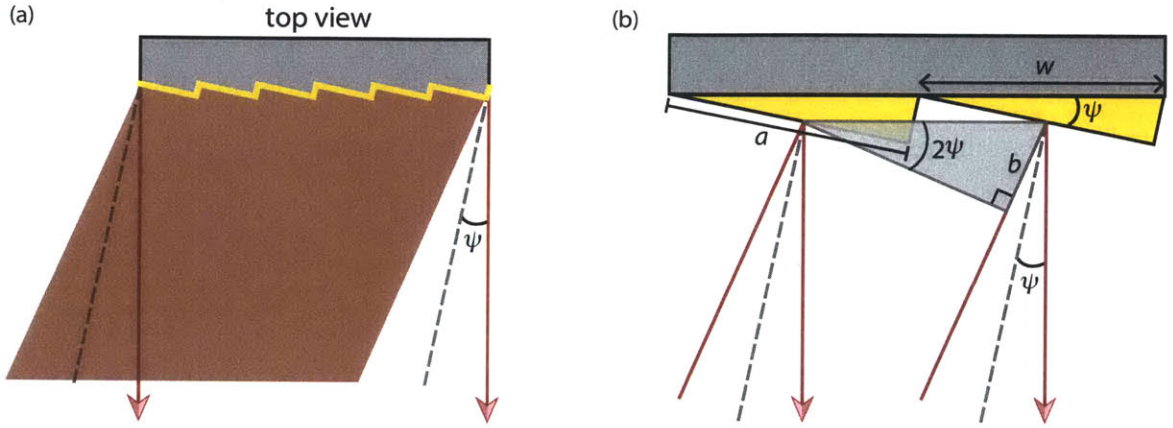

Figure 5-7: **Reflective echelon design.** (a) Top view of a reflection-mode echelon, where the steps have been plated with $\sim$ 300 μm of gold. An input angle of $2\psi = 23.6°$ (drawn to scale) is designed to yield a time window of 20 ps and the output is reflected normal to the single plane shared by all the steps. (b) A zoomed in view of two steps showing the relevant parameters used to calculate a single time step.

The largest added benefit of the reflection-mode scheme is that the echelon can be designed and fabricated such that the incident surfaces giving rise to the time delays are all in the same object plane, and hence negate any depth of focus imaging problems. The design is shown in Fig. 5-7(a), where an incident probe beam impinges on a few steps of the reflective echelon at an angle 2ψ and is reflected normal to the object plane shared by all the steps, which simplifies the subsequent alignment of downstream optics. The zoomed-in view of the steps in Fig. 5-7(b) shows the incident and output beamlets emerging from two steps, where the time delay resulting from the path length difference, b, is illustrated to give the time delay for one step: $\tau_{\text{refl}} = b/c_0$. In terms of the dimensions of the steps to yield a fixed τ_{refl} (or the parameter b), these are easily found using trigonometry to be: $\sin 2\psi = b/w$, $cos\psi = a/w$, and $d = w \sin \psi$. These expressions may be used to give the following expression for the time

delay of each step:

$$\tau_{\text{refl}} = \frac{w}{c_0} \sin 2\psi \tag{5.16}$$

For a 20-step reflective echelon, the relevant design parameters can be calculated by firstly fixing $\tau_{\text{refl}} = 1$ ps and $w = 750$ μm (to match the width of the small transmission echelon for square beamlet images): $\psi = 11.8°$, $a = 734.15$ μm, and $d = 153.37$ μm. The general experimental setup is shown in Fig. 5-8 and involves imaging the large reflective echelon steps onto the transmission echelon with a 1:1 two lens, $4f$ imaging system ($f_1 = f_2$). Then, the new object plane at the position of the transmission echelon is imaged with a 1:2 imaging system ($f_3 = 2f_4$) to shrink the image to fit onto the array detector chip. In this scenario, the overall depth of focus required by the imaging system is now simply set by the thickness of the new complementary 20-step small transmission echelon (32 μm/step, thickness = 704 μm). Assuming that the size of the ZnTe crystal (diameter = 1 cm), located in the Fourier plane of the second imaging system, apertures the diffracted light, then the minimum focal length that can be used to achieve the depth of focus required is $f_3 \approx 20$ cm and $f_4 \approx 10$ cm.

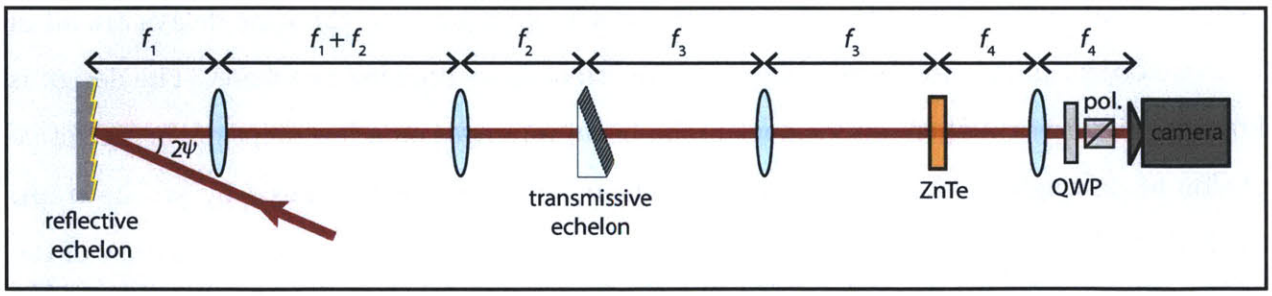

Figure 5-8: **Modified single-shot setup with reflection-mode echelon.** The experimental geometry shows the probing scheme using a large reflection-mode echelon, which is subsequently imaged onto a small transmission-mode echelon.

5.4.2 Methodology and Data Processing

5.4.2.1 Temporal dispersion of ultrafast Gaussian beamlets through glass echelons

As a result of the broad spectral bandwidth inherently present in ultrafast pulses (compared to the very narrow bandwidth of CW lasers), the propagation through an optical medium is accompanied by dispersion of light. In a dispersive medium, different frequencies that make up the broadband pulse travel at different speeds (or group velocities) and hence cause lengthening of the temporal pulse width. For a Gaussian pulse, this is the temporal analog of spatial dispersion, where different frequencies propagate to different positions in space, transverse to the propagation direction, but will not be considered here. The following treatment will focus on the introduction of linear chirp (or quadratic phase) in a Gaussian ultrafast pulse in accordance with [78].

A transform-limited Gaussian pulse has the shortest pulse duration for a pulse with a Gaussian spectral profile of a given bandwidth; in the time domain, the envelope of a pulse can be described by:

$$A(t) = A_0 \exp(-t^2/\tau^2) \tag{5.17}$$

where A_0 is the normalized Gaussian amplitude and τ is a time constant. The full E-field is simply:

$$E(t) = A(t)\exp(i\omega_0 t), \tag{5.18}$$

where ω_0 is the central radial frequency of the pulse. From Eq. 5.17, it is seen that the envelope of the pulse has constant phase ($\phi(t)$ = constant, time-independent phase). The intensity of the pulse then follows as:

$$I(t) = I_0 \exp(-2t^2/\tau^2) \tag{5.19}$$

where $I_0 = |A_0|^2$ is the peak intensity. The FWHM of the intensity of a pulse in Eq. 5.19 is given as:

$$\tau_{\mathrm{FWHM,i}} = \sqrt{2\ln 2}\tau \approx 1.18\tau \tag{5.20}$$

This is the pulse width normally referred to for an ultrafast laser pulse (e.g., 50-fs or 100-fs pulses). A transform-limited pulse has its time-bandwidth product at its minimum:

$$\tau_{\mathrm{FWHM,i}}\Delta\nu = 0.44, \tag{5.21}$$

which shows the inherent inverse relation between temporal pulse duration and FWHM spectral bandwidth, $\Delta\nu$. The pulse width of the amplitude of the pulse may also be calculated:

$$\tau_{\mathrm{FWHM,a}} = \sqrt{2}\tau_{\mathrm{FWHM,i}} \approx 1.67\tau. \tag{5.22}$$

The spectral bandwidth can also be written in terms of wavelength, where $\Delta\lambda \ll \lambda$:

$$\Delta\nu \approx \frac{c_0}{\lambda^2}\Delta\lambda \tag{5.23}$$

For a linear temporal chirp, Eq. 5.17 is modified to include a more general complex phase:

$$A(t) = A_0 \exp(-t^2/\tau^2)\exp(iat^2/\tau^2) \tag{5.24}$$

where a is the chirp parameter. The phase of a chirped Gaussian pulse, $\phi(t) = at^2/\tau^2$, is a time-dependent quadratic function, and similarly the spectral phase is a frequency-dependent quadratic function: $\phi(\omega) \propto \frac{1}{4\pi^2}a\omega^2$. Generally, a pulse is said to be chirped if it has a time-dependent instantaneous frequency:

$$\omega_i(t) = \omega_0 + \frac{\mathrm{d}\phi}{\mathrm{d}t}. \tag{5.25}$$

This results in a linear variation of the instantaneous frequency (referred to as linear chirp): $\omega_i(t) = \omega_0 + 2at/\tau^2$ and so a different central frequency will be measured at any instance of time. An up-chirped pulse has $a > 0$ such that the instantaneous frequency increases with time and vice versa for a down-chirped pulse with $a < 0$. The time-bandwidth product is also modified to include the chirp parameter:

$$\tau_{\mathrm{FWHM,i}}\Delta\nu = 0.44\sqrt{1+a^2}, \tag{5.26}$$

which as expected is minimized for a transform-limited pulse ($a = 0$). Because temporally chirping a pulse does not change its spectral width, the chirped pulse width, τ_{ch} must increase the initial transform-limited pulse width, τ, accordingly by the same factor $\sqrt{1+a^2}$ and consequently offsets any spectral broadening:

$$\tau_{\mathrm{ch}} = \tau\sqrt{1+a^2} \tag{5.27}$$

A pulse may be chirped if it propagates through a dispersive transparent medium due to the effects of a frequency-dependent refractive index (i.e. chromatic dispersion) or nonlinearities in the medium such as self-phase modulation. In the case of the echelons, the former cause is of interest, since the substrate, fused silica, has a frequency-dependent index, $n(\omega)$. The propagation of an E-field along a direction z in a linear lossless dispersive medium simply undergoes a phase shift: $\beta(\omega)z$, where $\beta = \omega n(\omega)/c_0$ is the frequency-dependent propagation constant. Firstly, in the time domain, Eq. 5.18 becomes spatially-dependent:

$$E(z,t) = A(z,t)\exp(i\omega_0 t)\exp(-i\beta_0 z) \tag{5.28}$$

where $\beta_0 = \beta(\omega_0)$. In the frequency domain, the Fourier transform of Eq. 5.28 is found using

the Fourier shift theorem is:

$$E(z,\omega) = \tilde{A}(z,\omega-\omega_0)\exp(-i\beta_0 z) \tag{5.29}$$

where $\tilde{A}(z,\omega-\omega_0) = A(0,\omega-\omega_0)\exp[-i(\beta(\omega)-\beta_0)z]$. This expression shows how propagation in the dispersive medium alters the phase due to frequency-dependent index, giving rise to chirp in the pulse, and therefore the dispersive medium can be thought of as a chirp filter, $\Psi(\omega)$ [78]. Eq. 5.29 is then:

$$E(z,\omega) = \tilde{A}(0,\omega-\omega_0)\Psi(\omega-\omega_0)\exp(-i\beta_0 z) \tag{5.30}$$

where $\Psi(\omega) = \exp[-i\beta(\omega)z]$.

For a slowly varying propagation constant $\beta(\omega)$, we may Taylor expand to second order as follows:

$$\beta(\omega) = \beta_0 + \left.\frac{\mathrm{d}\beta}{\mathrm{d}\omega}\right|_{\omega=\omega_0}(\omega-\omega_0) + \left.\frac{1}{2}\frac{\mathrm{d}^2\beta}{\mathrm{d}\omega^2}\right|_{\omega=\omega_0}(\omega-\omega_0)^2 \tag{5.31}$$

$$= \beta_0 + \beta'(\omega-\omega_0) + \frac{1}{2}\beta''(\omega-\omega_0)^2 \tag{5.32}$$

The first and second derivatives of the propagation constant have physical significance relating to the evolution of the pulse's envelope. The first derivative is inversely proportional to the velocity of the envelope (the group velocity, v_g):

$$\beta' = \frac{1}{v_g} \tag{5.33}$$

and the second derivative is called the group velocity dispersion (GVD):

$$\beta'' = \mathrm{GVD} \equiv \frac{\mathrm{d}}{\mathrm{d}\omega}\frac{1}{v_g} \tag{5.34}$$

The temporal broadening of a pulse therefore relies on the GVD since it introduces a frequency-dependent time delay: $\tau_d(z,\omega) = z/v_g(\omega)$. Eq. 5.28 can be rewritten to include this:

$$E(z,t) = A(t - \tau_d(z,\omega_0)) \exp[i\omega_0(t - z/c)] \tag{5.35}$$

where c is the velocity of light in the medium at the central frequency: $c = c_0/n(\omega_0)$ (the phase velocity).

Because the index of refraction is usually expressed in terms of wavelength (e.g., the Sellmeier Equation), it is more convenient to describe the group velocity as a function of $n(\lambda_0)$ using $\beta = 2\pi n(\lambda_0)/\lambda_0$ where $\lambda_0 = 2\pi c_0/\omega$ is the wavelength in vacuum and $\mathrm{d}\beta/\mathrm{d}\omega = (\mathrm{d}\beta/\mathrm{d}\lambda_0)(\mathrm{d}\lambda_0/\mathrm{d}\omega)$:

$$v_g = \frac{c_0}{n(\lambda_0) - \lambda_0 \frac{\mathrm{d}n(\lambda_0)}{\mathrm{d}\lambda_0}} \tag{5.36}$$

Similarly, the GVD in Eq. 5.34 is rewritten by using $\mathrm{d}/\mathrm{d}\omega = (\mathrm{d}\lambda_0/\mathrm{d}\omega)(\mathrm{d}/\mathrm{d}\lambda_0) = -\frac{\lambda_0^2}{2\pi c_0}(\mathrm{d}/\mathrm{d}\lambda_0)$:

$$\beta'' = \frac{\lambda_0^3}{2\pi c_0^2} \frac{\mathrm{d}^2 n(\lambda_0)}{\mathrm{d}\lambda_0^2} \tag{5.37}$$

Lastly, in order to determine the chirped temporal width τ_{ch} from a transform-limited pulse τ, we need to determine the relationship between β'' and the chirp parameter a. The Fourier transform of Eq. 5.24 for a chirped pulse can explicitly be written as:

$$A(\omega - \omega_0) = \tilde{A}_0 \exp\left[- \frac{\tau_{\mathrm{ch}}^2 (\omega - \omega_0)^2}{4(1 - ia)} \right] \tag{5.38}$$

$$= \tilde{A}_0 \exp\left[- \frac{\tau_{\mathrm{ch}}^2 (\omega - \omega_0)^2 + ia\tau_{\mathrm{ch}}^2 (\omega - \omega_0)^2}{4(1 + a^2)} \right] \tag{5.39}$$

Equivalently, we can write the amplitude according to Eq. 5.30 by applying the chirp filter

to a transform-limited pulse:

$$A(\omega-\omega_0)=\tilde{A}_0\exp\left[-\frac{\tau_0^2(\omega-\omega_0)^2}{4}\right]\exp\left[-i(\beta_0+\beta'(\omega-\omega_0)+\frac{1}{2}\beta''(\omega-\omega_0)^2)z\right] \quad (5.40)$$

Now, comparing the real and imaginary parts of Eqs. 5.39 and 5.40, we find the following relationship:

$$a=\frac{2\beta''z}{\tau_0^2}=\frac{4\ln 2\beta''z}{\tau_{0,\mathrm{FWHM,i}}^2}. \quad (5.41)$$

Substituting this expression in Eq. 5.27 yields the chirped temporal width:

$$\tau_{\mathrm{ch}}=\tau_0\sqrt{1+\frac{\lambda_0^3 z}{\tau_0^2\pi c_0^2}\left(\frac{\mathrm{d}^2n(\lambda_0)}{\mathrm{d}\lambda_0^2}\right)} \quad (5.42)$$

In order to extract the temporal width after propagation in a real material, we can see from Eq. 5.42 that we need an expression for the experimentally measured refractive index. Conveniently, the refractive index has been measured for many materials over a wide wavelength range and is expressed as the Sellmeier equation:

$$n^2(\lambda_0)=1+\lambda_0^2\left[\frac{B_1}{\lambda_0^2-C_1}+\frac{B_2}{\lambda_0^2-C_2}+\frac{B_3}{\lambda_0^2-C_3}\right] \quad (5.43)$$

For fused silica, the refractive index was measured in the range of $\lambda_0 = 0.21$ to 3.71 μm to be given by [147]:

$$B_1=0.6961663, B_2=0.4079426, B_3=0.8974794$$

$$C_1=0.00467914826, C_2=0.0135120631, C_3=97.9340025\ [\mu\mathrm{m}^2].$$

The index of fused silica is shown in Fig. 5-9(a), where n=1.4533 at 800 nm. Since it is analytically easier to work with the derivatives of $\varepsilon = n^2$, then the derivatives of the index

can be re-expressed in terms of ε' and ε'':

$$\frac{\mathrm{d}n}{\mathrm{d}\lambda_0} = \frac{1}{2}\varepsilon^{-1/2}\varepsilon' \tag{5.44}$$

$$\frac{\mathrm{d}^2 n}{\mathrm{d}\lambda_0} = -\frac{1}{4n^3}\varepsilon'^2 + \frac{1}{2n}\varepsilon'' \tag{5.45}$$

where $\varepsilon' = \frac{\mathrm{d}\varepsilon}{\mathrm{d}\lambda_0}$ and $\varepsilon'' = \frac{\mathrm{d}^2\varepsilon}{\mathrm{d}\lambda_0^2}$.

Therefore, substituting Eq. 5.45 in Eq. 5.42, the chirped temporal FWHM width experienced by each beamlet in the fused silica echelons can be calculated. The results are shown for three different transform-limited pulse durations at 800 nm in Fig.5-9(b) for the differential amount of broadening from the thinnest to the thickest step. The shortest pulse duration, $\tau_{0,\mathrm{FWHM,i}} = 35$ fs (i.e. the largest bandwidth), undergoes the largest dispersion and consequently the greatest pulse width difference, $\Delta\tau = \tau_{\mathrm{ch,FWHM,i}} - \tau_{0,\mathrm{FWHM,i}}$. But, for the longer pulse durations such as for the laser used in our experiments, $\tau_{0,\mathrm{FWHM,i}} = 50$ fs, there is minimal temporal broadening for all beamlets at 800 nm (< 2 fs for the largest step thickness, corresponding to a 10 ps time delay).

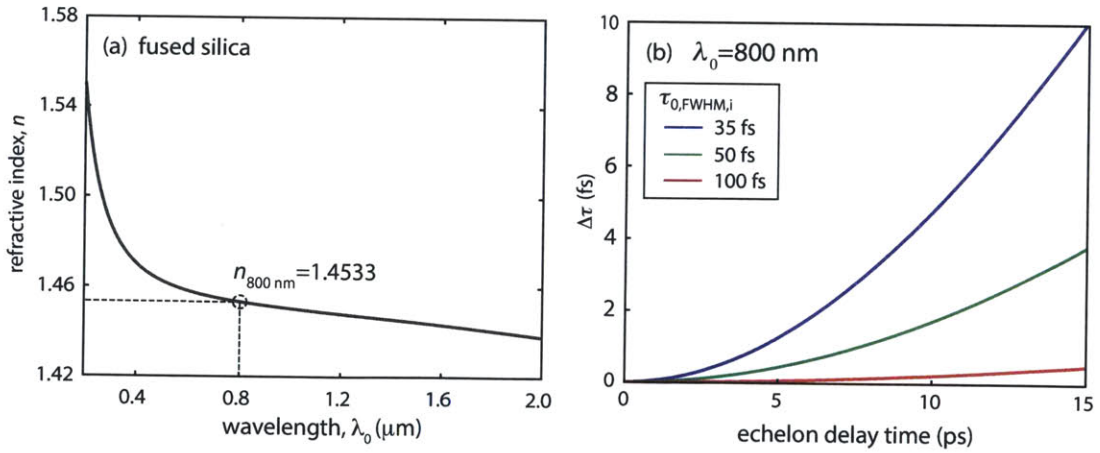

Figure 5-9: **Temporal broadening in fused silica.** (a) The wavelength-dependent refractive index of fused silica derived from the measured Sellemeier equation [147]. (b) Temporal broadening of beamlets emerging from fused silica echelons for three different initial transform-limited pulses at 800 nm as a function of beamlet delay time.

5.4.2.2 General extraction procedure for echelons

In the dual echelons method, two successive laser shots yields two pairs of images: one pair with the THz pulse present (the signal) and one pair with the THz pulse blocked (the reference) (see Fig. 5-10(a) for an example of such a pair of images). For demonstrative purposes, Fig. 5-10(b) shows an image with the signal divided by the reference. The probe intensity is visibly modulated by the THz field near the center of the grid, and the sign of modulation is opposite in the left and right images. Here, the directionality of time is increasing from up to down and left to right.

In reality, the data processing requires that a time trace is firstly extracted from both signal and reference images like those in Fig. 5-10(a). Prior to extraction, a geometric transformation "projective" in Matlab is applied globally to each raw grid in the images; this effectively corrects for any tilt in the image. This makes it possible to methodically average over the pixels within each square spatial region in the echelon and thus unwrap the 20×20 grid of values into a 400×1 vector corresponding to sequential time delays. In this experiment, because the last row of the echelons we used were damaged, we discarded every other row to instead yield a 200×1 time sequence with 50 fs steps. Division of the recovered signal and reference traces retrieves a THz time trace for each polarization state labeled as (+) and (-) in Fig. 5-10(c). Balancing is implemented by subtracting the two time traces in Fig. 5-10(c), which doubles the signal modulus and reduces common mode noise, in accordance with Eq. 5.14. The balanced trace derived from the two laser shots is shown in Fig. 5-10(d).

Numerous signal and reference images can be collected in succession and averaged to yield further suppression of uncorrelated noise. This is most pertinent in the event of investigating systems with reversible time dynamics, where many more images may be averaged to yield marked improvement in S/N. Here, the averaging of N images is implemented by firstly summing $N/2$ signal and $N/2$ reference images and then applying the extraction process

described above to recover the balanced time trace. This order of operations is the least computationally intensive, another aspect that cannot be overlooked when the overarching objective is to reduce acquisition time significantly.

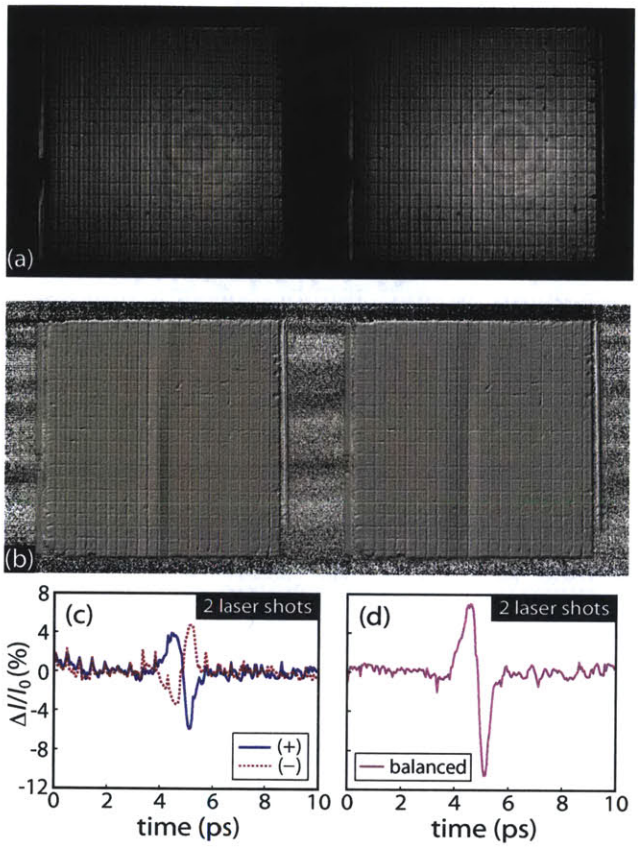

Figure 5-10: **Data processing in dual echelons single-shot THz method.** (a) An example of a raw pair of signal images (THz pulse present). A reference image (not shown) with the THz pulse blocked looks very similar to this. (b) Image pair computed by dividing the signal image by the reference image (THz modulation is visible in several columns near the center of the grid). Time is increasing from top to bottom and left to right of the grid. (c) THz time trace retrieved for left and right echelon images shown in (a), following division of extracted signal and reference time traces. Balanced traces have opposite signs as expected. (d) THz time trace with balancing implemented by subtraction of traces in (c). This doubles the magnitude of signal and suppresses noise.

5.4.3 Experimental Results and Analysis

To reiterate, for the single-shot method to be a viable tool for multidimensional THz spectroscopy, two criteria must be met: (i) the dual echelons technique must be capable of quantitatively recording the THz time trace, and (ii) for a given acquisition time, the S/N must be better than the conventional scanning delay-line method.

5.4.3.1 Assessing quantitative ability of the dual echelons method

The first criterion was evaluated by acquiring THz time traces with the dual echelons method and the conventional scanning delay-line method. Here, the number of traces averaged, N, and laser pulses per time delay, κ, and number of time points per trace, n, were kept constant between both methods. The images were processed separately for the signal and reference traces, but followed the same procedure. In the dual echelons method, after every κ laser shots, images were collapsed into a single trace and repeated for a total of N traces. Ideally, the same S/N between both methods each requires the following total number of laser pulses: $N\kappa n$ (delay-line) vs. $N\kappa$ (single-shot). We will show that for a 1D trace the acceleration of acquisition time is slightly less than the optimal reduction of $1/n$, but still provides substantial timesaving.

For each method, Fig. 5-11 shows the average of many traces and resulting spectra with the same number of averages per time delay ($N = 55$, $\kappa = 250$), but with the dual echelons using the number of laser pulses divided by n compared to the delay-line. As seen in the time traces in Fig. 5-11(a) and their Fourier transforms in Fig. 5-11(b), the dual echelons method (solid pink trace) was able to replicate a THz time trace collected by the delay-line method (dashed green trace). In addition to the closely matched time dynamics, the signal modulation amplitudes also agreed quantitatively (Fig. 5-11(a) and (b) traces have not been normalized to each other). This demonstrates the dual echelons method's ability to accurately record THz spectra, which enables quantitative E-field measurement with reliable

spectral features. Small deviations in the time traces and Fourier domain spectra in Fig. 5-11 may be a result of physical imperfections in the echelons themselves that may be seen in the images in Fig. 5-10(a) or due to the distinct sources of noise in each system as discussed below.

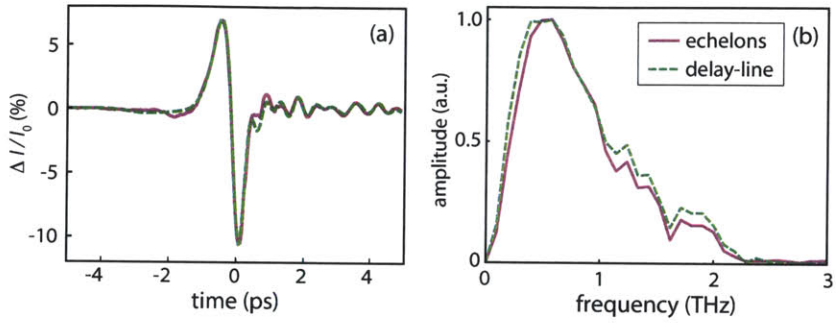

Figure 5-11: **Direct comparison of dual echelons method and conventional EO sampling.** (a) THz time traces for dual echelons method and scanning delay-line method for the same number of averages per time delay (dual echelons uses a factor of n fewer total number of laser pulses as the delay-line). (b) Fourier transforms of the time traces given in (a).

5.4.3.2 Understanding sources of noise and noise suppression techniques in dual echelons system

In a single-shot THz trace like that shown in Fig. 5-10(c), the most noticeable feature of the noise is its periodic structure. This observation led to the final evaluation on expediting THz acquisition using the dual echelons, which was conducted with the THz pulse blocked and only probe light collected. Additionally, the probe-noise-limited baseline normalized for the total number of pulses (i.e. the same total acquisition time) between both methods and was calibrated with no detection crystal to simulate the best-case scenario (aberrations in crystals degrade image quality and consequently interfere with signal extraction process). Fig. 5-12(a) shows the unbalanced averaged probe-only traces for each polarization state, where strongly periodic noise components are visible.

The periodic artifacts stem from the imaging-based detection that is more susceptible to shot-to-shot beam pointing fluctuations and slow laser drift, consequently leading to jitter

and drift of the spatial 2D image that negatively impacts the extraction process. This structural noise occurs at the period of a large echelon step (i.e. 500 fs or 2 THz) and has the largest magnitudes at the perimeters, with locations specified by the spikes. For a beam with a Gaussian intensity profile, if the beam is only slightly larger than the transverse dimensions of the echelons, the spatial variation will be most noticeable in moving from the echelon step located at the last row to one at the top row (representing sequential time delays). Expansion of the beam such that only the peak (varying by very small amounts in intensity across space) passes through the echelons is only possible with enough probe power since most of it would be unused. Compared to the large area photodiodes, the echelons has a reduced active detection area per time point on the camera, which raises the sensitivity of the trace extraction to laser fluctuations. Averaging over a more homogeneous beamlet region a few pixels removed from all four edges minimizes this phenomenon, but faces two competing factors: selecting one too large is more susceptible to shot-to-shot changes in diffraction while one too small falls in the regime where electrical detector noise dominates.

However, the periodic noise itself does not necessarily stifle the single-shot method since averaging effectively suppresses random noise from pointing fluctuations. High-frequency chopping also reduces noise sources such as varying spatial inhomogeneity in the probe beam and $1/f$ laser noise. Lastly, the structural noise is a prime candidate for implementation of balancing since the noise in each (+) and (-) polarization trace is highly correlated, as seen in Fig. 5-12(a), while any THz signal would appear with opposite sign. Through balancing, the rms noise was effectively suppressed by more than a factor of two (compare traces in Fig. 5-12(a) with the balanced trace, solid pink, in Fig. 5-12(b)). These noise suppression techniques were equally effective in the delay-line method (see dashed green in Fig. 5-12(b)).

The remaining but most important difference between the two methods lies in the number of traces averaged, N, which was a maximum of $N_{\text{ech,max}} = 3200$ traces for the dual echelons, a factor of 200 more traces than the delay-line method (or the number of time points in a trace, $n = 200$). As illustrated in Fig. 5-12(b), the noise floor of the echelons method

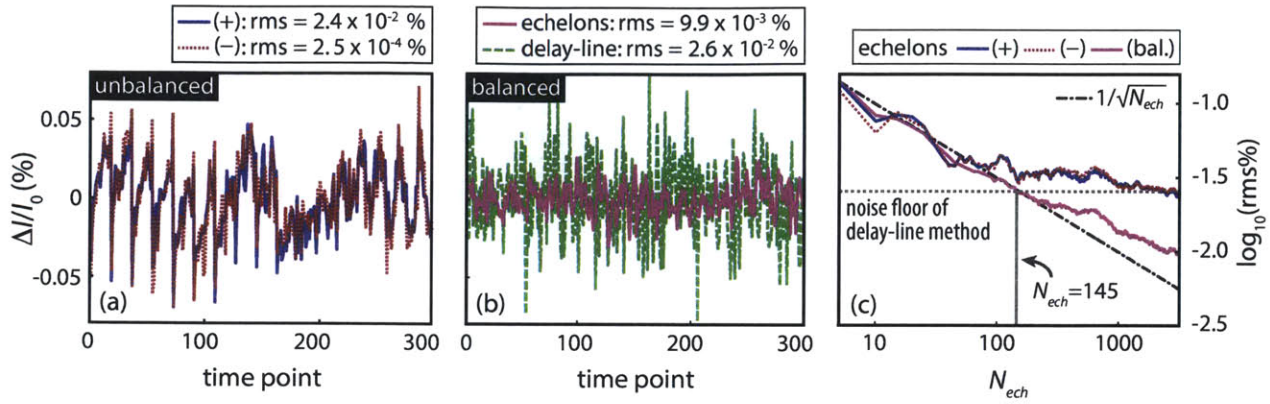

Figure 5-12: **Probe noise traces where THz pump is blocked and total number of pulses acquired is maintained between both echelons and delay-line methods.** (a) The averaged unbalanced traces from the echelons method, where periodic noise is strong. (b) The balanced traces from both methods; the rms of the echelons trace is expectedly lower than that of the delay line as it averages 200 times more traces. Also, periodic noise in the echelons method is greatly suppressed with balancing. (c) The rms of the echelons system in response to averaging a number of traces given by N_{ech}, which when plotted on a logarithmic scale yields close to $1/\sqrt{N_{\text{ech}}}$ scaling. The echelons method attains the same noise floor of the delay-line method at $N_{\text{ech}} = 145$ traces (290 laser shots); this is approximately 4.5% of the total shots required by the delay-line method (6400 laser shots).

is lower than that of the delay-line method when collected with the same number of laser shots, however this is not consistent with a relative reduction factor of $\sqrt{200}$ estimated from averaging. The major contributions to this discrepancy are the different noise sources discussed previously in the EO-imaging scheme required for the echelons.

The nature of averaging in the echelons system was further studied by determining the rms noise as a function of N. In Fig. 5-12(c), the data are plotted on a logarithmic scale and reveal roughly $1/\sqrt{N}$ scaling (dot-dash line). While this is particularly true at short time scales, where averaging many laser shots at a high frequency effectively suppresses beam-pointing instability, there is a deviation after $N_{ech} \approx$ 220 for (+), (-), and balanced traces. Although the effectiveness of balancing is clearly maximized due to the high level of correlation between the (+) and (-) traces over time as the laser fluctuates, the deviation results from uncompensated slow laser drift in the system occurring on the several hundreds of milliseconds timescale. An iterative optimization algorithm for the extraction parameters

on this timescale is likely to benefit noise performance since the initial parameters were optimized based on the average static diffraction features (assumed only to randomly jitter). In spite of this, from Fig. 5-12(c), the most significant metric discovered was that the dual echelons method required 145 averaged traces (or 290 laser shots) to have rms noise equivalent to the noise floor of the delay-line method (shown in Fig. 5-12(b)). This represents a mere 4.5% of the averaging time required by the delay-line method to recover an equivalent level of S/N.

5.4.3.3 Optimization algorithm to suppress laser drift

For EO-imaging, noise suppression techniques are more sensitive to the parameters chosen since a spatial dimension is involved. In the case of balancing, noise suppression may be negligible or reduced due to non-identical imaging of balanced images or improper selection of initial parameters for extraction, even if the rms noise is similar in magnitude (see Fig. 5-13). In terms of data processing, it is imperative that the same area of the echelons is sampled because of the unevenness or structure present in the grid, particularly the diffraction pattern retained in every box that represents a single time point. Overall, the goal is to have both the same structure and magnitude of the noise across all extracted time points to attain the lowest noise following balancing.

The noise traces shown in Fig. 5-12(a) and (b) are derived from the same data set, except that following initial manual grid selection, the (-) grid was optimized for a small subset of the data ($\sim$ 100 averaged traces) by simple translation of the horizontal and vertical positions to match the (+) grid. The observed feedback was the similarity of the structural noise content in the unbalanced traces, as seen in Fig. 5-12(a), but most clearly seen in the balanced trace in Fig. 5-12(b) that has a lower noise magnitude and relatively flat trace (although some periodicity continues to leak in). Similarly, one could also optimize the sizes of the integrated

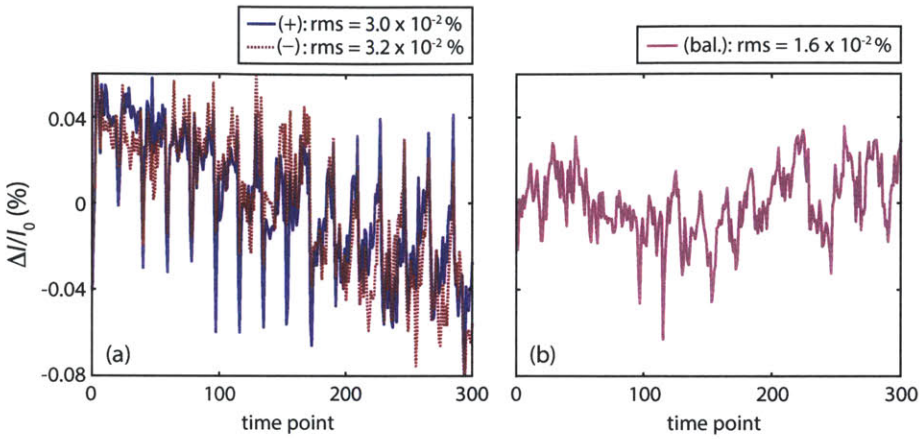

Figure 5-13: **Noise traces extracted with no optimization of the initial grid that was independently selected for (+) and (-) polarizations.** (a) Averaged unbalanced traces, where due to non-similarity in the grid chosen, the noise traces have different structure. (b) Averaged balanced noise trace, which visibly still contains the unsuppressed structure.

boxes of either the (+) or (-) grid to match the other. However, as mentioned previously, there is a divergence from the $1/\sqrt{N}$ scaling in the rms noise in Fig. 5-12(c) due to laser drift, which is uncompensated over the course of the measurement. This aspect will become even more important as scan times approach the order of hours since it is already noticeable on the seconds timescale.

In general, averaging suppresses random motion of images, but in this case, any net directional movement of the echelons from the initial selected grid points will strongly introduce noise into the measurement. In order to compensate for both the jitter and drift of the images, an optimization algorithm needs to be applied to redefine the grid coordinates every few hundred milliseconds. The initial grid is iteratively optimized by choosing a range of x (horizontal) and y (vertical) pixel offsets (typically varying from ± 2 pixels in either spatial coordinate), which sets the predicted random spatial walk of the images. The rms noise from a balanced noise trace is then recorded for every point in the 2D offset range specified and the pair of (x, y) offsets that give the minimal rms noise determines the new position of the grid. In Fig. 5-14(a) and (b), the noise traces of the unbalanced and balanced averaged traces following this simple optimization are shown. The unbalanced traces show an improvement

in noise by $\sim 20\%$ while balancing is even more effective (reduction of factor of 3.3 compared to a reduction of 2.5 in Fig. 5-12). Lastly, the scaling of the noise follows as approximately $1/\sqrt{N}$ as expected.

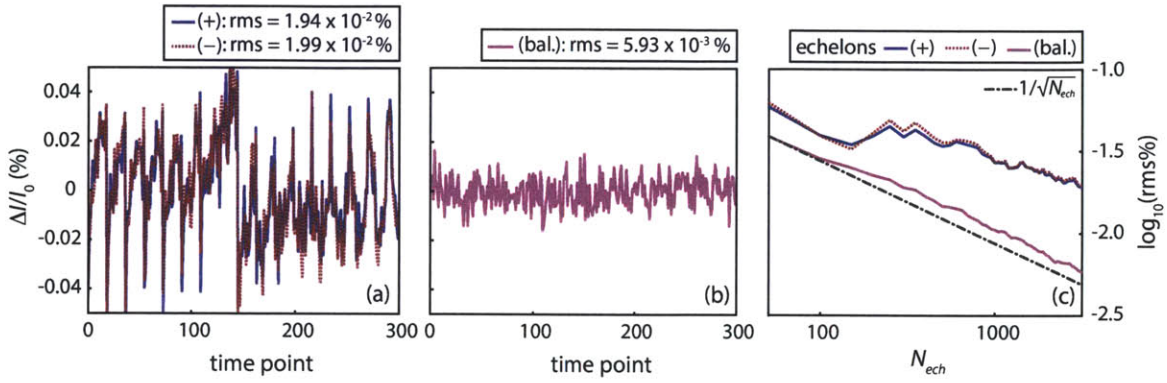

Figure 5-14: **Noise traces with optimization of relative grid location between (+) and (-) polarization and iterative optimization every 100 laser shots ($N = 50$) to compensate for laser drift and jitter.** (a) Averaged unbalanced noise traces, where the noise has been minimized. (b) Averaged balanced noise trace. (c) demonstrates the effectiveness of the iterative optimization procedure with $1/\sqrt{N}$ scaling of rms noise of the balanced trace. The noise of the unbalanced traces trend together as expected.

5.5 Conclusions and Outlook

For two THz single-shot methods, we carefully evaluated the following central criteria that would enable their use as a viable tool for multidimensional THz spectroscopy: signal reproducibility and noise floor. Expectedly, there was a fundamental tradeoff between fast acquisition and measurement noise, however the degree of effectiveness of noise suppression techniques was essential to the success of the single-shot method in achieving both criteria.

THz spectral interferometry presented a multitude of technical difficulties in terms of accurate alignment and interferometric phase stability, which led to unreliable signal strengths and a higher noise floor than standard scanning EO sampling, albeit sufficient time resolution. Common path optics, for example using phase masks and spatial light modulators, would be highly desirable for its success, but would significantly limit the time window.

In contrast, the dual echelons were able to accurately encode a THz signal into a spatial 2D image which is consequently mapped to the time domain, having well matched field strengths, spatio-temporal waveform, and frequency content. The imaging-based detection, compared to measuring laser intensity on low-noise photodiodes, is more sensitive to shot-to-shot pointing fluctuations and laser drift. These resulted in periodic artifacts in the time domain and a larger base-level noise from a single trace, but are lessened significantly with high-frequency and balanced detection along with extensive averaging. EO detection using the echelons substantially sped up acquisition time, without any concession to E-field accuracy, by attaining the same noise floor as the delay-line method in $1/20^{\text{th}}$ the number of laser shots required for a 10 ps temporal window of 50 fs increments at a 1 kHz acquisition rate. The amount of time saved is even greater for experiments that require additional time points for larger time windows (like temporally long resonant features) since acquisition time increases for the delay-line method, but not the single-shot method.

With respect to the relative ease of implementation of this fast-acquisition method that gives quantitative traces with a low noise floor, the dual echelons method is a convincing first alternative when transitioning to higher-dimension THz experiments. Specifically, there are additional advantages to recording a 2D trace quickly since pump-induced fluctuations (typically the dominant source of noise in strong pumping regimes) are largely minimized. Additionally, the method easily lends itself to measurements of small, nonlinear signals, like vibrational couplings, where higher sensitivity is needed, or of small changes in large THz signals, where both high sensitivity and high dynamic range are needed. Future experiments aim to use a lower-noise detector with larger bit depth, such as a scientific CMOS camera, to lower the minimum detectable signal, and a data transfer speed that is not rate-limiting. Furthermore, transitioning to a reflective large echelon would yield larger time windows for finer spectral resolution and allow for all steps to lie in the same image plane. In light of these recent measurements, we find that expediting THz detection using dual echelons is a powerful technique that may be implemented in a straightforward manner.

Chapter 6

Terahertz Photoconductivity of Semiconductors

In this chapter, I will describe our recent measurement of the minority carrier lifetime and photoconductivity of a thin-film semiconductor, tin (II) sulfide (SnS), at THz frequencies by using an optical pump-THz probe experimental setup. Picosecond carrier dynamics form an integral process in photovoltaic devices, which rely on efficient charge separation and transport. Our collaborators are interested in using THz-TDS to characterize the effects of defect chemistry that is closely tied to carrier lifetimes in SnS photovoltaics [148]. SnS has been proposed as a non-toxic, earth-abundant material, and cheap alternative for photovoltaic applications, specifically towards its application in solar cells [8]. This material was selected as a model system to evaluate the practical implementation of single-shot THz detection in terms of improvement in acquisition speed, S/N, and the ease of hardware and software integration. Most importantly, although we do not expect any frequency-dependence of the carrier lifetimes, this initial measurement serves as a prototype for future 2D Fourier transform THz spectroscopy. In that case, we would replace the optical pump with a THz pump, and probe a system with responses that may have very strong frequency-dependence in the

THz range, and so there is much merit in developing and demonstrating the ability of the new detection technique.

6.1 THz Transmission Experimental Setup

The THz transmission experimental setup is shown in Fig. 6-1, which consists of three arms: a 400 nm optical pump, a broadband THz probe, and an EO-sampling probe (i.e. the echelon beamlets). The generation and detection were carried out in 2 mm and 1 mm thick ZnTe crystals, respectively, yielding a bandwidth of approximately 0.2-2 THz. The detector in this case was a 16-bit scientific CMOS (sCMOS) camera (Andor Zyla) that operated at a maximum frame rate of 50 Hz. We chopped the THz probe at 25 Hz such that sequential images were detected with THz radiation absent and present; the 400 nm optical pump irradiated the sample at a 1 kHz repetition rate. The sample was a 1 μm thick film of SnS deposited on a 0.5 mm thick BK7 glass substrate (unfortunately the substrate absorbs a significant amount of THz radiation across THz probe bandwidth) fabricated by the Buonassisi group in the Department of Mechanical Engineering at MIT. The fluence of the 400 nm ($\sim$ 3 eV) optical pump at the sample was $\sim$ 0.1 mJ/cm^2; as a point of reference, SnS has an indirect band gap at 1.07 eV [148]. Additionally, the sample was measured to be 15-20% reflective at 400 nm. The setup was purged with dry air for several hours prior to the measurement.

The experimental setup was used to collect a THz time trace for every time delay between the optical pump and THz probe, T, for both the reference (substrate only) and sample (SnS on substrate). An example of a 2D time trace for the sample is shown in Fig. 6-2, where a vertical line-out yields a THz field temporal profile and a horizontal line-out essentially yields a 'peak scan' measurement that is representative of the carrier relaxation dynamics following optical excitation. In this particular measurement, it took around 2 hours to construct one 2D trace made up of 150 pump-probe time delays for a total time window of $\Delta T = 40$ ps and

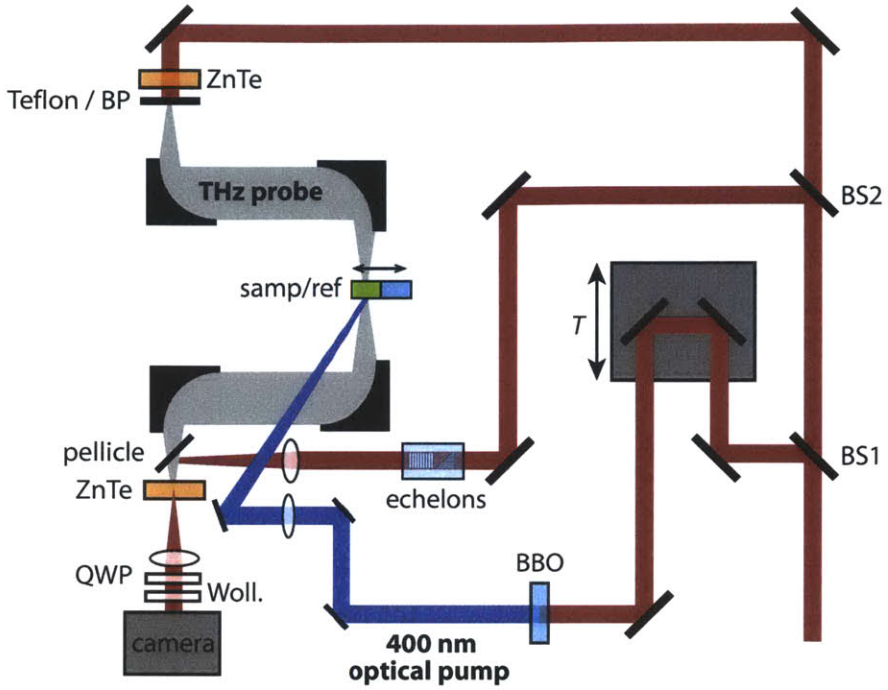

Figure 6-1: **Optical pump-THz probe experimental setup.** The input 800 nm beam is initially split by the first beamsplitter (BS1) into the pump and probe arms. The optical pump is directed onto a mechanical stage that gives the pump-probe time delay, T, and then through a SHG generation crystal to generate 400 nm light. The probe arm is split again by a second beamsplitter (BS1) into the THz generation and EO-sampling arms. The THz radiation was generated and detected in ZnTe. In this case, the EO-sampling arm is directed through two crossed echelons to give the time delay, t, for the THz time traces. Both the THz probe and optical pump are focused onto the same spot at the sample/reference position located after the first two off-axis parabolas. The EO-sampling beam (echelon beamlets) were consequently detected with a quarter wave plate (QWP) and Wollaston prism on a sCMOS camera.

averaged over 150 THz field time traces of 200 time delays for a time window of $\Delta t = 10$ ps for both the sample and reference; four 2D traces were averaged to yield the data in Fig. 6-2(a). It is important to note that we are measuring a 10% change in a 1% peak signal strength in this experiment; depending on the required S/N, acquisition times may be much shorter. The differential 2D time trace is shown in Fig. 6-2(a), where a pre-time-zero THz trace ($T = -5$ ps) has been subtracted from each THz trace at all pump-probe time delays.

We calibrated the system to be $\sim 8\times$ faster in absolute time including data collection and processing than conventional EO-sampling. It is possible that the factor of time im-

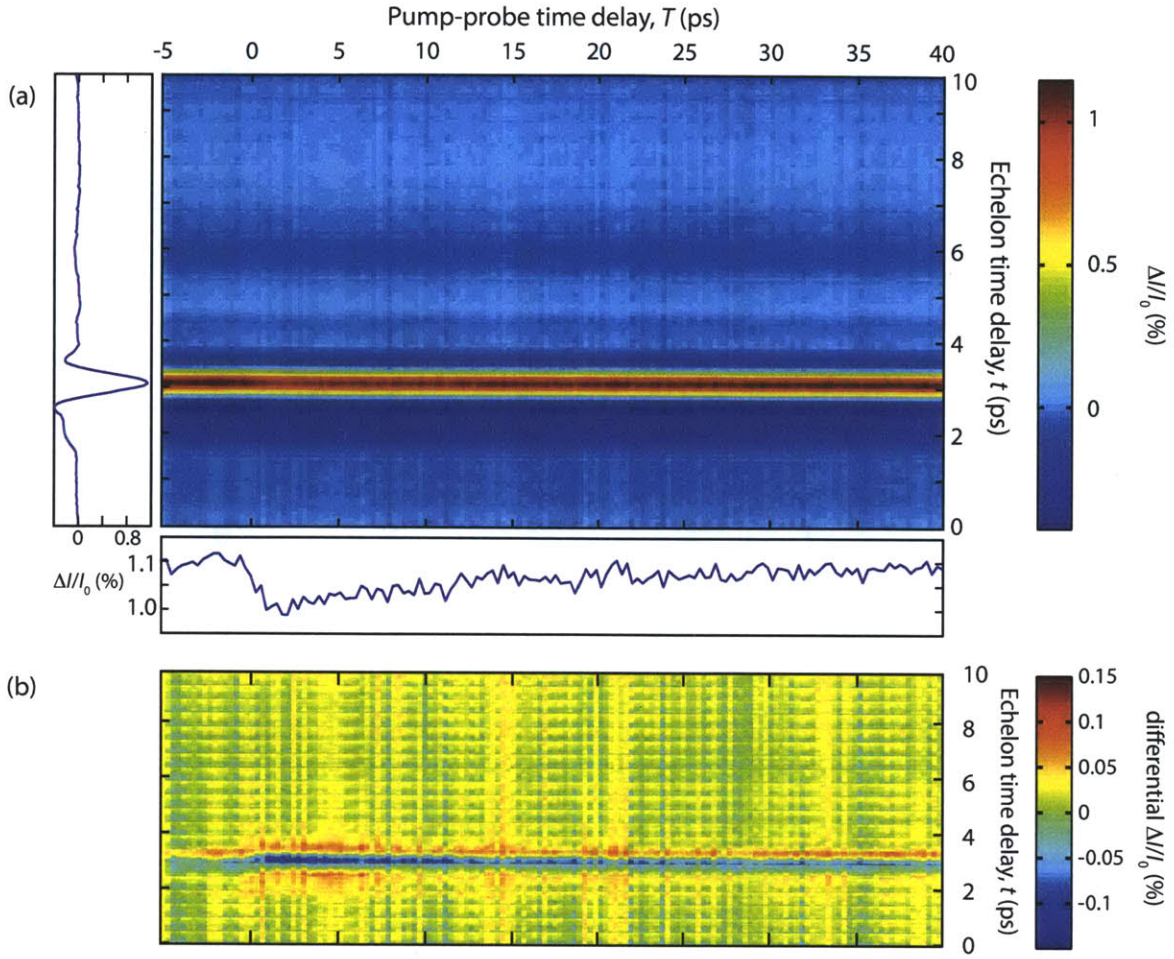

Figure 6-2: **Optical pump-THz probe 2D time traces with echelons.** (a) A 2D time trace that plots the THz time trace for each pump-probe time delay, T. This particular example is for the sample trace (SnS on substrate). A vertical line-out (left) at a selected pump-probe time delay, $T = -2$ ps. clearly shows an example of a THz field temporal profile; a reference trace (substrate only) is similar. A horizontal line-out (bottom) at a selected echelon time delay, $t = 3$ ps, shows the equivalent of a THz peak scan typically used to determine the carrier lifetime. (b) The relaxation dynamics are more evident in this 2D differential plot, where the a pre-time-zero THz trace (i.e. the first column of (a)) is subtracted from each THz trace at all pump-probe time delays.

provement may be increased by modifying the way the data are streamlined off the camera (complete bypass of the onboard camera RAM and directly to computer RAM instead) and the order of data processing. This acquisition time is longer than what was predicted in the previous chapter since here we account for data transfer time and the fact that the camera

acquires data at a lower rate (higher $1/f$ noise). However, because many fewer images are collected, overall the sCMOS is much faster and has better S/N than our previous 1 kHz CMOS camera. We are currently troubleshooting the data transfer process since ideally, the data transfer in this particular sCMOS camera should not be limiting our acquisition time. This camera interfaces with the computer via Dual Camera Link Interface (10-tap) with a bandwidth limitation of 850 MB/sec, however, currently we are only operating at a data transfer rate of 230 MB/sec. We believe that as data transfer rates become even faster, it will be possible to acquire at a rate of 1 kHz without the current detrimental impact on acquisition time and attain the predicted reduction factor of 20× determined in Chapter 5. Additionally, acquisition at 1 kHz will allow for the straightforward implementation of differential chopping, which is technically difficult to implement and less effective at the 50 Hz acquisition rate here.

6.2 THz Transmission

Time-domain THz detection has many benefits, most of which directly follow from the ability to coherently measure both the amplitude and phase of the THz E-field for the sample and reference, denoted as $E_{\mathrm{s}}(t)$ and $E_{\mathrm{r}}(t)$. The main advantage of particular interest for the characterization of material properties is the fact that complex optical properties (e.g., index of refraction, conductivity) can be extracted without using Kramers-Kronig relations, which are only effective if a very wide frequency range is covered. In addition, the measurements provide a non-contact electrical probe, which is very beneficial for thin or small-area samples that present technical difficulties in physical attachment of electrical contacts for photoconductive measurements as in a conventional four-point probe measurement. Finally, the measurement offers far higher bandwidth than can be achieved through conventional electrical measurement methods.

Prior to calculating the complex properties of the system, we need to consider the

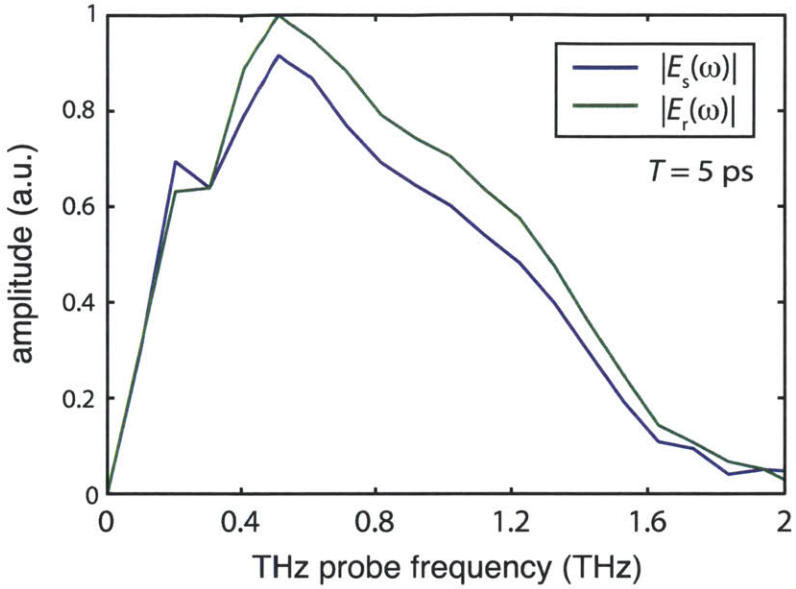

Figure 6-3: **Transmission spectra for sample and reference.** The transmission spectra are plotted for a pump-probe time delay of 5 ps, after the optical pump has irradiated the (sample+substrate)/substrate. Both spectra have been normalized to the substrate. The transmission spectrum of the sample shows that, following the generation of free carriers, free carrier absorption occurs across much of the THz bandwidth within the conduction band.

frequency-dependent transmission through the sample. The field transmission, $T_E(\omega)$, is calculated by firstly Fourier-transforming both $E_s(t)$ and $E_r(t)$ and dividing their respective amplitudes:

$$T_E(\omega) = \frac{|E_s(\omega)|}{|E_r(\omega)|}, \tag{6.1}$$

where $E_i(\omega) = \int_{-\infty}^{\infty} E_i(t)e^{-i\omega t}dt$. The transmission spectra for the sample and reference are plotted in Fig. 6-3 at a pump-probe time delay of 5 ps (i.e. THz probe arrives 5 ps after the 400 nm pump). It is already clear that the presence of the optical pump, which generates free carriers, leads to increased free carrier THz absorption across a wide relatively large bandwidth (below the peak at $\sim$ 0.4 THz, the inversion point in the THz spectrum yielded unphysical data that is indicative of a THz generation problem). The power transmission,

$T_P(\omega)$, follows by similarly using the intensity of the field:

$$T_P(\omega) = T_E(\omega)^2 = \frac{|E_s(\omega)|^2}{|E_r(\omega)|^2}. \tag{6.2}$$

Consequently, the optical density (OD) of the sample is:

$$\mathrm{OD}(\omega) = -\log_{10}\left(T_P(\omega)\right). \tag{6.3}$$

For the remainder of the section, the OD will be the measured quantity that we discuss.

6.3 Frequency-resolved Optical Density and Lifetimes

The OD as a function of pump-probe time delay and THz probe frequency is shown in Fig. 6-4. The frequency-dependence of the sample's OD is immediately apparent from the 2D plot, and is corroborated by a vertical line-out at $T = 5$ ps on the left. A horizontal line-out at 0.8 THz shows the carrier relaxation dynamics. At $T = 0$ ps the optical pump (3 eV) hits the sample and excites carriers from the valence band to way above the band gap (1.07 eV), high in the conduction band. Subsequently, the carriers relax to the bottom of the conduction band, during which time they can undergo free carrier THz absorption within the conduction band. This initial free carrier relaxation rate is observed as an exponential decay in the OD and has a characteristic time constant referred to as the carrier lifetime, τ, of the sample. At longer T, the system undergoes carrier recombination to the ground state in the valence band.

It is easier to compare the lifetimes across the THz bandwidth by normalizing to their peak ODs and subtracting off a pre-time-zero OD to yield an approximately zero baseline for each frequency. The normalized OD spectra are shown in Fig. 6-5(a). We fit the normalized

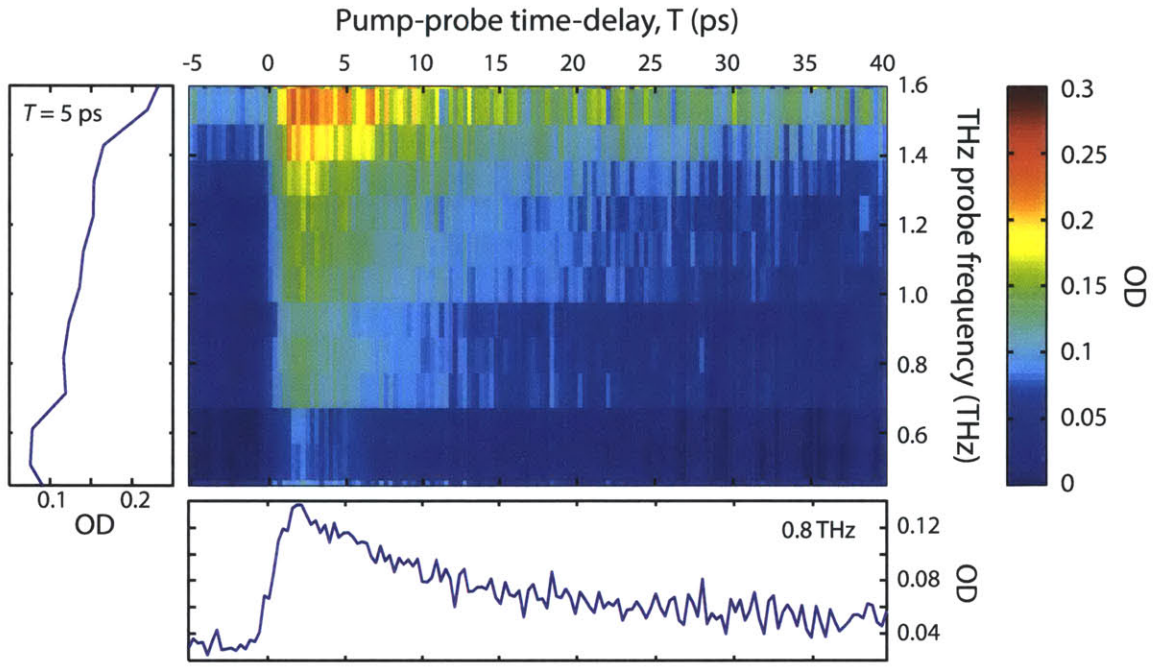

Figure 6-4: **Optical density spectra.** The measured frequency-dependent optical density for the thin-film sample of SnS is plotted as a function of the pump-probe time delay. The 2D plot shows frequency-dependent THz absorption following free carrier generation by the optical pump, illustrated by the vertical line-out at $T = 5$ ps (left). The system then slowly relaxes back to its unperturbed state on the picosecond timescale, which is clearly illustrated by the horizontal line-out at 0.8 THz (bottom).

exponential decays to the function:

$$F(t) = \exp(-t/\tau) + C, \tag{6.4}$$

where τ is the $1/e$ decay time and C is a constant offset from the pre-time-zero baseline that represents the carrier population at long times following relaxation to the conduction band. By definition, the carrier lifetime is the average time over which the minority carriers (either the electrons or holes, depending on whether the semiconductor is n- or p-type) take to recombine. We fit the exponential decays after $T = 2.5$ ps to avoid fitting around the peak. An example of one of the carrier lifetime fits is shown at 0.8 THz in Fig. 6-5(b).

We fit the exponential decays of the OD in the sample shown in Fig. 6-5(a) for a range of

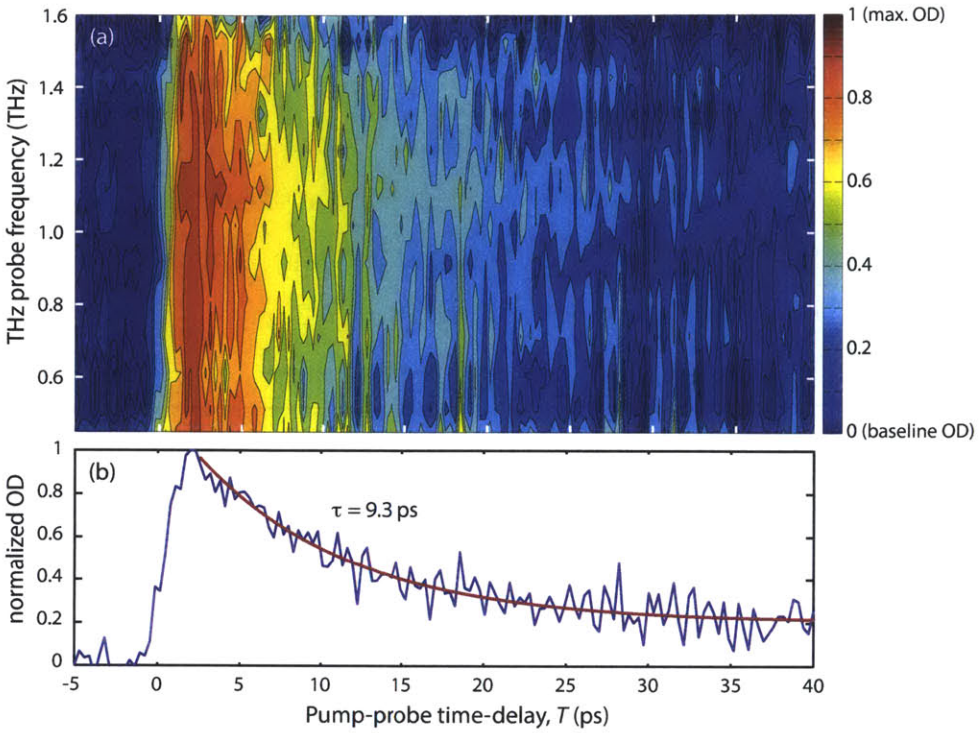

Figure 6-5: **Normalized OD spectra.** (a) The OD has been normalized to the peak for each frequency. The contour plot clearly illustrates the initial relaxation of the carriers, following optical excitation, to the bottom of the conduction band. On the nanosecond timescale, the carriers recombine to the ground state in the valence band and recover the baseline value (prior to optical excitation). (b) A horizontal line-out at 0.8 THz shows the exponential decay of the carriers. The exponential decay is fitted after $T = 2.5$ ps (red line) to yield the carrier lifetime, $\tau = 9.3$ ps.

frequencies (0.4-1.5 THz) that had good S/N, mostly dependent on the bandwidth of the THz probe, to yield accurate fit parameters. The extracted lifetimes, τ, for each THz frequency are plotted in Fig. 6-6(a). The data show relatively frequency-independent behavior, which is evident from the contour plot of the OD in Fig. 6-5(a). The average lifetime across the frequencies is $\tau_{\text{avg}} = 9.6 \pm 0.8$ ps, indicated by the dashed line in Fig. 6-6(a). We further confirmed the accuracy of this value by conducting a conventional peak scan using the EO sampling method, only measuring the peak value of the THz E-field in the time-domain as a function of pump-probe time delay, T. The peak scan in Fig. 6-6(b) also depicts the photoexcitation of carriers to the conduction band that results in THz free carrier absorption,

indicated by a rapid increase in the OD across the THz probe bandwidth. Subsequently, the OD decays to a value higher than that at pre-time-zero, before the optical pump arrives, as the carriers relax to the bottom of the conduction band. Only on the nanosecond time scale do all the holes and electrons undergo recombination at the valence band, such that the peak scan should recover to the baseline or ground state value. The peak scan measurement essentially recovers the same value for the lifetime, $\tau = 10.2$ ps.

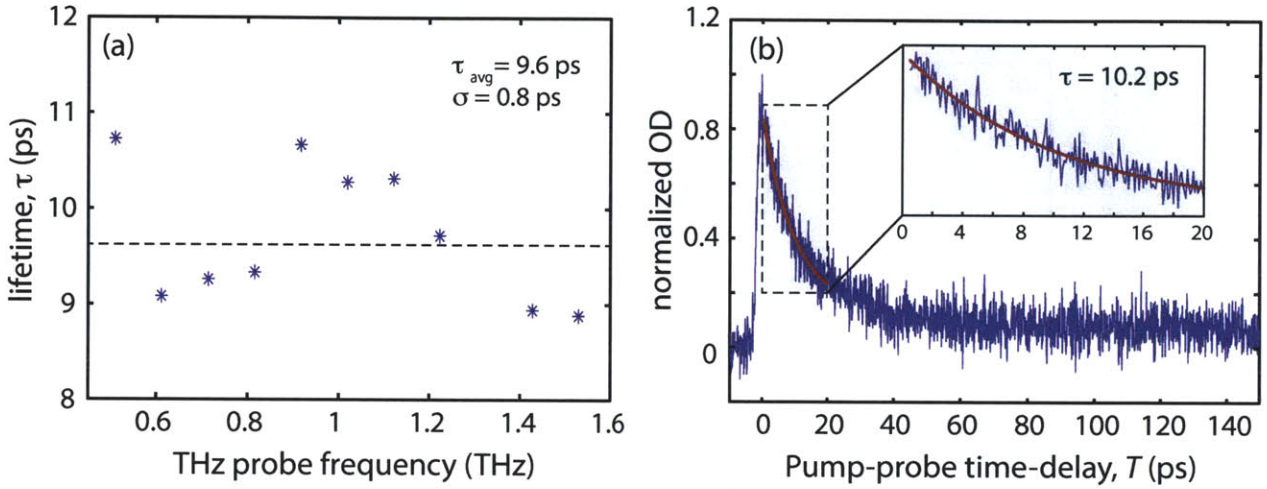

Figure 6-6: **Carrier lifetimes in SnS thin films.** (a) The exponential decays of the ODs in Fig. 6-5(a) were fitted to yield the lifetimes as a function of THz frequency over the range of 0.4-1.5 THz. Overall, no obvious frequency-dependence was observed in the lifetimes and so an average lifetime was calculated to be $\tau_{\mathrm{L,avg}} = 9.6 \pm 0.8$ ps. (b) A conventional peak scan of the THz E-field as a function of pump-probe time delay yields a comparable figure for the lifetime, $\tau = 10.2$ ps.

6.4 Complex Index of Refraction and Conductivity

As previously stated, the time-domain measurement of the THz E-field gives its amplitude and phase, both of which are used to determine the complex index of refraction. In the previous calculation of the transmission spectra, we only took advantage of the amplitude, but the phase becomes important for many measurements including 2D THz spectroscopy

measurements that we anticipate. The complex index of refraction has the general form:

$$\tilde{n}(\omega) = n(\omega) + i\kappa(\omega), \tag{6.5}$$

where n is the real index of refraction related to dispersive properties and κ is the imaginary index of refraction related to absorptive losses. The refractive index can be cast into an analytical form by taking the extreme limits of a thick and thin film. For a film of intermediate thickness, the index of refraction can be found by modeling $\tilde{n}$ and comparing the parameters to experimental results.

6.4.1 Thick Film Limit

In the thick film limit, we assume that absorption in the sample is minimal such that $\kappa \ll n$ and consequently, the Fresnel transmission coefficients that we use later can be approximated by real numbers (i.e. the real part of the material indices). Firstly, if we consider a plane wave propagating along z, the spatiotemporal E-field has the form: $E(z,t) = E_0 e^{i(\tilde{k}z - \omega t)}$, where $\tilde{k} = \omega\tilde{n}/c = \omega(n + i\kappa)/c$ is the complex wave vector. The intensity of the field follows as:

$$I = EE^* = I_0 \exp(-2\omega\kappa z/c) \tag{6.6}$$

The absorption coefficient, α, from Beer's law ($I(z) = I_0 e^{-\alpha z}$) is related to the imaginary part of the index, κ, according to the equation above:

$$\alpha(\omega) = \frac{2\omega\kappa(\omega)}{c}. \tag{6.7}$$

However, it is more useful to have both n and κ in terms of the complex, frequency-dependent transmission (or OD), which we can easily attain experimentally. If we focus on

the spatial propagation on the plane wave in the time-domain, we can simplify the E-field to:

$$E(z,t) = E_0(t)\exp\left(-\frac{\omega}{c}\kappa z + i\frac{\omega}{c}nz\right) \tag{6.8}$$

The Fourier transform of the (6.8) gives the frequency-dependent form of the E-field. For propagation through a sample of thickness d, we set $z = d$ to yield:

$$E(z=d,\omega) = E_0(\omega)\exp\left(-\frac{\omega}{c}\kappa(\omega)d + i\frac{\omega}{c}n(\omega)d\right) \tag{6.9}$$

The experimentally measured transmission through a sample can be approximated by taking account of the Fresnel losses at the interfaces. At normal incidence, moving from medium 1 (air) to medium 2 (sample), the transmission coefficient is:

$$T^{(1)} = \frac{2n_2}{n_1 + n_2}, \tag{6.10}$$

where n_1 and n_2 are the frequency-dependent real indices of medium 1 and 2 (assume that $\kappa \ll n$). Similarly, the E-field exits the sample by moving from medium 2 into medium 1, after reflecting off the back surface of the sample, and so the overall transmission coefficient is: $T = T^{(1)}T^{(2)} = (4n_1n_2)/(n_1 + n_2)^2$. The E-field as it is transmitted from air ($n_1 = 1$) through the sample ($n_2 = n_s$) and back to air is then:

$$E_s(\omega) = T \cdot E(\omega) = \frac{4n_s(\omega)}{(1+n_s(\omega))^2}E_0(\omega)\exp\left(-\frac{\omega}{c}\kappa_s(\omega)d + i\frac{\omega}{c}n_s(\omega)d\right) \tag{6.11}$$

The complex transmission of a sample can be calculated by using a blank reference (i.e. air, $\tilde{n} = n = 1$) so that $E_r(\omega) = E_0(\omega)\exp(i\omega d/c)$ according to (6.9):

$$\tilde{T}(\omega) = \frac{E_s}{E_r} = \frac{4n_s(\omega)}{[1+n_s(\omega)]^2}\exp\left[-\frac{\omega}{c}\kappa_s(\omega)d + i\frac{\omega}{c}(n_s(\omega)-1)d\right]. \tag{6.12}$$

6.4.1.1 Complex Index of Refraction

It is straightforward from here to assign the real index component, n_s, to the phase of the complex transmission ($\tilde{T}(\omega) = A(\omega)e^{i\phi(\omega)}$); rearranging the phase term in (6.12) gives:

$$n_s(\omega) = 1 + \frac{c}{\omega d}\phi(\omega). \tag{6.13}$$

Similarly, the imaginary index component of the sample, κ_s, can be given by the amplitude of the complex transmission:

$$\kappa_s(\omega) = -\frac{c}{\omega d}\ln\left[A(\omega)\frac{[1+n_s(\omega)]^2}{4n_s(\omega)}\right]. \tag{6.14}$$

It is evident that once we determine the real index from the phase of the experimentally-determined complex transmission, we can calculate the imaginary index knowing the complementary frequency-dependent amplitude of the complex transmission, $A(\omega)$, without ever employing the Kramers-Kronig relation. Subsequently, the absorption coefficient given in (6.7) may be calculated from $\kappa_s(\omega)$, which represents the $1/e$ decay length.

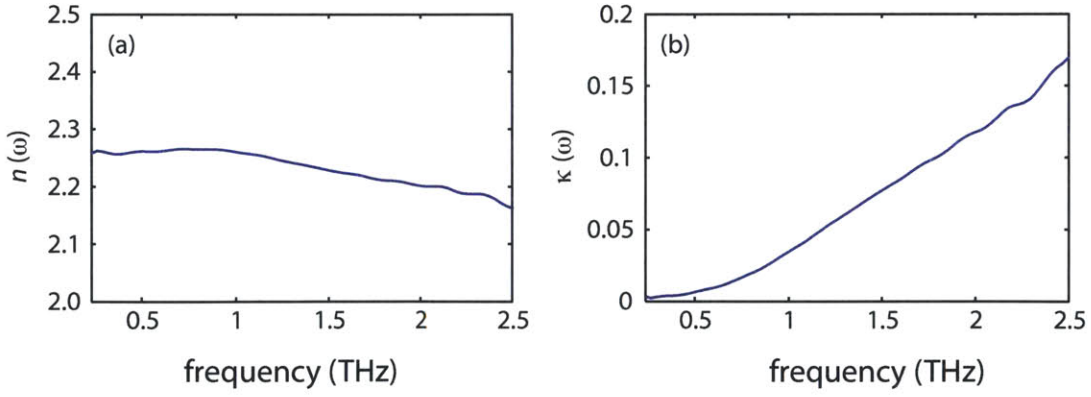

Figure 6-7: **Complex index of refraction of BK7 glass substrate.** (a) Real part of the refractive index. (b) Imaginary part of refractive index.

As we will see in the next section, the determination of the conductivity of the thin film, SnS, requires that we know the complex index of refraction of the substrate that the film is

deposited on. The substrate is a bulk material that can be considered a thick film; therefore, the 'sample' is the BK7 glass substrate and the 'reference' is air. The real and imaginary index are shown in Fig. 6-7.

6.4.1.2 Complex Conductivity

Although not used here, but described for completeness, the complex conductivity of the substrate can be found directly from the real and imaginary parts of the complex index of refraction. Firstly, the complex dielectric function for a nonmagnetic material ($\mu = 1$) is:

$$\tilde{\varepsilon}(\omega) = \tilde{n}(\omega)^2 = [n(\omega) + i\kappa(\omega)]^2 \tag{6.15}$$

$$= \varepsilon_\infty + \frac{i\tilde{\sigma}(\omega)}{\omega\varepsilon_0}, \tag{6.16}$$

where ε_∞ is the high-frequency dielectric constant resulting from the bound electrons in the valence band and $\tilde{\sigma}$ is the complex conductivity. The second term in the equation above is the contribution from the free carriers. The complex dielectric function can be written as:

$$\tilde{\varepsilon}(\omega) = \varepsilon_1(\omega) + i\varepsilon_2(\omega). \tag{6.17}$$

The real and imaginary parts of the dielectric function directly follow from (6.15):

$$\varepsilon_1 = n(\omega)^2 - \kappa(\omega)^2 \tag{6.18}$$

$$\varepsilon_2 = 2n(\omega)\kappa(\omega). \tag{6.19}$$

Similary, we can express the complex conductivity by additionally using (6.16) [149, 150]:

$$\tilde{\sigma}(\omega) = \sigma_\mathrm{r}(\omega) + i\sigma_\mathrm{i}(\omega), \tag{6.20}$$

where the real and imaginary parts of the conductivity are respectively given by:

$$\sigma_r(\omega) = 2n(\omega)\kappa(\omega)\omega\varepsilon_0 \tag{6.21}$$

$$\sigma_i(\omega) = \left(\varepsilon_\infty - n(\omega)^2 + \kappa(\omega)^2\right)\omega\varepsilon_0. \tag{6.22}$$

6.4.2 Thin Film Limit

For a thin conductive film, the complex transmission takes on a different analytical form given by Glover and Tinkham [151]. In this regime, the sample is a thin film deposited on a thick substrate. The complex E-field transmission of a thin film is the ratio of the complex E-field transmitted through both the film and substrate and the substrate only, and can be written according to the Tinkham formula: [152–154]:

$$\tilde{T}_E(\omega) = \frac{\tilde{E}_{\text{film+sub}}(\omega)}{\tilde{E}_{\text{sub}}(\omega)} = \frac{n_{\text{sub}}(\omega) + 1}{n_{\text{sub}}(\omega) + 1 + Z_0\tilde{\sigma}(\omega)d} \tag{6.23}$$

where n_{sub} is the real index of refraction of the substrate (here, of BK7 glass), $Z_0 = 377\ \Omega$ is the vacuum impedance, and d is the thickness of the conducting layer. In our case, the thickness of the conducting layer in the SnS film is approximately the penetration depth of the 400 nm optical pump the material. The remaining depth of the film retains its bulk properties since it is not directly excited by the optical pump. The absorption coefficient at 400 nm was measured to be $\alpha_{400\text{nm}} = 72\ \mu\text{m}^{-1}$ and so the penetration depth is approximately 14 nm.

Using the complex index of the BK7 glass substrate determined in the previous section and the experimental complex transmission spectra, we determined the real and imaginary parts of the conductivity of the SnS film, depicted in a 2D plot in Fig. 6-8. The real part of the conductivity, commonly referred to as just the conductivity, significantly affects the absorptive (or imaginary) part of the dielectric function. This means that the higher

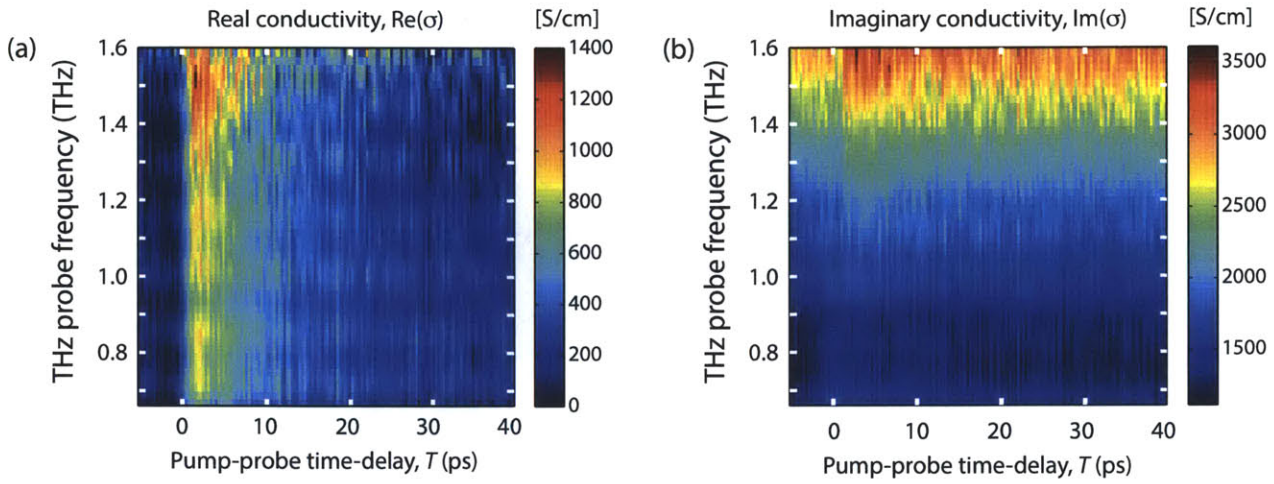

Figure 6-8: **THz complex conductivity of SnS film as a function of T.** (a) Real part of the conductivity. (b) Imaginary part of the conductivity.

the conductivity, the more quickly the material will absorb the E-field and become more opaque. The real part of the conductivity of SnS at THz frequencies is shown in Fig. 6-8(a). At the onset of the optical pump at $T = 0$, the interband transitions cause the conductivity to quickly rise from zero due to the generation of free carriers, and then the conductivity decreases with T to an equilibrium state that is frequency-independent and follows Drude-like behavior. The generation of a large amount of carriers forces the system into a non-equilibrium state, where the system deviates from the classical Drude model; similar effects have been seen in GaAs [155]. This explains the frequency-dependence of the conductivity at early pump-probe delay times since the Drude model predicts a flat conductivity across the frequencies. Alternatively, the imaginary part of the conductivity, which affects the real part of the dielectric constant, is called the susceptance and is a measure of how much the system is susceptible to conducting a changing current. The imaginary part of the conductivity is shown in Fig. 6-8(b) increases slightly after the optical pump arrives but shows no dynamical change as a function of T. The fact that both the real and imaginary parts of the complex conductivity are positive is characteristic of a non-polarizable material (a polarizable material has positive σ_r and a negative σ_i) [150].

A very important application of measuring the conductivity of thin films via time-domain THz spectroscopy is the determination of the dc electrical conductivity and carrier mobilities by extrapolation from the experimental data in a non-contact method. This relies on the fact that the material does not have any low-lying THz resonances that can obscure the measurement. In that case, the Drude model and its variants can be used for the extrapolation. Furthermore, the ability to directly measure the THz conductivity of a material will become more important in the future development of devices (e.g., in THz transistors that use materials like mercury telluride thin films [2]).

Bibliography

[1] D. H. Auston, K. P. Cheung, J. A. Valdmanis, and D. A. Kleinman, "Cherenkov Radiation from Femtosecond Optical Pulses in Electro-Optic Media," *Physical Review Letters*, vol. 53, no. 16, pp. 1555–1558, 1984.

[2] A. M. Shuvaev, G. V. Astakhov, A. Pimenov, C. Brüne, H. Buhmann, and L. W. Molenkamp, "Giant Magneto-Optical Faraday Effect in HgTe Thin Films in the Terahertz Spectral Range," *Physical Review Letters*, vol. 106, p. 107404, Mar. 2011.

[3] T. Feurer, N. S. Stoyanov, D. W. Ward, J. C. Vaughan, E. R. Statz, and K. A. Nelson, "Terahertz Polaritonics," *Annual Review of Materials Research*, vol. 37, pp. 317–350, Aug. 2007.

[4] C. A. Werley, S. M. Teo, B. K. Ofori-Okai, P. Sivarajah, and K. A. Nelson, "High-Resolution, Low-Noise Imaging in THz Polaritonics," *IEEE Transactions on Terahertz Science and Technology*, vol. 3, no. 3, pp. 239–247, 2013.

[5] C. A. Werley, Q. Wu, K. H. Lin, C. R. Tait, A. Dorn, and K. A. Nelson, "Comparison of phase-sensitive imaging techniques for studying terahertz waves in structured $LiNbO_3$," *JOSA B*, vol. 27, no. 11, pp. 2350–2359, 2010.

[6] I. P. Kaminow, W. L. Mammel, and H. P. Weber, "Metal-clad optical waveguides: analytical and experimental study," *Applied optics*, vol. 13, pp. 396–405, Feb. 1974.

[7] C. A. Werley, K. Fan, A. C. Strikwerda, S. M. Teo, X. Zhang, R. D. Averitt, and K. A. Nelson, "Time-resolved imaging of near-fields in THz antennas and direct quantitative measurement of field enhancements," *Optics Express*, vol. 20, no. 8, pp. 8551–8567, 2012.

[8] P. Sinsermsuksakul, K. Hartman, S. Bok Kim, J. Heo, L. Sun, H. Hejin Park, R. Chakraborty, T. Buonassisi, and R. G. Gordon, "Enhancing the efficiency of SnS solar cells via band-offset engineering with a zinc oxysulfide buffer layer," *Applied Physics Letters*, vol. 102, no. 5, p. 053901, 2013.

[9] D. Jin, A. Kumar, K. Hung Fung, J. Xu, and N. X. Fang, "Terahertz plasmonics in ferroelectric-gated graphene," *Applied Physics Letters*, vol. 102, no. 20, p. 201118, 2013.

[10] P. R. Smith, D. H. Auston, and M. C. Nuss, "Subpicosecond Photoconducting Dipole Antennas," *IEEE Journal of Quantum Electronics*, vol. 24, no. 2, pp. 255–260, 1988.

[11] C. Fattinger and D. Grischkowsky, "Terahertz beams," *Applied Physics Letters*, vol. 54, no. 6, p. 490, 1989.

[12] J. E. Pedersen, S. R. Keiding, C. B. Sorensen, P. E. Lindelof, W. W. Ruhle, and X. Q. Zhou, "5-THz bandwidth from a GaAs-on-silicon photoconductive receiver," *Journal of Applied Physics*, vol. 74, no. 11, p. 7022, 1993.

[13] D. You, R. R. Jones, and P. H. Bucksbaum, "Generation of high-power sub-single-cycle 500-fs electromagnetic pulses," *Optics Letters*, vol. 18, no. 4, pp. 290–292, 1993.

[14] A. Nahata, D. H. Auston, T. F. Heinz, and C. Wu, "Coherent detection of freely propagating terahertz radiation by electro-optic sampling," *Applied Physics Letters*, vol. 68, no. 2, p. 150, 1996.

[15] A. G. Stepanov, L. Bonacina, S. V. Chekalin, and J.-P. Wolf, "Generation of 30 μJ single-cycle terahertz pulses at 100 Hz repetition rate by optical rectification," *Optics Letters*, vol. 33, pp. 2497–9, Nov. 2008.

[16] K.-L. Yeh, M. C. Hoffmann, J. Hebling, and K. A. Nelson, "Generation of 10 μJ ultrashort terahertz pulses by optical rectification," *Applied Physics Letters*, vol. 90, no. 17, p. 171121, 2007.

[17] M. Liu, H. Y. Hwang, H. Tao, A. C. Strikwerda, K. Fan, G. R. Keiser, A. J. Sternbach, K. G. West, S. Kittiwatanakul, J. Lu, S. A. Wolf, F. G. Omenetto, X. Zhang, K. A. Nelson, and R. D. Averitt, "Terahertz-field-induced insulator-to-metal transition in vanadium dioxide metamaterial," *Nature*, vol. 487, pp. 345–8, July 2012.

[18] Y. R. Shen, "Far-Infrared Generation by Optical Mixing," *Progress in Quantum Electronics*, vol. 4, pp. 207–232, 1976.

[19] R. W. Boyd, *Nonlinear Optics.* Elsevier Inc., 3rd ed., 2008.

[20] A. Nahata, D. H. Auston, T. F. Heinz, and C. Wu, "Coherent detection of freely propagating terahertz radiation by electro-optic sampling," *Applied Physics Letters*, vol. 68, no. 2, p. 150, 1996.

[21] A. Nahata, D. H. Auston, C. Wu, and J. T. Yardley, "Generation of terahertz radiation from a poled polymer," *Applied Physics Letters*, vol. 67, no. 10, p. 1358, 1995.

[22] D. T. F. Marple, "Refractive Index of ZnSe, ZnTe, and CdTe," *Journal of Applied Physics*, vol. 35, no. 3, p. 539, 1964.

[23] T. Hattori, Y. Homma, A. Mitsuishi, and M. Tacke, "Indices of refraction of ZnS, ZnSe, ZnTe, CdS, and CdTe in the far infrared," *Optics Communications*, vol. 7, pp. 229–232, Mar. 1973.

[24] A. Rice, Y. Jin, X. F. Ma, X.-C. Zhang, D. Bliss, J. Larkin, and M. Alexander, "Terahertz optical rectification from 110 zinc-blende crystals," *Applied Physics Letters*, vol. 64, no. 11, p. 1324, 1994.

[25] M. Ebrahim-Zadeh and I. T. Sorokina, *Mid-Infrared Coherent Sources and Applications*. Springer, 1st ed., 2008.

[26] S. A. Ku, C. M. Tu, W. Chu, C. W. Luo, K. H. Wu, A. Yabushita, C. C. Chi, and T. Kobayashi, "Saturation of the free carrier absorption in ZnTe crystals," *Optics Express*, vol. 21, no. 12, pp. 13930–13937, 2013.

[27] M. C. Hoffmann, K.-L. Yeh, J. Hebling, and K. A. Nelson, "Efficient terahertz generation by optical rectification at 1035 nm," *Optics Express*, vol. 15, pp. 11706–13, Sept. 2007.

[28] T. Löffler, T. Hahn, M. Thomson, F. Jacob, and H. Roskos, "Large-area electro-optic ZnTe terahertz emitters," *Optics Express*, vol. 13, pp. 5353–62, July 2005.

[29] J. Hebling, G. Almasi, I. Kozma, and J. Kuhl, "Velocity matching by pulse front tilting for large area THz-pulse generation," *Optics Express*, vol. 10, pp. 1161–6, Oct. 2002.

[30] Y. Shen, T. Watanabe, D. Arena, C.-C. Kao, J. Murphy, T. Tsang, X. Wang, and G. Carr, "Nonlinear Cross-Phase Modulation with Intense Single-Cycle Terahertz Pulses," *Physical Review Letters*, vol. 99, p. 043901, July 2007.

[31] D. H. Auston and M. C. Nuss, "Electrooptic Generation and Detection of Femtosecond Electrical Transients," *IEEE Journal of Quantum Electronics*, vol. 24, no. 2, pp. 184–197, 1988.

[32] B. Bartal, I. Kozma, A. Stepanov, G. Almási, J. Kuhl, E. Riedle, and J. Hebling, "Toward generation of μJ range sub-ps THz pulses by optical rectification," *Applied Physics B*, vol. 86, pp. 419–423, Dec. 2007.

[33] T. P. Dougherty, G. P. Wiederrecht, and K. A. Nelson, "Impulsive stimulated Raman scattering experiments in the polariton regime," *Journal of the Optical Society of America B*, vol. 9, p. 2179, Dec. 1992.

[34] K. Huang, "On the Interaction between the Radiation Field and Ionic Crystals," *Proceedings of the Royal Society A: Mathematical, Physical and Engineering Sciences*, vol. 208, pp. 352–365, Sept. 1951.

[35] M. Born and K. Huang, *Dynamical Theory of Crystal Lattices.* Oxford University Press, 1st ed., 1954.

[36] M. Nakamura, S. Higuchi, S. Takekawa, K. Terabe, Y. Furukawa, and K. Kitamura, "Optical Damage Resistance and Refractive Indices in Near-Stoichiometric MgO-Doped $LiNbO_3$," *Japanese Journal of Applied Physics*, vol. 41, pp. L49–L51, Jan. 2002.

[37] L. Palfalvi, J. Hebling, J. Kuhl, A. Peter, and K. Polgar, "Temperature dependence of the absorption and refraction of Mg-doped congruent and stoichiometric $LiNbO_3$ in the THz range," *Journal of Applied Physics*, vol. 97, no. 12, p. 123505, 2005.

[38] D. Marcuse and I. P. Kaminow, "Modes of a Symmetric Slab Optical Waveguide in Birefringent Media, Part II: Slab with Coplanar Optical Axis," *IEEE Journal of Quantum Electronics*, vol. 15, no. 2, pp. 92–101, 1979.

[39] C. Yang, Q. Wu, J. Xu, K. A. Nelson, and C. A. Werley, "Experimental and theoretical analysis of THz-frequency, direction-dependent, phonon polariton modes in a subwavelength, anisotropic slab waveguide," *Optics Express*, vol. 18, no. 25, pp. 26351–26364, 2010.

[40] A. S. Barker, Jr. and R. Loudon, "Dielectric Properties and Optical Phonons in $LiNbO_3$," *Physical Review*, vol. 158, no. 2, pp. 433–445, 1967.

[41] N. S. Stoyanov, T. Feurer, D. W. Ward, E. R. Statz, and K. A. Nelson, "Direct Visualization of a Polariton Resonator in the THz Regime," *Optics Express*, vol. 12, pp. 2387–96, May 2004.

[42] A. Yariv, *Quantum Electronics.* John Wiley & Sons, Inc., 3rd ed., 1989.

[43] P. C. M. Planken, H.-K. Nienhuys, H. J. Bakker, and T. Wenckebach, "Measurement and calculation of the orientation dependence of terahertz pulse detection in ZnTe," *Journal of the Optical Society of America B*, vol. 18, no. 3, p. 313, 2001.

[44] C. A. Werley, *THz polaritonics : Optical THz generation, detection, and control on a chip.* PhD thesis, Massachusetts Institute of Technology, 2012.

[45] E. Hecht, *Optics*. Addison-Wesley Longman, Incorporated, 4th ed., 2002.

[46] Z. Jiang, F. G. Sun, Q. Chen, and X.-C. Zhang, "Electro-optic sampling near zero optical transmission point," *Applied Physics Letters*, vol. 74, no. 9, p. 1191, 1999.

[47] C. A. Werley, S. M. Teo, and K. A. Nelson, "Pulsed laser noise analysis and pump-probe signal detection with a data acquisition card," *Review of Scientific Instruments*, vol. 82, no. 12, p. 123108, 2011.

[48] T. Feurer, J. C. Vaughan, and K. A. Nelson, "Spatiotemporal coherent control of lattice vibrational waves," *Science*, vol. 299, pp. 374–7, Jan. 2003.

[49] K. Katayama, H. Inoue, H. Sugiya, Q. Shen, T. Toyoda, and K. A. Nelson, "Generation and detection of tunable phonon polaritons using a single transmission grating," *Applied Physics Letters*, vol. 92, no. 3, p. 031906, 2008.

[50] K.-H. Lin, C. A. Werley, and K. A. Nelson, "Generation of multicycle terahertz phonon-polariton waves in a planar waveguide by tilted optical pulse fronts," *Applied Physics Letters*, vol. 95, no. 10, p. 103304, 2009.

[51] N. S. Stoyanov, D. W. Ward, T. Feurer, and K. A. Nelson, "Terahertz polariton propagation in patterned materials," *Nature Materials*, vol. 1, pp. 95–8, Oct. 2002.

[52] E. R. Statz, D. W. Ward, and K. A. Nelson, "Phonon-Polariton Excitation in Ferroelectric Slab Waveguides and Photonic Crystals," in *Ultrafast Phenomena XV*, pp. 7–9, 2006.

[53] C. A. Werley, K. A. Nelson, and R. C. Tait, "Direct visualization of terahertz electromagnetic waves in classic experimental geometries," *American Journal of Physics*, vol. 80, no. 1, p. 72, 2012.

[54] N. S. Stoyanov, T. Feurer, D. W. Ward, and K. A. Nelson, "Integrated diffractive terahertz elements," *Applied Physics Letters*, vol. 82, no. 5, p. 674, 2003.

[55] P. Peier, S. Pilz, and T. Feurer, "Time-resolved coherent imaging of a THz multilayer response," *Journal of the Optical Society of America B*, vol. 26, p. 1649, July 2009.

[56] P. Peier, H. Merbold, V. Pahinin, K. A. Nelson, and T. Feurer, "Imaging of THz waves in 2D photonic crystal structures embedded in a slab waveguide," *New Journal of Physics*, vol. 12, p. 013014, Jan. 2010.

[57] D. W. Ward, J. D. Beers, T. Feurer, E. R. Statz, N. S. Stoyanov, and K. A. Nelson, "Coherent control of phonon-polaritons in a terahertz resonator fabricated with femtosecond laser machining," *Optics Letters*, vol. 29, pp. 2671–3, Nov. 2004.

[58] R. M. Koehl, S. Adachi, and K. A. Nelson, "Direct Visualization of Collective Wavepacket Dynamics," *The Journal of Physical Chemistry A*, vol. 103, pp. 10260–10267, Dec. 1999.

[59] P. Peier, S. Pilz, F. Müller, K. A. Nelson, and T. Feurer, "Analysis of phase contrast imaging of terahertz phonon-polaritons," *Journal of the Optical Society of America B*, vol. 25, p. B70, May 2008.

[60] Q. Wu, C. A. Werley, K.-H. Lin, A. Dorn, M. G. Bawendi, and K. A. Nelson, "Quantitative phase contrast imaging of THz electric fields in a dielectric waveguide," *Optics Express*, vol. 17, pp. 9219–25, May 2009.

[61] F. Zernike, "Phase contrast: A new method for the microscopic observation of transparent objects," *Physica*, vol. 9, pp. 686–698, 1942.

[62] J. W. Goodman, *Introduction to Fourier Optics.* Roberts, 3rd ed., 2005.

[63] A. Yariv and P. Yeh, *Photonics: Optical Electronics in Modern Communications.* Oxford Univ. Press, 6th ed., 2007.

[64] P. Sivarajah, C. A. Werley, B. K. Ofori-Okai, and K. A. Nelson, "Chemically assisted femtosecond laser machining for applications in $LiNbO_3$ and $LiTaO_3$," *Applied Physics A*, July 2013.

[65] S. Inoué and R. Oldenboug, *Handbook of Optics.* McGraw-Hill, 2nd ed., 1995.

[66] H. Tao, N. I. Landy, C. M. Bingham, X. Zhang, R. D. Averitt, and W. J. Padilla, "A metamaterial absorber for the terahertz regime: Design, fabrication and characterization," *Optics Express*, vol. 16, no. 10, pp. 1494–1496, 2008.

[67] D. Schurig, J. J. Mock, B. J. Justice, S. A. Cummer, J. B. Pendry, A. F. Starr, and D. R. Smith, "Metamaterial electromagnetic cloak at microwave frequencies," *Science*, vol. 314, pp. 977–80, Nov. 2006.

[68] H. Tao, A. C. Strikwerda, K. Fan, C. M. Bingham, W. J. Padilla, X. Zhang, and R. D. Averitt, "Terahertz metamaterials on free-standing highly-flexible polyimide substrates," *Journal of Physics D: Applied Physics*, vol. 41, p. 232004, Dec. 2008.

[69] P. Bak, C. Tang, and K. Wiesenfeld, "Self-Organized Criticality: An Explanation of $1/f$ Noise," *Physical Review Letters*, vol. 59, no. 4, pp. 381–384, 1987.

[70] F. Blanchard, K. Ooi, T. Tanaka, A. Doi, and K. Tanaka, "Terahertz spectroscopy of the reactive and radiative near-field zones of split ring resonator," *Optics Express*, vol. 20, pp. 19395–403, Aug. 2012.

[71] Y. A. Vlasov, H. F. Hamann, and S. J. Mcnab, "Active control of slow light on a chip with photonic crystal waveguides," *Nature*, vol. 438, no. November, pp. 65–69, 2005.

[72] W. M. Green, M. J. Rooks, L. Sekaric, and Y. A. Vlasov, "Ultra-compact, low RF power, 10 Gb/s silicon Mach-Zehnder modulator," *Optics Express*, vol. 15, pp. 17106–13, Dec. 2007.

[73] J. B. Khurgin, "Optical buffers based on slow light in electromagnetically induced transparent media and coupled resonator structures: comparative analysis," *Journal of the Optical Society of America B*, vol. 22, no. 5, pp. 1062–1074, 2005.

[74] J. T. Mok and B. J. Eggleton, "Photonics: Expect more delays," *Nature*, vol. 433, no. 7028, pp. 811–812, 2005.

[75] M. A. Seo, H. R. Park, S. M. Koo, D. J. Park, J. H. Kang, O. K. Suwal, S. S. Choi, P. C. M. Planken, G. S. Park, N. K. Park, Q. H. Park, and D. S. Kim, "Terahertz field enhancement by a metallic nano slit operating beyond the skin-depth limit," *Nature Photonics*, vol. 3, no. March, pp. 152–156, 2009.

[76] D. R. Ward, F. Hüser, F. Pauly, J. C. Cuevas, and D. Natelson, "Optical rectification and field enhancement in a plasmonic nanogap," *Nature Nanotechnology*, vol. 5, pp. 732–6, Oct. 2010.

[77] D. R. Smith and J. B. Pendry, "Homogenization of metamaterials by field averaging (invited paper)," *Journal of the Optical Society of America B*, vol. 23, no. 3, p. 391, 2006.

[78] B. E. A. Saleh and M. C. Teich, *Fundamental of Photonics.* John Wiley & Sons, Inc., 2nd ed., 2007.

[79] H. Kim, C. M. Gilmore, A. Pique, J. S. Horwitz, H. Mattoussi, H. Murata, Z. H. Kafafi, and D. B. Chrisey, "Electrical, optical, and structural properties of indium-tin-oxide thin films for organic light-emitting devices," *Journal of Applied Physics*, vol. 86, no. 11, p. 6451, 1999.

[80] T. Bauer, J. S. Kolb, T. Loffler, E. Mohler, H. G. Roskos, and U. C. Pernisz, "Indium-tin-oxide-coated glass as dichroic mirror for far-infrared electromagnetic radiation," *Journal of Applied Physics*, vol. 92, no. 4, p. 2210, 2002.

[81] C. G. Granqvist and A. Hultaker, "Transparent and conducting ITO films: new developments and applications," *Thin Solid Films*, vol. 411, pp. 1–5, 2002.

[82] J. Jin, *The Finite Element Method in Electromagnetics.* Wiley, 2014.

[83] M. Sadiku, *Numerical Techniques in Electromagnetics, Second Edition.* Taylor & Francis, 2000.

[84] J. Hu and C. R. Menyuk, "Understanding leaky modes: slab waveguide revisited," *Advances in Optics and Photonics*, vol. 1, p. 58, Jan. 2009.

[85] E. Cassedy and M. Cohn, "On the Existence of Leaky Waves Due to a Line Source Above a Grounded Dielectric Slab," *IRE Transactions on Microwave Theory and Techniques*, vol. 9, no. May, pp. 243–247, 1961.

[86] L. Goldstone and A. Oliner, "Leaky-Wave Antennas I: Rectangular Waveguides," *IRE Transactions on Antennas and Propagation*, vol. 7, no. 4, pp. 307–319, 1959.

[87] H. A. Haus and D. A. B. Miller, "Attenuation of Cutoff Modes and Leaky Modes of Dielectric Slab Structures," *IEEE Journal of Quantum Electronics*, vol. 22, no. 2, pp. 310–318, 1986.

[88] D. B. Hall, "Leaky waves in a heteroepitaxial film," *Journal of Applied Physics*, vol. 44, no. 5, p. 2271, 1973.

[89] H. A. Haus, *Waves and Fields in Optoelectronics.* CBLS, 2004.

[90] R. A. Serway, *Principles of Physics.* Saunders College Pub., 2nd ed., 1998.

[91] H.-T. Chen, J. F. O. Hara, A. K. Azad, A. J. Taylor, R. D. Averitt, D. B. Shrekenhamer, and W. J. Padilla, "Experimental demonstration of frequency-agile terahertz metamaterials," *Nature Photonics*, no. 100, pp. 295–298, 2008.

[92] C. A. Schmuttenmaer, "Exploring Dynamics in the Far-Infrared with Terahertz Spectroscopy," *Chemical Reviews*, vol. 104, no. 4, pp. 1759–1779, 2004.

[93] A. Bax and R. Freeman, "Investigation of complex networks of spin-spin coupling by two-dimensional NMR," *Journal of Magnetic Resonance (1969)*, vol. 44, pp. 542–561, Sept. 1981.

[94] M. Khalil, N. Demirdöven, and A. Tokmakoff, "Coherent 2D IR Spectroscopy: Molecular Structure and Dynamics in Solution," *The Journal of Physical Chemistry A*, vol. 107, pp. 5258–5279, July 2003.

[95] T. Brixner, J. Stenger, H. M. Vaswani, M. Cho, R. E. Blankenship, and G. R. Fleming, "Two-dimensional spectroscopy of electronic couplings in photosynthesis.," *Nature*, vol. 434, pp. 625–8, Mar. 2005.

[96] K. W. Stone, K. Gundogdu, D. B. Turner, X. Li, S. T. Cundiff, and K. A. Nelson, "Two-quantum 2D FT electronic spectroscopy of biexcitons in GaAs quantum wells," *Science*, vol. 324, pp. 1169–73, May 2009.

[97] D. H. Arias, K. W. Stone, S. M. Vlaming, B. J. Walker, M. G. Bawendi, R. J. Silbey, V. Bulović, and K. A. Nelson, "Thermally-limited exciton delocalization in superradiant molecular aggregates," *The Journal of Physical Chemistry B*, vol. 117, pp. 4553–9, Apr. 2013.

[98] K. P. H. Lui and F. A. Hegmann, "Ultrafast carrier relaxation in radiation-damaged silicon on sapphire studied by optical-pumpterahertz-probe experiments," *Applied Physics Letters*, vol. 78, no. 22, p. 3478, 2001.

[99] P. Uhd Jepsen, W. Schairer, I. H. Libon, U. Lemmer, N. E. Hecker, M. Birkholz, K. Lips, and M. Schall, "Ultrafast carrier trapping in microcrystalline silicon observed in optical pumpterahertz probe measurements," *Applied Physics Letters*, vol. 79, no. 9, p. 1291, 2001.

[100] P. A. George, J. Strait, J. Dawlaty, S. Shivaraman, M. Chandrashekhar, F. Rana, and M. G. Spencer, "Spectroscopy of the Carrier Relaxation Epitaxial Graphene," *Nano Letters*, vol. 8, no. 12, pp. 4248–4251, 2008.

[101] D. A. Yarotski, R. D. Averitt, N. Negre, S. A. Crooker, A. J. Taylor, G. P. Donati, A. Stintz, L. F. Lester, and K. J. Malloy, "Ultrafast carrier-relaxation dynamics in self-assembled InAs / GaAs quantum dots," *Journal of the Optical Society of America B*, vol. 19, no. 6, pp. 1480–1484, 2002.

[102] M. C. Hoffmann, J. Hebling, H. Y. Hwang, K.-L. Yeh, and K. A. Nelson, "Impact ionization in InSb probed by terahertz pumpterahertz probe spectroscopy," *Physical Review B*, vol. 79, p. 161201, Apr. 2009.

[103] J. Hebling, M. C. Hoffmann, H. Y. Hwang, K.-L. Yeh, and K. A. Nelson, "Observation of nonequilibrium carrier distribution in Ge, Si, and GaAs by terahertz pump-terahertz probe measurements," *Physical Review B*, vol. 81, p. 035201, Jan. 2010.

[104] B. I. Greene, J. F. Federici, D. R. Dykaar, A. F. Levi, and L. Pfeiffer, "Picosecond pump and probe spectroscopy utilizing freely propagating terahertz radiation," *Optics Letters*, vol. 16, pp. 48–9, Jan. 1991.

[105] P. N. Saeta, J. F. Federici, B. I. Greene, D. R. Dykaar, and D. F. L. Dykaar, "Intervalley scattering in GaAs and InP probed by pulsed farinfrared transmission spectroscopy lntervalley scattering in GaAs and InP probed transmission spectroscopy by pulsed far-infrared," *Applied Physics Letters*, vol. 60, no. 12, pp. 1477–1479, 1992.

[106] M. Nakajima, N. Takubo, Z. Hiroi, Y. Ueda, and T. Suemoto, "Photoinduced metallic state in VO_2 proved by the terahertz pump-probe spectroscopy," *Applied Physics Letters*, vol. 92, no. 1, p. 011907, 2008.

[107] E. Knoesel, M. Bonn, J. Shan, and T. Heinz, "Charge Transport and Carrier Dynamics in Liquids Probed by THz Time-Domain Spectroscopy," *Physical Review Letters*, vol. 86, pp. 340–343, Jan. 2001.

[108] R. H. M. Groeneveld and D. Grischkowsky, "Picosecond time-resolved far-infrared experiments on carriers and excitons in GaAs-AlGaAs multiple quantum wells," *Journal of the Optical Society of America B*, vol. 11, no. 12, pp. 2502–2507, 1994.

[109] W. Kuehn, K. Reimann, M. Woerner, T. Elsaesser, and R. Hey, "Two-dimensional terahertz correlation spectra of electronic excitations in semiconductor quantum wells," *The Journal of Physical Chemistry B*, vol. 115, pp. 5448–55, May 2011.

[110] W. Kuehn, K. Reimann, M. Woerner, T. Elsaesser, R. Hey, and U. Schade, "Strong Correlation of Electronic and Lattice Excitations in GaAs/AlGaAs Semiconductor Quantum Wells Revealed by Two-Dimensional Terahertz Spectroscopy," *Physical Review Letters*, vol. 107, p. 067401, Aug. 2011.

[111] M. Woerner, W. Kuehn, P. Bowlan, K. Reimann, and T. Elsaesser, "Ultrafast two-dimensional terahertz spectroscopy of elementary excitations in solids," *New Journal of Physics*, vol. 15, p. 025039, Feb. 2013.

[112] P. Bowlan, E. Martinez-Moreno, K. Reimann, T. Elsaesser, and M. Woerner, "Ultrafast terahertz response of multilayer graphene in the nonperturbative regime," *Physical Review B*, vol. 89, p. 041408, Jan. 2014.

[113] A. Tokmakoff, M. D. Fayer, and D. D. Dlott, "Chemical reaction initiation and hot-spot formation in shocked energetic molecular materials," *The Journal of Physical Chemistry*, vol. 97, pp. 1901–1913, Mar. 1993.

[114] J. Savolainen, S. Ahmed, and P. Hamm, "Two-dimensional Raman-terahertz spectroscopy of water," *Proceedings of the National Academy of Sciences of the United States of America*, vol. 110, no. 51, pp. 20402–20407, 2013.

[115] Z. Jiang and X. Zhang, "Electro-optic measurement of THz field pulses with a chirped optical beam Electro-optic measurement of THz field pulses with a chirped optical beam," *Applied Physics Letters*, vol. 72, no. 16, pp. 1945–1947, 1998.

[116] A. Galvanauskas, J. A. Tellefsen, A. Krotkus, M. Oberg, and B. Broberg, "Real-time picosecond electro-optic oscilloscope technique using a tunable semiconductor laser," *Applied Physics Letters*, vol. 60, no. 2, p. 145, 1992.

[117] P. Y. Han, Z. Jiang, J. A. Riordana, L. Wang, and X. Zhang, "Ultrafast electro-optic sensors and magneto-optic sensors for THz beams," *Proceedings of SPIE*, vol. 3277, pp. 198–207, 1998.

[118] J. R. Fletcher, "Distortion and uncertainty in chirped pulse THz spectrometers," *Optics Express*, vol. 10, no. 24, pp. 1425–1430, 2002.

[119] F. G. Sun, Z. Jiang, and X.-C. Zhang, "Analysis of terahertz pulse measurement with a chirped probe beam," *Applied Physics Letters*, vol. 73, no. 16, p. 2233, 1998.

[120] X.-Y. Peng, O. Willi, M. Chen, and A. Pukhov, "Optimal chirped probe pulse length for terahertz pulse measurement," *Optics Express*, vol. 16, pp. 12342–9, Aug. 2008.

[121] B. Yellampalle, K. Y. Kim, G. Rodriguez, J. H. Glownia, and A. J. Taylor, "Algorithm for high-resolution single-shot THz measurement using in-line spectral interferometry with chirped pulses," *Applied Physics Letters*, vol. 87, no. 21, p. 211109, 2005.

[122] K. Y. Kim, B. Yellampalle, G. Rodriguez, R. D. Averitt, A. J. Taylor, and J. H. Glownia, "Single-shot, interferometric, high-resolution, terahertz field diagnostic," *Applied Physics Letters*, vol. 88, no. 4, p. 041123, 2006.

[123] J. Shan, A. S. Weling, E. Knoesel, L. Bartels, G. A. Reider, and T. F. Heinz, "Single-shot measurement of terahertz electromagnetic pulses by use of electro-optic sampling," *Optics Letters*, vol. 25, no. 6, pp. 426–428, 2000.

[124] Y. Kawada, T. Yasuda, A. Nakanishi, K. Akiyama, and H. Takahashi, "Single-shot terahertz spectroscopy using pulse-front tilting of an ultra-short probe pulse," *Optics Express*, vol. 19, pp. 11228–35, June 2011.

[125] Y. Kawada, T. Yasuda, H. Takahashi, and S.-i. Aoshima, "Real-time measurement of temporal waveforms of a terahertz pulse using a probe pulse with a tilted pulse front," *Optics Letters*, vol. 33, no. 2, pp. 180–182, 2008.

[126] H. J. Bakker, G. C..Cho, H. Kurz, Q. Wu, and X.-C. Zhang, "Distortion of terahertz pulses in electro-optic sampling," *Journal of the Optical Society of America B*, vol. 15, p. 1795, June 1998.

[127] G. Gallot and D. Grischkowsky, "Electro-optic detection of terahertz radiation," *Journal of the Optical Society of America B*, vol. 16, p. 1204, Aug. 1999.

[128] O. E. Martinez, "Pulse Distortions in Tilted Pulse Schemes for Ultrashort Pulses," *Optics Communications*, vol. 59, no. 3, pp. 229–232, 1986.

[129] A. E. Kaplan, "Diffraction-induced transformation of near-cycle and subcycle pulses," *Journal of the Optical Society of America B*, vol. 15, p. 951, Mar. 1998.

[130] X. Xie, J. Dai, and X.-C. Zhang, "Coherent Control of THz Wave Generation in Ambient Air," *Physical Review Letters*, vol. 96, p. 075005, Feb. 2006.

[131] S. P. Jamison, A. M. Macleod, W. A. Gillespie, and D. A. Jaroszynski, "High-temporal-resolution, single-shot characterization of terahertz pulses," *Optics Letters*, vol. 28, no. 18, pp. 1710–1712, 2003.

[132] F. Salin, P. Georges, G. Roger, and A. Brun, "Single-shot measurement of a 52-fs pulse," *Applied Optics*, vol. 26, no. 21, pp. 4528–4531, 1987.

[133] R. Trebino, K. W. Delong, D. N. Fittinghoff, J. N. Sweetser, B. A. Richman, M. A. Krumbu, and D. J. Kane, "Measuring ultrashort laser pulses in the time-frequency domain using frequency-resolved optical gating," *Review of Scientific Instruments*, vol. 68, no. 9, pp. 3277–3295, 1997.

[134] N. H. Matlis, G. R. Plateau, J. V. Tilborg, and W. P. Leemans, "Single-shot spatiotemporal measurements of ultrashort THz waveforms using temporal electric-field cross correlation," *Journal of the Optical Society of America B*, vol. 28, no. 1, pp. 23–27, 2011.

[135] S. P. Le Blanc, E. W. Gaul, N. H. Matlis, A. Rundquist, and M. C. Downer, "Single-shot measurement of temporal phase shifts by frequency-domain holography," *Optics Letters*, vol. 25, pp. 764–6, May 2000.

[136] N. H. Matlis, S. Reed, S. S. Bulanov, V. Chvykov, G. Kalintchenko, T. Matsuoka, P. Rousseau, V. Yanovsky, A. Maksimchuk, S. Kalmykov, G. Shvets, and M. C. Downer, "Snapshots of laser wakefields," *Nature Physics*, vol. 2, pp. 749–753, Oct. 2006.

[137] K. Y. Kim, I. Alexeev, and H. M. Milchberg, "Single-shot supercontinuum spectral interferometry," *Applied Physics Letters*, vol. 81, no. 22, p. 4124, 2002.

[138] G. Sharma, K. Singh, I. Al-Naib, R. Morandotti, and T. Ozaki, "Terahertz detection using spectral domain interferometry," *Optics Letters*, vol. 37, pp. 4338–4340, Oct. 2012.

[139] G. P. Wakeham and K. A. Nelson, "Dual-echelon single-shot femtosecond spectroscopy," *Optics Letters*, vol. 25, pp. 505–7, Apr. 2000.

[140] K. Y. Kim, B. Yellampalle, A. J. Taylor, G. Rodriguez, and J. H. Glownia, "Single-shot terahertz pulse characterization via two-dimensional electro-optic imaging with dual echelons," *Optics Letters*, vol. 32, pp. 1968–70, July 2007.

[141] L. Lepetit, G. Chériaux, and M. Joffre, "Linear techniques of phase measurement by femtosecond spectral interferometry for applications in spectroscopy," *Journal of the Optical Society of America B*, vol. 12, p. 2467, Dec. 1995.

[142] J. V. Tilborg, C. Tóth, N. H. Matlis, G. R. Plateau, and W. P. Leemans, "Single-shot measurement of the spectral envelope of broad-bandwidth terahertz pulses from femtosecond electron bunches," *Optics Letters*, vol. 33, no. 11, pp. 1186–1188, 2008.

[143] P. R. Poulin and K. A. Nelson, "Irreversible Organic Crystalline Chemistry Monitored in Real Time," *Science*, vol. 313, pp. 1756–1760, 2006.

[144] G. P. Wakeham, D. D. Chung, and K. A. Nelson, "Femtosecond time-resolved spectroscopy of energetic materials," *Thermochimica Acta*, vol. 384, pp. 7–21, 2002.

[145] T. Shin, *Photoinduced Phase Transitions Studied by Femtosecond Single-shot Spectroscopy.* PhD thesis, Massachusetts Institute of Technology, 2010.

[146] Y. Minami, Y. Hayashi, J. Takeda, and I. Katayama, "Single-shot measurement of a terahertz electric-field waveform using a reflective echelon mirror," *Applied Physics Letters*, vol. 103, no. 5, p. 051103, 2013.

[147] I. H. Malitson, "Interspecimen Comparison of the Refractive Index of Fused Silica," *Journal of the Optical Society of America*, vol. 55, no. 10, pp. 1205–1209, 1965.

[148] J. Vidal, S. Lany, M. DAvezac, A. Zunger, A. Zakutayev, J. Francis, and J. Tate, "Band-structure, optical properties, and defect physics of the photovoltaic semiconductor SnS," *Applied Physics Letters*, vol. 100, no. 3, p. 032104, 2012.

[149] H. Chen, C. T. Chan, and P. Sheng, "Transformation optics and metamaterials," *Nature Materials*, vol. 9, pp. 387–96, May 2010.

[150] J. Lloyd-Hughes and T.-I. Jeon, "A Review of the Terahertz Conductivity of Bulk and Nano-Materials," *Journal of Infrared, Millimeter, and Terahertz Waves*, vol. 33, pp. 871–925, May 2012.

[151] R. E. Glover and M. Tinkham, "Conductivity of Superconducting Films for Photon Energies between 0.3 and 40 kT_c," *Physical Review*, vol. 108, no. 2, pp. 243–256, 1957.

[152] D. G. Cooke, F. A. Hegmann, E. C. Young, and T. Tiedje, "Electron mobility in dilute GaAs bismide and nitride alloys measured by time-resolved terahertz spectroscopy," *Applied Physics Letters*, vol. 89, no. 12, p. 122103, 2006.

[153] M. Walther, D. Cooke, C. Sherstan, M. Hajar, M. Freeman, and F. Hegmann, "Terahertz conductivity of thin gold films at the metal-insulator percolation transition," *Physical Review B*, vol. 76, p. 125408, Sept. 2007.

[154] M. Tinkham, "Energy Gap Interpretation of Experiments of Infrared Transmission through Superconducting Films," *Physical Review*, vol. 104, no. 3, pp. 845–846, 1956.

[155] M. Beard, G. Turner, and C. Schmuttenmaer, "Transient photoconductivity in GaAs as measured by time-resolved terahertz spectroscopy," *Physical Review B*, vol. 62, pp. 15764–15777, Dec. 2000.